Diode laser based velocity sensors for industrial applications

Iversen, Theis Faber Quist

Publication date:
2011

Document Version
Publisher's PDF, also known as Version of record

Diode laser based velocity sensors for industrial applications

Theis F. Q. Iversen

Ph.D. Thesis

OPDI Technologies A/S
Technical University of Denmark, Department of Photonics Engineering,
DTU Fotonik

Abstract

In this thesis the use of dynamic speckle patterns and interferometric techniques is investigated for measuring the motion of diffusely scattering, rigid objects that are illuminated by a coherent light source. The focus is on measuring pure object translation and pure rotation. Principles and methods from spatial filtering velocimetry are employed to perform the measurements.

A novel measurement principle is developed for three dimensional translational velocity measurements based on imaging speckle interferometry. A plane object is illuminated by a single beam of coherent light and an image of the illuminated part of the object is formed. The introduction of a coherent, angular off-set reference wave in the image plane introduces a fringe pattern in addition to the speckle pattern. It is observed that the fringe pattern translates in response to out-of-plane translation of the object, while the speckle pattern generally translates in response to in-plane object translation. This simple geometrical modification of the incidence angle of the reference wave allows measurement of out-of-plane translation, retaining the directional information, without the need for optical frequency shifting equipment used in conventional heterodyning configurations. Furthermore, the optical imaging geometry, connecting the object plane and observation plane, enables the measurement of local out-of-plane motion within the image itself.

To understand the interaction of the spatial filters with the intensity distribution and thus the impact on performance, both numerical and analytical models of the intensity dynamics are developed. The numerical model is developed with the specific task of evaluating the performance of rectangular apodized spatial filters that are designed to measure all three velocity components. Using the results of the numerical simulation, an optimum system configuration, utilizing the fringe orientation flexibility to eliminate cross-talk between the spatial filters measuring the in-plane and out-of-plane velocity components, is identified. The analytical model is based on the ensemble averaged intensity crosscorrelation function, derived using complex *ABCD* formalism, and is developed for general system studies of translational and rotational velocity measurements.

Using the results from the numerical and analytical models, spatial filters are applied to extract the velocity of an object translating in three dimensions. Specifically, a detector array arrangement is applied to measure the in-plane translation and an integrated optical spatial filter based on a lenticular lens array is applied to measure the out-of plane translation.

In the case of an in-plane rotating cylindrical object the analytical model predicts, under certain conditions, a spatially dependent displacement rate of the fringe pattern that depends on the image coordinate. This is exploited to extract the in-plane angular velocity of using spatial filters implemented as a specialized set of detector arrays.

The integrated optical spatial filter is used as a receiver in free space miniaturized translational sensors for cursor control solutions. The optical spatial filter consists of an array of cylindrical micro-lenses that, in combination with a focusing lens and detector arrangement, forms the spatial filter. The optical spatial filter is part of a single optical unit, combining an additional optical spatial filter and a transmitter

used for beam shaping. The optical unit used in the miniaturized sensor is acting in combination with an application specific integrated circuit (ASIC) fitted with appropriate detector arrays facilitating a two dimensional velocity measurement of in-plane translation of a rigid object (surface).
Particularly, the beam shaping transmitter optic is redesigned for optimum performance using a Fourier optical diffraction model. Furthermore, a ray tracing model is developed for the receiving part of the optical unit. The model shows a previously not recognized effect of aberration in the focusing lens that limits the number of lenslets contributing constructively to the signal. Furthermore, a source of unwanted passbands in the transfer function of the receiver is identified using a non-sequential ray tracing model. Prototypes, implementing the recommendations proposed by these models, were manufactured. The results of performance tests of the manufactured prototypes are presented and the results are discussed.
A method for characterizing the radius of curvature and array period of the micro-optical cylindrical lens array, used in the integrated optical spatial filter, is developed. The method is based on observing the far-field diffraction pattern of the cylindrical lens array when illuminated by a coherent light source. The diffraction pattern obtained in the far-field of the illuminated lens array reveals information about the average radius of curvature of the lenslets in the array via the diffraction efficiency while the angular separation between individual diffraction orders is measured to obtain the lens array period. Special emphasis is placed on the potential for minimizing the measurement cycle time, robustness and reliability of the method. Scanning probe microscopes are used to validate the accuracy of the proposed method.
The scattering properties of fingertip tissue structures known as dermal ridge patterns are investigated. A fingertip is placed in contact with a planar dielectric surface and illuminated by coherent light under total internal reflection conditions. The experimental observations provide a basis for further investigation into the associated effects on observed speckle pattern statistics and a theoretical model for the intensity crosscorrelation function is outlined and discussed. The observations made outlines possible advantageous properties that may be exploited to develop ultrathin touch sensitive sensors for use as cursor control devices in form-factor critical applications, such as e.g. mobile phones.

Resume

I denne afhandling behandles brugen af dynamiske speckle mønstre og interferometriske teknikker med henblik på at måle bevægelse af diffust spredende rigide objekter der er belyst af en kohærent lyskilde. Fokus er primært rettet mod at måle ren translation og ren rotation. Metoder fra rumlig filtrerings velocimetri bliver anvendt til at fortage målingerne.
Et nyt måleprincip, til at måle tredimensional translation, bliver udviklet. Princippet er baseret på at kombinere en kohærent referencebølge med et specklebillede optaget af det belyste område på objektet. Den kohærente referencebølge sammenfalder med specklebilledet, under en vinkel, hvilket resulterer i genereringen af et "fringe" interferens mønster der er overlejret det eksisterende specklebillede. Denne konfiguration betegnes som et billeddannende shearing interferometer. Det observeres at fringemønstret translaterer i billedeplanet som svar på objekt translation ud-af-planet, hvorimod specklebilledet selv generelt translaterer som svar på objekt translation i-planet.
Denne simple modifikation af indfaldsvinklen af referencebølgen muliggør både måling af ud-af-planet translation samt retnings bestemmelse af denne uden brug af fx frekvensskiftende udstyr som anvendes i konventionel heterodyn detektering. Ydermere, muliggøre den billedannede geometri bestemmelsen af lokal ud-af-planet translation af objektet ved at observere den lokale fringe bevægelse i billedeplanet.
For at opnå en dybere indsigt i samspillet mellem den dynamiske intensitetsdistribution, målt med det billeddannende shearing interferometer, og de rumlige filtre der bruges til at måle objektets bevægelse baseret på denne, bliver der udviklet både numeriske og analytiske modeller af den dynamiske intensitetsdistribution. Den numeriske model bliver udviklet med det specifikke formål at evaluere ydeevnen og signal karakteristikker for rektangulært vægtede rumlige filtre der er designet, hver især, til at måle alle tre hastigheds komponenter af et rigidt objekts translation. Ud fra disse numeriske resultater identificeres en optimal konfiguration der benytter retningsfleksibiliteten af fringemønstret til at eliminere krydstale fænomener mellem de rumlige filtre der måler hhv. ud-af-planet og i-planet hastigheds komponenterne. Den analytiske model er baseret på intensitets-krydskorrelationsfunktionen, der udledes ved hjælp af kompleks *ABCD* matrix teori, og er beregnet til at foretage generelle system studier af translation og rotations hastighedsmålinger. Resultaterne fra de numeriske og analytiske modeller bruges til, på mest effektiv vis, eksperimentelt at anvende rumlige filtre til at måle et objekts tredimensionelle translation. I eksperimentet bliver et detektorarrangement bliver anvendt til at måle i-planet translation af objektet hvorimod et integreret optisk rumligt filter bliver anvendt til at måle ud-af-planet translationen.
I det specifikke tilfælde hvor objektet er cylinderformet og roterer i planet viser den analytiske model, under visse omstændigheder, at fringemønstrets forskydingsrate afhænger lineært af billedekoordinaten. Denne egenskab udnyttes til at ekstrahere vinkel hastigheden af et roterende cylinderformet objekt ved anvendelse af en

rumlig filter konfiguration der tager højde for den rumligt afhængige forskydningsrate af fringemønstret.
Det integrerede optiske filter bliver brugt som modtager i miniaturiserede sensorer designet til at måle todimensionel translation af overflader i cursor kontrol applikationer. Det optiske rumlige filter består af et gitter af cylinderformede mikrolinser der sammen med en fokuseringslinse og et detektor arrangement implementerer det rumlige filter. Det optiske rumlige filter er del af en integreret optisk enhed der indeholder endnu et optisk rumligt filter samt en transmitter der står for konditionering af belysningen af overfladen der måles på. Den optiske enhed agerer i samspil med en applikations specifik integreret kreds (ASIC) der er udstyret med passende detektor arrangementer hvormed den todimensionelle hastighed af en translaterende overflade kan bestemmes.
Transmitter strukturen designes på ny ved hjælp af en Fourier optisk model for at opnå en mere optimal belysnings profil af overfladen. Ydermere, opstilles der ray-tracing modeller for modtagerdelen af den optiske enhed. En effekt, der akkrediteres til aberrationer i fokuserings linsen, viser en øvre grænse for hvor mange mikrolinser der kan medtages i gitteret som samtidigt bidrager konstruktivt til signalet. Ved at bruge en såkaldt ikke-sekventiel ray-tracing model identificeres en kilde til uønskede båndpas i overførselsfunktionen for det optiske rumlige filter. Der fremstilles og testes prototyper der implementerer modellernes anbefalinger. Resultaterne fra ydelsestest præsenteres og diskuteres.
En metode til at karakterisere både krumningsradius og gitterperiode af mikrolinserne i det optiske rumlige filter bliver udviklet. Metoden beror på at observere fjern-felts intensitetsdistributionen af mikrolinserne, belyst af en kohærent lyskilde. Det resulterende diffraktionsmønster indeholder information vedrørende gitterperioden via vinkelseparation af diffraktionsordnerne og krumningsradius via diffraktionseffektiviteten af diffraktionsordnerne. I udviklingen af metoden lægges der især vægt på at nedbringe måletiden, samt at opnå en høj grad af robusthed og pålidelighed. Der anvendes scanning-probe instrumenter til at efterprøve nøjagtigheden af metoden.
De spredende egenskaber af den specielle struktur af vævet på en fingerspids, kendt som ”dermal ridges” undersøges. En fingerspids placeres i kontakt med et fladt dielektrisk medium hvorpå kontakt området mellem fingerspidsen og det dielektriske medie belyses. Belysningen sker således at betingelsen for total intern refleksion er opfyldt. De eksperimentelle observationer danner basis for en dybere undersøgelse af de associerede effekter på den observerede specklestatistik. Ydermere, leder observationerne til skitseringen af en teoretisk model der beskriver intensitets-krydskorrelationsfunktionen for det observerede specklemønster, der baseres på de specielle egenskaber af fingerspidsens strukturer. Slutteligt, diskuteres hvorledes disse observationer kan bruges som et led til at fremstille tynde sensor prototyper til fingerbaseret cursor kontrol. Sådanne sensorer vil specielt egne sig til implementering i form-faktor kritiske applikationer som fx mobiltelefoner.

Contents

List of publications

This thesis is based on the following journal papers.

Paper I
T. F. Q. Iversen, S. G. Hanson, P. Kirkegaard, "Investigation of an optical method for determining the average radius of curvature of micro-optical lenticular lens arrays", J. Opt. A: Pure Appl. Opt., **11**, 6pp, (2009) .

Paper II
T. F. Q. Iversen and S. G. Hanson, "Geometrical characterization of micro-optical cylindrical lens arrays using angular resolved diffraction", Meas. Sci. Technol., **21**, 7pp, (2010).

Paper III
T. F. Q. Iversen, M. L. Jakobsen and S. G. Hanson, "Speckle based three-dimensional velocity measurement using spatial filtering velocimetry", Applied Optics, **50**, 1523-1533, (2011).

Paper IV
M. L. Jakobsen, T. F. Q. Iversen and S. G. Hanson, "Speckle and fringe dynamics in image shearing interferometry for spatial filtering velocimetry". Submitted for Applied Optics, April 2011.

Paper V
H. C. Pedersen, M. L. Jakobsen, S. G Hanson,
M. Mosgaard, T. F. Q. Iversen and J. K. Jensen, "Optical touch-screen technology based on waveguide sensing". Submitted for Applied Physics Letters, April 2011.

Proceeding contributions

T. F. Q. Iversen and Steen Grüner Hanson, "Analysis of laser speckle patterns from fingertips", Proc. SPIE, Vol. 7726, (2010).

S. G. Hanson, T. F. Q. Iversen and M. L. Jakobsen, "A closer look at dynamic speckles and the use of their fine-structure for object measurements", Proc. SPIE, 7387, (2010).

S. G. Hanson, T. F. Q. Iversen and R. S. Hansen, "Dynamical properties of speckled speckles", Proc. SPIE, 7387, (2010).

S. G. Hanson, M. L. Jakobsen, T. F. Q. Iversen and H. C. Pedersen, "Opportunities for optics within high-tech of tomorrow", Proc. IEEE, Information Photonics, Ottawa 2011.

Patent

M. L. Jakobsen, T. F. Q. Iversen, V. S. G. Hanson, P. J. Rodrigo and C. Pedersen, "Vector velocimeter", 61/371, 830. Date of submission: 26.11.2009.

Other

Theis Faber Quist Iversen, ”There seems to be no end to the possibilities”, Part of *Beyond optical horizons, today and tomorrow with photonics*, p. 267, (DTU Fotonik Kgs. Lyngby, 2009).

Honours

Award for best student presentation at the FASIG conference, Photon08, Edinburgh, 2008.

Author Contribution

My contribution to the scientific papers that form the basis of this thesis was the following:

Paper I
The idea was developed by Steen Hanson and the initial experimental verification was performed by me. I carried out the subsequent experimental work assisted by Jørgen Stubager who operated the DEKTAK instrument. The paper was written by me and assisted by Steen Hanson.

Paper II
The idea and experimental configuration was developed by me, assisted by Henrik Pedersen and Steen Hanson. The experiments were carried out by me, assisted by Kai Dirscherl who operated the atomic force microscope instrument at Danish Fundamental Metrology A/S. The paper was written by me, assisted by Steen Grüner Hanson.

Paper III
The idea was developed by Michael Jakobsen and the initial experimental verification was performed by me. The numerical model used to theoretically investigate the interaction of the intensity dynamics and spatial filters was developed and implemented by me, assisted by Michael Jakobsen. The experiment was designed and carried out by me. The paper was written by me, assisted by Michael Jakobsen and Steen Hanson.

Paper IV
The experiment was designed and carried out by me. I assisted Michael Jakobsen in the presentation of the data in the paper.

Paper V
I primarily acted as consultant on aspects of the working principles of the "WaveTouch" technology as well as selection of light source and ray tracing models.

Preface

The research presented in this Ph.D. thesis was performed partly at OPDI Technologies A/S (OPDI) and partly at DTU Fotonik, Department of Photonics Engineering, Technical University of Denmark, Risø campus in the period 2008 - 2011. The Ph.D. project was conducted under the Industrial Ph.D. programme (ErhversPh.D.-ordningen) which is administrated by Forsknings og Innovationsstyrrelsen. The project was funded by OPDI Technologies A/S and Forsknings og Innovationsstyrelsen.

The main supervisor of the project was Steen Grüner Hanson who is Research Specialist at DTU Fotonik, Risø Campus. The company supervisor was initially the chief technical officer (CTO) at OPDI, Claus Friis Pedersen. The role of company supervisor was assumed by OPDI CEO Jørgen Korsgaard Jensen in April 2008.

The Ph.D. project was from the start outlined to address several areas of interest. Among these was the need to address quality assurance in high-volume production of complex micro optical elements, especially the micro-optical lens arrays used in the OPDI optical mouse sensor. I had experience in working with atomic force microscopes (AFM) from Aarhus University (AU), and I was able to arrange measurements of the lenses using one of AU's AFMs. Using this technique, we gained a lot of insight into the lens geometry and topography, which was not previously achieved. However, AFM is a time consuming measurement method and Steen Hanson suggested that the diffraction pattern of the micro-lenses might be utilized to measure at least some aspects of the lens shape, and overcome the measurement time issue. This principle became the theme of **Papers I** and **II**.

The micro-lenses used in the OPDI optical mouse is part of an optical configuration that implements spatial filtering velocimetry (SFV) to measure the two dimensional movement of surfaces, which is the basic function of the optical mouse. The use of VCSEL diode lasers for illumination and cheap injection moulded optics facilitates a low sensor cost prize, which is critical to be competitive on the market. This theme is repeated in the second part of the project which was aimed at developing new laser Doppler lidar sensors based on relatively cheap diode-lasers for wind speed measurements. During a project meeting, discussing the possibilities of using diode lasers in lidars, Christian Pedersen asked whether it would be possible to combine the measurement principle used in the OPDI computer mouse (i.e. spatial filtering velocimetry) and the laser Doppler technique. This spurred Michael Linde Jakobsen on and he later proposed the combination of shearing speckle interferometry and spatial filtering velocimetry to measure out-of-plane motion of translating objects. This particular proposal subsequently leads to a patent submission in November 2009 and is the theme of **Papers III** and **IV**. Although the project was intended to lead directly to diode laser based prototypes suitable for wind speed measurements, it was early on decided that for proof-of-concept purposes Helium-Neon lasers would be used in the experiments due to their ease of use. I believe though, that the experiences learned from these bulky and unpractical experimental setups will help avoid costly mistakes and facilitate the rapid development of diode laser based prototypes, subsequent to the work presented here.

Not all the work performed during this project was directly suitable for scientific publication. I have sought to include the most relevant of this work in the subsequent chapters in a way that coincides best with the overall theme of the thesis, and serves to further enlighten the reader on the work that was carried out.

The work presented in this thesis could not have taken place without the generous help and support from many great colleges, friends and family. I would especially like to extend my thanks to my supervisors Steen Hanson and Jørgen Korsgaard for the guidance they provided during the project. I would also like to thank:

- Michael Jakobsen, for the many fruitful discussions about the curiosities of speckles and the many hours spent in the lab working to apply the theory in real life.
- Harold Yura for his assistance with the development of the theoretical aspects of **Paper IV**.
- Henrik Pedersen, for his sharp observations and helpful second pair of eyes.
- Peter John Rodrigo and Christian Pedersen for their helpful insights into the workings and subtleties of the laser Doppler technique.
- Jørgen Stubager, Finn Pedersen and Hennning Larsen for laying much of the ground work of the experimental setups.
- My good friend and collegue in OPDI, Morten Mosgaard, for providing the breaks when they where needed.
- My family and friends for the support they have generously provided throughout the project.

Finally, I would like to thank Claus Friis Pedersen for setting the project in motion and giving me the opportunity to work with the all the great people at OPDI and DTU. Although he could not be there for the entire extend of the project, his efforts are greatly appreciated.

Theis Faber Quist Iversen

Risø, Roskilde
May 2, 2011

Part I

Introduction

The industrial applications of velocimetry span a wide range from measuring the motion of translating surfaces, rotating cylinders to flow measurements. Often, in these applications, it is desirable to eliminate the need for establishing mechanical contact between the object and the measuring device or in some way marking (encoding) the object to enable the measurement. Non-contacting methods of measuring velocity have the benefit of not disturbing the motion of the object appreciably and it allows remote measurements to be performed. In many industrial applications the most effective way of implementing non-contacting velocity measurement is to use optical sensors. Generally, optical sensors used in velocimetry can be either passive or active. Passive devices rely on ambient light illuminating the object or flow under investigation. Such systems usually implement a camera and imaging system combined with an image processing algorithm to extract the velocity information. Active devices typically implement some type of on-board and dedicated light source to provide appropriate illumination of the object. Using lasers as these light sources provide a range of advantages over lamps and light emitting diodes (LEDs). Particularly, in applications where the object is remote or weakly scattering, the high brightness of lasers is called for. Diode lasers in particular have the advantage of relatively low cost and compactness that benefit their use in industrial applications, while the coherent properties of lasers also can be exploited to enhance measurement performance.

When a non-specular object is illuminated by fairly coherent light a distinctly random granulated intensity pattern, known as speckle, generally appears to an observer at some distance away from the object. The earliest observations of speckle where made in the late part of the nineteenth century. However, with the advent of the laser in 1960 and thus, the introduction of a highly coherent light source, the speckle effect became more readily observable and has since been investigated extensively. The granular appearance of a speckle pattern is the result of the superposition of many coherent, but randomly de-phased, field contributions originating from illuminated scattering points on the surface. The de-phasing of the coherent components is a result of the roughness of the surface. If the roughness on average is greater then a wavelength of the illuminating light a highly modulated speckle pattern, also known as a fully developed speckle pattern, is observed. Because most everyday surfaces and objects are rough on an optical scale, fully developed speckle patterns are readily observed from most objects, when illuminated by laser light. An excellent review of speckle theory and intensity statistics can be found in [1].

The properties of speckle patterns are closely linked to the scattering structure that generates it, and the optical system through which, it is observed. Generally, if the scattering structure is moving so does the speckle pattern. Thus, if the motion of the speckle pattern can be extracted then information about the object motion can also be extracted. This property can be utilized to construct sensors that measure the speckle translation, and thereby, measure the true object motion.

Although in principle a simple task, care must be taken when designing velocity sensors based on tracking speckle patterns. As will be evident in the following chapters, both random and systematic errors, as well as the nature of the illumination and the optical system used to observe the speckles, impact the achievable accuracy and performance. Because speckle patterns are inherently stochastic in nature, the task becomes a matter of determining the average behaviour of the speckles. Thus, it is important to understand the dynamic evolution of the intensity distributions from a statistical point of view. For this purpose the ensemble averaged crosscovariance function [2] of the intensity distribution is usually the quantity of interest. Occasionally, the closely related crosscorrelation function is needed. However, for most cases the crosscovariance function provides all the information needed to characterize the dynamic behaviour of the speckle pattern from a statistical viewpoint. This quantity is the focal point of the theoretical considerations treated in this thesis.

The principle of using dynamic speckle patterns to measure object motion is utilized in a number of both research and industrial applications such as flow analysis [3], [4] and electronic speckle photography (ESP) [5] for deformation analysis. Many of these implement an imaging lens and a camera sensor (detector array) to form an image of the object of interest, illuminated by a laser source. In ESP, the crosscovariance is utilized to extract information about local object deformations by measuring the speckle translation within the image.

An example of this measurement principle, applied in a commercial system, is the laser based optical mouse. Here, only collective translation of the object surface is of interest, as it can safely be assumed that the surface does not deform during the movement. However, it must be able to resolve rapid movement and acceleration applied by the user. To accommodate the need for higher temporal resolution the full crosscovariance calculation is abandoned in favour of other types of signal processing algorithms such as optical flow methods [6].

Spatial filtering velocimetry (SFV) is a fundamentally different way of measuring speckle translation. The basic principle relies on letting the intensity distribution of interest (e.g. a speckle pattern) shear across a periodically transmitting and absorbing structure, implemented typically as an amplitude grating. The transmitted part of the intensity, incident on the grating, is integrated by a photodetector. The resulting time dependent photocurrent will generally exhibit an oscillatory behaviour. The frequency of this oscillation is proportional to the velocity component of the speckle translation perpendicular to the grating lines. Thus, extracting the frequency of this oscillation gives a measure of the speckle velocity. This basic principle can be implemented in many ways depending on the implementation and measurement needs.

The commercial partner of this Ph.D. project, the company OPDI Technologies A/S, develops miniaturized sensors for use in human input devices for pointing and cursor control. Among the products under development is an implementation of the measurement principle described in [7] used as a new type of laser based optical mouse for cursor control. It utilizes an optical implementation of the spatial filtering technique to derive two dimensional displacement of a translating surface. Surveys of the market, performed by OPDI Technologies A/S, indicate that the current market of camera based optical mice, represent approximately 300 million units, annually worldwide. This number is distributed approximately 50/50 between

retail and original equipment manufacturers (OEMs). For this high-volume market then, cost-competiveness and production yield are major areas of concern. In addition, the sensor under development by OPDI Technologies A/S is intended for direct competition with the high-end segment of the market, which places special demands on the performance, power consumption and reliability.
Therefore, one of the main goals of this project is addressed at developing rapid characterization methods for the sophisticated micro-optical structures of the spatial filters used in the sensor. The development of such methods will facilitate increased production yield and sensor reliability in high volume production. Furthermore, it is a goal to develop design tools in order to validate new enhanced performance prototype designs and aid in the development of these.
The second part of this project is focused on the development of optical sensors for measuring wind velocity. The laser Doppler anemometer is a well-known way of measuring velocity components of aerosol flow in the atmosphere first demonstrated by Huffaker [8]. The most commonly used light source for this application is the CO_2 laser system, and more recently [9], fiber based lasers. Although, these laser systems readily provide the necessary optical power for wind speed measurements at long range, they tend to bulky and expensive.
The company Windar Photonics A/S, a subsidiary of OPDI Technologies A/S, has been started to facilitate the development and commercialization of a laser Doppler anemometer (LDA) prototype system developed at DTU Fotonik [10]. The prototype uses an all semiconductor distributed feedback (DFB) master oscillator and monolithically integrated tapered power amplifier laser system [11]. This type of diode laser source is commercially available and supplies on the order of 1W of optical power at a wavelength of 1550nm and a typical linewidth of 500 kHz. The available optical power and linewidth allows wind speed measurement in ranges up to 300m using this type of diode laser. The use of diode lasers is a major commercial advantage as it is projected to the bring unit prize of LDA systems down by approximately a factor 10 compared to systems, that are based on fiber or CO_2 laser systems, currently on the market.
The commercial interest for remote measurement of wind speed is presently focused mainly on use in airports to measure the presence of wind shear. However, the wind turbine and the wind energy industry in general, are showing interest in these types of systems [12]. Recent studies [13] suggest that monitoring the wind direction ahead of a wind turbine and periodically adjusting the azimuthal alignment can increase efficiency on the order of 10%. This demands that components of the transverse wind velocity, in relation to the line-of-sight measurement, are obtained. This is partly achieved in some current commercial systems by implementing beam scanning setups such as the velocity azimuth display (VAD) [14].
The major goal of the second part of this project was to develop a measurement principle and the means to extract information about all three components of the translational velocity while overcoming the need for beam scanning mechanics or frequency modulation equipment thus retaining a point-like, local measurement of the velocity.
The first chapter reviews aspects of optical wave propagation using the Huygens-Fresnel principle. The Greens's function is introduced for arbitrary optical systems

represented by complex *ABCD* matrices. The ensemble averaged intensity crosscovariance function is introduced in the context of *ABCD* matrices and applied to describing the dynamical properties of speckles in one and two beam illumination configurations.

Chapter 2 addresses aspects of spatial filtering velocimetry in terms of the general methodology, filter characteristics and the properties of signals obtained. Furthermore, specific implementations of spatial filters are outlined and discussed with emphasis of obtaining directional information of the velocity measurement, suppression of low frequency noise and some aspects of desirable power spectral characteristics of the intensity distribution are discussed briefly. The specific implementation of an optical spatial filter embodied in the DragonFly (Df) technology is reviewed in chapter 3. Special emphasis is placed on the design and functionality of the optical unit, especially the beam-shaping (transmitter) and optical processing (receiver) optics. The injection moulding process is described and the manufacturing process of the mould master is discussed. Lastly, the performance of the developed prototypes are evaluated and discussed in the light of the proposed designs.

Chapter 4 addresses the use of various characterization methods to evaluate mainly geometrical parameters of the micro-optics of the Df optical units. Topographical data, obtained by scanning probe measurements, are presented. Lastly, an optical method for rapid evaluation of geometrical parameters of the receiver is presented and discussed.

A review of several different techniques and methods for extracting three dimensional displacement or velocity components are presented in chapter 5. The review includes the basic concept of laser Doppler velocimetry (LDV) as well as two variations on speckle interferometry for measuring three dimensional displacement fields. Furthermore, a measurement principle for full three dimensional velocity measurements is presented and discussed. The principle is based on both concepts from LDV and speckle interferometry. The measurement of all three velocity components are accomplished using spatial filters. A comparison between signal levels, obtained in the conventional LDV configuration and using spatial filtering, is presented. Finally, it is shown that modifying the measurement configuration of the spatial filters, an object-radius independent measurement of angular velocity of an in-plane rotating cylinder, can be achieved.

Chapter 6 briefly reviews a selection of current technologies used in touch-sensitive devices for pointing and tracking for human input applications. These technologies are implemented in a wide variety of devices such as mobile phones, laptops and tablet PCs, and thus represent a market on the increase. A novel optically based pointing device, currently being developed by OPDI Technologies A/S and DTU Fotonik, is presented in the context of the competing technologies.

Touch sensors for tracking and cursor control is also being developed at OPDI Technologies A/S and the working principles of these are outlined and discussed. Lastly, results from an experiment designed to investigate the scattering properties and speckle characteristics of a fingertip, illuminated by a laser in waveguide geometry, are presented. The purpose of this experiment is to explore the potential for combining waveguide principles with Df technology to achieve ultra thin, touch sensitive finger tracking devices, suitable for integrating in mobile phones and tablets where the sensor form-factor is critical.

1. Laser speckle

In this chapter aspects of optical wave propagation through arbitrary optical systems are considered. The analysis is based on the complex *ABCD* matrix formalism combined with scalar diffraction theory enabled by the Green's function. Special emphasis is placed on the laser speckle patterns in the observation plane of various optical systems when illuminating the surface of a rough and rigid object, placed in the object plane of the optical system, with a coherent light source. Furthermore, the dynamical properties of these speckle patterns are investigated in response to motion of the object in the object plane.
Finally, the introduction of multiple coherent Gaussian beams in the object plane is considered as well as the dynamical properties of the resulting fringe patterns (fine structure) in response to object motion.

1.1 Scalar wave theory

The classical theory of optical wave propagation is fundamentally governed by Maxwell's equations in the absence of free charges (see e.g. [15]). This set of differential equations describes the behaviour, in both time and space, of electrical and magnetic field vectors as they propagate through a given medium. However, all but the simplest cases of optical wave propagation are difficult to treat in a general manor by a full vector model and for most practical applications far simpler descriptions yield sufficiently accurate and more tangible results.
Consider a monochromatic wave propagating in a linear dielectric medium. The medium is assumed to be isotropic in the sense that its properties are independent of the direction of the electric and magnetic fields. Furthermore, the medium is assumed to be homogeneous and non-magnetic. Then the electric field $\mathbf{E}$ is subject to the wave equation given by

$$\nabla^2\mathbf{E}-\frac{n^2}{c^2}\frac{\partial^2\mathbf{E}}{\partial t^2}=0\,, \tag{1.1}$$

where n is the refractive index of the medium and c is the speed of light in vacuum. It can be shown that the magnetic field $\mathbf{H}$ satisfies an identical wave equation as eq. (1.1). Because both the electric and the magnetic field satisfies eq. (1.1), then so does each of their vector components. As a result, the scalar wave equation can be re-defined simply as

$$\nabla^2\mathrm{u}(\mathbf{r},t)-\frac{n^2}{c^2}\frac{\partial^2\mathrm{u}(\mathbf{r},t)}{\partial t^2}=0\,, \tag{1.2}$$

where

$$\mathrm{u}(\mathbf{r},t)=\mathrm{Re}\{U(\mathbf{r})\exp(-i2\pi\nu_0 t)\}, \tag{1.3}$$

represents any of the field vector components and ν_0 is the optical carrier frequency. The complex function of space $U(\mathbf{r})$ is the phasor representation of the optical wave at the position $\mathbf{r} = (x, y)$. The function $U(\mathbf{r})$ can be written as an amplitude and phase function in the form

$$U(\mathbf{r}) = A(\mathbf{r})\exp[i\phi(\mathbf{r})]. \tag{1.4}$$

The scalar wave equation given by eq. (1.2) is valid only as long as the coupling between the field components is negligible. Coupling between field components can occur when boundary conditions are applied e.g. in the form of a diffracting aperture. Generally, scalar wave theory applies to the interaction of optical waves with diffracting structures that are significantly larger than the wavelength λ of the optical field. If this is not the case, e.g. in a high resolution grating with large aspect ratio, then a full vector treatment must be applied to the electric and magnetic fields to obtain accurate results.

Given a field distribution $U(\mathbf{r})$ present at a plane in space, it is then of considerable interest to obtain the field distribution $U(\mathbf{p})$ present at another plane in space, at the position $\mathbf{p} = (p_x, p_y)$. For this purpose the Huygens-Fresnel principle can be employed:

$$U(\mathbf{p}) = \int_S U(\mathbf{r})\,G(\mathbf{r},\mathbf{p})\,d^2\mathbf{r}\,, \tag{1.5}$$

where

$$G(\mathbf{r},\mathbf{p}) = -\frac{ik}{2\pi}\frac{\exp(ik\Delta_{12})}{\Delta_{12}}\cos(\theta)\,, \tag{1.6}$$

and

$$\Delta_{12} = \sqrt{L^2 + (p_x - x)^2 + (p_y - y)^2}\ . \tag{1.7}$$

The integration in eq. (1.5) is carried out over the aperture S of the field distribution. The geometry of the Huygens-Fresnel principle is illustrated in figure 1.1

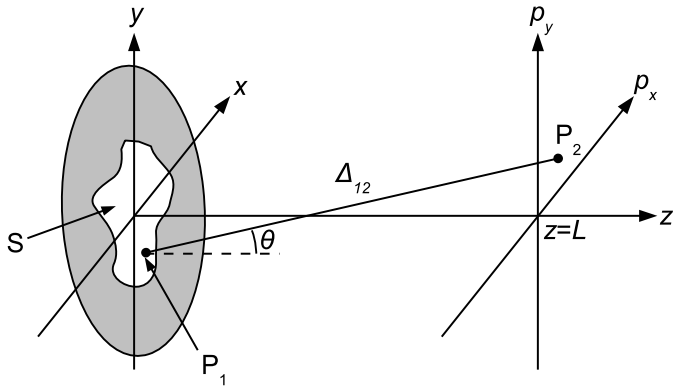

Figure 1.1 - Diffraction geometry of the Huygens-Fresnel principle.

In stating eq. (1.5) – eq. (1.7), it is assumed that $\Delta_{12} >> \lambda$ and that the inherent assumptions of scalar theory apply. The term Δ_{12} can be subject to the Fresnel and Fraunhofer approximations which imposes limitations on the distance between object $\mathbf{r}=(x,y)$ plane and observation plane $\mathbf{p}=(p_x,p_y)$, given the lateral extent of the field distribution in the object plane. The Huygens-Fresnel principle, subject to the Fresnel approximation, can be obtained by applying the binomial series expansion (cf. e.g. [16]) to Δ_{12} and retaining only the two first terms of the series. In this case eq. (1.5) can be written as

$$U(p_x, p_y) = -\frac{ik\exp(ikL)}{2\pi L}\int_{-\infty}^{\infty}\int_{-\infty}^{\infty} U(x,y)\exp\left\{\frac{ik}{2L}\left[(p_x - x)^2 + (p_y - y)^2\right]\right\}dxdy\,. \tag{1.8}$$

In addition to the free space propagation of an arbitrary field distribution in the object plane described by eq. (1.8), it is also of considerable interest to evaluate the effects of combinations of common optical components, e.g. a lens limited by an aperture, on the field that is observed in the observation plane. Such calculations have been carried out (see e.g. [17] p. 110). However, most optical systems are usually comprised of many optical elements and the complexity of such calculations quickly multiply. The complexity issue can be resolved, in part, by combining ray transfer matrices and the Green's function which will be the subject of the next section.

1.2 Complex ABCD matrix formalism

The *ABCD* matrix formalism [18] is derived from concepts of geometrical optics and makes use of matrices to describe the effect of non-diffracting optical elements on rays. Rays are geometrical constructs that represent transport of electromagnetic energy in the theory of geometrical optics. Geometrical optics is derived from Maxwell's equations as the wavelength is allowed to go to zero. Thus, the wave

nature of optical waves is entirely neglected, and the optical propagation properties are interpreted as a result of the laws of reflection and refraction applied to the rays.

The strength of the *ABCD* matrix formalism lies in the fact that individual optical elements (e.g. lenses, free space propagation, etc.) are described by matrices and, by appropriate combination of these matrices, entire optical systems can be synthesized. The use of matrices not only applies to propagation of rays. Using the Green's function, a connection between the scalar diffraction theory and the ray transfer matrix of arbitrary optical systems can be made, thus enabling the propagation of arbitrary field distributions through arbitrary optical systems defined by a single ray transfer matrix although with limitations to be described in the following.

The theory of ray transfer matrices is inherently paraxial and the functionality of the optical surfaces can only be accounted for up to second order (i.e. parabolic surfaces). As a consequence, higher order effects such as aberrations, cannot be included in the analysis. The Green's function used will be specified in the Fresnel approximation, which can be shown [19] to satisfy the paraxial approximation.

Lastly, absorptive apertures can also be represented by a ray transfer matrix. This step is critical to obtaining realistic descriptions of optical systems because physical apertures are present in all optical systems and can have profound effects on the propagation characteristics of optical waves through the optical arrangement.

1.2.1 *ABCD* matrix formalism

The function of the ray transfer matrix is to operate on a ray with a given input position and input angle, transforming it due to the properties of the optical system represented by the transfer matrix. The transformed (output) ray obtains an output position and output angle, generally different from the input ray. Anamorphic optical systems can be considered [20] but in this context only rotationally symmetric systems are considered. Consequently, ray transfer matrices considered here are sized 2×2 rather than 4×4. The principle of the ray transfer matrix, operating on an input ray to generate an output ray, is illustrated in figure 1.2.

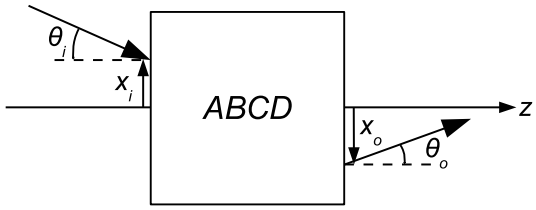

Figure 1.2 – The ray transfer matrix and operation on an input ray.

The operation can be written formally as

$$\begin{bmatrix} x_o \\ \theta_o \end{bmatrix} = \begin{bmatrix} A & B \\ C & D \end{bmatrix} \begin{bmatrix} x_i \\ \theta_i \end{bmatrix} = \begin{bmatrix} Ax_i + B\theta_i \\ Cx_i + D\theta_i \end{bmatrix}. \tag{1.9}$$

If the optical system is composed of multiple (N) elements the corresponding ray matrix can be calculated as

$$\begin{bmatrix} A & B \\ C & D \end{bmatrix} = \begin{bmatrix} A_N & B_N \\ C_N & D_N \end{bmatrix} \cdots \begin{bmatrix} A_2 & B_2 \\ C_2 & D_2 \end{bmatrix} \begin{bmatrix} A_1 & B_1 \\ C_1 & D_1 \end{bmatrix}, \tag{1.10}$$

where the matrix to the far right represents the first element of the optical system. When analysing optical systems it is frequently of interest to locate e.g. a focus point or the location of an image. Special significance can be attributed to zero matrix elements. Two important and generic cases are $A = 0$ and $B = 0$. Eq. (1.9) can be examined for each case. When the A element is zero we have

$$x_o = B\theta_i . \tag{1.11}$$

This means that the position of the output ray is independent on the input position and the output position is proportional to the input angle with a factor B. This is the characteristic of a focusing (Fourier transforming) optical system, which essentially converts input angles into output positions. If the B element is zero we have

$$x_o = Ax_i . \tag{1.12}$$

From eq. (1.12) it is observed that all rays emanating from a position x_i in the input plane, regardless of their angle, are transferred to a position x_o in the output plane. This means that the input and output planes are conjugate planes, i.e. when the B element is zero, the optical system is an imaging configuration.

A set of generic optical elements and interfaces can be defined from which most optical configurations of interest can be synthesized. The simplest of these is free space propagation. Using eq. (1.9), the relationship between the position and angle of the outgoing ray and the position and angle of the ray entering the optical system can be deduced for this simple case. For a free space propagation of length L the following must apply:

$$x_o = Ax_i + B\theta_i = x_i + L\theta_i , \tag{1.13a}$$

$$\theta_o = Cx_i + D\theta_i = \theta_i . \tag{1.13b}$$

Thus, the ray transfer matrix can be identified as

$$\begin{bmatrix} A & B \\ C & D \end{bmatrix} = \begin{bmatrix} 1 & L \\ 0 & 1 \end{bmatrix}. \tag{1.14}$$

Now, consider a dielectric slab of thickness L and refractive index n_2 immersed in another dielectric medium of refractive index n_1 as illustrated in figure 1.3.

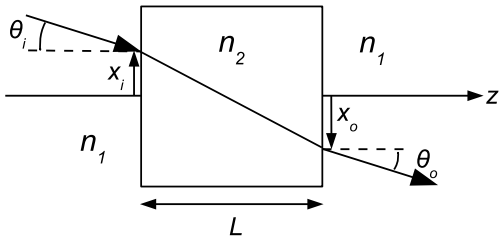

Figure 1.3 – Ray propagation through a dielectric slab with refractive index $n_2 < n_1$ and thickness L

Using Schnell's law of refraction the following must apply

$$x_o = Ax_i + B\theta_i = x_i + \frac{Ln_1\theta_i}{n_2}, \tag{1.15}$$

$$\theta_o = \theta_i . \tag{1.16}$$

The ray transfer matrix is then given by

$$\begin{bmatrix} A & B \\ C & D \end{bmatrix} = \begin{bmatrix} 1 & n_1 L / n_2 \\ 0 & 1 \end{bmatrix} \tag{1.17}$$

If the propagation is terminated within the dielectric medium eq. (1.17) becomes

$$\begin{bmatrix} A & B \\ C & D \end{bmatrix} = \begin{bmatrix} 1 & n_1 L / n_2 \\ 0 & n_1 / n_2 \end{bmatrix} \tag{1.18}$$

It is noted that the determinant of the matrix is always unity in case the refractive index of the input and output medium is identical.
Another important optical element is the thin lens. Similar considerations that lead to eq. (1.17) and eq. (1.18) can be made for other surfaces that are described by a second order polynomial in the transverse coordinates. The *ABCD* matrix representing a thin lens with focal length *f* is given by

$$\begin{bmatrix} A & B \\ C & D \end{bmatrix} = \begin{bmatrix} 1 & 0 \\ -1/f & 1 \end{bmatrix} \tag{1.19}$$

An overview of other common optical elements and their *ABCD* matrices can be found in [18].

1.2.2 The Green's function

The *ABCD* matrix formalism and scalar diffraction theory can be connected by the introduction of the Green's function. The Green's function is used to propagate an arbitrary optical field distribution through an arbitrary optical system defined by an *ABCD* ray transfer matrix. The Green's function for a rotationally symmetric paraxial optical system that starts and ends in a medium with the same refractive index can be written as [18]

$$G(\mathbf{r},\mathbf{p}) = -\frac{ik\exp(-ikL')}{2\pi B}\exp\left[-\frac{ik}{2B}\left(A\mathbf{r}^2 - 2\mathbf{r}\cdot\mathbf{p} + D\mathbf{p}^2\right)\right], \tag{1.20}$$

where L' is the optical path length between the object plane and the observation plane of the optical system. Given an input field distribution $U(\mathbf{r})$, the field distribution at the output plane of the optical system can be calculated by performing the integration described by eq. (1.5).

The significance of zero matrix elements was discussed in section 1.2. In particular when $B = 0$, an image of the input plane is formed in the output plane. Examining the relationship described by eq. (1.20), it is clear that a problem occurs when $B \to 0$ because the *B* element is present in the denominator of both the amplitude and the phase of the Green's function. This is a consequence of the geometric optics origin of the *ABCD* matrix formalism. The image, predicted by geometrical optics, of a hypothetical point source located in the object plane of a perfect imaging system is again point-like. This only applies when the wavelength can be considered to be infinitesimally small. However, in scalar diffraction theory the wavelength is no longer infinitesimally small, but indeed finite. The Green's function in eq. (1.20) actually approaches a delta function for $B \to 0$.

The issue can be resolved by introducing absorbing apertures in the *ABCD* matrix formalism. Consider the effect of a thin lens, with a focal length *f*, on an incoming field distribution $U(\mathbf{r})$:

$$U'(\mathbf{r}) = \exp\left(-ik\frac{\mathbf{r}^2}{2f}\right)U(\mathbf{r}). \tag{1.21}$$

The field distribution $U'(\mathbf{r})$ is the field distribution immediately behind the lens. This can be recognized as a pure phase transformation of the incoming field. An absorbing aperture with Gaussian transmission functionality can be introduced by recognizing that if

$$f^{-1} = \frac{2i}{k\sigma^2}, \tag{1.22}$$

eq. (1.21) then becomes

$$U'(\mathbf{r}) = \exp\left(-\frac{\mathbf{r}^2}{\sigma^2}\right) U(\mathbf{r}). \tag{1.23}$$

The transformation is now a pure amplitude transformation. It is straightforward to identify the corresponding (complex) *ABCD* matrix for the Gaussian aperture

$$\begin{bmatrix} A & B \\ C & D \end{bmatrix} = \begin{bmatrix} 1 & 0 \\ -\frac{2i}{k\sigma^2} & 1 \end{bmatrix}. \tag{1.24}$$

It is noted that the introduction of absorption (or gain) into the optical system will generally make the elements of the *ABCD* matrix complex but still having a determinant of unity. Consequently, the conditions discussed earlier for a Fourier transforming system and an imaging system become $\mathrm{Re}\{A\} = 0$ and $\mathrm{Re}\{B\} = 0$, respectively. It could be argued that apertures and stops with Gaussian transmission characteristics are rarely realized in real optical systems. However, the Gaussian functionality simplifies analytical calculations and subsequently facilitates parametric system studies that benefit the design process of real applications.

1.3 Dynamic laser speckle

Laser speckle is a phenomenon that is characterized by a random granular appearance of light scattered from a rough surface when illuminated by a coherent light source. Speckles are particular obvious when laser sources are employed due to their high degree of both spatial and temporal coherence. Generally, when the illuminated object is brought in motion, the speckle pattern also moves and evolves in time. The dynamical properties of laser speckle patterns can be related to the motion, be it translation, rotation or associated vibrations, of the illuminated object when viewed through appropriate optical arrangements. It is within this context that the complex *ABCD* formalism is particular useful due to its ability to model the speckle dynamics when observed through arbitrary optical systems defined by a ray transfer matrix.

Speckle patterns are fundamentally stochastic in nature and thus the analysis must take this into account. Assuming that the object is illuminated by a (time-independent) coherent field distribution, the objective is then to obtain the ensemble averaged space and time-lagged intensity crosscovariance function obtained in the observation plane of the optical system. The normalized crosscovariance of the intensity distributions before and after an object displacement provides the necessary information to describe the speckle pattern behaviour in the observation plane. This function is given by

$$C_I(\mathbf{p}_1,\mathbf{p}_2,\tau)=\frac{\langle I(\mathbf{p}_1,t)I(\mathbf{p}_2,t+\tau)\rangle-\langle I(\mathbf{p}_1,t)\rangle\langle I(\mathbf{p}_2,t+\tau)\rangle}{\sqrt{\left(\langle I(\mathbf{p}_1,t)^2\rangle-\langle I(\mathbf{p}_1,t)\rangle^2\right)\left(\langle I(\mathbf{p}_2,t+\tau)^2\rangle-\langle I(\mathbf{p}_2,t+\tau)\rangle^2\right)}}, \tag{1.25}$$

where the angular brackets denote the ensemble average, τ is the time lag and $\mathbf{p}_1$ and $\mathbf{p}_2$ are the two vector positions of interest in the observation plane. In figure 1.4 the configuration used here is illustrated.

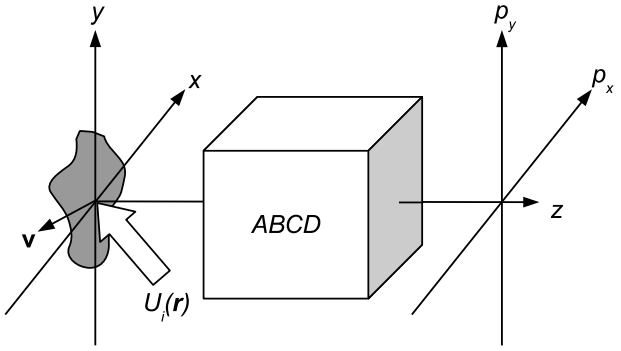

Figure 1.4 – Theoretical configuration. An arbitrary optical system connects the object plane with the observation plane. The object moves with a velocity v.

It is assumed that the complex field in the observation plane adhere to circular complex Gaussian random statistics [21]. In other words the speckle field is fully developed. This is valid if the rms. surface roughness of the object is larger than the wavelength and if the lateral scales of the surface roughness is unresolved by the optical system that is used. When this is the case eq. (1.25) becomes:

$$C_I(\mathbf{p}_1,\mathbf{p}_2,\tau)=\left|\gamma(\mathbf{p}_1,\mathbf{p}_2,\tau)\right|^2, \tag{1.26}$$

where

$$\gamma(\mathbf{p}_1,\mathbf{p}_2,\tau)=\frac{\Gamma(\mathbf{p}_1,\mathbf{p}_2,\tau)}{\sqrt{\Gamma(\mathbf{p}_1,\mathbf{p}_1,0)\Gamma(\mathbf{p}_2,\mathbf{p}_2,0)}}, \tag{1.27}$$

is the complex degree of coherence of the optical field, "*" denotes the complex conjugate and

$$\Gamma(\mathbf{p}_1,\mathbf{p}_2,\tau)=\left\langle U(\mathbf{p}_1,t)U^*(\mathbf{p}_2,t+\tau)\right\rangle, \tag{1.28}$$

is the mutual coherence function of the field distribution in the observation plane. The field distribution $U(\mathbf{p},t)$ can be obtained from

$$U(\mathbf{p},t)=\int_{-\infty}^{\infty}U_s(\mathbf{r},t)G(\mathbf{r},\mathbf{p})d^2\mathbf{r}\,. \tag{1.29}$$

It is assumed that the optical system connecting the object and the observation plane is rotationally symmetric and represented by the Green's function given by eq. (1.20). The field scattered from the surface $U_s(\mathbf{r},t)$ is modelled as

$$U_s(\mathbf{r},t)=U_i(\mathbf{r})\Psi(\mathbf{r},t), \tag{1.30}$$

where $U_i(\mathbf{r})$ is the incoming deterministic field illuminating the surface and $\Psi(\mathbf{r},t)$ is the stochastic time-varying complex reflection coefficient assumed to represent a stationary stochastic process. Furthermore, it is assumed that $|\Psi(\mathbf{r},t)|=1$ and $\langle\Psi(\mathbf{r},t)\rangle=0$. Considering, for the time being only in-plane translation with a constant velocity $\mathbf{v}$, complete spatial incoherence of the complex reflection coefficient is assumed, which can be expressed by

$$\left\langle\Psi(\mathbf{r}_1,t)\Psi^*(\mathbf{r}_2,t+\tau)\right\rangle=\frac{4\pi}{k^2}\delta(\mathbf{r}_1-\mathbf{r}_2+\mathbf{v}\tau). \tag{1.31}$$

Eq. (1.31) ensures that the reflected field amplitudes are uncorrelated at points $\mathbf{r}_1\neq\mathbf{r}_2$ in space for zero time delay. Furthermore, eq. (1.31) implies that the surface moves as a frozen pattern and does therefore not exhibit any deformation or turbulent behaviour. The mutual coherence function at the observation plane can be obtained by combining eq. (1.28)-(1.31):

$$\Gamma(\mathbf{p}_1,\mathbf{p}_2,\tau)=\frac{4\pi}{k^2}\int_S d^2\mathbf{r}U_i(\mathbf{r})U^*{}_i(\mathbf{r}')G(\mathbf{r},\mathbf{p}_1)G^*(\mathbf{r}',\mathbf{p}_2), \tag{1.32}$$

where

$$\mathbf{r}'=\mathbf{r}+\mathbf{v}\tau\,. \tag{1.33}$$

Eq. (1.32) provides a general model for evaluating the dynamic properties of fully developed speckle patterns observed through arbitrary optical systems specified by a complex *ABCD* matrix.

1.3.1 Single beam illumination

The specific case where a single Gaussian beam, given by

$$U_i(\mathbf{r})=\sqrt{\frac{2P}{\pi w_0{}^2}}\exp\left[-\mathbf{r}^2\left(\frac{1}{w_0{}^2}+\frac{ik}{2R_0}\right)\right], \tag{1.34}$$

where w_0 is the spot size (e^{-2} intensity radius) and R_0 is the radius of curvature, illuminates a plane surface object is illustrated in figure 1.5.

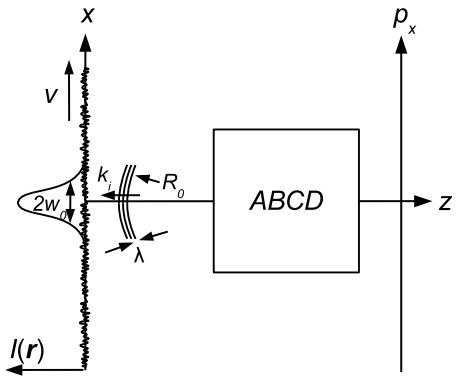

Figure 1.5 – A plane surface object illuminated by a single Gaussian beam and observed through an arbitrary optical system represented by an *ABCD* matrix.

This case has been solved generally for partially developed speckle patterns by Yura *et al.* [22]. The crosscovariance function can in the case of fully developed speckles be written as

$$C_I(\Delta\mathbf{p},\tau)=\exp\left\{-2\frac{\left(A_i-\frac{2B_r}{kw_0{}^2}\right)^2(\mathbf{v}\tau)^2+\left[\Delta\mathbf{p}-\left(A_r+\frac{2B_i}{kw_0{}^2}\right)\mathbf{v}\tau\right]^2}{\rho_0{}^2}\right\}, \quad (1.35)$$

where $\Delta\mathbf{p}=\mathbf{p}_1-\mathbf{p}_2$ and

$$\rho_0=\sqrt{\frac{8|B|^2}{k^2w_o{}^2}+\frac{4}{k}\mathrm{Im}\{BA^*\}}. \quad (1.36)$$

ρ_0 is the average speckle size in the observation plane. The matrix elements $(A,B)_{r,i}$ are the real and imaginary parts, respectively. From eq. (1.35) all information about the dynamical behaviour of the speckle pattern, obtained in the observation plane, can be derived. Specifically, identifying the position $\Delta\mathbf{p}$ of the peak value of the crosscovariance after the object has been allowed to move a distance $\Delta\mathbf{r}=\mathbf{v}\tau$, yields the speckle displacement in the observation plane in

response to the object translation. The rate of decrease of the peak value of the crosscovariance function for increasing object displacement $\Delta\mathbf{r}$ describes the rate of decorrelation of the speckle pattern. The terms

$$K_T = A_r + \frac{2B_i}{kw_0^2}, \tag{1.37}$$

$$K_B = A_i - \frac{2B_r}{kw_0^2}, \tag{1.38}$$

$$\beta = \frac{K_B}{\sqrt{K_B^2 + K_T^2}}, \tag{1.39}$$

describe the dynamical properties of the speckle pattern and are seen to be related to the *A* and *B* elements of the optical system connecting the object and observation plane. When $|K_B| >> |K_T|$ the decorrelation length of the speckle pattern, given by ρ_0 / β, is short. This is a phenomenon known as "speckle boiling". In the limit of complete speckle boiling the speckle decorrelation length is on the order of the average speckle size. In this case the speckle translation, and thus the object motion cannot be deduced. On the other hand if $|K_B| << |K_T|$ the dynamics of the speckle pattern is dominated by speckle translation, meaning that the speckles do not change shape as the pattern moves as a whole. The speckle velocity $\mathbf{v}_s$ can thus be written as

$$\mathbf{v}_s = K_T \mathbf{v} = \left(A_r + \frac{2B_i}{kw_0^2} \right) \mathbf{v}. \tag{1.40}$$

The speckle dynamics of objects such as a cylinder with finite radius of curvature *R*, rotating with angular velocity ω in the object plane can be also be accounted for within the existing analytical framework. The effect of rotation is incorporated directly into the existing crosscovariance function by introducing a simple modification of the *ABCD* elements of the optical system. In the context of the analysis provided by *ABCD* matrices, the effect of the rotating object is equivalent to observing a plane surface translating with a speed ωR, but observed through a lens with focal length $f = -R/2$, placed directly against the (plane) surface [23].

Thus an object that rotates in-plane can be analytically described by letting $v \to \omega R = v_T$ and substituting $A \to A + 2B/R$, where v_T is the tangential velocity component of the rotating cylinder surface. This configuration is illustrated in figure 1.6.

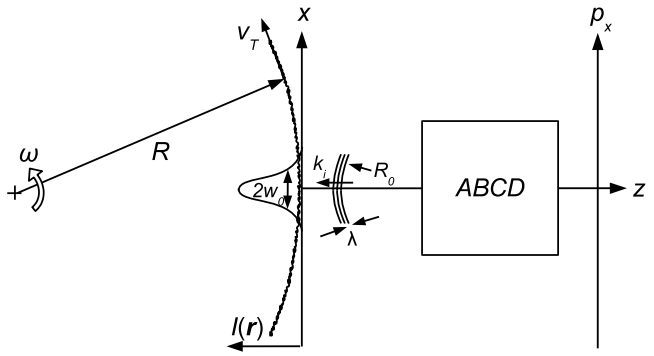

Figure 1.6 - Cylinder object with radius *R*, rotating in-plane with angular velocity ω, illuminated by a single Gaussian beam and observed through and arbitrary optical system represented by an *ABCD* matrix.

1.3.2 Two beam illumination

A case, which is of particular interest, is illumination of the object with two coherent (Gaussian) beams. The configuration is illustrated in figure 1.7.

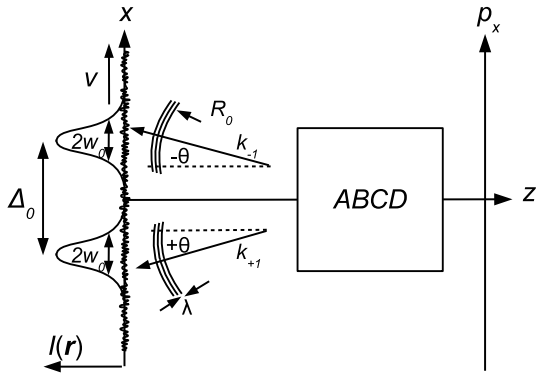

Figure 1.7 – A plane surface object illuminated by two separated Gaussian beams and observed through an arbitrary optical system represented by an *ABCD* matrix.

The presence of two beams can be accounted for by introducing the incoming field as

$$U_i(\mathbf{r}) = U_1(\mathbf{r}) + U_2(\mathbf{r}), \tag{1.41}$$

where

$$U_{1,2}(\mathbf{r}) = U_0 \exp\left[-\frac{\left|\mathbf{r} \pm \boldsymbol{\Delta}_\mathbf{0} / 2\right|^2}{{w_0}^2} - \frac{ik\left|\mathbf{r} \pm \boldsymbol{\Delta}_\mathbf{0} / 2\right|^2}{2R_0} \mp ik\left(\mathbf{r} \mp \boldsymbol{\Delta}_\mathbf{0} / 2\right) \cdot \boldsymbol{\theta} \right]. \quad (1.42)$$

It is assumed that $\sin|\boldsymbol{\theta}| \approx |\boldsymbol{\theta}|$. Without loss of generality the following can be assumed: $\mathbf{v} = (v_x, 0)$ and $\boldsymbol{\Delta}_\mathbf{0} = (\Delta_{0x}, 0)$. It is also assumed that $|\boldsymbol{\Delta}_\mathbf{0}| >> 2w_0$ and that $|\boldsymbol{\Delta}_\mathbf{0}|/|\mathbf{v}| >> \tau$, which signifies that the illuminating beams do not overlap on the object and that the time scales involved are short compared to the transit time of the surface structure between the two beams (i.e. time-of-flight contributions are not considered). With these assumptions in place Yura *et al*. [2] solved the problem for a general optical system assuming that no apertures are present, i.e. for real-valued *ABCD* matrices. Given the one-dimensional case where $\Delta\mathbf{p} = (\Delta p_x, 0)$ the intensity crosscovariance becomes

$$\begin{aligned} C_I(\Delta p_x, \tau) = \exp\left\{ -\frac{(v_x\tau)^2}{{w_0}^2} - \frac{\left[\Delta p_x - v_x\tau(A - B/R_0)\right]^2}{{\rho_0}^2} \right\} \\ \times \cos^2\left\{ \frac{k\Delta_{0x}}{2B}\left[\Delta p_x - v_x\tau\left(A + \frac{2B\theta}{\Delta_{0x}} \right) \right] \right\} \end{aligned}, \quad (1.43)$$

where

$$\rho_0 = \frac{2B}{kw_0}, \quad (1.44)$$

is the average speckle size. From eq. (1.43) it is observed that there are two distinct contributions to the crosscovariance. The exponential term is recognized as the ordinary speckle contribution. The additional cosine term represents the so-called fine structure. The fine structure is a high spatial frequency component that arises within the individual (bright) speckles. In figure 1.8 such a pattern is shown, obtained with a similar two-beam illumination configuration as illustrated in figure 1.7.

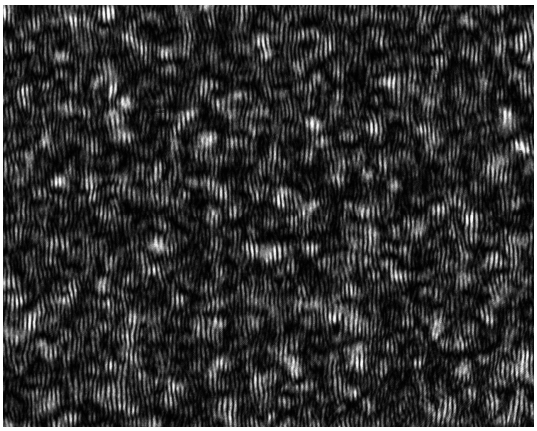

Figure 1.8 – Speckle and fine structure pattern obtained by two-beam illumination of a rough object surface observed through free space propagation.

From eq. (1.43) some of the general characteristics of both the speckle and fine structure components can be deduced. The speckle characteristic is the same as for the single beam illumination case, where

$$v_{s,x} = v_x\left(A - B / R_0\right) , \tag{1.45}$$

is the speckle velocity component along the x direction in response to the object velocity component along the same direction. The fine structure component is determined by the cosine term of eq. (1.43). The characteristics of the fine structure are:

$$\Lambda_{fr,x} = \frac{2\pi B}{k\Delta_{0x}}, \qquad \text{(Fringe spacing)} \tag{1.46}$$

$$v_{fr,x} = v_x\left(A + \frac{2B\theta}{\Delta_{0x}}\right). \text{ (Fringe velocity)} \tag{1.47}$$

The average number of fringes within a speckle is given by $\Delta_{0x} / \left(\pi w_0\right)$. Furthermore, when comparing eq. (1.45) and eq. (1.47) it is clear that the fine structure and the speckle patterns do generally not translate with the same velocity. The speckle pattern depends on the radius of curvature of the illuminating beams while the fine structure depends on the angle of incidence of beams illuminating the object surface. Finally, it is observed that the speckle pattern, and thus the fringe pattern as well, decorrelate when the object has moved a distance $v_x\tau >> w_0$.

2. Spatial filtering velocimetry

Spatial filtering velocimetry (SFV) is one of many techniques that can be employed to extract velocity information from a variety of objects in motion. Of competing techniques can be mentioned differential Doppler velocimetry [24], particle image velocimetry (PIV) [25] and time-of flight velocimetry [26], [27]. Spatial filtering velocimetry does however provide a range of advantages that are desirable for the scope of applications considered here. Very high sampling rates can be achieved, which makes the method applicable to high speed measurements. Furthermore, most SFV implementations are fairly simple and can be made very robust and cheap using well established manufacturing processes.
The traditional application of SFV employs incoherent imaging of the surface or particle flow of interest onto a spatial filtering arrangement, thus measuring the in-plane translational properties of the object or particle field. When combining the SFV measurement principles with laser speckles, the range of applications increases significantly. By using coherent illumination of the object, the speckle patterns can serve as virtual "particle images", equivalent to the incoherent imaging case. Employing an appropriate optical system then allows the measurement of other velocity parameters, such as angular velocity and, as will be demonstrated in the subsequent sections, even out-of-plane motion can be measured by applying principles from speckle interferometry.

The first treatment of the basic principles of spatial filtering velocimetry was given by Gédance [28] and Ator [29]. Gédance investigated the use of transmission gratings in scanning systems for image tracking purposes. Ator proposed the use of transmission grating arrangements to measure ground velocity in aerial photography applications and based his analysis on correlation theory for stochastic processes. The first experimental demonstration was given by Gaster [30] who used spatial filtering velocimetry to measure fluid flow velocities. A comprehensive treatment of SFV principles and applications can be found in [31].
In this chapter, some of the basic principles of operation and properties of spatial filters used in velocimetry applications are treated theoretically and discussed in relation to the specific speckle-based applications that are of interest in this context.

2.1 Methodology

Spatial filtering velocimetry, in its most basic form, is a technique that employs periodic arrangements of alternating transmitting and opaque apertures forming a transmittance function $h(\mathbf{p})$ that modulate a generally time dependent intensity pattern $I(\mathbf{p},t)$ (e.g. an image of a particle field or a speckle pattern) that is incident upon it. The transmitted intensity is collected by a detector that produces a photocurrent $i(t)$ which can be viewed on an oscilloscope. Conceptually, the working principle can be understood by considering the image of a single particle transiting two single apertures, separated by a known distance, as shown in figure 2.1 (Left).

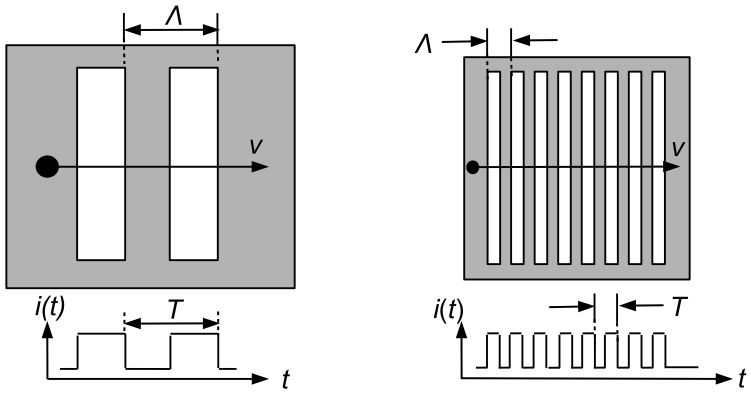

Figure 2.1 – (Left) A single particle image (speckle) transiting two separated apertures. (Right) A single particle image or speckle transiting a multiple slit arrangement. Below the resulting detector signal $i(t)$ for each case is shown.

Assuming that the image is moving with constant velocity between the two apertures the time signal detected by the detector will exhibit two features separated in time. The time separation is given by

$$T = \frac{\Lambda}{v}, \tag{2.1}$$

where Λ is the aperture separation and v is the speed of the particle image (cf. figure 2.1). This principle is similar to laser time-of-flight velocimetry. A natural extension of the principle is to include additional apertures arranged in a periodic manner as this will increase the number of times the particle velocity is measured and thus increase the measurement accuracy. This is illustrated in figure 2.1 (Right). It is observed that the detected signal from this configuration clearly contains an oscillatory component of frequency $f_0 = T^{-1} = v/\Lambda$.

In chapter 1 the stochastic properties of dynamic laser speckle, i.e. average size of the individual speckles and associated decorrelation effects was reviewed as well as the dynamic properties such as the translational velocity and gearing effects between fine structure and speckle in response to object motion in the case of more than one beam illuminating the object. Applying spatial filters to measure speckle translation in the observation plane of an optical system calls for an analytical framework addressing the stochastic nature of speckles and the deterministic periodic structure of a spatial filter. Fortunately, the filter performance is well described in the framework of linear filtering theory. The output signal observed is given by a convolution operation

$$i(\mathbf{p_1}) = \int_{-\infty}^{\infty} d^2\mathbf{p} I(\mathbf{p} - \mathbf{p_1}) h(\mathbf{p}), \tag{2.2}$$

where $\mathbf{p_1} = \mathbf{v}t + \mathbf{p}_0$ and $\mathbf{p}_0$ is a constant vector. The vector $\mathbf{v}$ is the velocity vector of the intensity pattern moving in the observation plane. If it is assumed that the dynamic intensity distribution at the input of the transmittance function is a stationary (ergodic) random process, then the spatial power spectrum of the photocurrent $P(\boldsymbol{\xi})$ can be written, by virtue of the Wiener-Khinchine theorem, as

$$P(\boldsymbol{\xi}) = \left|S_I(\boldsymbol{\xi})\right|^2 \left|H(\boldsymbol{\xi})\right|^2 \tag{2.3}$$

Where $\boldsymbol{\xi} = (\xi_x, \xi_y)$ is the spatial frequency vector and $S_I(\boldsymbol{\xi})$ is the spatio-temporal spectrum of the intensity distribution which is generally time dependent and $H(\boldsymbol{\xi})$ is the spatial (time independent) spectrum of the transmittance function $h(\mathbf{p})$, which is similar to the transfer function known from signal processing theory. If it is assumed that $\mathbf{v} = (v,0)$ then $\xi_x = f / v$ and the temporal power spectrum of the photocurrent signal can then be obtained from [31]

$$G(f) = \frac{1}{v}\int_{-\infty}^{\infty} \left|S_I\left(\frac{f}{v}, \xi_y\right)\right|^2 \left|H\left(\frac{f}{v}, \xi_y\right)\right|^2 d\xi_y \,. \tag{2.4}$$

The power spectrum described by eq. (2.4) or the photocurrent signal itself can then be processed to provide the desired velocity information.

2.2 Filter characteristics

In this section some of the characteristic features of spatial filters used for SFV are investigated in terms of transmittance functions and the corresponding power spectra. The performance is treated with emphasis on accuracy and signal characteristics and their relation to filter parameters. Furthermore, the average speckle size is discussed in relation to practical implementations.

2.2.1 Transmittance functions

In accordance with the analogy of multiple measurements of the transit time of a single particle passing multiple apertures, it is required that these apertures be separated by the same spacing across the entire window of the spatial filter in order to achieve a consistent transit time measurement and thus a high degree of accuracy. The criterion can be expressed through the relationship

$$h(p_x) = h(p_x - n\Lambda), \quad n = 1,2,3,... \tag{2.5}$$

where Λ is the period (pitch) of the spatial filter and the periodicity of the filter is imposed along the p_x-direction. A typical transmission function is illustrated in figure 2.2, and will form the basis of the analysis.

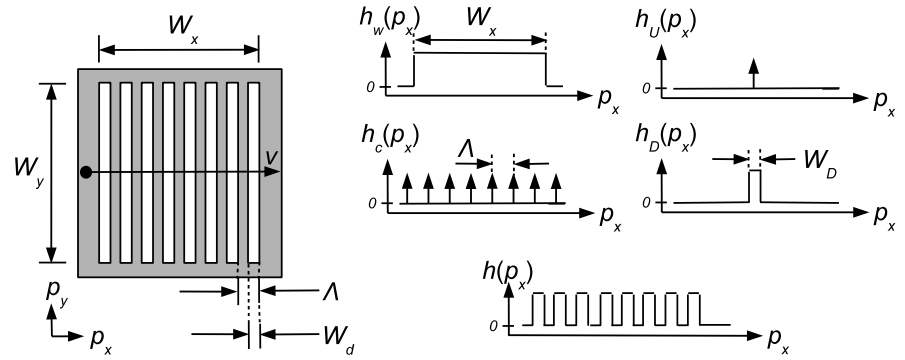

Figure 2.2 – Parameters and functionality of the spatial filter transmission function.

To aid the analysis of the filter characteristics, the transmission function is broken into constituent parts in the form of elementary spatially dependent response functions. Firstly, the periodicity requirement is accounted for by a comb function $h_C(\mathbf{p})$ that consists of an infinite sum of Dirac delta functions equidistantly separated by Λ. The transmission function will be subject to a finite number of unit cells. This is accounted for by introducing the filter window function $h_W(\mathbf{p})$. The filter window function can adopt a range of functionalities depending on the specific implementation. Here, a rectangular function of width $W_{x,y}$ is adopted. The number of unit cells in the spatial filter is then $N = W_x / \Lambda$. The unit cell function $h_U(\mathbf{p})$ accounts for the positioning of the transmitting and opaque apertures within the unit cell of the filter. Lastly, the function $h_D(\mathbf{p})$ defines the functionality of the transmitting aperture. The functionality most often encountered in reality is rectangular, and this type (of width W_D) is also adopted here. Now, the transmission function describing the spatial filtering effect shown in figure 2.2 can be written as

$$h(\mathbf{p}) = [h_C(\mathbf{p}) h_W(\mathbf{p})] \otimes [h_U(\mathbf{p}) \otimes h_D(\mathbf{p})], \tag{2.6}$$

where

$$h_C(\mathbf{p}) = \sum_{n=-\infty}^{\infty} \delta(p_x - n\Lambda), \tag{2.7}$$

$$h_W(\mathbf{p}) = \mathrm{rect}\left(\frac{p_x}{W_x}\right)\mathrm{rect}\left(\frac{p_y}{W_y}\right), \tag{2.8}$$

$$h_D(\mathbf{p}) = \mathrm{rect}\left(\frac{p_x}{W_D}\right), \tag{2.9}$$

$$h_U(\mathbf{p}) = \delta(p_x) \tag{2.10}$$

Using the convolution theorem the corresponding magnitude square of the transfer function (power spectrum) can then be written as [32]

$$\begin{aligned}\left|H(\boldsymbol{\xi})\right|^2 &= \left|\left[H_C(\boldsymbol{\xi}) \otimes H_W(\boldsymbol{\xi})\right] H_U(\boldsymbol{\xi}) H_D(\boldsymbol{\xi})\right|^2 \\ &= \left(\frac{W_x W_y W_D}{\Lambda}\right)^2 \sum_{n=-\infty}^{\infty} \operatorname{sinc}^2\left[W_x\left(\xi_x - \frac{n}{\Lambda}\right)\right] \operatorname{sinc}^2\left(W_y \xi_y\right) \operatorname{sinc}^2\left(W_D \xi_x\right),\end{aligned} \tag{2.11}$$

where $h \overset{FT}{\leftrightarrow} H$ is a Fourier transform pair. The passband located at $\xi_x = 1/\Lambda$ is known as the fundamental passband and is the signal generating band. In this filter configuration all passbands located at even integer multiples of the fundamental frequency (i.e. $\xi_x = \pm 2/\Lambda, \pm 4/\Lambda, \pm 6/\Lambda, \ldots$) are suppressed by the Fourier transform of the aperture function $h_D(\mathbf{p})$ because the zeros of the corresponding sinc-function are located at these positions in spatial spectrum.. The contribution located at - and around - $\xi_x = 0$ is the low-frequency (LF) passband. In figure 2.3 the magnitude square of the transfer function, described by eq. (2.11), is shown.

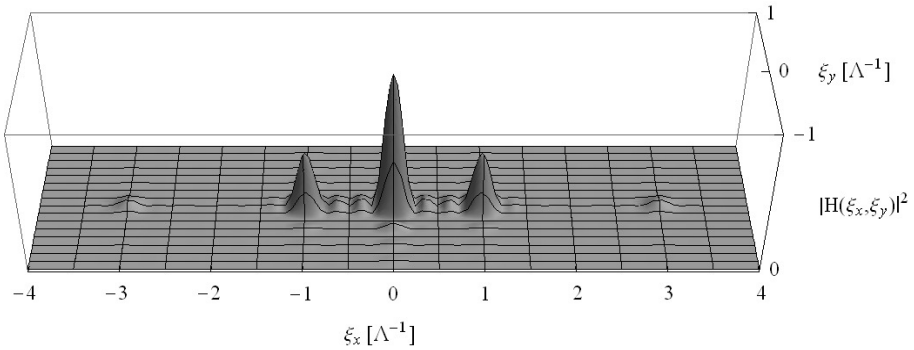

Figure 2.3 – The magnitude squared of the transfer function described by eq. (2.11) for parameters: $W_x = W_y = 4\Lambda$ **,** $W_D = \Lambda/2$ **.**

From figure 2.3 an important property of this type of filter is observed, namely the presence of a third harmonic of the fundamental filter frequency. Generally, the odd harmonics produce a significant passband region in the filter spectrum.
A simpler spatial filter is sometimes considered with a transmittance function given by

$$h(\mathbf{p}) = \frac{h_W(\mathbf{p})}{2}\left[1 + \cos\left(\frac{2\pi p_x}{\Lambda}\right)\right], \tag{2.12}$$

The corresponding spectrum in the spatial frequency domain is then given by

$$H(\boldsymbol{\xi}) = H_W(\boldsymbol{\xi}) \otimes \left\{ \frac{\delta(\boldsymbol{\xi})}{2} + \frac{1}{4}\left[\delta\left(\xi_x - \frac{1}{\Lambda} \right) + \delta\left(\xi_x + \frac{1}{\Lambda} \right) \right] \right\}. \tag{2.13}$$

Selecting

$$h_W(\mathbf{p}) = \exp\left(-\frac{\mathbf{p}^2}{2{W_{xy}}^2} \right), \tag{2.14}$$

The corresponding spatial power spectrum becomes

$$\left|H(\boldsymbol{\xi})\right|^2 = \pi^2 {W_{xy}}^4 \left\{ \exp\left(-2\pi^2 {W_{xy}}^2 \xi^2\right) + \frac{1}{2} \left[\begin{array}{l} \exp\left\{ -2\pi^2 {W_{xy}}^2 \left[\left(\xi_x - \frac{1}{\Lambda} \right)^2 + {\xi_y}^2 \right] \right\} \\ + \exp\left\{ -2\pi^2 {W_{xy}}^2 \left[\left(\xi_x + \frac{1}{\Lambda} \right)^2 + {\xi_y}^2 \right] \right\} \end{array} \right] \right\}^2$$

. (2.15)

In figure 2.4 a plot of eq. (2.15) is shown.

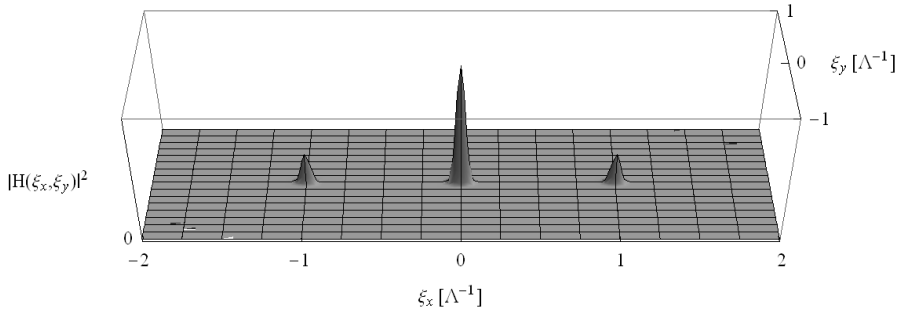

Figure 2.4 - The magnitude squared of the transfer function described by eq. (2.15) for $W_{xy} = 4\Lambda$.

The spatial filter described by eq. (2.15) is difficult to realize in reality but is well suited for analytical purposes. Most importantly, this particular spatial filter does not exhibit the higher harmonic passbands as introduced by the rectangular apodized spatial filter described by eq. (2.11).

The number of unit cells, effectively contributing to the output signal, is a parameter of major importance when designing spatial filters. A measure of the filter selectivity and thus the attainable measurement accuracy, related to the filter alone, is the specific bandwidth. This parameter is defined as the width of the fundamental passband *B* normalized by the fundamental centre frequency $\xi_0 = 1/\Lambda$. For a spatial filter with functionality given by eq. (2.15) the specific bandwidth is given by [31]

$$D_g = \frac{B}{\xi_0} = \frac{1.665}{\pi N}. \tag{2.16}$$

The error in the frequency determination is highly dependent on the specific bandwidth. If it is assumed that the frequency can be determined within $\pm B/2$, the relative accuracy is then roughly given by $D_g/2$. It must be noted, however, that the signal processing scheme that determines the location of the fundamental frequency in the observed spectrum will significantly influence the ultimate accuracy.

When operating with spatial filters that exhibit a significant LF component such as those described by eq. (2.11) and (2.15), it must be noted that deviations in the centre frequency can occur due to the overlap of the "tail" of the LF component with the fundamental passband. This effect is most prevalent if the number of unit cells is low, further emphasizing the importance to maximize this number in practical applications. It can be shown [31] that a spatial filter with a sinusoidal transmittance function and circular window function that operate $N = 10$ unit cells exhibit a systematic error in the fundamental centre frequency below 1% which is acceptable for most applications.

Generally then, a spatial filter should be designed to include as many unit cells as possible. However, the properties of the intensity distribution incident on the spatial filter also play a role according to eq. (2.3). Especially, when applying spatial filters to speckle and fringe patterns the average speckle size and fringe period, in relation to the filter period, is important. This will be addressed further in section 2.3.4. Also, the dynamics of the intensity patterns are important. An example is the presence of a spatially varying velocity field as was encountered in the work presented in **Paper IV**. The presence of such effects imposes a compromise between filter selectivity and power spectral broadening in the signal spectra. The issue then, is complex and generally application- and implementation specific.

2.3 Implementation

In the practical application of spatial filters for velocity measurements, some additional features can be required. One addition, that usually is of interest, is the ability to determine the direction of object motion, i.e. the velocity (component) rather than merely the speed of the object. Furthermore, it is of considerable interest to remove the low frequency (LF) component from the detected signal as it introduces low frequency variations in the signal that can have severe consequences for the performance of, and requirements to, the signal processing scheme. The low frequency signal component also limit the dynamic range of measurable speeds due to the fact that the signal frequency can be confused with the low frequency oscillations at low speeds. These issues can to a large extent be resolved by various arrangements of spatial filters of the types discussed above. Another way is to directly implement an array of detectors that are combined in various ways by sum and difference amplifiers to facilitate beneficial filtering effects directly in the detection process.

2.3.1 Differential detection

An elegant way to suppress the low frequency components is to use two mutually phase shifted spatial filters. In effect, a dynamic high pass filter is implemented directly in the spatial filter itself. This technique is of great importance for highly dynamic velocity measurements where the use of post processing electronic or digital filters are limited or even prohibited. In addition, the technique is also useful when the LF component is overlapping the fundamental pass band, and thus cannot be filtered out. In figure 2.5 the principle of differential detection is illustrated.

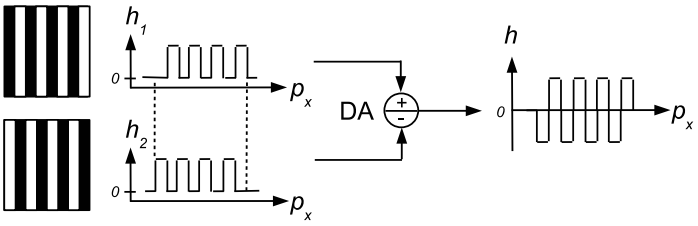

Figure 2.5 – Principle of differential detection.

The implementation of differential detection includes two spatial filters $h_1(\mathbf{p})$ and $h_2(\mathbf{p})$ probing the same intensity distribution. The signals obtained from the filters are passed to a differential amplifier (DA) where the two signals are subtracted, resulting in a new signal. The effect of differential detection on the spatial filter, described by eq. (2.15), can be analysed by examining the combined transmission function

$$h(\mathbf{p}) = h_1(\mathbf{p}) - h_2(\mathbf{p}), \tag{2.17}$$

where

$$h_1(\mathbf{p}) = \frac{h_W(\mathbf{p})}{2}\left[1+\cos\left(\frac{2\pi p_x}{\Lambda}\right)\right], \tag{2.18}$$

$$\begin{aligned} h_2(\mathbf{p}) &= \frac{h_W(\mathbf{p})}{2}\left[1+\cos\left(\frac{2\pi p_x}{\Lambda}-\pi\right)\right] \\ &= \frac{h_W(\mathbf{p})}{2}\left[1-\cos\left(\frac{2\pi p_x}{\Lambda}\right)\right] \end{aligned}. \tag{2.19}$$

Thus

$$h(\mathbf{p}) = h_W(\mathbf{p})\cos\left(\frac{2\pi p_x}{\Lambda}\right). \tag{2.20}$$

Assuming a Gaussian window function $h_W(\mathbf{p})$ described by eq. (2.20) the corresponding magnitude square of the transfer function can be calculated as

$$|H(\boldsymbol{\xi})|^2 = \frac{\pi^2 W_{xy}{}^4}{4}\left[\begin{array}{l}\exp\left\{-2\pi^2 W_{xy}{}^2\left[\left(\xi_x - \frac{1}{\Lambda}\right)^2 + \xi_y{}^2\right]\right\} \\ +\exp\left\{-2\pi^2 W_{xy}{}^2\left[\left(\xi_x + \frac{1}{\Lambda}\right)^2 + \xi_y{}^2\right]\right\}\end{array}\right]^2 . \quad (2.21)$$

In figure 2.6 the spatial power spectrum of the combined spatial filter, described by eq. (2.21) is shown.

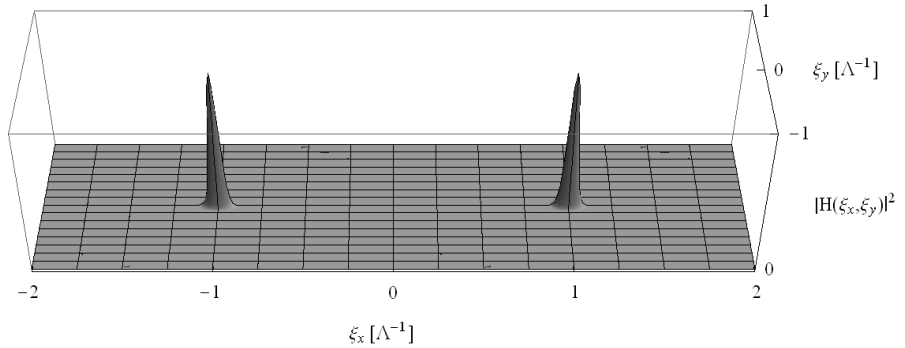

Figure 2.6 - The magnitude squared of the transfer function described by eq. (2.21) for $W_{xy} = 4\Lambda$.

Comparing figures 2.4 and 2.6, it is clear that the passband located around $\boldsymbol{\xi} = (0,0)$ in figure 2.4 is completely eliminated in figure 2.6 due to the differential detection arrangement, which is also evident from eq. (2.21). It is stressed here that only a careful alignment and balancing of the transmission gratings represented by $h_1(\mathbf{p})$ and $h_2(\mathbf{p})$ will result in effective suppression of the low frequency component. A complete elimination is difficult to achieve in practical applications.

2.3.2 Determination of directionality

So far, the spatial filter arrangements that have been considered cannot determine the direction of the speckle translation. This introduces a directional ambiguity of the measured speckle velocity component and thus the object velocity component.
One way to overcome this is to move the spatial filter itself at a constant velocity. This introduces a frequency offset $f_g = v_g / \Lambda$ in the signal power spectrum where v_g is the speed of the grating. If the motion of the speckle pattern incident upon the spatial filter is directed along the same direction as the motion of the grating the observed signal frequency will be $f_s = f_g - f_0$, where $f_0 = v/\Lambda$. Conversely, if

the motion is in the opposite direction, the observed signal frequency will be $f_s = f_g + f_0$. This technique is equivalent to the heterodyne detection schemes used in laser Doppler velocimetry. However, moving parts are usually not a preferred solution in most industrial applications, due to risk of mechanical failures and stability issues.

The phase shifting method used for differential detection can also be utilized to determine the directionality of the motion. Again, two spatial filters are arranged in a similar fashion to figure 2.6. However, the phase shift is now $\pi/2$ rather then π and the differential amplifier is removed. The two resulting output signals from the spatial filters will exhibit a mutual phase angle of $\pi/2$ (90°), i.e. they are in phase quadrature. The signal relationship is illustrated in figure 2.7

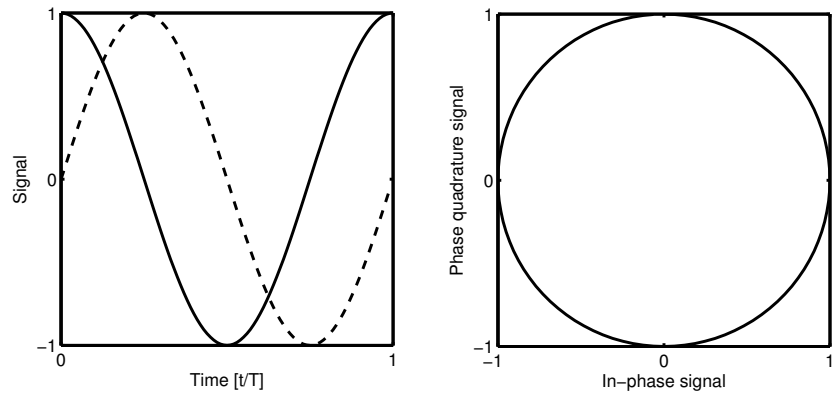

Figure 2.7 – (Left) In-phase (-) and phase-quadrature (--) signal of period *T*. (Right) Parametric plot of the in-phase and phase quadrature signal.

In this way, the direction of motion can then be determined unambiguously by establishing the sign of the phase relationship between the in-phase and phase quadrature signal.

2.3.3 Array of detectors

Implementing both differential detection and directional determination with transmission gratings is difficult to realize in a practical system because it, in principle, requires a four fold splitting of the incoming optical signal. This issue can be resolved using an array of detectors instead of transmission gratings. By arranging sets of detectors in a suitable periodic structure, both the differential detection and directional discrimination can be accomplished without the need for splitting the optical signal. One possible implementation of the principle is illustrated in figure 2.8.

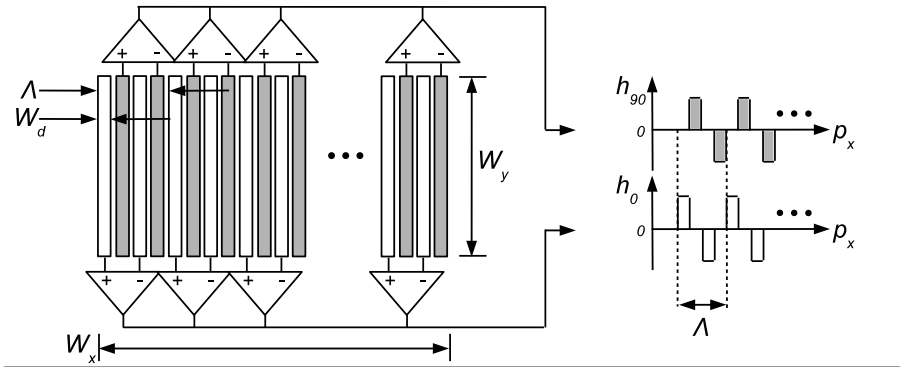

Figure 2.8 – Detector array with differential detection and in-phase and phase quadrature signals for directional discrimination.

Considering eq. (2.6), it is evident that by letting

$$h_U(\mathbf{p}) = \delta\left(x + \frac{\Lambda}{4}\right) - \delta\left(x - \frac{\Lambda}{4}\right), \tag{2.22}$$

the transmittance function of e.g. $h_0(\mathbf{p})$ (cf. figure 2.8) can be realized. The spatial power spectrum of $h_0(\mathbf{p})$ can be written as [33]

$$\begin{aligned} |H(\xi)|^2 = &\left(\frac{W_x W_y W_D}{\Lambda}\right)^2 \sum_{n=-\infty}^{\infty} \operatorname{sinc}^2\left[W_x\left(\xi_x - \frac{n}{\Lambda}\right)\right] \cdot \\ &\times\left[1 - \cos(\pi\Lambda\xi_x)\right]\operatorname{sinc}^2(W_y\xi_y)\operatorname{sinc}^2(W_d\xi_x) \end{aligned} \tag{2.23}$$

In figure 2.9 the spatial power spectrum given by eq. (2.23) is shown.

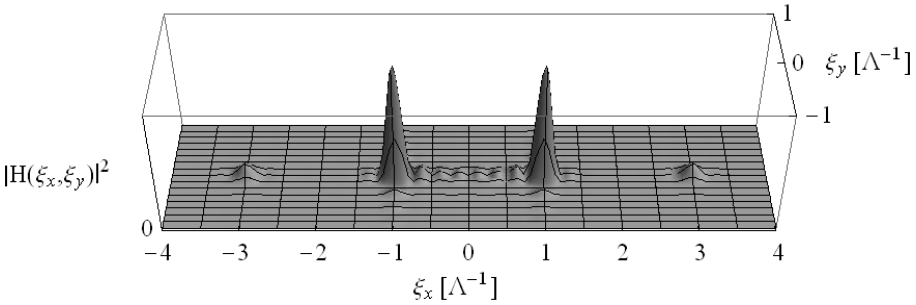

Figure 2.9 - The magnitude squared of the transfer function described by eq. (2.23) for parameters: $W_x = W_y = 4\Lambda$, $W_D = \Lambda/4$

From figure 2.9 it is observed that the passband around $\xi = (0,0)$ is eliminated which is due to the third (cosine) term in eq. (2.23). However, the higher harmonic passband regions at $\xi_x = \pm 3/\Lambda, \pm 5/\Lambda, \ldots$ remain.

2.3.4 Structure size

Generally, different speckle size criteria exist for different applications and filter implementations. One consideration on the speckle size, associated with the use of rectangular apodized spatial filters, can be made with emphasis on eliminating overlap between speckle signal and unwanted harmonics. This may concern harmonics as low as the second harmonic as was implemented in the work by Schnell *et al*. [32], where the aperture of the imaging system was adjusted to accommodate the desired spatial power spectral cut-off of the speckle signal. From this criterion the average speckle size should meet the requirement $\rho_0 \geq 2\Lambda/\pi$.

In the work [33] the effective width of an individual detector used was implemented in such a way as to suppress the third harmonic of the spatial filter, thus relaxing the requirement to confinement of the speckle signal within the fifth harmonic of the filter (provided that the second and fourth harmonic was neglected). For that particular implementation the average speckle size must then meet the requirement $\rho_0 \geq 4\Lambda/5\pi$.

The special fringe dynamics of the "fine structure" described in [7] or the fringe patterns described in **Paper III** and **IV** calls for a different tuning of the spatial filter. Here, the spatial frequency must match identically with the spatial filter to obtain an optimum signal, i.e. the fringe spacing must be identical to the spatial filter period. The spatial frequencies of the fringe patterns in these applications are separated from the speckle part of the spectrum and located at higher frequencies. Therefore, the presence of higher harmonics in the spatial filters, probing the lower frequency speckle region, can overlap with the spectral region occupied by the fringe pattern, resulting in spurious frequencies in the measurements. This phenomenon is discussed and addressed in **Paper III**.

It is possible to derive some basic requirements to the size of the structures, be it particle images, speckles or fringes from general analytic considerations. However, obtaining the optimum signal characteristic is a matter of analyzing the specific properties of both the available intensity signal and the filter implementation, evaluating what provides the best compromise for the application and signal processing scheme that is used to extract the velocity information.

2.3.5 Signal processing

Several different methods exist to process the signals obtained using the SFV technique to extract the measured velocity. Given the oscillatory nature of SFV signal, spectral analysis is a natural choice of processing the signals. Fast Fourier Transform (FFT) algorithms and hardware such as field programmable gate arrays (FPGA) enable widespread use of this technique in many practical applications.

Spectral analysis combined with a peak finding algorithm is well suited and proven technique for measurements of relatively stationary velocities.

If, on the other hand, the velocity can change very rapidly, spectral analysis might not be an effective processing method. An alternative method is simply to count the number of times the time domain signal crosses a given level (e.g. zero) in a given time period. Implementing such a method with certain upper and lower bounds on what defines a crossing is simply known as zero-crossing detection [34]. However, the signal must be free from low frequency noise and signal harmonics as well as exhibit a good signal-to-noise ratio. Otherwise, false counts can occur that leads to spurious velocity measurements.

3. DragonFly technology

The DragonFly (Df) sensor platform is developed specifically to enable two dimensional velocity measurement of a flat, translating, rigid surface. This is achieved by applying methods from spatial filtering velocimetry to the translating speckle and fringe patterns generated by illuminating the surface with a coherent light source. The primary application of the Df sensor is a cursor control peripheral for computers, i.e. a computer mouse.

To achieve a competitive advantage over existing solutions on the market today, several aspects must be taken into consideration. Most importantly a low cost price must be maintained while matching performance or out-performing other devices. Secondly, a low power consumption and small form factor, especially in terms of overall height must also be obtained. To accomplish this, the Df sensor is designed to work in free space, meaning that no optical elements are used to collect or shape the light scattered off the illuminated surface. Furthermore, because the optical mouse market is a high volume (~300M/year) market, it is imperative to ensure that the manufacturing process employed to fabricate the designed components is highly reliable and can maintain a high yield in mass production. This is especially true for the optical unit of the sensor system.

The requirements to the overall system package are addressed in several different ways in the Df sensor. The Df sensor consists of three main components: a compact laser diode light source, an application specific integrated circuit (ASIC) and a single-piece injection moulded optical unit. These components are readily mass-produced at low cost and upon assembly occupy a volume less than $1cm^3$. The assembled Df sensor is shown in figure 3.1.

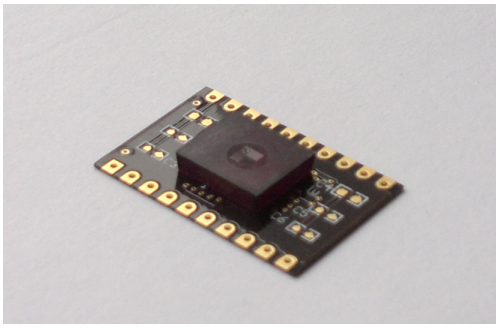

Figure 3.1 - Assembled Df sensor. The assembly measures (H× W× B) (2.5-3mm× 21mm× 14mm). The height is dependent on the specific optical unit used.

The small form factor is mainly attributed to the highly integrated optical unit that incorporates both beam conditioning optics for the illumination and the receiver optics that optically processes the backscattered light from the surface. The optical signals are directed onto the detector arrangements that, in conjunction with the receiver part of the optical unit, facilitate the spatial filtering process and generate the electrical signals for subsequent analogue and digital processing in the ASIC. In

addition, the laser diode is mounted directly on the ASIC unit, effectively integrating the internal sensor electronics into a single unit.
An effective and well functioning sensor system depends on all stages from design to manufacturing and assembly. In this chapter these stages are described individually and discussed. Firstly, the basic functionality of the sensor is described. An overview of the light sources used is then given. Next, attention is turned to the optical unit. Aspects of both design and manufacturing are addressed with special emphasis on optimization of the beam shaping and receiving optics. Lastly, results obtained from testing prototypes developed using the described design principles are presented.

3.1 Functionality

In figure 3.2 the basic working principle of the Df sensor is outlined.

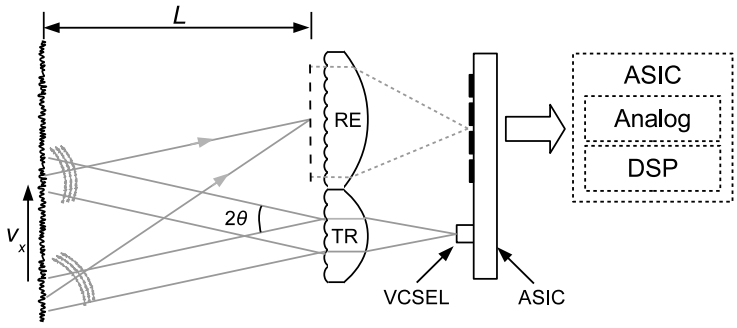

Figure 3.2 – Basic functionality of the Df sensor.

A coherent but divergent field from the light source (VCSEL) is directed towards the collimation lens of the transmitter (TR). The collimated beam is directed towards a diffractive optical element (DOE) that generates a suitable intensity pattern on the surface structure, in the form of a series of equidistantly localized spots. The dynamic and statistical properties of the speckle and fine structure at the receiver entrance plane is well described by eq. (1.43), where $A=1$ and $B=L$. Assuming again, that $\mathbf{v}=(v_x,0)$ and that the observation plane (**p**-plane) is located at the receiver entrance plane and that the receiver is sensitive to translation along the p_x direction, the intensity crosscovariance becomes

$$C_I(\Delta p_x,\tau)=\exp\left\{-\frac{(v_x\tau)^2}{{w_0}^2}-\frac{[\Delta p_x-v_x\tau(1-L/R_0)]^2}{{\rho_0}^2}\right\} \times\cos^2\left\{\frac{k\Delta_{0x}}{2L}\left[\Delta p_x-v_x\tau\left(1+\frac{2L\theta}{\Delta_{0x}}\right)\right]\right\}, \tag{3.1}$$

Where the average speckle size becomes

$$\rho_0 = \frac{2L}{kw_0}. \tag{3.2}$$

The speckle velocity is observed to be

$$v_{sp,x} = g_{sp} v_x = \left(1 - \frac{L}{R_0}\right) v_x \ , \tag{3.3}$$

Where R_0 is the radius of curvature of the illuminating beams and g_{sp} depicts the speckle to object velocity gearing factor. In the Df sensor it is desired that the fringe structure is tracked rather than the speckle pattern. This is accomplished by selecting the angular separation of the two illuminating beams to be $\theta = \pi/(k\Lambda)$, where Λ is the period of the spatial filter implemented in the receiver. As a consequence the fringe spacing and fringe velocity become

$$\Lambda_{fr,x} = \Lambda \text{, (Fringe spacing),} \tag{3.4}$$

$$v_{fr,x} = g_{fr} v_x = 2v_x \text{. (Fringe velocity),} \tag{3.5}$$

where, similarly to g_{sp}, g_{fr} is the fringe velocity gearing factor. This means that the spatial frequency of the fringe pattern exactly matches the fundamental spatial frequency of the filter in the receiver and that the fringe pattern translates with twice the velocity of the object surface. From these considerations it is evident that controlling the geometrical parameters of the DOE is imperative.
Studies [35] have shown that virtually arbitrary intensity distributions can, in principle, be attained. However, in the Df application the requirements imposed by the manufacturing process, limits the complexity of the DOE design and implementation, to relatively simple geometries.
The spatial filtering operation implemented in the receiver is achieved by combining an array of cylindrical lenses (lenticular array) with a large focusing lens to form a compound imaging system that is arranged so that an image of the detector arrangement is formed in a plane in front of each individual lenslet in the array. Thus a repeated image of the detector array is formed at the input plane of the receiver. The principle is illustrated in figure 3.3.

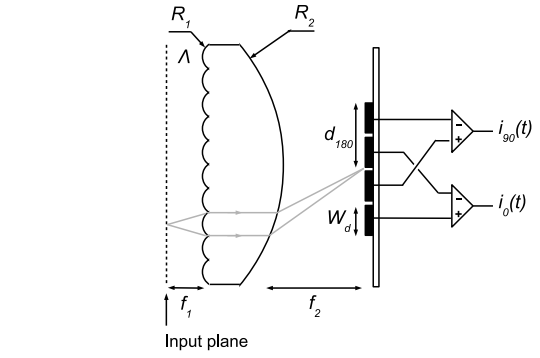

Figure 3.3 – Working principle of the Df receiver.

If perfect imaging is assumed, i.e. no diffraction or aberrations, then the resulting spatial filtering effect of the receiver can be accurately described by the array of detectors described in section 2.3.3 and the corresponding spatial power spectrum of the filter is thus described by eq. (2.23).

However, in real implementations of the receiver optics, significant aberrations will be present as well as diffraction effects. These must be taken into account when designing and evaluating the performance of the optical system and will be addressed in details in section 3.3.2.

The in-phase and phase quadrature signals $i_0(t)$ and $i_{90}(t)$ provides the directional information about the velocity component perpendicular to the lenticular array and the frequency of the signals is given by $f_0 = g_{fr} v_x / \Lambda$.

Two basic considerations on performance are provided by the counts pr. inch (*CPI*) and inches pr. second (*IPS*) numbers. These relationships define the resolution and maximum speed of the sensor system, respectively. They are given by

$$CPI = \frac{g_{fr}}{\Lambda} = \frac{2}{\Lambda}, \tag{3.6}$$

$$IPS = \frac{\nu_{clock}}{4SPC} CPI^{-1}, \tag{3.7}$$

where SPC is the samples pr. count, an algorithm-specific number, that typically is in the range 10-15. The factor of 4 in the denominator of eq. (3.7) is due to multiplexing of the four detector channels. The Df sensor must be able to measure both components of the in-plane translational velocity. In order to achieve this, two sets of receivers are arranged so that the lenticular array of each receiver is oriented in a perpendicular fashion with respect to the other. The transmitter DOE must correspondingly be two dimensional in order to provide the correct illumination pattern for each of the two measurement directions. In figure 3.4 an example of the configurations of the optical unit is illustrated along with the ASIC layout and diode laser light source.

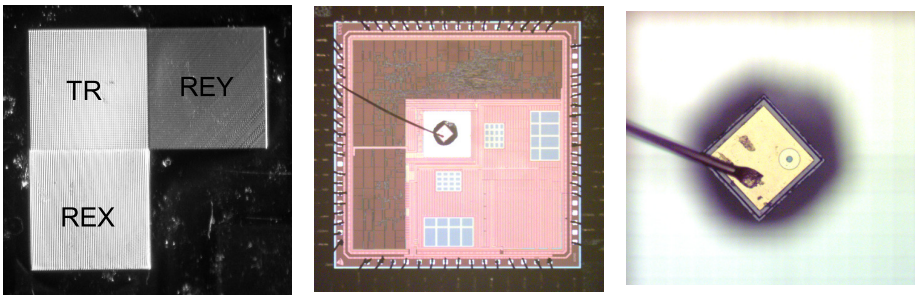

Figure 3.4 – (A) Top view of the optical unit. (B) ASIC layout. (C) Laser diode light source.

3.2 Light source

To maintain a small form factor and low cost in a subsequent high volume production, commercially available vertical cavity surface emitting laser diodes (VCSELs) are used as coherent light sources. The cavity in the VCSEL type diode is oriented vertically in contrast to the edge emitting type laser diode where the cavity is in the plane of the wafer they on which are fabricated. In figure 3.5 a typical internal structure of the VCSEL light source is shown along with typical dimensions.

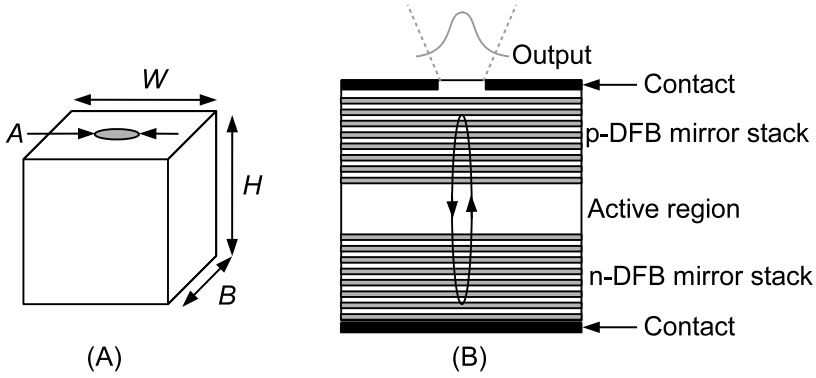

Figure 3.5 – (A) Dimensions of a typical VCSEL light source (H× W× B) (0.2mm× 0.2mm× 0.2mm) *A*=10-15 μm . (B) Typical internal structure of the VCSEL light source.

VCSEL light sources have several advantages in relation to the traditional edge emitting laser diodes when considering their use in the Df sensor. Firstly, the vertical configuration of the laser cavity makes them ideal when the direction of

light emission needs to be perpendicular to the ASIC plane. This also makes the integration with the ASIC, which provides the current for the operation of the VCSEL, easy. The intensity profile of the output beam is generally symmetric and approximately Gaussian. Thus, no additional optics is needed to correct for anamorphic beam profiles as usually is the case for edge emitting laser diodes.
Several parameters can be specified to evaluate the performance of a given VCSEL, depending on the application. In the Df sensor application the most relevant include the optical output power, beam divergence, wavelength, slope efficiency and threshold current.
The threshold current determines the minimum amount of current needed to operate the VCSEL as a laser source. The optical output power versus the injected current characteristic is also of considerable interest. After threshold is reached, and lasing is achieved, the optical output power will exhibit a linear relationship with the injected current in a limited region of injected current. In figure 3.6 a typical power characteristic is shown.

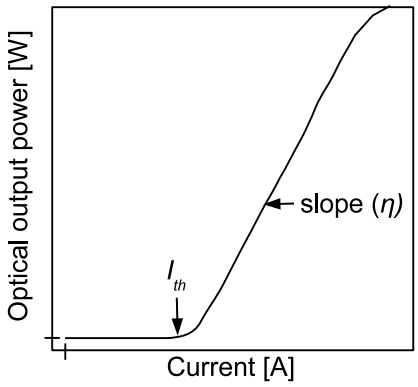

Figure 3.6 – Power characteristic of a typical VCSEL light source illustrating the relationship between optical power output from the VCSEL versus the injected current.

The slope efficiency determines the increase in optical output power pr. unit current in the linear region of operation. The beam divergence is also of importance in the Df sensor as it largely determines the spot size formed on the DOE for the transmitter via the collimator optics, and subsequently influences the spot size on the object surface. The beam divergence is usually stated as the angle subtended at the FWHM intensity diameter.
Several different wavelengths are available, both visible and near-infrared. From a performance standpoint the optical wavelength matters little in the Df sensor application as long as the detectors that are used are sensitive to the selected wavelength. However, some consideration must be taken to ensure eye safety requirements. In table 3.1 the most relevant parameters are listed for some of the VCSELs used in the sensor system.

Table 3.1 – Specifications of some commercially available VCSEL light sources used in the Df sensor.

Manufacturer / Series	Wavelength λ [nm]	Threshold current i_{th} [mA]	Slope eff. η [mW/mA]	Optical power P_{out} [mW]	Beam divergence α [$^\circ$] (FWHM)	Remarks
Avalon Photonics / AVAP – 850SM	850	2	0.4	1.4	12	SM*, PS**
Optowell / SS85 – 7U001P	850	2	0.4	0.7	9	SM,PS
Truelight / TSD – 8B12 – 000	850	1.5	0.4	1.5	16	N/A
Optowell / SS67 – 4U001	670	2.5	0.3	0.5	7	SM

* SM=Single-Mode, ** PS = Polarization stabilized

For details on the fabrication, materials and performance of VCSELs see e.g. [36], [37].

3.3 Optical design

To a large extent the design of the optical unit used in the Df sensor can be facilitated by using complex *ABCD* matrix formalism and this tool is valuable in determining the dynamics and statistical properties of the speckle and fringe patterns. However, complex *ABCD* matrix formalism is inherently paraxial and cannot be used to analyze aberrations.
Ray tracing provides a tool for incorporating virtually any lens shape and modelling its performance. Professional ray tracing software like ZEMAX™, provides a wide range of analysis and optimization tools that effectively models the performance of individual optical elements as well as complete system integrations. In this section both the matrix formalism and the ray tracing tools are combined to provide a comprehensive modelling framework of the Df optical unit.

3.3.1 Transmitter

The first optical surface the light from the VCSEL sources encounters is the collimation optics. A simple spherical lens is used here. The most important function of the collimation lens is to form a suitable single spot illumination of the DOE structure located at the exit plane of the transmitter unit. Of most importance is the spot size. The specific functionality of the intensity pattern is not critical to

the performance of the transmitter. The optical collimation system is illustrated in figure 3.7.

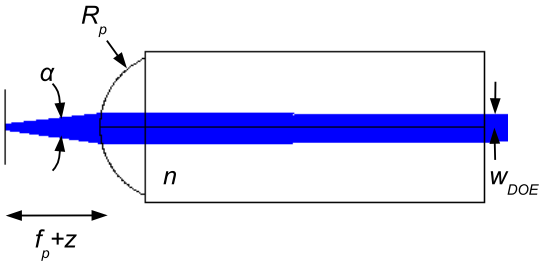

Figure 3.7 – Collimation (z=0) of the VCSEL light source.

The spot size is in most cases of interest adequately described by the simple geometric relation

$$w_{DOE} = \sqrt{2\ln 2} f_p \tan\left(\frac{\alpha}{2}\right), \tag{3.8}$$

where $f_p = R_p/(n-1)$ is the focal length of the collimation lens and w_{DOE} is the e^{-2} intensity radius spot size. The now collimated beam illuminates the DOE of the transmitter. The purpose of the DOE is to redistribute the intensity in a multitude of spots on the target surface structure. In the case of two dimensional translation measurements the properties of the ideal distribution is a four spot pattern illustrated in figure 3.8

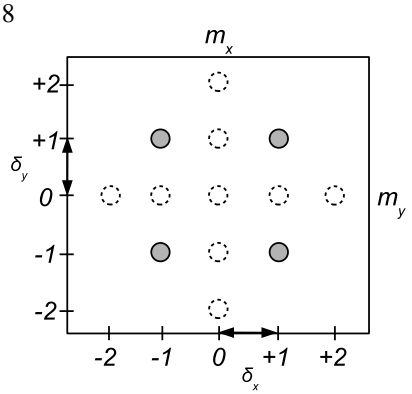

Figure 3.8 – Ideal intensity distribution at the target surface structure.

The power P_{m_x,m_y} contained in each spot should in the ideal case be completely confined to diffraction orders $m_x, m_y = \{1,1;-1,1;1,-1;-1,-1\}$, i.e. 25% diffraction efficiency for each of the four orders. The diffraction order separation must facilitate the correct spatial frequency of the fine structure at the input plane of the receiver. If the system operates at a working distance L then $\delta_x = \delta_y = \lambda L/(2\Lambda)$ must be fulfilled.

To this end a binary phase grating structure is considered. The generalized unit cell is illustrated in figure 3.9. The cells within the grating unit cell are composed materials with refractive indexes n_2 and n_3 while the surrounding material has an index of refraction n_1.

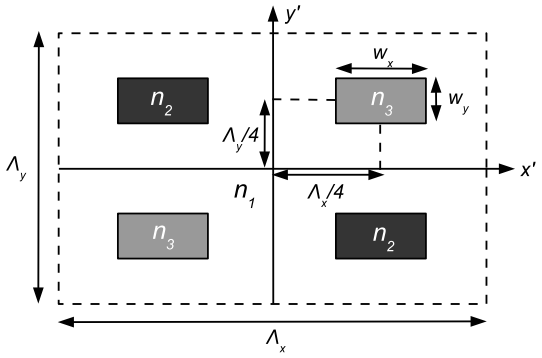

Figure 3.9 – Unit cell of a general binary phase grating structure.

The grating structure $h(\mathbf{r}')$ is assumed to be illuminated by a field distribution given by

$$U_{i,DOE}(\mathbf{r}') = U_0 \exp\left(-\frac{\mathbf{r}'^2}{{w_{DOE}}^2}\right). \tag{3.9}$$

The field distribution, obtained in the far-field, has been solved generally by Daria et al. [38]. Here, a special case is considered where $w_x = w_y = \Lambda_x/2 = \Lambda_y/2$, $n_2 = n$ and $n_1 = n_3 = 1$. The field distribution at the object surface is then

$$U(f_x, f_y) = U_0 \left[\begin{array}{l} \exp\left[\frac{i\varphi}{2} - \pi^2 {w_{DOE}}^2 \left({f_x}^2 + {f_y}^2 \right)\right] \\ -\frac{i}{2}\sin\left(\frac{\varphi}{2}\right) \sum_{m_x,m_y} \left\{1 + \exp\left[-i\pi\left(m_x + m_y\right)\right]\right\} \mathrm{sinc}\left(\frac{m_x}{2}, \frac{m_y}{2}\right) \\ \times \exp\left\{-\pi^2 {w_{DOE}}^2 \left[\left(f_x - \frac{m_x}{\Lambda}\right)^2 + \left(f_y - \frac{m_y}{\Lambda}\right)^2\right]\right\} \end{array} \right], \tag{3.10}$$

where $f_j = j/(\lambda L)$ for $j = \{x, y\}$. The phase depth φ of the grating is in this case given by

$$\varphi = (n-1)\, k\, H, \tag{3.11}$$

where H is the height of the structure. The intensity distribution in the far-field is obtained as

$$I(f_x, f_y) = \left|U(f_x, f_y)\right|^2, \tag{3.12}$$

In figure 3.10 the unit cell geometry and corresponding far-field intensity distribution for $\phi = \pi$ is shown.

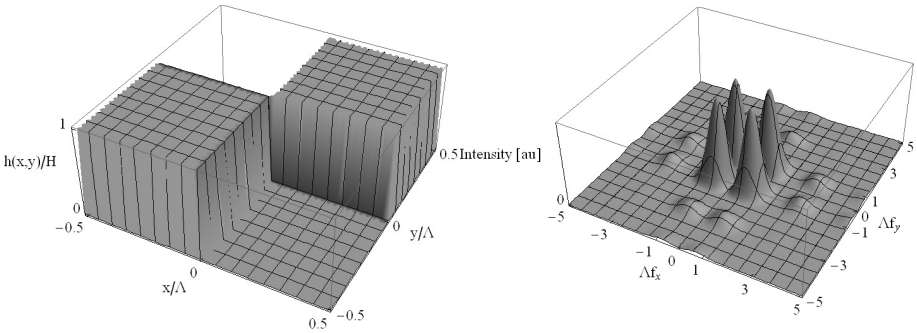

Figure 3.10 – (Left) "Checkerboard" DOE geometry. (Right) Far-field diffraction pattern where $\phi = \pi$.

The condition $\phi = \pi$ ensures that the zero order (0,0) is completely eliminated. The height H_π required to achieve the desired suppression of the zero diffraction order can be calculated by rearranging eq. (3.11) yielding

$$H_\pi = \frac{\lambda}{2(n-1)}. \tag{3.13}$$

The diffraction efficiencies of can be estimated by evaluating $I(f_x, f_y)$ at integer values of (m_x, m_y) and eliminating common factors. The three most important contributions are

$$I(0,0) = 0, \tag{3.14}$$

$$I(1,1) = \frac{16}{\pi^4} \approx 16.4\%, \tag{3.15}$$

$$I(1,3) = \frac{16}{9\pi^4} \approx 1.8\%. \tag{3.16}$$

This means that a maximum of 65.7% of the power, incident on the grating structure, will be present in the desired diffraction orders, i.e. $m_x, m_y = \{1,1;-1,1;1,-1;-1,-1\}$.

3.3.2 Receiver

The receiver of the optical unit consists of a lenticular array which in combination with a large focusing lens forms a compound imaging system that, in combination with the detector arrangement on the ASIC, implement the optical spatial filter. The power spectrum of the optical spatial filter is in principle given by eq. (2.23). However, this implies that the compound imaging system formed by the lenticular array and focusing lens performs perfectly. This is not the case even for an imaging system operating at the diffraction limit. Several effects come into play when dealing with real systems. These effects modify the ideal transfer function of the spatial filter and must be understood in order optimize the design and subsequent performance of the optical unit.
A set of basic design rules is now stated. It is important for the proper operation of the sensor system that the magnification of the individual imaging system in the array is correct. A relationship linking the half width of the detector array to the period of the lenticular array can be established as (cf. figure. 3.3):

$$d_{180} = \frac{\Lambda f_2}{2 f_1} = \frac{\Lambda R_2}{2 R_1} . \tag{3.17}$$

Furthermore, a condition that satisfies refractive operation of the cylindrical micro lenses in the lenticular array can be deduced by observing that this will be the case if

$$\mathrm{Re}\{A\} >> \mathrm{Im}\{A\}, \tag{3.18}$$

where A is the matrix elements of an optical system illustrated in figure 3.11. The element is given by

$$A = -\frac{f_2}{f_1} + \frac{2 i f_2}{k \sigma^2} , \tag{3.19}$$

This optical system represents a single unit of the compound imaging system.

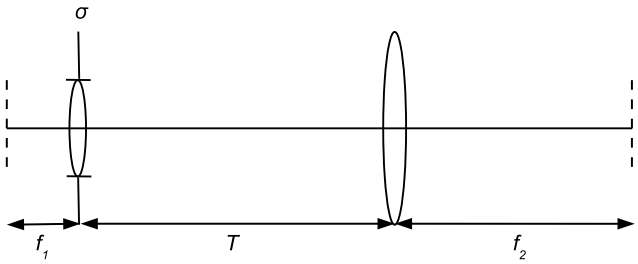

Figure 3.11 – Single unit of the compound imaging system forming the optical spatial filter of the Df receiver.

Substituting $\sigma \to \Lambda / 2$ and enforcing the condition given by eq. (3.18) results in the following requirement [39]

$$\mathrm{X}_d \equiv \frac{\Lambda^2}{\lambda f_1} >> \frac{4}{\pi} \approx 1 . \tag{3.20}$$

Another important design parameter is the number of lenslets that can be accommodated in the array. This property depends on several features. Firstly, the separation of the lenticular array from the focusing lens. The condition imposed in this case ensures that the contribution from the outermost lenslet in the array is fully collected by the focusing lens. This relationship can be expressed by [33]

$$NA_2 \geq NA_{2,c} = \frac{\Lambda}{2 f_1 f_2}\left[T + f_1 (N-2)\right], \tag{3.21}$$

where NA_2 is the numerical aperture of the focusing lens and T is the separation between the lenticular array and the focussing lens. In table 3.2 the most relevant design parameters are listed for to different optical units.

Table 3.2 – Selected design parameters of two manufactured Df optical units

Name	Λ [μm]	R_1 [μm]	R_2 [μm]	n	f_1 [μm]	f_2 [μm]	λ [μm]	N	T [μm]	NA_2
Df3400*	15	18	1000	1.65	28	1550	0.85	65	700	0.44
Df2000**	26	50	1700	1.65	78	2636	0.85	32	700	0.26

* *CPI*=3387, ***CPI*=1954

In table 3.3 the design criteria, for the two optical units, are listed.

Table 3.3 – Design criteria for Df3400 and Df2000 optical units.

Name	$NA_{2,c}$	$d_{180} / 4W_d$	X_d
Df3400	0.44	1.11	9.45
Df2000	0.19	1.18	10.3

From Table 3.3 it is observed that the criteria to the numerical aperture of the focusing lens are significantly higher for the Df3400 unit than for the Df2000 unit. This is in part due to the number of lenslets included in the lenticular array. Furthermore, an (intentional) magnification error is introduced as can be observed from the third entry in table 3.3. This is implemented based on experience with earlier versions that seemed to perform better with this error introduced. One explanation for this empirical experience might be found in a more even illumination profile of the detector array due to the overmatched magnification of the compound imaging system. This explanation is supported by ray tracing models of the focusing lens, presented below. The drawback of this is a non-optimal phase difference between the signals in the four detectors.

The use of spherical lens profiles in the optical unit can introduce severe aberrations. However, spherical lenses are implemented in the optical unit due to the lack of suitable alternative methods for lens fabrication. The design must then take into account the impact of using spherical lens shapes and, if necessary, compensate or compromise to achieve the best attainable performance.
Using ray tracing the imaging performance of a single imaging unit in the lenticular array is now evaluated. Four object positions in the front focal plane of an individual lenslet are traced to the detector plane for different positions of that lenslet in the array. In figure 3.12 the used ray tracing model is illustrated and the results are plotted on the right hand side.

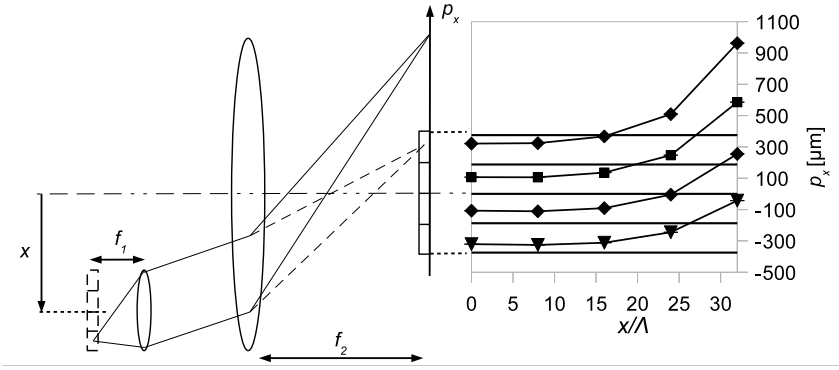

Figure 3.12 – (Left) Illustration of the effect of spherical aberration on the imaging performance of an off-axis lenslet in the array. The stippled line (---) represents the optimum imaging performance and the solid line (-) the actual one. (Right) The actual ray tracing data is shown for the Df2000 optical unit.

The effect of aberration is evident for the outermost lenslets as the image points are located beyond the detector array. It is thus observed that lenslets in the array beyond a certain number of periods do not contribute to the detector signal. A cut-off can be identified in this particular case at (in total) 32 lenslets. For the Df3400 design this number was estimated, using the corresponding parameters of that design, at 52 lenslets which is fewer than the design prescribed (cf. table 3.2). This particular design was first implemented in November of 2006 and was not subject to the full range of design considerations implemented for the Df2000 unit.
When considering the transmitter and receiver parts of the Df optical unit as a integrated system it becomes evident that the relative positions of the VCSEL in relation to the detector arrays has implications not only for the position of the focusing lens but also for the angle under which it must collect the main part of the light scattered off the target structure. A cross section view in figure 3.13(Left) illustrates the configuration. The focusing lens must be positioned to maximize the collected light onto the detector arrays in both directions of velocity measurement. A model scattering source is positioned directly above the VCSEL aperture. In figure 3.13(Right) the resulting intensity pattern on the detector array is shown. The calculation is performed using non-sequential ray tracing.

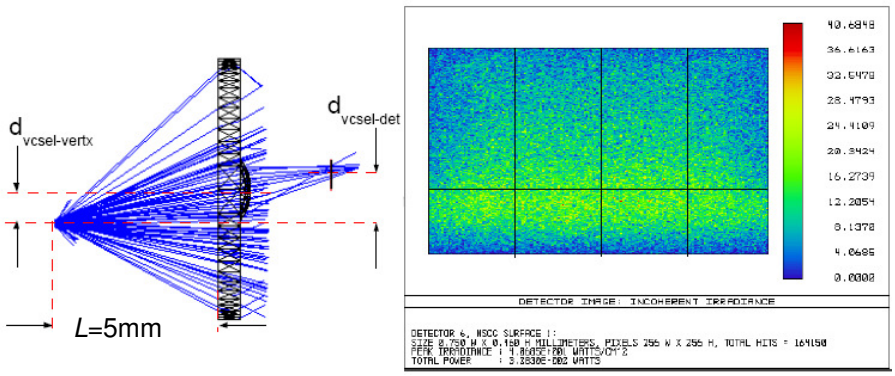

Figure 3.13 (Left) Ray tracing model layout with a scattering source. (Right) The resulting incoherent intensity distribution on the detector array calculated by ray tracing. The horizontal line is an actual detector separator in the array, but usually the vertical detector pairs are combined electronically in the ASIC.

The effect of the lenticular array is seen widen the distribution to cover the majority of the detector array in accordance with eq. (3.17). This ray tracing model is primarily used to determine the vertex position of the focusing lens in new designs. However, the model also hints at more fundamental effects. For instance the distribution is seen to be centred on the detector array, but it is not homogeneously distributed on all four detectors. The implications of this effect are important. Consider the transmittance function described by eq. (2.6) where a window function $h_{DW}(\mathbf{p})$ is introduced into the unit cell

$$h(\mathbf{p}) = \left[h_C(\mathbf{p})h_W(\mathbf{p})\right] \otimes \left[(h_U(\mathbf{p}) \otimes h_D(\mathbf{p}))h_{DW}(\mathbf{p})\right], \tag{3.22}$$

where

$$h_{DW}(\mathbf{p}) = \exp\left(-\frac{2\mathbf{p}^2}{\sigma^2}\right), \tag{3.23}$$

In figure 3.14(Left) the unit cell transmittance function is shown for three different widths of the window function $h_{DW}(\mathbf{p})$, given that the terms $h_C(\mathbf{p})$, $h_W(\mathbf{p})$, $h_U(\mathbf{p})$ and $h_D(\mathbf{p})$ are described by eq. (2.7)-(2.10). In figure 3.14(Right) the corresponding power spectrum is shown (here evaluated numerically by FFT).

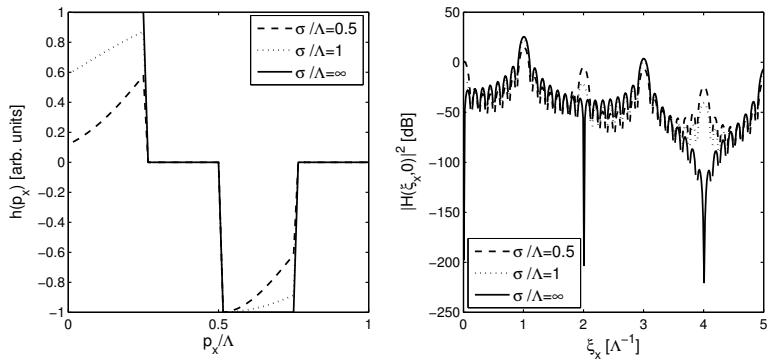

Figure 3.14 – (Left) Spatial impulse response of the detector array. (Right) Power spectrum of the transfer function of the detector array, *N*=8.

It is observed that the suppression of even harmonics of the fundamental passband of the spatial filter decreases as the window width σ decreases. Also, the low frequency contribution around $\xi_x = 0$ is observed to decrease in suppression which is readily understood in terms of the introduced imbalance between the two detectors.

In reality, the window function that envelopes the detector array exhibits a complex functionality due to diffraction effects from the lenticular array and aberrations of the focusing lens. The window function can therefore, only approximately, be modelled as a Gaussian function and the conclusions that can be drawn are qualitative. The model does however demonstrate that an optical spatial filter implemented in this way generally will exhibit significant passbands both in the low frequency region and in the higher harmonic domains which is also observed in experiments (cf. section 3.5).

In the Df system the low frequency part can be suppressed additionally by adjusting the gain of the individual detectors in the array, in effect, balancing the differential detection. However, the presence of significant power in the unwanted orders of diffraction in the intensity distribution illuminating the object surface will also introduce power at unwanted spatial frequencies in the intensity power spectrum at the entrance plane of the receiver. The power at these spatial frequencies might overlap with the higher harmonic pass band of the receiver, introducing unwanted artefacts in the detected signal.

Considering figure 3.14(Right), it is observed that the second and third harmonic band passes of the filter are the most significant. Of these, the potentially most disruptive is the second. Of considerable interest is then, the suppression of second order contributions, due to the intensity distribution that illuminate the target structure. The power spectrum at the entrance plane (p_x, p_y) of the receiver can be related to the autocorrelation function of the intensity pattern $I_i(\mathbf{r}) = |U_i(\mathbf{r})|^2$ on the target structure and is generally given by [1]

$$\left|S_I(\xi)\right|^2 = \langle I \rangle^2 \left[\delta(\xi) + \frac{\int_{-\infty}^{\infty}\int_{-\infty}^{\infty} \left|U_i(x,y)\right|^2 \left|U_i\left(x-\lambda L\xi_x, y-\lambda L\xi_y\right)\right|^2 dxdy}{\left(\int_{-\infty}^{\infty}\int_{-\infty}^{\infty} \left|U_i(x,y)\right|^2 dxdy\right)^2} \right]. \tag{3.24}$$

Here, a simplified model, based on eq. (3.24), is implemented to estimate the suppression ratio between the signal and second harmonic, due to the illumination profile.

The suppression of second and higher order terms of the spatial power spectrum at the entrance plane of the receiver can be estimated by considering the peak power of the diffraction orders. This approximation is valid only if the diffraction order spot functionality is the same for all considered diffraction orders and if the spots do not overlap. Furthermore, estimates can vary depending on the number of contributions included in the calculation and a rigorous result calls for a calculation of the autocorrelation function of the intensity distribution. However, referring to figure 3.10, the most significant contributions to the (desired) fundamental spatial frequency band, when assuming the intensity pattern of the "checkerboard" DOE described by eq. (3.12), can be written as

$$\begin{aligned} FUN = {} & P_{1,1}P_{-1,1} + P_{-1,-1}P_{1,-1} + \\ & P_{-1,3}P_{1,3} + P_{-1,-3}P_{1,-3} + P_{1,1}P_{3,1} + P_{1,-1}P_{3,-1} + , \\ & P_{-3,1}P_{-1,1} + P_{-3,-1}P_{-1,-1} \end{aligned} \tag{3.25}$$

where

$$P_{m_x,m_y} = \int_{spot} d^2\mathbf{r} I\left(m_x, m_y\right), \tag{3.26}$$

is the power contained in the $\left(m_x, m_y\right)$ diffraction order spot. Similarly the contribution to the second harmonic spatial frequency band is written as

$$2H = P_{-3,1}P_{1,1} + P_{-1,1}P_{3,1} + P_{-3,-1}P_{1,-1} + P_{-1,-1}P_{3,-1} . \tag{3.27}$$

The ratio $2H / FUN$ gives the suppression of second harmonic contributions in relation to the fundamental band. For the optimum checkerboard DOE intensity pattern this ratio is -7.5dB.

It must be noted that the suppression ratios calculated here only gives the suppression due to the specific illumination of the object structure. If the transfer function of the receiver is ideal then contributions to e.g. the second harmonic will be further suppressed. However, as can be observed from figure 3.14(Right) the

transfer function of the receiver exhibit added complexity due to the windowing effect of the detector array.
Generally, these effects are complex and can in reality only be evaluated experimentally. However, the principles discussed in this section aid the understanding of these effects and provide insight that may, in future designs, be applied to remedy them.

3.4 Manufacturing

The optical unit of the Df sensor is manufactured using injection moulding. Injection moulding is a reliable way of mass producing especially polymer based optics, and is widely used.
The standard injection moulding process involves two mould masters that are machined to form a cavity outlining the part that is to be moulded. The two masters are combined and the hot material is injected into the cavity. After cooling the part is ejected from the mould and the process is repeated. Figure 3.15 illustrates the basic injection moulding process.

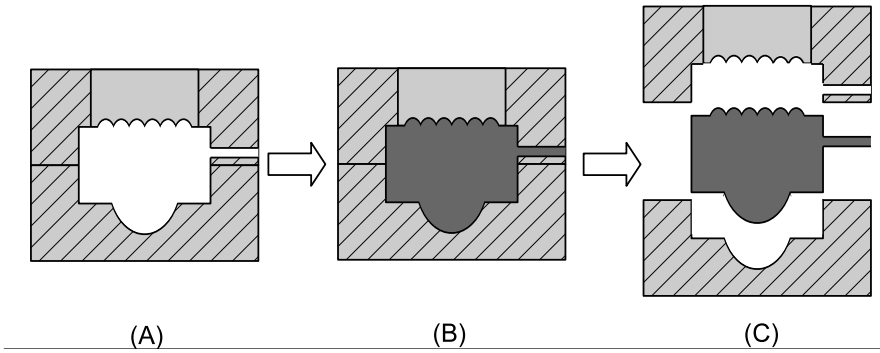

Figure 3.15 – The injection moulding process. (A) Cycle start with an empty mould. (B) Injection of molten material into the cavity. (C) Cooling and ejection of the moulded part.

The material used depends on the application but is usually a polymer. Several parameters affect the quality of the parts that emerge from the process. These include, but are not limited to: injection pressure, temperature and flow characteristics of the material as well as cooling time and general mould shape. The optimum operational parameters of the process will in most cases be determined by trial and error. Most important is achieving a complete filling of the cavity, especially when injection moulding parts with optical surfaces. If this is not achieved, the surface quality will be severely compromised and lens shapes can be distorted.
Two of the most important commercial parameters of the injection moulding process are the cycle time and the yield. The cycle time is the time it takes to mould, cool and eject the part. The cycle time is highly dependent on the size and

complexity of the part. In the case of the Df optical unit, the cycle time is approximately 5s. The yield is the ratio of usable parts to non-usable parts that emerges from the moulds. These parameters translate directly into the cost of the optical units and thus affect the competitiveness of the final product.
Initial start-up costs in terms of equipment are significant and injection moulding is not particularly well suited for prototyping purposes. This can be partly remedied by modifying the mould masters to accommodate so-called inserts that can be replaced if a better design or another application is desired. This feature eliminates the need to acquire completely new and expensive moulds every time a modification is made to the optics. In the prototype stages this ability to test new designs at a reduced cost is very advantageous.
In figure 3.16 pictures of the two master moulds of the optical unit used in the Df sensor are shown. The mould masters are designed to accommodate 6 separate cavities yielding 6 optical units for every cycle, further boosting production rate.

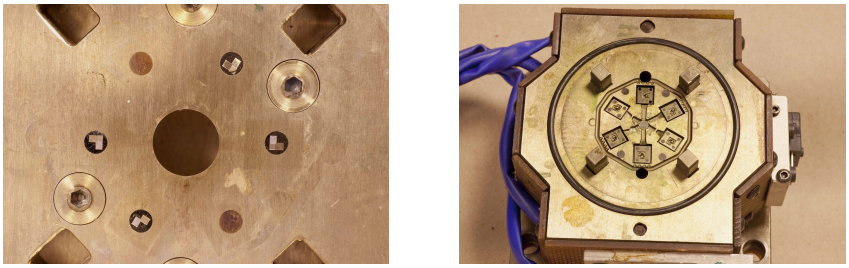

(A) (B)

Figure 3.16 – (A) Front master mould with inserts containing the micro-optical transmitter and receiver optics. (B) Backside master mould with macro-lens inserts.

The front side master contains insert in which the lenticular arrays and DOE structure are imprinted. The backside master contains inserts with collimation and focusing (macro) lenses. Both inserts, front and back, can be replaced.

3.4.1 Micro-machining

To achieve the high degree of precision needed to fabricate lenticular arrays of sufficient quality, sophisticated micromachining equipment is utilized. By a process known as ruling each individual lenslet is formed by a diamond tool that is dragged over the insert surface. The insert consist of a steel core covered by nickel plating. The nickel is softer than the steel and thus more easily processed by the tool while still maintaining sufficient toughness to endure several million moulding cycles. The diamond tool is precision ground to match the desired lenslet profile, i.e. cylindrical with a fixed radius of curvature. This means that an individual lenslet is formed by dragging the tool, only once, across the insert surface, dramatically reducing the fabrication time of the micro-optical inserts. This process and the lenslet profile and parameters are illustrated in figure 3.17.

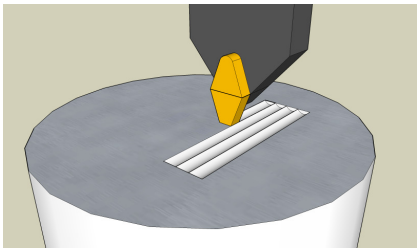

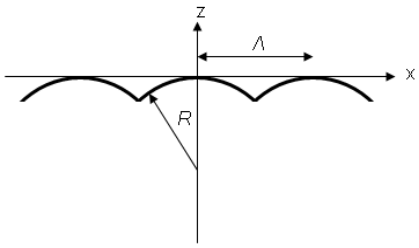

Figure 3.17 – (Left) The ruling process. (Right) The lenslet profile and parameters of the injection moulded part.

Another advantage of this process is that every lenslet is completely identical, resulting in identical performance. However, care must be taken to ensure that the tool profile is correct. The spherical profile tool used to fabricate the lenticular array is specified by its radius of curvature (R) and waviness. The tool profile function $P(x)$ is given by

$$P(x) = w(x) - R + \sqrt{R^2 - x^2} \tag{3.28}$$

where $w(x)$ is the waviness *profile* of the tool. The waviness *parameter* is defined as the peak-peak maximum deviation of the tool profile from the desired profile. A high quality tool can be manufactured within $\pm 1\mu$m @ $R = 18\mu$m and a waviness parameter of <50nm.

A precision profile of the tool is not enough to ensure high performance of the micro-optics. Precision control is also needed in positioning and manipulation of the tool itself. Especially the period of the array is critical. This is achieved using state-of-the art micro milling machines. The tool positioning is accurate to within $\pm 1.5\mu$m over a displacement of 200mm as stated by Kaleido Technology A/S who provides this service.

Depending on the application the transmitter structure can vary, and for some industrial sensing applications be left blank. However, in the case of the Df sensor a two dimensional diffractive structure is desirable as discussed in the previous section. To simplify the fabrication process the DOE can be fabricated using the same tool as for the lenticular array by simply continuing the ruling process creating a crossover region of lenslets. This in turn ensures the correct diffraction angles to match the spatial frequencies of the fringe pattern to the fundamental passband of the receiver. This "crossed-lenticular array" or CLA structure works reasonably well even though the intensity pattern it produces contains significant power in the zero- and higher diffraction orders.

The checkerboard geometry is the most effective DOE structure evaluated in section 3.3.1. However, this geometry cannot effectively be fabricated directly using micro-machining methods due to the nature of the unit cell. To implement this transmitter design, other methods must be applied.

3.4.2 Ion-beam etching

The potential performance characteristic of the checkerboard geometry, when used as the transmitter DOE, prompted several attempts using ion beam etching [40] as means of realizing the geometry on the nickel plated micro-optical inserts.
The ion beam etching methodology relies on masking the surface to be etched by applying a layer of photo resist in the desired pattern. When the etching process is initiated, the unmasked areas will have material removed by the ion beam. The photo resist will also be removed by the beam, generally at a different rate, but as long as the photo resist is present it will protect the area it covers. When the desired etching depth is reached, the remaining photo resist is removed revealing the desired pattern imprinted in the nickel layer of the insert, which subsequently can be used for injection moulding.
The first step in the process is to generate the correct pattern of photo resist on the insert. Firstly, the entire insert is spin coated with photo resist. Next, a commercially available chrome mask that contains the checkerboard geometry is positioned on top of the photo resist. The insert is then exposed to UV radiation rendering the photo resist in the areas, not protected by the chrome. After development of the photo resist, the insert is etched by the ion beam to the correct depth and the remaining photo resist is removed using acetone. The process is illustrated in figure 3.18.

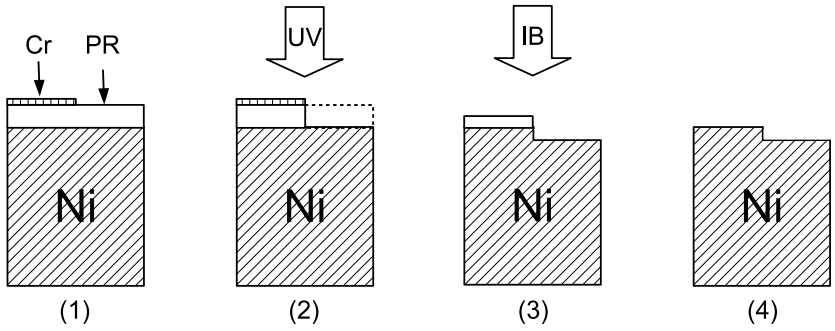

Figure 3.18 – Ion beam etching process. (1) Coating the nickel insert with photo resist and positioning of chrome mask. (2) Exposure with UV radiation. (3) Ion beam milling. (4) Removal of photo resist residue.

The insert was subsequently supplemented with lenticular arrays by normal micro-machining, and several optical units were manufactured. In figure 3.19 an image obtained with a microscope of the transmitter structure is shown.

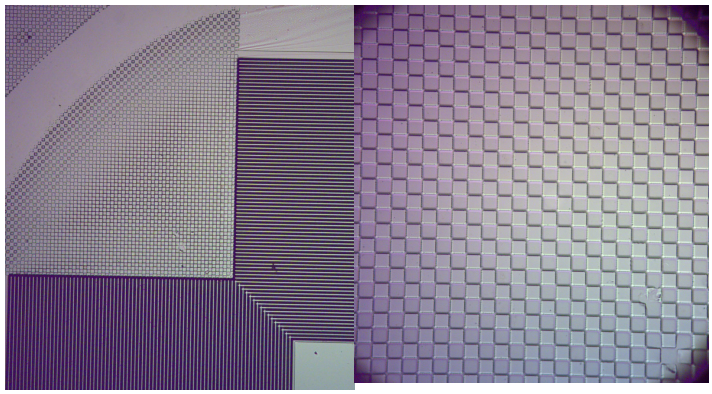

Figure 3.19 – (Left) Microscope image of insert with the DOE structure fabricated with the ion-beam etching process (Right) High magnification image of the DOE structure.

In figure 3.20 a plot of a DEKTAK scan (cf. section 4.1.1), revealing the depth of the structure, is shown. Both a scan of the insert structure and the moulded optical element is included.

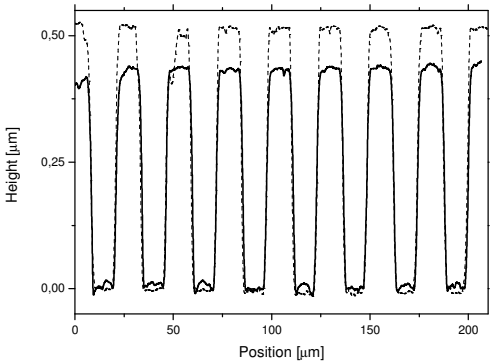

Figure 3.20 – DEKTAK scan of DOE on the insert (---) and the moulded optical unit (-).

The average depth of the DOE on the insert was 0.514 μm um and 0.432 μm was achieved for the moulded optical unit. It must be noted that the DEKTAK scans presented in figure 3.20 do not represent the exact same location on the insert and moulded part, respectively. Local variations are to be expected, so the direct comparison of the two scans must be made with caution. It is reasonable to conclude though, that the required depth of the structure in accordance with eq. (3.13) has not been met. Several attempts were made to obtain the correct depth of 0.654 μm . Unfortunately, the etching rate was too unstable, fluctuating with 5-8% between runs, to achieve consistent results. This instability of the etching rate must be resolved if the method is to be a viable choice for forming the transmitter DOE structure.

3.4.3 Materials

For most Df sensor applications either polycarbonate (PC) or ULTEM, which is another polymer material, are used in the injection moulding process. PC has a refractive index of n = 1.58 @ 670nm and is used for visible wavelength applications while ULTEM, with a refractive index of n = 1.65 @ 850nm, is used for near-infrared applications.

3.5 Performance

The performance of the Df sensor is ultimately evaluated at system level when the sensor is completely assembled. System level tests are typically performed in an x-y table that can recreate arbitrary patterns of motion of specific object surfaces at various speeds and accelerations. Various surfaces are typically inserted in front of the sensor to evaluate signal quality and ensure that the sensor can track motion on the broadest range of different surfaces as possible.
In the optical mouse application, the signal frequencies occupy a dynamic range of approximately 10^0-10^5 Hz. This makes standard digital filtering very difficult, especially due to the fast changes (acceleration) in frequency the sensor has to accommodate. In the actual application a sophisticated time domain algorithm is applied to each of the two measurement directions (x and y) that effectively tracks the in-phase and phase quadrature signals and counts the number of oscillations and the relative phase of the two signals to deduce the displacement and direction.
The transmitter performance is evaluated by recording the diffraction efficiencies of relevant diffraction orders. The power in each diffraction spot is measured by a photodetector, making sure that the aperture of the detector is large enough to encompass the spot, but small enough to block neighbouring spots. In figure 3.21 the diffraction pattern and associated diffraction efficiencies are shown for the injection moulded part with the checkerboard DOE transmitter geometry. As expected from the DEKTAK measurements (cf. figure 3.20) the phase depth of the structure is too shallow and significant zero order efficiency remains and only 8% efficiency is present in the desired first order contributions.

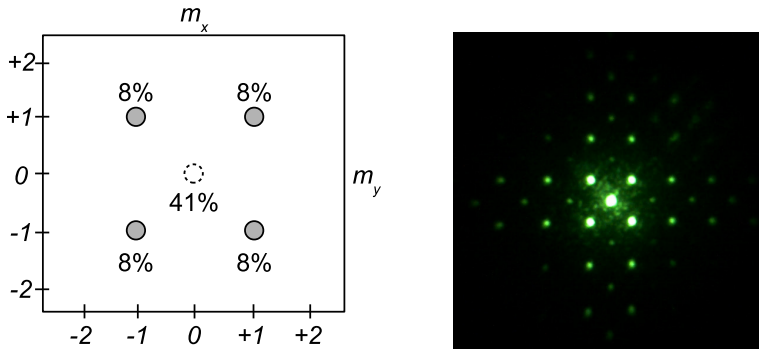

Figure 3.21 – (Left) Measured diffraction efficiencies of the moulded optical unit implementing the checkerboard transmitter DOE. (Right) A photograph of the intensity distribution obtained through an IR viewer.

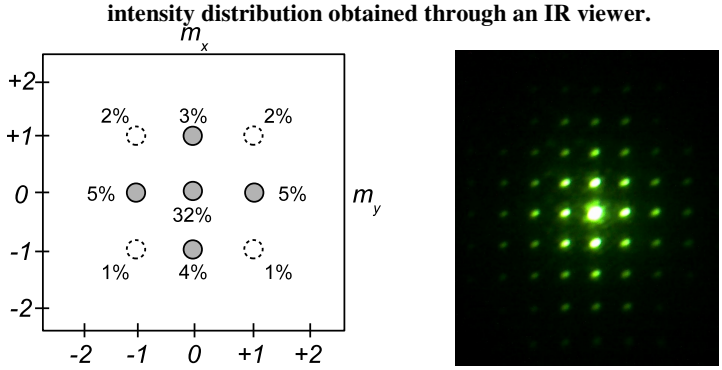

Figure 3.22– (Left) Measured diffraction efficiencies of the moulded optical unit implementing the crossed lenticular array (CLA) transmitter DOE. (Right) A photograph of the intensity distribution obtained through an IR viewer.

In figure 3.22 the diffraction pattern and associated diffraction efficiencies are shown for the injection moulded part with the CLA DOE transmitter geometry. Most notably, an imbalance in the efficiencies for the vertical and horizontal directions are observed

The optical unit is tested in conjunction with the ASIC, the detector arrays and amplifiers that will be used in the final assembly. The signals are routed out of the ASIC at the analogue-to-digital level that immediately follows the differential amplifier stage (cf. figure 3.3). No processing other than the filtering properties of the analogue amplifier chain is imposed on the signals. The sensor optical unit is aligned with the ASIC and placed in front of a surface that moves in a direction that engages both measurement directions of the sensor. The signals then represent the raw digitized output from the detector and amplifier arrangement and are well suited for evaluating the performance of the optical unit. Figure 3.23 shows a typical time domain and power spectrum signal.

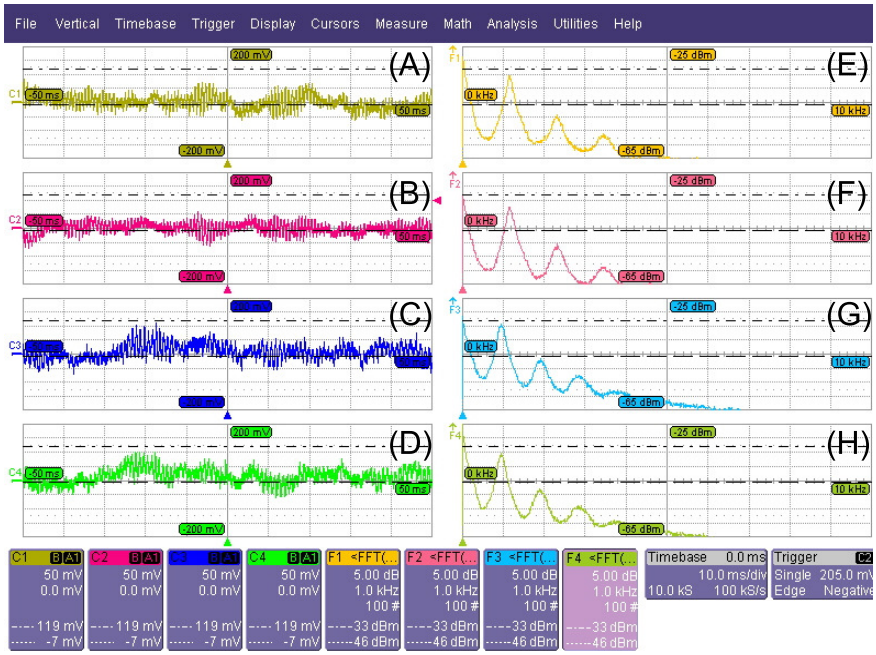

Figure 3.23 – Typical oscilloscope signal complex used to evaluate performance of the optical unit. The signal shown here are obtained from tests of the 3400 CPI optical unit utilizing the CLA DOE structure. (A)-(D) Time domain signals from the differential amplifiers. (E)-(H) Average power spectra obtained from the average of 100 FFTs of the time domain signals.

Several features are present in both the time domain signals and the power spectral densities. Examining the time domain signals, a quasi sinusoidal signal is observed as expected. This component is the fundamental signal that is used to determine the two transverse velocity components of the surface motion. From the time domain signals it is also possible to determine whether or not the relevant signals maintain phase quadrature, i.e. the prerequisite for directional determination. The averaged power spectra of the output signal reveal additional information of the frequency components present in the signals that can be hard to determine from the time domain signals alone. Several characteristic features can be identified. The most important ones are (cf. figure 3.24):

Fundamental component (FUN): Relates to the translation of the fringe pattern. The fringe pattern translates in response to the surface translation given by $v_{fr,x} = 2v_x$ in response to the object surface velocity component along *x*.

Second harmonic component (H2): Relates to the translation of the second harmonic part of the fringe pattern.

Low frequency component (LF): Relates to the signal frequency band around zero frequency (DC). The effect of this component is readily observed in the time domain signals as a fluctuating offset value of the quasi sinusoidal signals. This component is very disruptive and can in severe cases impair the ability of the signal processing to extract the velocity information from the signals. Suppression of this signal component is a major design goal.

Speckle component: Relates to the translation of the speckle pattern. The speckle pattern translates in response to the surface translation given by eq. (3.3). The radius of curvature R_o is determined by the positioning of the collimation optics in relationship to the VCSEL light source.

In figure 3.24 as series of averaged power spectra for a single signal component, recoded using the Df2000 optical unit, is shown. A fixed working distance of $L = 5\text{mm}$ is maintained while the defocusing parameter z (cf. figure 3.7) is varied. The object surface is sand blasted aluminium.

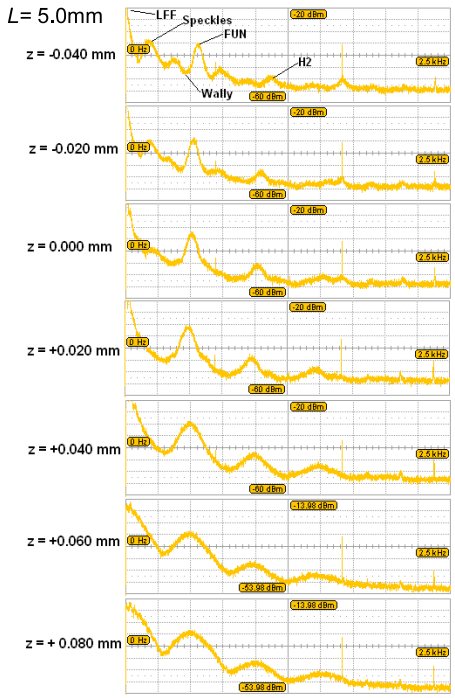

Figure 3.24 – Recorded power spectra at different values of defocus (z) for the Df2000 optical unit for L = 5mm. The object surface is sand-blasted aluminium.

When z<0 the beams emanating from the transmitter are diverging and the spot size on the object surface is comparatively large. The radius of curvature R_o will in this case be negative. In case z>0 the beams will be converging, the spot size on the

object will comparatively small and the radius of curvature will be positive. When z=0 the beams are collimated and the radius of curvature is very large.
It is observed that for z<0 the speckle contribution is significant. This can be attributed to the large spot size on the object that in turn results in small speckles. The spatial frequency of the speckle part then partially overlaps the fundamental passband of the receiver. As z increases and becomes $z > 0$ a distinct widening of the fundamental signal components is observed. This can be attributed to the smaller spot size on the object. As the spots become smaller so does the speckle correlation length, and because the fringe pattern is limited by the speckles the fundamental signal peak broadens. The optimum configuration can be argued to be z = 0.020-0.040mm in terms of speckle suppression and signal frequency bandwidth. For this particular design a reasonable second harmonic suppression, in relationship to the fundamental signal, of 13-14dB also allows for satisfactory performance.

4. Characterization methods

The ability to evaluate the quality and characterize the properties of the manufactured optical units is of great importance. Reliable characterization tools play important roles in all phases of manufacturing complex optical elements. From basic research and development to design validation and quality assurance in final production stages, these tools are crucial. Depending on the specific area of interest different characterization methods are usually necessary in order to get a complete picture of the quality of the manufactured part.
The Df optical unit is a highly integrated piece of optics that incorporates several different functionalities. The most critical parts of the unit is the micro optics of the transmitter DOE and the lenticular array of the receiver. Moreover, several stages of manufacturing go into fabricating these structures and careful control of each one is necessary to ensure acceptable performance of the finished unit. The microscopic size of these optical structures also place special demands on the characterization methods that can be considered. Most commercially available solutions that can perform measurements on such structures are usually very expensive.
The Df optical unit is ultimately destined for mass production. This presents a significant quality assurance challenge, especially due to the fast cycle time (typically on the order of seconds) of the injection moulding process. Furthermore, a large number of process parameters affect the quality of the moulded parts. Any deviation in these can result in defective optical units. Maximizing the yield is a top priority in high volume production and having a method that can monitor quality directly in the production line, possibly supplying quasi real-time feedback to the injection moulder, is highly desirable.
In this chapter the two main types of characterization methods, used in conjunction with the Df optical unit, are described. Firstly, scanning probe instruments are described in terms of functionality, performance and applicability. Secondly, non-invasive instrumentation is discussed. In this part the commercially available scanning white light interferometer (SWLI) [41],[42] is briefly discussed. The method developed in **Paper I** and **Paper II** is discussed in relation to the commercially available instrumentation and a possible implementation of the method, into an application specific instrument, is also addressed.

4.1 Scanning-probe microscopy

Scanning-probe microscope instruments utilize a needle like probe that usually is in contact or near proximity with the surface under investigation. When the probe is placed in contact with the sample surface either the sample or the probe performs a horizontal line scan, simultaneously logging the relative probe-sample distance. This provides a height profile of the surface at that particular scan position. If three dimensional (topographical) data is required the line scan is repeatedly performed at a number of adjacent scan positions forming a matrix of height data providing a topographical map over that particular region. Scanning probe instruments are very

sensitive to height variations of the sample surface and routinely operate in the sub nanometer ranges. Unfortunately, this sensitivity also leaves them susceptible to ambient noise and vibration.

4.1.1 Stylus profilometer (DEKTAK)

The DEKTAK instrument draws on a stylus with a tip radius on the order of 10-50 μm depending on the manufacturer. The advantage of DEKTAK is its ability to accept large samples both in terms of scan range but also more importantly in height. Typically, a sample can have features up to 0.5mm in height and still be accommodated by the system. Horizontal scan ranges can be as large as 50mm. The vertical resolution generally depends on the maximum feature height on the sample. The vertical position of the tip is measured using a low inertia force gauge. Typical resolutions are in the order of 0.5-1nm.
The large range and height acceptance of the DEKTAK instrument makes it ideal for investigating the profiles of the collimating and focusing lenses of the Df optical unit. The DEKTAK provides a means of characterizing the geometrical parameters of both the macro and micro lenses and structures of the Df optical unit. The DEKTAK was used to verify the optical measurements performed in **Paper I** and to provide the data presented in figure 3.20. However, when characterizing the moulded optical units, clear tracks are left behind by the stylus. This was made evident by subsequent analysis by microscope inspection and atomic force measurements. The force applied by the stylus under the scan procedure was enough to damage the surface. This fact rules out the use of DEKTAK on the master moulds and inserts used for injection moulding as this might permanently damage them and thus imprinting this damage in every moulded unit produced using that particular master. Furthermore, the comparatively large radius of curvature of the tip limits the feature sizes that can be resolved (see e.g. [43]).

4.1.2 Atomic Force Microscopy (AFM)

The atomic force microscope is based on a physical probe that is brought in contact or close proximity with the sample surface. Most modern AFM instruments implement a silicon cantilever with a sharpened tip, used as probe. A typical tip geometry is shown in figure 4.1. Cantilevers tips for AFM can take on many specialized shapes depending on the application. The tip radius is typically in the order of 5-10nm.
The AFM is used in one of two main modes of operation: contact and dynamic mode. In dynamic mode the tip is held at a given distance above the surface and driven to oscillate by a transducer. As the cantilever is brought closer to the sample, the frequency and amplitude of the cantilever oscillation generally changes. This effect can be used to probe the complex interaction forces between the probe and surface [44].
In contact mode the cantilever tip is brought into contact with the surface. In this case, the interaction force between tip and sample results in a deflection of the cantilever. The deflection of the cantilever should be much larger than the

combined deformation of the tip and surface. The criterion is met if the cantilever spring constant (k_c) is significantly smaller than the inter-atomic spring constant of the sample and probe materials. For most practical metrology applications using solid surfaces this amounts to ensuring that $k_c << 10$N/m [44].

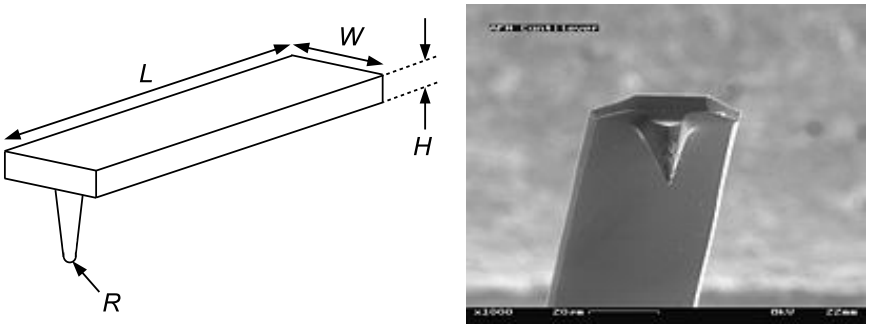

Figure 4.1 - Typical cantilever geometry.

Scanning the tip across the surface and measuring the cantilever deflection then renders a topographic map of the scanned region. The scanning motion is accomplished by mounting the cantilever on a xyz piezo stage that enables the tip to move in all three directions. An alternative configuration can also be encountered where the sample itself is mounted on a xyz piezo stage and the tip is fixed in relation to the sample. The deflection can be measured in a number of ways. The most common one is the "beam bounce method". Here a laser beam is focused on the top of the cantilever and the reflection is directed towards a detector split in two halves.
The basic functionality of a typical commercially available AFM is shown in figure 4.2.

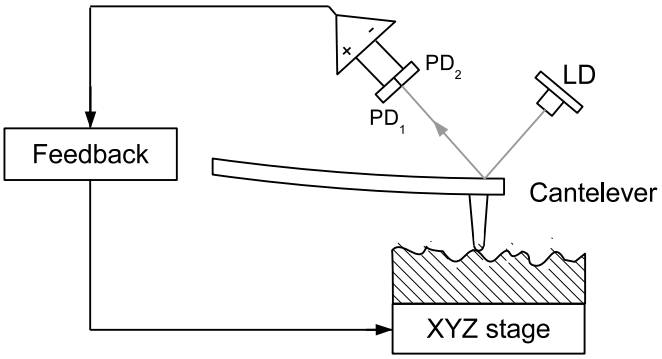

Figure 4.2 – Basic AFM functionality with beam bounce detection.

As the tip is scanned across the sample, the features of the surface deflect the cantilever from its equilibrium position. This causes the position of the laser beam to shift slightly on the split detector. Subtracting the two photo signals gives an error signal proportional to the cantilever deflection (for small deflections). A feedback mechanism receives the error signal from the detector and corrects the vertical piezo position to minimize the error signal. The x, y and z positions of the piezo stages are logged and when processed provides the desired topographical map of the scan region.
In figure 4.3 an AFM image of the receiver part of a Df optical unit is shown. This was obtained using a table top commercially available AFM.

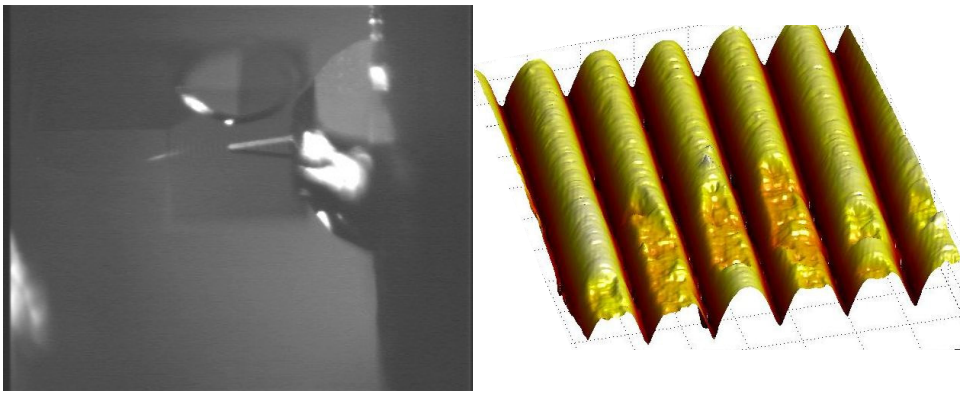

Figure 4.3 – (Left) Image of the scanner head probing the lenticular array of a Df optical unit (Right) AFM image of a small region of a receiver in a Df optical unit is shown. In this case the injection moulding was incomplete resulting in areas where the lens shape is destroyed.

Some specifications of this instrument are shown in table 4.1.

Table 4.1 – Specifications and operating limits of the Nanosurf EasyScan™ AFM instrument.

Scan range	$70\,\mu\text{m} \times 70\,\mu\text{m}$
Transverse resolution	2 nm
Vertical range	~ 5 μm
Vertical resolution	0.5 nm

The parameters of the cantilever used here was (cf. figure 4.1): $T = 1.8\mu\text{m}$, $W = 48\mu\text{m}$, $L = 446\mu\text{m}$ and a spring constant of $k_c = 0.14\text{N/m}$.
The scan range of this particular instrument is limited to $70\,\mu\text{m} \times 70\,\mu\text{m}$. Furthermore, the measurement time is in the order of minutes and very sensitive to sound and vibrations. The alignment and lowering of the tip onto the sample can be difficult and cantilevers are prone to breakage. The limited scan range can be resolved though. The AFM instrument at Danish Fundamental Metrology A/S (DFM) addresses the issue by implementing a stationary tip and sample translation

stage with an interferometric position sensor. This allows for much longer scans (~500 μm) while maintaining sub-nanometer precision in both the vertical and horizontal directions. This instrument was used to verify the measurements performed in **Paper II**.
The AFM instrument can achieve a very high degree of resolution and is effective when used in conjunction with prototype verification (i.e. small number of samples). However, due to its high sensitivity to vibration, long scan time and limited range, its use as a fast characterization instrument, suitable for implementation in an industrial environment, is limited.

4.2 Optical methods

To address the need for a fast and robust characterization method of the micro-optical structures of the Df optical unit several optical methods can be considered. The lenticular array of the receiver is the most challenging structure to test and will be the main focus of this discussion.
The non-invasive nature of optical testing is attractive because the measurement will not damage the optical surfaces. The applicability of a specific methodology is dependent on two main parameters. Firstly, the measurement cycle time must be comparable to the cycle time of the injection moulding process, and secondly the accuracy and resolution must enable efficient and reliable discrimination between sub-standard optical units and units that meet the specification.
The scanning white light interferometer (SWLI) is a commercially available optical characterization method that provides topographical information of the surface under test. The measurement principle is based on the Mirau correlation microscope. Most commercial versions can be fitted with microscope objectives of different magnification depending on the application. The most important parameters are the field of view (FOV), axial and in-plane resolution as well as the axial range. In table 4.2 these parameters are listed for a commercial SWLI instrument. Typical measurement cycle times are on the order of 2-5s.

Table 4.2 – Selected parameters for the Zygo NewView™ 7100 series scanning white light interferometer.

Field-of-view (FOV)	0.07mm – 9.3mm*
Transverse Resolution	0.36 μm - 9.5 μm *
Vertical range	150 μm
Vertical resolution	<0.1 nm
* Microscope objective dependent	

As with any microscope system there is a trade off between resolution and FOV. This is also the case with the SWLI instrument. Given a typical Df optical unit where the receiver array has dimensions of 1mm$\times$ 1mm and lenticular array period of e.g. $\Lambda = 13\mu$m, the sampling of a single lenslet can be roughly estimated by interpolating the FOV and resolution parameters assuming a linear relationship. The resolution, given the full field of view of 1mm, can be calculated to be $\sim 1.3\mu$m i.e. approximately 10 sampling points of an individual lenslet profile. This

will be sufficient to deduce a radius of curvature from the profile. However, the topographical data still needs to be post processed in order to extract e.g. average radius of curvature and pitch of the entire array. This will further increase measurement cycle time.
Although the SWLI instrument is highly versatile and provides relatively fast cycle times, the cost of a commercial system ranges in several tens of kEUR. In high volume production the optical units will be manufactured on anywhere in between 10-100 injection moulding machines running in parallel. This means that the cost price of the implemented characterization system becomes relevant.
Taking these considerations into account, calls for a characterization system that is simple, cheap and easily maintained. A method that has potential to fulfil many of these requirements was investigated by Büttner *et al* [45]. This method is based on observing the far field diffraction pattern of the lens array illuminated by a collimated laser diode. Implementing an iterative phase-retrieval algorithm, the average radius of curvature and aberrations of the entire array can be extracted. The system configuration is simple and cheap. The algorithm is readily implemented in most post processing solutions, e.g. Matlab™. However, the method is demanding in terms of pixel size and number. Furthermore, the algorithm can be prone to erroneous convergence if initial parameters are not selected correctly. In addition, a large number of iterations (~10000) needs to be performed in order to achieve convergence.
In **Paper I** a method is investigated which is similar to the method described in [45]. It does, however, differ in some key points. Again the lenticular array is illuminated by a plane wave of laser light but the light is collected in reflection mode rather than transmission. The diffracted light is collected, in the far-field, by a single detector mounted on a swivel. The measured intensity distribution or rather the diffraction efficiencies of the diffraction orders are compared to an analytical model derived using scalar diffraction. The analytical model of the diffraction efficiencies is given by

$$\eta(m) = \frac{|U(m)|^2}{\sum_m |U(m)|^2}, \tag{4.1}$$

where

$$U(m) = U_0 \exp\left(\frac{i\pi m^2}{\Xi}\right)\left\{\operatorname{erf}\left[\sqrt{\frac{\pi}{8\Xi}}(1+i)(\Xi-2m)\right] + \operatorname{erf}\left[\sqrt{\frac{\pi}{8\Xi}}(1+i)(\Xi+2m)\right]\right\}, \tag{4.2}$$

where $\Xi \equiv 2\Lambda^2 / \lambda R$ and m is the diffraction order. In figure 4.4, typical measured and calculated diffraction efficiencies, are shown.

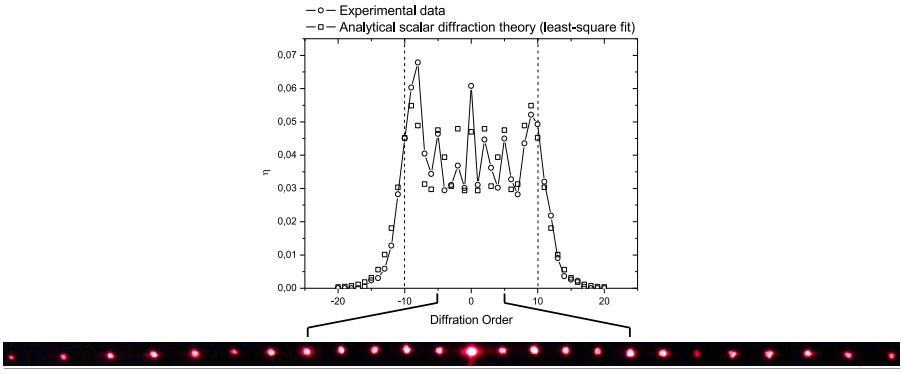

Figure 4.4 – Typical measured and theoretical diffraction efficiencies along with a photographed intensity distribution (bottom).

The task then becomes finding the minimum value of the squared sum of the residuals between data and theory. The sum-squared-error (*SSE*) is calculated in the following way

$$SSE = \sum_{m} [\eta_{meas}(m) - \eta_{theo}(m)]^2 \ . \tag{4.3}$$

The value of Ξ at $\min(SSE)$ is interpreted as the best fit of the theory to the measurement. Through this simple and easily automated operation, the parameter Ξ for the lenticular array under test can be determined. However, deriving the radius of curvature relies, in principle, on prior knowledge of period Λ of the lenticular array.

Paper II investigates how the method discussed in **Paper I** can be extended to include a simultaneous measurement of the array period as well as the radius of curvature. Fixing the detector and rotating the optical elements under test allows, by measurement of the rotation angle, to extract the pitch and the diffraction efficiency simultaneously. This configuration has the added benefit of fixing both the light source and the detector making the setup more rugged, easier to construct and less susceptible to vibration. The only precision equipment needed is a high resolution (~1/60 degree) rotation stage with an encoder and digital readout. In figure 4.5 a possible implementation is shown.

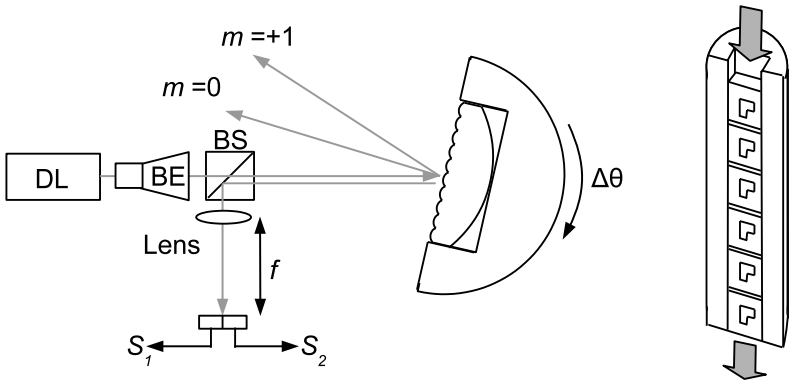

Figure 4.5 – Possible implementation of the characterization method discussed in Paper II. The optical units under test are mounted in racks to allow for continuous fast throughput for large scale testing.

To illuminate the entire array, a telescope system with variable magnification is implemented. The setup is arranged so that the detectors are placed in the back focal plane of the lens. This means that the diffraction pattern observed in the plane of the detector is in far field of the lenticular array [17]. The split detector arrangement allows accurate determination of the centre of the diffraction spots by monitoring the error signal $E = S_1 - S_2$. When $E = 0$, a readout of the angle is performed and the power signal $P = S_1 + S_2$ is recorded. The lenticular array is then rotated through all available diffraction orders and from the measurement vectors of rotation angles and corresponding power signals the average radius of curvature of the lenticular array, as well as the period, can be extracted.

The limiting factor for the measurement cycle time will depend on the specific rotation stage used. A possible implementation of a dedicated system, such as illustrated in figure 4.5, is yet to be assembled and evaluated. However, cycle times on the order of a second or less are realistic.

5. 3D velocimetry

The Df technology, described in the previous chapters was designed for measurement of two dimensional translation velocity. In many applications a full three dimensional velocity measurement is called for. This can be achieved in a number ways depending on the specific application and what type of data is needed. Especially non-invasive and remote sensing methods are of great scientific and industrial interest and have been investigated extensively.
Three-dimensional velocity measurements address, in particular, applications in flow and fluid dynamics ranging from atmospheric studies [46] , [47] to combustion dynamics [48]. Among other industrial applications can be mentioned strain and stress studies of surfaces under load [49] and structural dynamics [50].
An emerging field of industrial research is the use of wind velocity sensors in the wind energy industry. Wind velocity data are used to prospect areas for potential wind turbine farms and investigate the dynamics of existing ones [51]. As mentioned previously, studies based on the use of laser Doppler velocimeters have shown that wind velocity data can also be used to significantly increase the effectiveness of individual wind turbines in terms of power output. However, the use of such sensors in conjunction with individual turbines presents several commercial issues that need to be resolved before a widespread use can be implemented. This is mainly due to the high cost prize of these systems that range in the order of 100 kEUR.
In this chapter a novel approach to the measuring of three-dimensional velocities is addressed and discussed in relation to other methods. The work presented in **Paper III** discusses and demonstrates, experimentally and numerically, the basic principle of measuring three-dimensional translations, while **Paper IV** addresses analytically and experimentally the use of the same principle for measuring angular velocity of rotating objects. Firstly, a brief review of some of the most relevant existing methods, related to three-dimensional velocity measurements, is given. These include several variations on the well known technique of laser Doppler velocimetry (LDV) as well as electronic speckle interferometry (ESPI). Finally, an analytical comparison of the expected signal levels between the method described in **Paper III** and the conventional LDV method is given.

5.1 Background

Speckle photography and speckle interferometry are well established techniques that have been used extensively to investigate whole-field deformation of different rigid structures under load. Usually, the deformation field of a certain region of the surface is of interest. This differs from techniques related to laser Doppler velocimetry. Here, the measurement is localized to a point-like region of space. The distinction between a full-field measurement and a point measurement must usually be made and taken into consideration in relation to the specific measurement application.

5.1.1 Laser Doppler velocimetry

Laser Doppler velocimetry or LDV is based on measurement of Doppler shifts associated with light scattering from rigid objects or particles in motion. Homodyne and heterodyne detection is most commonly used to detect the frequency shifts that arise due to the Doppler shift of the scattered radiation. This detection principle relies on the use of a coherent local oscillator that is combined with the signal coming from the scattering object. The two fields are combined, or "mixed", on a non-linear device such as a photomultiplier tube or photodetector. A photo detection device is sensitive to the absolute square of the field incident upon it, i.e. the intensity of the optical signal. The incident intensity results in a photocurrent that can be converted into a voltage signal for analysis in e.g. a spectrum analyzer or an oscilloscope. The detection principle is shown in figure 5.1

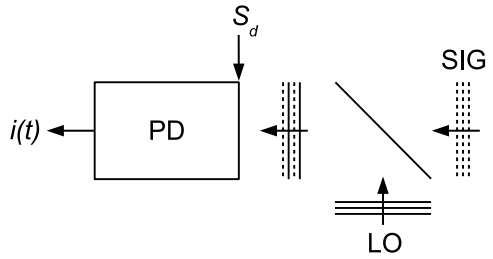

Figure 5.1 – Homodyne detection. Local oscillator (LO) is combined with the incoming optical signal (SIG) on the photodetector (PD). Photo sensitive area of the PD is S_d.

The photocurrent signal exhibits an oscillatory behaviour that is directly related to the motion of the object or particles scattering the light illuminating them. The distinction between heterodyne and homodyne detection differ slightly in the literature. In this context heterodyne detection refers to the mixing of a frequency shifted local oscillator with the signal, whereas homodyne detection refers to the mixing with an un-shifted local oscillator.
A simple and idealized analytical model is now developed based on the setup illustrated in figure 5.2 in order to outline some basic characteristics of the LDV technique. This model does not take into consideration practical aspects such as finite linewidth of the laser system, effects of diffraction and aberration in the optical system and the only source of noise considered in relation to system performance will be photon induced shot noise.

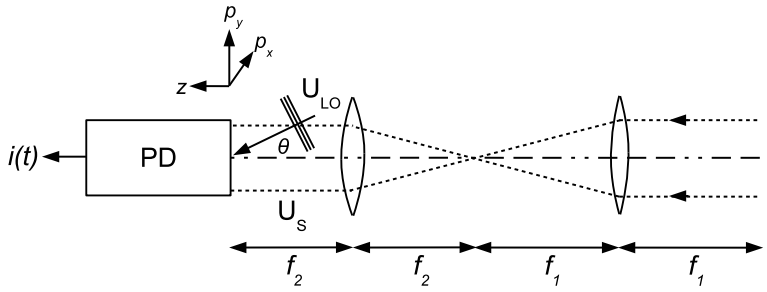

Figure 5.2 – Homodyne detection with telescope.

For added simplicity, reflection from a mirror with reflectance *A*, is considered. Extending the model to include a rigid object with a diffusely scattering surface is addressed in **Paper IV**. Consider a laser illuminating the mirror with a linear polarized, fundamental Gaussian beam with a spot size w_i (e^{-2} intensity radius)

$$U_i(\mathbf{r}) = \sqrt{\frac{2A^2P_i}{\pi {w_i}^2}} \exp\left(-\frac{\mathbf{r}^2}{{w_i}^2}\right), \tag{5.1}$$

where P_i is the power of the illuminating beam. The image, $U_s(\mathbf{p},\Delta z)$, of the field distribution described by eq. (5.1) can be calculated using eq. (1.5) and eq. (1.20), with $A \to -f_2/f_1$, $B \to -2if_1f_2/(k\sigma^2)$ and $D \to -f_1/f_2$. For the purpose of this analysis, perfect imaging is assumed, which can be obtained by letting $\sigma \to \infty$. The field distribution obtained in the observation plane is then

$$U_s(\mathbf{p},\Delta z) = \sqrt{\frac{2A^2P_i}{\pi w^2}} \exp\left(-\frac{\mathbf{p}^2}{w^2}\right) \exp(-i2k\Delta z), \tag{5.2}$$

where $w = f_2 w_i / f_1 = |M| w_i$ and *M* is the magnification of the telescope given by $M = -f_2/f_1$. The additional phase factor $\exp(-i2k\Delta z)$ is due to a displacement Δz of the mirror along the optical axis of the imaging system, assuming that the angle of incidence of the illuminating field is perpendicular to the mirror. In stating eq. (5.2), the mirror is assumed to be at rest at the start and at the end of the displacement Δz. The local oscillator field at the detector is assumed to exhibit the same spatial functionality as the image of the illuminating beam, i.e. a Gaussian beam with a spot size w coinciding with the image. The local oscillator beam (LO) is allowed to form an angle $\boldsymbol{\theta} = (\theta_x, \theta_y)$ with the optical axis of the telescope. The field distribution of the LO field in the observation plane is written as

$$U_{LO}(\mathbf{p}) = \sqrt{\frac{2P_{LO}}{\pi w^2}} \exp\left(-\frac{\mathbf{p}^2}{w^2}\right) \exp(ik\mathbf{p}\cdot\boldsymbol{\theta}). \tag{5.3}$$

The phase of the LO field is selected to be zero at the observation plane. To obtain the intensity incident on the photodetector area, the contributions due to the signal and the LO fields, must be added coherently. The intensity can thus be written as

$$I(\mathbf{p}) = |U_s(\mathbf{p}) + U_{LO}(\mathbf{p})|^2 = I_s(\mathbf{p}) + I_{LO}(\mathbf{p}) + 2\,\mathrm{Re}\{U_s(\mathbf{p})U_{LO}{}^*(\mathbf{p})\}, \tag{5.4}$$

Evaluating eq. (5.4) the following expression for the intensity is obtained:

$$I(\mathbf{p},\Delta z) = \frac{2}{\pi w^2}\left[\begin{array}{l}\exp\left(-\dfrac{2\mathbf{p}^2}{w^2}\right)\left(A^2P_i + P_{LO}\right) + \\ 2A\sqrt{P_iP_{LO}}\cos(2k\Delta z - k\boldsymbol{\theta}\cdot\mathbf{p})\end{array}\right]. \tag{5.5}$$

The photocurrent generated by the detector can then be written as

$$i(\Delta z) = \alpha\int_S I(\mathbf{p})d^2\mathbf{p}, \tag{5.6}$$

where S is the photosensitive area of the detector and α is the detector responsivity. The responsivity is given by $\alpha = e\eta/h\nu_0$ where e is the electronic charge, η is the detector quantum efficiency, h is Planck's constant and ν_0 is the optical carrier frequency in Hz. The detector is assumed to be located at the origin $\mathbf{p} = (0,0)$ of the observation plane. The phase difference of the reflected field, due to the mirror displacement Δz, is given by $\Delta\phi = 2k\Delta z$. If the mirror moves at a constant (axial) speed $v_z = \Delta z/\Delta t = const.$ and $|v_z| << c$, where c is the speed of light, the instantaneous optical frequency of the reflected field is given by

$$\nu = \nu_0 + \frac{1}{2\pi}\frac{d\phi}{dt} = \nu_0 + \frac{2v_z}{\lambda}. \tag{5.7}$$

When combining the reflected field and the LO field, at the detector surface, a beat frequency arises due to the small difference in optical frequency between the fields. The frequency of the beat is just the Doppler frequency [24], which for homodyne detection is given by

$$f_D = \nu - \nu_{LO} = \nu - \nu_0 = \frac{2v_z}{\lambda}. \tag{5.8}$$

In homodyne detection the beat frequency is observed as an oscillation of the photocurrent signal at the Doppler frequency. It is clear that determining the beat frequency from the photocurrent, obtained in the backscattering configuration,

results in a direct measurement of the speed of the moving object along the line-of-sight (LOS) of the telescope.
Certain restrictions apply to the detector size and the effective receiving aperture of the optical system. In order to maintain homodyne detection it can be argued that the phase variation of the phase fronts of the signal and LO beams should not deviate by more than a wavelength within the active area of the detector surface. This condition is expressed in a general form by the antenna theorem [52]

$$\Omega_R A_R \leq \lambda^2 , \tag{5.9}$$

where Ω_R is the solid angle of the field-of-view of the optical system implemented and A_R is the effective aperture of the receiver. Consider e.g. the homodyne detection geometry illustrated in figure 5.1. Here, $A_R = S_d$ and the condition for the phase variation can thus be written as

$$\Delta\theta \leq \lambda / d , \tag{5.10}$$

where $\Delta\theta$ is the angle of incidence of the signal and d is the (largest) linear dimension of the photosensitive area. This condition ensures that the phase difference over the detector does not exceed 2π (i.e. one wavelength). Squaring and rearranging eq. (5.10) results in eq. (5.9).
A similar argument can be applied to the homodyne detection geometry outlined in figure 5.2. Here, the telescope placed in the signal beam magnifies the apparent active area of the detector by a factor of M^2 ($A_R' = M^2 A_R$). However, by the same token the angular selectivity is also increased by a factor of M^2 ($\Omega_R' = M^{-2}\Omega_R$). Thus, the condition for homodyne detection becomes, again

$$A_R'\Omega_R' = M^2 A_R M^{-2}\Omega_R \leq \lambda^2 . \tag{5.11}$$

Generally, introducing optical elements before combining the signal and LO fields results in modification of both A_R and Ω_R. To maintain coherent detection the product of A_R and Ω_R must be subject to the condition described by eq. (5.9).
When considering LDV methods for wind speed measurements or in other conditions where the signal is weak, the effect of noise becomes important. One of the main advantages of homodyne detection is the signal gain achieved by introducing the coherent local oscillator. This is especially advantageous when the signal return is small. Consider, for the time being, the case where $S_d << \pi w^2$ and $\boldsymbol{\theta} = (0,0)$. Eq. (5.6) then becomes $i(t) \approx \alpha S_d I(0,0,t)$. The photocurrent consists of an AC term, which constitutes the signal, and a DC term. The AC term is given by

$$i_S(t) = \frac{4\alpha S_d}{\pi w^2} A\sqrt{P_i P_{LO}} \cos(2\pi f_D t). \tag{5.12}$$

The signal power (mean-square voltage) is then given by

$$S = R_e{}^2 \left\langle i_S{}^2 \right\rangle = \frac{8\alpha^2 S_d{}^2 R_e{}^2}{\pi^2 w^4} A^2 P_i P_{LO} \,. \tag{5.13}$$

where R_e is the equivalent resistance of the detector (and any subsequent amplifier arrangement). The average is taken over time. The DC current term is given by

$$i_{DC} = \frac{2\alpha S_d}{\pi w^2}\left(A^2 P_i + P_{LO}\right). \tag{5.14}$$

The parameter of most importance in dealing with LDV systems is not the signal itself but rather the signal-to-noise ratio (SNR). A fundamental source of noise is shot noise. Shot noise is a consequence of the intrinsic discreteness of the generation of photoelectrons in photomultiplier tubes or electron-hole pairs in semiconductor detectors. The noise power due to shot noise is given by [53]

$$N = R_e{}^2 \left\langle i_N{}^2 \right\rangle = 2eBR_e{}^2 i_{DC} \,, \tag{5.15}$$

where e is the electronic charge B is the bandwidth of the detector and amplifier arrangement. In this analysis, effects of dark current and thermal noise are not considered. The SNR is then defined by the ratio of eq (5.13) and eq (5.15)

$$SNR = \frac{\left\langle i_S{}^2 \right\rangle}{\left\langle i_N{}^2 \right\rangle} = \frac{2\alpha S_d}{\pi e B w^2} \frac{A^2 P_i P_{LO}}{A^2 P_i + P_{LO}} \,. \tag{5.16}$$

Examining eq. (5.16), it is observed that increasing P_{LO} so that $P_{LO} >> A^2 P_i$, leads to a saturation of the SNR at a value

$$\left(SNR\right)_{MAX} = \frac{2\alpha S_d}{\pi e B w^2} A^2 P_i \,. \tag{5.17}$$

Even though this indicates a maximum attainable signal-to-noise ratio, independent on any further increase of LO power, it has been shown [53] that there is an optimum LO power level for realistic detector systems. This value has to be evaluated for the specific detector implemented. Generally, the signal to noise ration will decrease if the LO power is increased beyond a certain level.

5.1.2 Velocity azimuth display

When using homodyne detection methods for e.g. wind speed measurements only the line-of-sight (LOS) speed can be measured. One way to obtain additional information about wind speed direction is to scan the illumination beam in a conical

fashion. The principle, also known as velocity azimuth display (VAD) [14], is illustrated in figure 5.3.

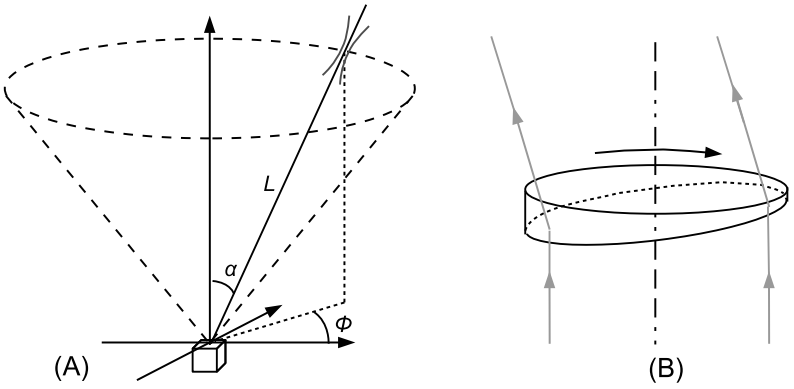

Figure 5.3 – (A) The conical scan method. The beam is focused at a distance L. (B) A rotating wedge prism used to direct and scan the outgoing beam.

Several different systems incorporating a form of the VAD method are now commercially available. Assuming a homogeneous wind field across the scan area it can easily be shown that the LOS wind speed measurement is related to the horizontal and vertical wind speed components through

$$v_{LOS}(\varphi) = A\sin(\varphi - \varphi_0) + B\,, \tag{5.18}$$

where

$$A = v_{hor}\sin\alpha\,, \tag{5.19}$$

$$B = v_{ver}\cos\alpha\,, \tag{5.20}$$

and φ_0 relates to the angle between the observation direction and the first zero of the sine function of eq. (5.18) is related to the wind direction φ_w by $\varphi_w = \varphi_0 + 3\pi/2$. It is important to note that the Doppler frequency, which is measured in the case of homodyne detection, is ambiguous when used to determine the direction of the measured LOS speed.

One drawback of this method is the decreased temporal resolution due to the time it takes to perform a full scan, which is typically 1-5s. Also, the VAD method is not a point measurement of the wind velocity, which for many applications will be a serious drawback. The cone angle and measurement distance *L* defines the circular pattern over which the beam is scanned. Decreasing the cone angle for a fixed value of L decreases the area but this will in turn also increasingly diminish the accuracy of the measurement of the horizontal wind speed components.

5.1.3 Speckle correlation in LDV

Measuring transverse velocity components of an object passing through the measurement volume of single beam homodyne LDV systems have been extensively treated. Measuring systems based on the differential laser Doppler technique [24],[54] measure this component directly. Differential LDV is however not well suited to extract the LOS velocity. Reports [55], [56] have been made on observing intensity fluctuations of the obtained Doppler signal from conventional LDV systems in order to extract transverse components of the object translation. Measurements of transverse wind speeds using this method was reported, showing good correspondence with cup anemometer data. However, this method cannot determine the directionality of the transverse wind velocity.
A similar approach has been reported by Churnside *et al.* [57] using two detectors, arranged to provide a homodyne signal. The measurement principle relies on the extraction of Doppler signal envelopes, obtained from the raw signal recorded by the detectors. It turns out that the slope of the envelope crosscorrelation function, evaluated at zero timelag, is under certain conditions proportional to the transverse velocity component. The measurement setup that was used is illustrated in figure 5.4.

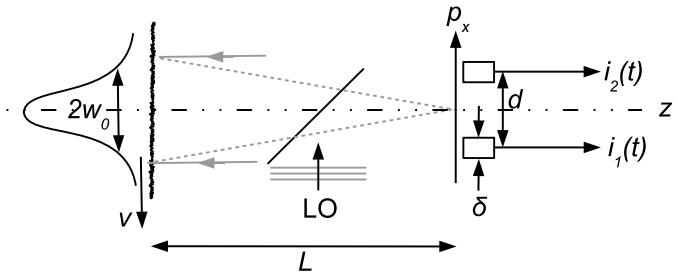

Figure 5.4 – Measurement setup used for speckle correlation in LDV measurements .

The object is illuminated with a single Gaussian beam which is assumed to give rise to fully developed speckles due to the scattering structure. The speckle pattern is observed at a distance of L at the mixing plane (cf. figure 5.4). Here the speckle pattern is combined with a coherent local oscillator. Two detectors, with a diameter significantly smaller than the average speckle size, are placed symmetrically around the optical (z-axis) of the setup and separated by a distance *d*. The correlation between the two detector signals, evaluated for pure transverse object motion, is the quantity of interest and is given by

$$C_{12}(\tau) = \left\langle i_1(t) i_2^*(t+\tau) \right\rangle \propto \left\langle U_s(\mathbf{p}_1, t) U_s^*(\mathbf{p}_2, t+\tau) \right\rangle, \tag{5.21}$$

In stating eq. (5.21) it must be noted that $i_1(t)$ and $i_2(t)$ are complex representations of the homodyne signals that relate directly to the optical fields rather than the intensity. Differentiating eq. (5.21) with respect to the time lag τ and evaluating this for $\tau = 0$ yields

$$\left. \frac{dC_{12}(\tau)}{d\tau} \right|_{\tau=0} \propto \left(1 - \frac{L}{R_i} \right) \exp\left[-\frac{1}{2} \left(\frac{k w_0 d}{2L} \right)^2 \right] \mathbf{d} \cdot \mathbf{v}, \tag{5.22}$$

where R_i is the radius of curvature of the illuminating field and $\mathbf{d}$ is the vector separating the two detectors in the $\mathbf{p}$ plane while $\mathbf{v}$ is the transverse velocity. The detailed analysis leading to eq. (5.22) is treated in [57]. The main point of eq. (5.22) is to realize that the slope of the correlation function is, under certain circumstances, proportional to the transverse velocity. Firstly, both the transverse velocity components can be extracted by orienting the detector separation vector according to the desired measurement axis. Secondly, if $R_i = L$, i.e. if the illuminating beam is converging towards the observation plane, the measurement of the speckle translation becomes impossible. This is due to speckle decorrelation. If out-of-plane motion is also present the Doppler signal component will also be present in the photocurrent signal and the LOS speed can be extracted using conventional LDV techniques, e.g. by using a spectrum analyzer. When using homodyne detection the ambiguity of direction will remain though. This could supposedly be resolved by using heterodyne detection [24]. The directional ambiguity is in this way resolved by offsetting the local oscillator frequency (using e.g. an acoustic optical modulator) by an amount larger than the expected Doppler frequency range. Detecting whether the Doppler signal is red shifted or blue shifted with respect to the local oscillator frequency allows determination of the direction. However, this does complicate the setup considerably and increases the cost due to the need for RF generators, control electronics etc.

The experiments performed in [57] confirm the theoretical findings. However, the analysis also reveals limitations in measurement range of transverse velocities imposed by the finite difference estimator used. Furthermore, to the best knowledge of the author, the method described has not yet been demonstrated in the literature for wind speed measurements.

5.1.4 Electronic speckle interferometry (ESPI)

Electronic speckle interferometry (ESPI) [58], [59] is a method in speckle metrology dedicated to measure both in-plane and out-of-plane components of deformation fields observed for a great variety of objects. The ability to non-destructively measure the deformation of especially semi-rigid rough objects has lead to a wide field of application in experimental mechanics, industrial testing and areas of fluid dynamics. The measurement principle combines ESP to measure in-

plane displacements of the object, while using interferometric concepts to deduce out-of-plane deformations. Several variations on the principle exist. In this section two of these are described.

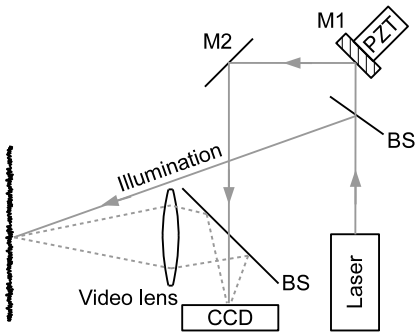

Figure 5.5 – Electronic speckle interferometry generic setup

In figure 5.5 one possible implementation of a phase stepping ESPI setup is illustrated. The surface of the object is illuminated by a laser source. A lens images the illuminated part of the object onto a CCD camera. The intensity distribution of the image is denoted $I_s(\mathbf{p})$. A beamsplitter allows the combination of the image with a coherent reference beam that was previously split off from the laser source (equivalent to the local oscillator of LDV). The intensity distribution of the reference beam incident on the CCD camera is denoted $I_r(\mathbf{p})$. To extract the out-of-plane displacement component a phase stepping mirror is implemented in the reference beam. The mirror (M1) position is controlled with a high degree of accuracy using a piezo-electric transducer (PZT). The procedure is then to obtain a series of four images of the object before the displacement, were the phase is shifted by $\pi/2$ between each image using the phase stepper mirror. The four intensity distributions are then

$$I_0(\mathbf{p}) = I_s(\mathbf{p}) + I_r(\mathbf{p}) + I_c(\mathbf{p})\cos[\varphi(\mathbf{p})], \tag{5.23A}$$
$$I_{90}(\mathbf{p}) = I_s(\mathbf{p}) + I_r(\mathbf{p}) + I_c(\mathbf{p})\cos[\varphi(\mathbf{p}) + \pi/2], \tag{5.23B}$$
$$I_{180}(\mathbf{p}) = I_s(\mathbf{p}) + I_r(\mathbf{p}) + I_c(\mathbf{p})\cos[\varphi(\mathbf{p}) + \pi], \tag{5.23C}$$
$$I_{270}(\mathbf{p}) = I_s(\mathbf{p}) + I_r(\mathbf{p}) + I_c(\mathbf{p})\cos[\varphi(\mathbf{p}) + 3\pi/2], \tag{5.23D}$$

where $I_c = 2\sqrt{I_s I_r}$ and $\varphi(\mathbf{p})$ is the random speckle phase. Once the object has undergone displacement, a series of four new images are obtained using the same phase stepping procedure. These new intensity distributions are

$$I_0'(\mathbf{p}) = I_s'(\mathbf{p}) + I_r(\mathbf{p}) + I_c'(\mathbf{p})\cos[\varphi(\mathbf{p}) + \Omega(\mathbf{p})], \tag{5.24A}$$
$$I_{90}'(\mathbf{p}) = I_s'(\mathbf{p}) + I_r(\mathbf{p}) + I_c'(\mathbf{p})\cos[\varphi(\mathbf{p}) + \pi/2 + \Omega(\mathbf{p})], \tag{5.24B}$$

$$I_{180}'(\mathbf{p}) = I_s'(\mathbf{p}) + I_r(\mathbf{p}) + I_c'(\mathbf{p})\cos[\varphi(\mathbf{p}) + \pi + \Omega(\mathbf{p})], \quad (5.24C)$$
$$I_{270}'(\mathbf{p}) = I_s'(\mathbf{p}) + I_r(\mathbf{p}) + I_c'(\mathbf{p})\cos[\varphi(\mathbf{p}) + 3\pi/2 + \Omega(\mathbf{p})], \quad (5.24D)$$

where $\Omega(\mathbf{p})$ is the phase change due to the out-of-plane displacement of the object and primed parameters correspond to measurements on the displaced object. It is noted that only $I_s(\mathbf{p})$ and the phase changes due to the object displacement. Now four mathematical constructs are formed based on eq. 5.23(A)-(D) and eq. 5.24(A)-(D)

$$C_1 = I_0 - I_{180} = 2I_c(\mathbf{p})\cos[\varphi(\mathbf{p})] \quad (5.25A)$$
$$S_1 = I_{270} - I_{90} = 2I_c(\mathbf{p})\sin[\varphi(\mathbf{p})] \quad (5.25B)$$
$$C_2 = I_0' - I_{180}' = 2I_c'(\mathbf{p})\cos[\varphi(\mathbf{p}) + \Omega(\mathbf{p})] \quad (5.25C)$$
$$S_2 = I_{270}' - I_{90}' = 2I_c'(\mathbf{p})\sin[\varphi(\mathbf{p}) + \Omega(\mathbf{p})] \quad (5.25D)$$

It is observed that I_0, I_0' and I_r are cancelled in the process. From these constructs the out-of-plane displacement $\Delta z(\mathbf{p})$ can be obtained by calculating [49]

$$\Delta z(\mathbf{p}) = 2k\Omega(\mathbf{p}), \quad (5.26)$$

where it is assumed that the angle of incidence of the illumination is perpendicular to the optical axis of the imaging system (video lens) and

$$\Omega(\mathbf{p}) = \arctan\left[\frac{(C_1 + S_2)^2 + (S_1 - C_2)^2 - (C_1 - S_2)^2 - (S_1 + C_2)^2}{(C_1 + C_2)^2 + (S_1 + S_2)^2 - (C_1 - C_2)^2 - (S_1 - S_2)^2}\right]. \quad (5.27)$$

The sign of the out-of-plane displacement is given by the sign of the denominator of eq. (5.27). To extract the in-plane displacement the phase coding provided by the reference beam can be eliminated to reveal two speckle patterns that contain the in-plane displacement. Two new constructs are formed in order to do this:

$$I_c(\mathbf{p}) = \frac{\sqrt{C_1^2 + S_1^2}}{2}, \quad (5.28)$$
$$I_c'(\mathbf{p}) = \frac{\sqrt{C_2^2 + S_2^2}}{2}. \quad (5.29)$$

Methods from ESP are applied to the two speckle fields $I_c(\mathbf{p})$ and $I_c'(\mathbf{p})$ in order to determine the two-dimensional in-plane displacement of the object after displacement. This involves the calculation of crosscorrelation of the speckle patterns in a number of sub-images (typically 32x32 pixels) extracted from the full image field. This allows the measurement of the average deformation within each

sub-image and thus provides a means to measure the local displacements across the full image.
The need for obtaining four images before and after the object displacement and the subsequent image processing severely limits the temporal resolving capabilities of this particular implementation. Begemann *et al.* [60] uses an angular offset reference wave in combination with a Fourier transform algorithm [61] and ESP to measure three-dimensional displacement fields with only a single image taken before and after object displacement.

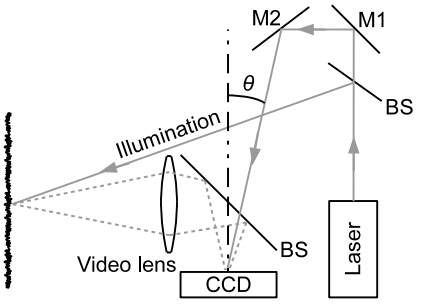

Figure 5.6 – Measurement principle for spatial phase shifting ESPI.

The measurement setup used in this technique is shown in figure 5.6. The setup is similar to the setup used in the phase stepping method described above. However, the two setups differ in one important aspect. In the latter case the reference wave is incident on the CCD camera under an angle. This introduces carrier fringes in the intensity received by the camera. The obtained intensity distribution is then

$$I(\mathbf{p}) = \left|U_s(\mathbf{p}) + U_r(\mathbf{p})\exp\left[ik\mathbf{p}\cdot\boldsymbol{\theta}\right]\right|^2, \tag{5.30}$$

Assuming that the reference wave is plane and has constant amplitude $U_r(\mathbf{p}) = U_r$ and $\boldsymbol{\theta} = (\theta_x, 0)$, eq. (5.30) becomes

$$I(\mathbf{p}) = I_s(\mathbf{p}) + \left|U_r\right|^2 + U_r{}^* U_s(\mathbf{p})\exp\left[-ikp_x\theta_x\right] + U_r U_s{}^*(\mathbf{p})\exp\left[ikp_x\theta_x\right]. \tag{5.31}$$

The Fourier transformation of the intensity distribution can be written as

$$S_I(\boldsymbol{\xi}) = \left|U_r\right|^2 \delta(\boldsymbol{\xi}) + FT\{I_s(\mathbf{p})\} + U_r{}^* S_s\left(\xi_x + \frac{k\theta_x}{2\pi}, \xi_y\right) + U_r S_s{}^*\left(\xi_x - \frac{k\theta_x}{2\pi}, \xi_y\right), \tag{5.32}$$

where $S_s(\boldsymbol{\xi}) = FT\{U_s(\mathbf{p})\}$. The first term in eq. (5.32) is the zero frequency part (DC term) of the image intensity. The second term is identified as the speckle spectrum. The speckle spectrum exhibits functionality proportional to the

autocorrelation of the aperture function of the imaging system, apart from a delta function [1]. The two remaining terms are due to the angular offset reference beam and are spatial frequency shifted replicas of the speckle spectrum. Ensuring that the sidebands and the spackle halo do not overlap in spatial frequency, one of the two sidebands is isolated (e.g. by bandpass filtering). The sideband is shifted in spatial frequency to occupy the origin. An inverse Fourier transform is applied to obtain the following expression

$$FT^{-1}\left\{U_r^{*} S_s\left(\xi_x,\xi_y\right)\right\} = U_r^{*}\left|U_s(\mathbf{p})\right|\exp\left(i\varphi(\mathbf{p})\right). \tag{5.33}$$

After object displacement, a second intensity pattern $I'(\mathbf{p})$ is recorded by the camera and the procedure is repeated. The inverse Fourier transform operation now yields

$$U_r^{*}\left|U_s'(\mathbf{p})\right|\exp\left[i\varphi'(\mathbf{p})\right] \tag{5.34}$$

Where $U_s'(\mathbf{p})$ and $\varphi'(\mathbf{p})$ are the field and phase distribution after the object displacement, respectively. The ratio of eq. (5.34) and eq. (5.33) reveals the phase difference $\Omega(\mathbf{p})$

$$\frac{U_r^{*}\left|U_s'(\mathbf{p})\right|\exp\left[i\varphi'(\mathbf{p})\right]}{U_r^{*}\left|U_s(\mathbf{p})\right|\exp\left[i\varphi(\mathbf{p})\right]} = \frac{\left|U_s'(\mathbf{p})\right|}{\left|U_s(\mathbf{p})\right|}\exp\left[i\Omega(\mathbf{p})\right], \tag{5.35}$$

which can be extracted from eq. (5.35) by a logarithm operation. The out-of-plane displacement can then be obtained from eq. (5.26). To extract the actual displacement, a phase unwrapping algorithm [61] must be applied to the obtained phase map.
To extract the in-plane component, the ESP method is applied to the sub-images of the absolute squared amplitude functions, given by

$$I_s(\mathbf{p}) = \left|U_s(\mathbf{p})\right|^2, \tag{5.36}$$

$$I_s'(\mathbf{p}) = \left|U_s'(\mathbf{p})\right|^2. \tag{5.37}$$

It is commonly accepted [49] that the out-of-plane measurement range using ESPI methods is limited to approximately 5 wavelengths of the illuminating light. However, the attainable accuracy is on the order of $\lambda/100$. The measurement range of the in-plane measurement is limited by the decorrelation rate of the speckle pattern which can vary depending on the specific conditions of the experiment. Sub-pixel precision is attainable in some cases. One of the major disadvantages of ESPI and ESP is the time consuming image processing and limited frame rate of the camera systems used. This severely limits the temporal resolution and thus the use of these methods for real-time studies of object motion.

5.2 Spatial filtering velocimetry

The laser Doppler technique utilizes the Doppler shift of radiation as it is scattered from dynamic objects or particles in motion. It is inherently based on coherent detection and benefits from the signal gain achieved by the coherent local oscillator used to obtain optical beating with the scattered radiation. The beat frequency is observed in the oscillatory component of the photocurrent output of the detector and is directly proportional the LOS speed of the object.

The coherent detection scheme provides a sensitivity that allows the technique to be applied to extremely weak scattering media such as aerosol flows used for measuring winds speed probed at distances of several hundred meters. However, using this technique for three-dimensional velocity measurements presents several problems, especially due to ambiguity issues in detecting directionality. Efforts reported so far to address these problems compromises either the point measurement characteristic, simplicity or the full three-dimensional velocity measurement. The introduction of multiple spatial modes (speckles) in the detection aperture as reported by Churnside *et al.* [57] is a viable method to extract the transverse components of the velocity while maintaining the sensitivity of coherent detection. However, this method utilizes homodyne detection of the Doppler shift to measure the axial velocity component and thus suffers from the directional ambiguity. As mentioned, this could be resolved by using heterodyne detection, but this will increase cost and complexity of the system significantly, which is not desirable for industrial applications.

Electronic speckle interferometry is inherently a full-field method that provides measurement of three-dimensional displacement fields with a high degree of sensitivity. The major disadvantage of this method is the temporal resolution. This is mainly due to the algorithms needed to perform the image processing and the frame rate of the camera systems used. The use of the spatially phase biased interferograms and FFT-based algorithms, as reported in [60], may provide some improvement in the temporal performance. However, these methods are in particular not well suited for real time measurements.

The work described in **Paper III** and **Paper IV** seeks to bridge the gap between the ESPI and LDV methodologies. The methodology described there retains both the point measurement characteristic and high measurement speeds of LDV techniques by using an optical spatial filter based on the receiver used in the Df technology to measure the axial velocity component. The transverse velocity components are measured using a detector arrangement implemented as a spatial filter and configured in the same way as the optical spatial filter. Using the optical spatial filter to measure speckle translation is a well established method [62]. Thus, although not demonstrated, the application of optical spatial filters to measure the transverse components in this implementation should present no fundamental problems. Furthermore, the ambiguity in determination of the directionality of the axial velocity component present in the homodyne LDV method is resolved by angular offsetting the local oscillator in relation to the observation plane, providing carrier fringes tuned to the fundamental band pass of the optical spatial filter. This approach was used in a similar way in [60] to extract the out-of-plane displacement field. The fringe pattern translates in the image plane in response to the axial

velocity. The direction of translation of the fringe pattern provides the information needed to solve the axial velocity ambiguity and is directly measured by the use of the in-phase and phase quadrature signal provided by the optical spatial filter and detector arrangement. Thus, using a simple geometrical modification and spatial filtering techniques the need for heterodyne detection is eliminated.

Paper III demonstrates the use of spatial filtering methods to extract the full velocity vector of a rigid object translating in three dimensions trough the measurement volume. The high temporal bandwidth capabilities of optical spatial filters allow the investigation of fast phenomena

In figure 5.7 a sample intensity distribution and corresponding spatial power spectrum is shown. The angle of incidence of the reference wave is selected so that the fringe translation direction forms an angle of 45° in relationship to the p_x and p_y axis. This eliminates the possibility of cross-talk between the spatial filters monitoring the speckle and fringe translation, respectively.

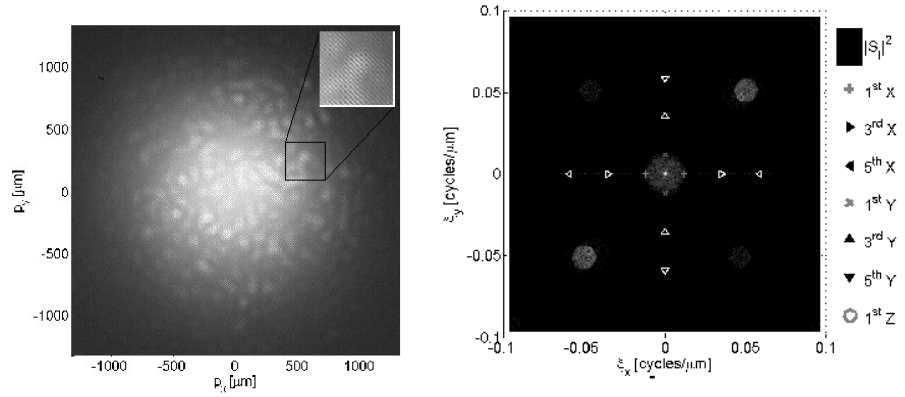

Figure 5.7 – (Left) Recorded speckle pattern with a coherent reference wave incident at an angle $\boldsymbol{\theta} = (0.03\text{rad}, 0.03\text{rad})$. (Right) The spatial power spectrum of the intensity distribution shown to the left. The various markers correspond to centre positions of spatial filter passbands tuned to the speckle and fringe translation.

Paper IV addresses the development of an analytical model of the ensemble averaged intensity crosscorrelation function suitable for describing the intensity dynamics of the fringe and speckle patterns in the shearing interferometer configuration that was numerically and experimentally investigated in **Paper III**. The analytical model addresses both translating and rotating rigid objects observed in the image plane of a 4f-imaging system. The analytical model provides a theoretical basis for parametric studies of the measurement concept and will significantly aid future prototype development.

The experimental part of **Paper IV** focuses on measurement of the in-plane angular velocity of a rigid cylindrical object placed in the object plane of the imaging system (note that a different definition of angular velocity orientation is used here in relationship to **Paper IV**). It is demonstrated that, using the dynamical properties of the fringe pattern alone, the angular velocity can be derived using at least two spatial filters tuned to the spatial frequency of the fringe pattern. The axial velocity

component of the surface of a rotating cylinder object will vary linearly from zero (at the axis of rotation) to a maximum value of $v_{z,\max} = \omega R$ at the outermost edge (cf. figure 5.8).

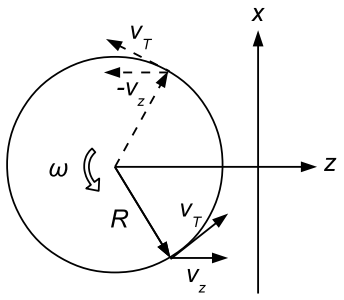

Figure 5.8 – Rotating cylindrical object of radius *R*.

Therefore, at a given position (x) within the radius of the object the (local) axial velocity component is given by $v_z = \omega x$, where the sign depends on the direction of rotation. The tangential velocity component is given by $v_T = \omega R$. Thus the axial velocity is independent of the radius of the cylinder object, while tangential velocity depends linearly on the radius.

One main result of **Paper IV** is to demonstrate that the appropriate measurement of the fringe translation results in an object-radius independent measurement of the angular velocity. In figure 5.9 a vector map shows the measured direction of the fringe translation. The magnitude of the arrows is proportional to the signal frequency derived from the output of localized spatial filters (at the arrow positions) and tuned to the spatial frequency of the fringe pattern.

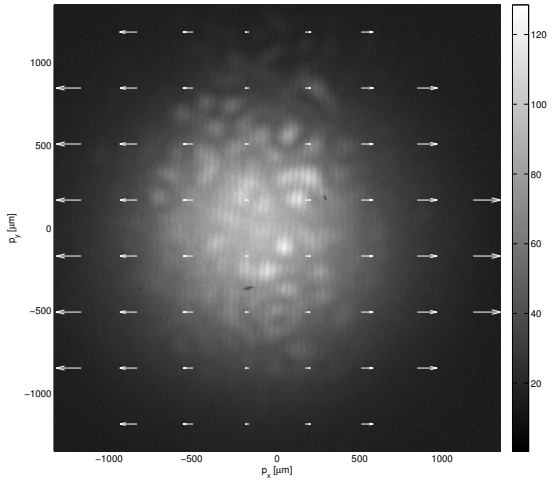

Figure 5.9 – Vector map plot of the local fringe translation direction and magnitude. The reference wave incidence angle is selected so that $\boldsymbol{\theta} = (0.017\text{rad}, 0\text{rad})$.

A number of observations can be made from figure 5.9. Firstly, it is observed that the fringes translate with linearly increasing velocity as a function of the image position. This spatially varying fringe displacement rate for a purely rotating object opposes the collective fringe motion observed in the case of pure translation of the object.

Based on the experimental parameters used in **Paper IV**, the analytically derived intensity crosscorrelation function can be used to predict the fringe translation in response to the object motion

$$\Delta p_x = -\frac{2}{\theta_x}\left(v_z \tau + \omega \tau p_x\right), \tag{5.38}$$

where Δp_x is the observed fringe translation at a fixed position in the image plane in the time τ and θ_x is the reference wave angle with respect to the optical axis of the imaging system. This prediction is verified by the experimental data presented in **Paper IV**.

Using the optical spatial filters also used in the Df technology for wind velocity measurements presents many challenges that need to be addressed. One of the main questions is the performance of the spatial filtering approach, compared with conventional approaches. To compare the relative performance of the two methods, the magnitude of the AC signal component can be utilized. Consider the square aperture detector arrangement outlined in figure 5.10 (B).

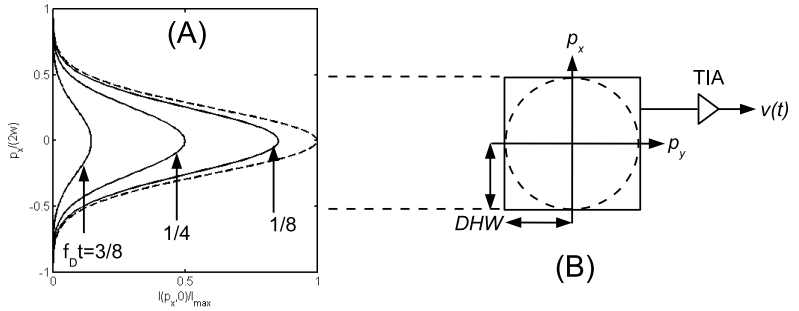

Figure 5.10 – (A) Normalized transverse intensity distribution $I(p_x, 0)$ for three different values of $\omega_D t$ and $P_i = P_{LO}$. (B) Square detector configuration of half-width $DHW = w$. A trans-impedance amplifier (TIA) converts the photocurrent into a voltage signal $V(t)$.

In the conventional configuration the incident intensity distribution is described by

$$I(\mathbf{p},t)=\frac{2}{\pi w^2}\left[\begin{array}{l}\exp\left(-\dfrac{2\mathbf{p}^2}{w^2}\right)\left(A^2P_i+P_{LO}\right)+\\ 2A\sqrt{P_iP_{LO}}\cos(2\pi f_D t)\end{array}\right], \tag{5.39}$$

where f_D is the Doppler frequency defined by eq. (5.8). When the area of the photosensitive surface of the detector S becomes comparable with the spot size w of the intensity distribution, the photocurrent is best described by

$$\begin{aligned} i(t) &= \alpha \int_{DHW\times DHW} I(\mathbf{p},t)\,d^2\mathbf{p} \\ &= \alpha\,\mathrm{Erf}\left(\frac{DHW\sqrt{2}}{w}\right)^2\left[A^2P_i+P_{LO}+2A\sqrt{P_iP_{LO}}\cos(2\pi f_D t)\right] \end{aligned}. \tag{5.40}$$

The voltage signal is given by $V(t)=R_e i(t)$. The AC signal magnitude is given by

$$AC\{V(t)\}=2\alpha AR_e\sqrt{P_iP_{LO}}\,\mathrm{Erf}\left(\frac{DHW\sqrt{2}}{w}\right)^2. \tag{5.41}$$

Now, consider the multiple detector configuration illustrated in figure 5.11 (B).

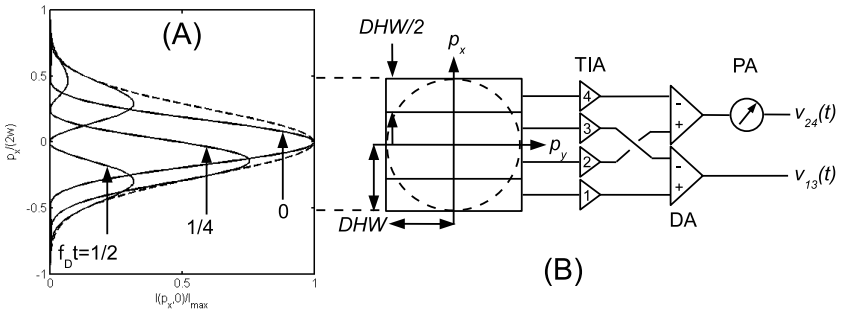

Figure 5.11 – (A) Normalized transverse intensity distribution for three different values of $f_D t$, $\boldsymbol{\theta}=(\lambda/2DHW,0)$ and $P_i=P_{LO}$. (B) A Four-detector configuration similar to the Df detector configuration.

The intensity distribution obtained at the detector surface is now given by

$$I(\mathbf{p},t)=\frac{2}{\pi w^2}\left[\begin{array}{l}\exp\left(-\dfrac{2\mathbf{p}^2}{w^2}\right)\left(A^2P_i+P_{LO}\right)+\\ 2A\sqrt{P_iP_{LO}}\cos(2\pi f_D t-k\boldsymbol{\theta}\cdot\mathbf{p})\end{array}\right], \tag{5.42}$$

and is illustrated in figure 5.11(A). Each detector is connected to an individual TIA 1-4 and subtracted in pairs by a stage of differential amplifiers (DA), yielding voltage signals $V_{13}(t)$ and $V_{24}(t)$. An analog phase adjuster (PA) can arbitrarily adjust the phase of the $V_{24}(t)$ signal with respect to $V_{13}(t)$. Selecting $\boldsymbol{\theta} = (\lambda / 2DHW, 0)$, the AC signal magnitude of the voltage signal $V_{13}(t)$ is given by (cf. Appendix)

$$AC\{V_{13}(t)\} = \alpha A R_e \sqrt{P_i P_{LO}} \exp\left(-\frac{\pi^2 w^2}{8DHW^2}\right) \operatorname{erf}\left(\frac{DHW\sqrt{2}}{w}\right) \times \left| \begin{bmatrix} \operatorname{erf}\left(\frac{DHW\sqrt{2}}{w} + \frac{i\pi w}{2DHW\sqrt{2}}\right) - \operatorname{erf}\left(\frac{DHW}{w\sqrt{2}} - \frac{i\pi w}{2DHW\sqrt{2}}\right) - \\ \operatorname{erf}\left(\frac{DHW}{w\sqrt{2}} + \frac{i\pi w}{2DHW\sqrt{2}}\right) - \operatorname{erf}\left(\frac{i\pi w}{2DHW\sqrt{2}}\right) \end{bmatrix} \right| . \tag{5.43}$$

Selecting $DHW = w$ and computing the ratio of eq. (5.43) and eq. (5.41) yields

$$\frac{AC\{V_{13}(t)\}}{AC\{V(t)\}} = 0.45 . \tag{5.44}$$

This means that the AC signal amplitude obtained in the Df detector configuration is slightly less than half of the amplitude obtained in the conventional configuration. However, the signal $V_{24}(t)$ will exhibit the same amplitude as the $V_{13}(t)$ signal although it is phase shifted by $\pm 90^\circ$, depending of the sign of the axial object motion. This property is exactly what allows the determination of the direction of the axial translation of the object, but prohibits the addition of the two signals to obtain the maximum amplitude signal. Assuming that the axial speed is constant and nonzero, the phase of the $V_{24}(t)$ signal can be adjusted to be in-phase with $V_{13}(t)$. The two signals can then be added in phase

$$V_\Sigma(t) = V_{13}(t) + V_{24}^{(\pm 90)}(t) . \tag{5.45}$$

where $V_{24}^{(\pm 90)}(t)$ is the $V_{24}(t)$ signal phase shifted, appropriately, by the phase shifter (PA). The ratio of eq. (5.45) and eq. (5.41) then becomes

$$\frac{AC\{V_\Sigma(t)\}}{AC\{V(t)\}} = 2 \times 0.45 = 0.90 . \tag{5.46}$$

In a real implementation it could be imagined that in conditions of large axial speeds, the phase shifter is adjusted appropriately by $\pm 90^{\circ}$ to maximize the amplitude of the signal $V_{\Sigma}(t)$ and when the signal frequency approaches zero it is adjusted back to zero to monitor the direction using the signals $V_{13}(t)$ and $V_{24}(t)$ just as in the Df system. These considerations are highly idealized and lack experimental verification, but eq. (5.46) at least suggests that similar signal levels can be achieved using a detector configuration similar to the one used in the Df system, while still allowing the measurement of the directionality of the axial object translation.

When attempting to measure the velocity of atmospheric aerosol flows, one must also take into account the added complexity due to turbulence that is not present when investigating the motion of rigid objects. The presence of turbulence, i.e. aerosol velocity variation within the measurement volume or perturbing media along the optical axis, will introduce decorrelation of the speckle pattern and thus in the fringe pattern used to measure the axial velocity. This effect is generally observed as a line broadening of the Doppler peak in the spectrum obtained with conventional LDV systems. Turbulence will therefore impose another limiting factor on measurement accuracy and perhaps more importantly on data availability.

Papers III and **IV** provide a comprehensive analysis of the shearing interferometer applied to in-plane translating and rotating rigid objects and the above comparison of signal amplitudes suggests only marginal performance degradation as compared to the conventional LDV method. In addition, the application of optical spatial filters retain a high degree of temporal resolution when measuring both transverse and axial velocity components while maintaining the ability to measure the direction of these as well.

6. Finger tracking

The use of fingers to navigate the virtual environments of a wide variety of consumer electronic products has become a significant industry and the competition to develop the best solutions is sharp. Today, most laptops are equipped with a touch sensitive area or “touchpad”, designed for cursor navigation when the use of a traditional computer mouse is unpractical or impossible, e.g. in a confined environment such as in an airplane. Also, many new mobile phones, personal digital assistants (PDA) and the more recently tablet computers, are equipped with a touch sensitive screen that acts as a pointing device to navigate the environment presented on the screen of the device. The “touchscreen” device can be implemented in a number of different ways depending on the working principle of the device and the application. These include both electrical and also optical solutions.
Another category is tracking devices for cursor control. This type of navigation device is based on detecting the motion of a mechanically rotating ball or optically detecting the motion of a fingertip. Implementations of these principles are found in some mobile phones and PDA’s and resembles early forms of cursor control on some of the first laptops, and is similar in working principle to the computer mouse. The active part of the device occupies only a small region and the cursor on the screen can be moved around by swiping the tip of a finger across this region. This category is a niche that Df sensor solutions can occupy, and thus it is of interest to investigate possible ways to implement the technology into a sensor solution.
In the following, a selected range of touch technologies that are available today is presented. Lastly, the possibilities of using Df based sensors and principles, as alternatives to the existing tracking devices, are addressed.

6.1 Technological overview

Generally, two fundamentally different approaches to the touch sensor principle exist. Firstly, the absolute position device encompasses the touchscreen and touchpad solutions found on mobile phones, laptops and tablets. This type of device continually senses the *position* of the fingertip (or stylus) on the comparatively large touch sensitive area. Secondly, the tracking approach senses only *displacement* of the fingertip and employ a much smaller sensitive area. This approach is suitable for cursor control rather than being used as a direct (finger) pointing device.

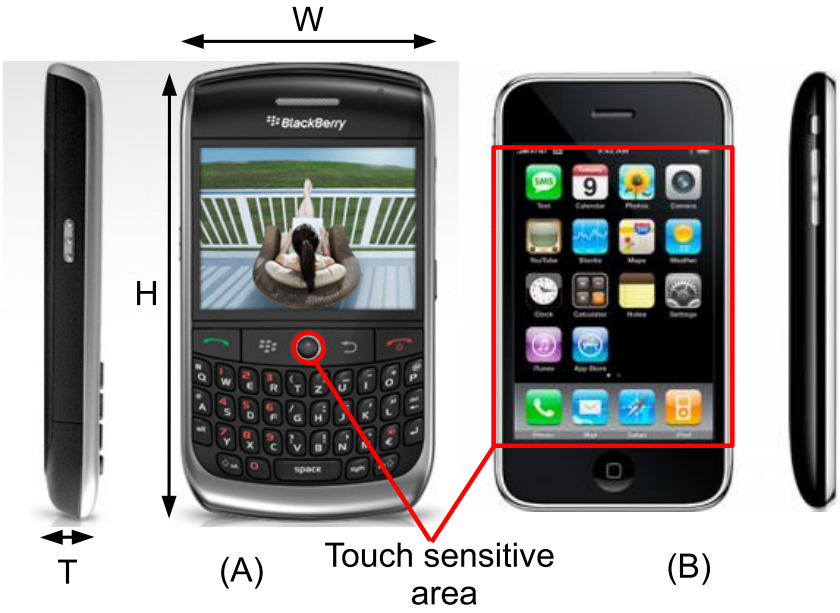

Figure 6.1 – (A) Blackberry™ mobile phone with dimensions ($H \times W \times T$) 109mm× 60mm× 13.5mm. Some Blackberry™ phones utilizes a trackball type solution. (B) An iPhone™ with dimensions 115mm× 62mm× 12.5mm utilizing a touch screen solution with a large touch sensitive area.

Figure 6.1 shows two mobile phones, each of which implement one of the two types of touch solutions.

Touchpads and screen technology is dominated by two electrical methods of determining the touch position. The simplest of these is the resistive. Resistive touch devices employs an arrangement of two layers of parallel conductive strips generally arranged in a mutually perpendicular fashion, forming a grid. The two layers are separated by thin deformable spacers. The locations where the strips intersect are called nodes and occupy every grid point across the active area of the device. When pressure is applied to the surface, the strips compress in the region of contact establishing an electrical contact creating a short circuit. Detecting the position of the short circuit allows the determination of the position of the object applying pressure. Resistive touch devices are sensitive to almost anything, as long as enough force is applied to create the short circuit.

A simple capacitive touch device used for a touch screen is shown in figure 6.2. It consists of sandwiched layers of different materials. The transparent conductive layer is made from either Antimony Tin Oxide (ATO), Tin Oxide (TO) or in some cases Indium Tin Oxide (ITO). All these materials are conductive but exhibit a high resistivity while also maintaining a high degree of (optical) transparency. In the corners of the device are four electrodes connected to the conductive layer. The four electrodes are each driven by an AC voltage signal, supplied from the controller (cf. figure 6.2), that has the same amplitude, frequency and phase. This

causes a small current to flow - known as the "baseline" current. When a conductive object such as a finger contacts the top layer, a small amount of electrical energy is coupled capacitively to the fingertip, which in turn causes a small excess current (in relation to the baseline current) to flow in the electrodes.

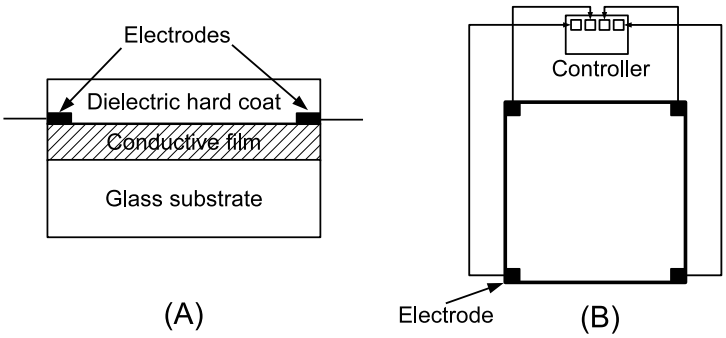

Figure 6.2 – (A) cross-section view of a simple capacitive touch device consisting of a top layer forming the touch interface. Next, a transparent conductive layer is sandwiched between the top layer and a glass substrate. (B) Electrodes are connected to the conducting layer from the four corners of the touch sensitive area of the device.

The controller determines the amount of current it must supply to each electrode to re-establish the baseline current. The amount of current is, under the right circumstances, directly proportional to the distance between the touch location and the corresponding electrode, thus enabling the determination of the touch position by triangulation. Typically the drive frequencies of the applied voltage signals are in the range 25-200 kHz, and the amount of current absorbed by a fingertip touching the device surface is ~1uA [63]. The major issues with the capacitive technology are high manufacturing costs, complexity and scalability. Furthermore, the touch device itself acts as an antenna that both emits significant electro-magnetic interference (EMI) which can disturb adjacent circuitry and is also itself susceptible to EMI, which can disturb the electrical signals used to recognize a touch event by introducing ghost events (false positives) or inhibiting recognition of a true touch event. As the market tendency seems to be going towards larger and larger touch screens as can be seen e.g. with the introduction of the tablet pc, these issues multiply in significance.

Optically based devices solve many of the above mentioned issues and are becoming commercially available. One of the most straightforward ways of implementing a touch sensitive screen with simple optical components is outlined in figure 6.3(A).

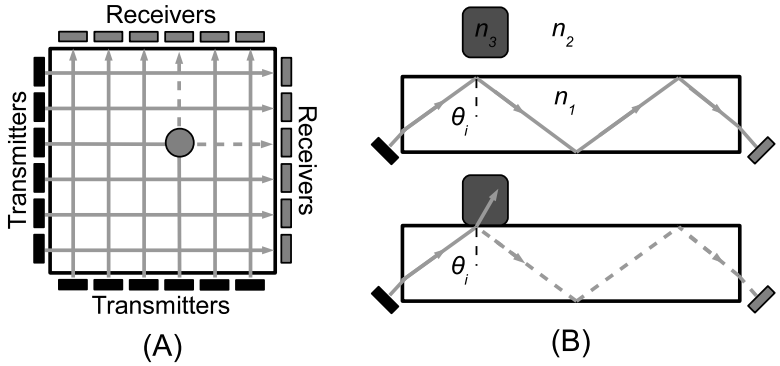

Figure 6.3 – (A) Simple optical touch device. Arrays of transmitters (LED) along the edges form a grid of light beams, travelling just above the surface, which are received by corresponding arrays of detectors. Interruption of a grid position corresponds to a touch event. (B) Waveguide principle. An emitter injects a ray into the waveguide where it undergoes Total-Internal-Reflection (TIR) (top). Touch event (bottom) occurs when an object interrupts the TIR condition by establishing contact with the surface.

Collimated light emitting diodes, in the infrared typically, are positioned along two of the edges of the device, while receivers in the form of photodiodes are positioned at the opposite edges, forming a grid. The light beams travel just above the surface of the device, and when interrupted by, e.g. a fingertip, the position can be extracted by observing which pair of photodiodes experience a drop in signal. The same principle can also be implemented by using a waveguide structure. The principle is illustrated in figure 6.3(B). Light travelling inside the waveguide will experience total internal reflection (TIR), as long as the incident angle with the surface fulfils the requirement

$$\theta_i \leq \theta_c = \arcsin\left(\frac{n}{n_1}\right), \tag{6.1}$$

where θ_c is the critical angle for TIR, n_1 is the refractive index of the waveguide medium and n is the refractive index of the medium in contact with the surface at the point of illumination. Figure 6.3(B) shows a no-touch state (top) where air with refractive index $n \to n_2$ is in contact with the waveguide and a touch event (bottom) where an object with refractive index $n \to n_3$ is in contact with the surface of the waveguide. Because the refractive index of tissue for a typical fingertip is around 1.47, the angle of incidence can be selected so that only a finger touch will decrease the amount of light received by the photodetector, while the presence of lower refractive index materials such as air ($n_{air} \approx 1$) and water ($n_{water} = 1.32$) will not result in a significant change in signal level.

The specific implementation outlined in figure 6.3 is not a particular elegant solution and will suffer from several disadvantages. The resolution is a major issue for this type of device. Increasing the resolution becomes a matter of increasing the

number of individual transmitters and receivers along the edges, which significantly increases cost and power consumption.
OPDI Technologies A/S is currently, in collaboration with DTU Fotonik, developing a waveguide-based device where only a single light source and a line camera are needed. The working principle of the "WaveTouch" (WT) is similar to the optical grid type, but the grid is formed by the use of optics in the form of Fresnel reflectors, eliminating the need for receiver arrays distributed along the entire edge of the device. The working principle is outlined in figure 6.4.

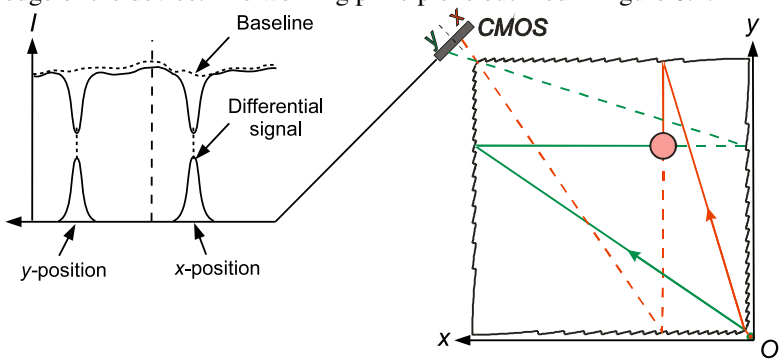

Figure 6.4 – Working principle of the "WaveTouch" device. The dimensions of the waveguide is ($H \times W \times T$) 40mm× 40mm× 1mm.

A single light source is placed at the origo *O*. The light source injects a fan of light into the waveguide, covering the entire 90° of the x-y plane. In figure 6.4 two sample rays are shown for clarity. The fan of rays are collimated by slightly tilted Fresnel edges that, due to the tilt, bring the rays into a touch sensitive angular range as they propagate along the x and y axis respectively. A second pair of equally tilted Fresnel reflectors at the opposite side of the device "rectifies" the angle of the incoming rays so that they again propagate in the plane of the waveguide. The second pair of reflectors also focuses the rays to a point just in front of a linear CMOS array. If a finger touches the waveguide surface some of the light will be coupled out, similar to current being coupled to the fingertip in the capacitive devices. The purpose of the Fresnel arrangement is to sensitize the rays that propagate along the x and y axis of the waveguide to the touch event and de-sensitizing the rays while they are propagating to the first reflector and leave the second reflector. A baseline intensity profile is recorded with the CMOS array when the waveguide is not touched. From this, a differential signal can be constructed by subtracting the intensity profile, recorded during the touch event, from the baseline profile. The touch position can then be derived from extracting the positions of peaks in the differential signal (cf. figure 6.4). A detailed treatment of the WT technology is given in **Paper V**.
The waveguide itself is a single-piece of polycarbonate manufactured by injection moulding and a VCSEL is used as light source. The line camera used in the prototype is readily integrated into an ASIC. The WT is therefore well suited for mass production while maintaining minimum manufacturing costs, giving it a competitive advantage over e.g. capacitive devices.

6.2 Speckle-based devices

The trackball solution found in e.g. some mobile phones is another way of introducing touch sensitivity into multimedia devices. This type of device is used to control a cursor on the screen with a finger tip rather than pointing directly on the screen. The main challenges of this type of device, is to maintain a low thickness and a high *CPI* (resolution). The thickness is most important when targeting mobile phones, because modern mobile phones rarely are thicker than 15mm. A high *CPI* is important because the touch sensitive region is relatively small. If the *CPI* is low, it can take multiple swipes of the finger to get from one side of the screen to the other, which is not acceptable for the user.
Mobile phones are the most challenging target for tracking devices to address mainly due to the requirements for the form factor. However, less demanding applications, such as remote controls for internet TVs and media centres may become a future market for tracking devices.
The Df sensor is implemented both as a computer mouse for traditional use and a modified version suitable for use as a touch sensitive tracking device. In figure 6.5 the sensor configuration of the "DfTouch" sensor is shown.

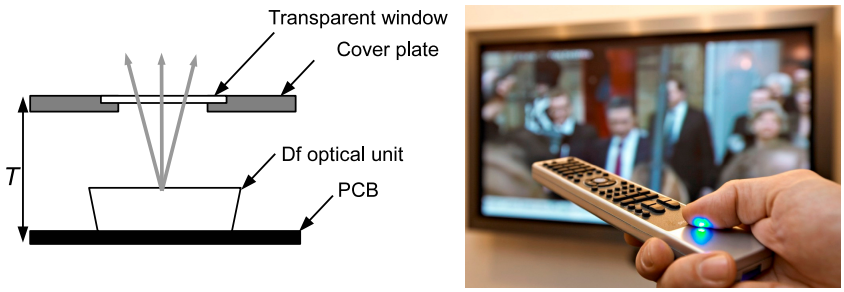

Figure 6.5 – Df mouse sensor modified for use as a touch sensitive tracking device.

A transparent window is placed over the sensor at the working distance (*L*) of the sensor. The sensor operates as an optical mouse, tracking the movement of the finger tip rather then the surface of e.g. a desktop. Using the Df2000 optical unit, discussed earlier, the overall thickness *T* is just under 8.5mm which is too large to fit inside most mobile phones, however, will be well dimensioned for integration into most remote controls.

For use in mobile phones the thickness of the sensor must be reduced. The main challenge, when considering Df based solutions, is to minimize the overall thickness. In order to achieve this, a combination of the waveguide principles used in the WT sensor and the Df sensor technology has been considered. The principle is outlined in figure 6.6.

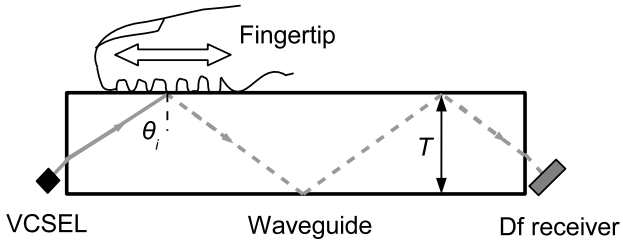

Figure 6.6 – Principle of a waveguide based Df touch sensitive tracking sensor.

The angle of incidence θ_i of the illumination is $\theta_i \geq \theta_c$, where θ_c is the critical angle of the air-waveguide interface, so that the TIR condition is satisfied.
There are several advantages to operating in TIR conditions. In terms of eye safety, no light is transmitted out of the device when it is not in use. This fact also translates into good power efficiency, a key factor when incorporating sensors into battery powered devices. Moreover, the internal dynamics of live tissue (e.g. blood flow) and other unwanted effects such as bulk scattering has minimum influence under TIR conditions. When a fingertip is brought into contact with the waveguide at the point of illumination, some of the incident light is coupled into propagating modes in the tissue. As what is the case for the WT this is due to refractive index matching between the tissue of the fingertip and the waveguide surface. However, if the refractive index of the waveguide material is different from the refractive index of the tissue (which generally will be the case) a fraction of the light will scatter reflectively from the tissue-waveguide interface and propagate inside the waveguide. Provided that the surface tissue of finger tip can be considered rough compared to the optical wavelength, a speckle pattern will be generated that will propagate inside the waveguide. Generally, the speckle pattern will move as the fingertip moves. Under the right circumstances this movement can be tracked by a Df receiver placed at the opposite end of the waveguide (cf. figure 6.6).
However, the structure of the vast majority of human fingertips is not uniform, but covered by a pattern of indentations and extrusions of the skin that are known as dermal ridges. This pattern is the basis of fingerprints. The dermal ridges follow complex patterns that indeed are unique to the individual person. However, certain general features repeat themselves in these patterns. This is true of the separation of two adjacent dermal ridges that is approximately 0.4-0.5mm [64]. Also, at the outermost part of the fingertip the ridge orientation nearly always follow a circular pattern centred in the middle of the fingertip. Figure 6.7 illustrates these general properties of dermal ridge patterns.

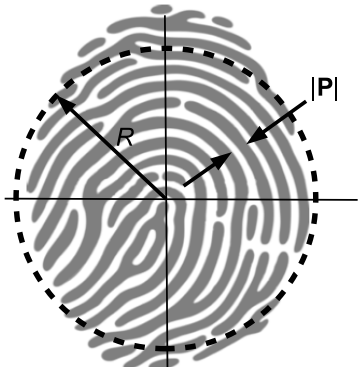

Figure 6.7 – Typical fingerprint pattern illustrating the dermal ridge structure. The dermal ridges (gray) of the upper part of the pattern seem to follow circular patterns of radius R centred at the middle of the finger print. The average dermal ridge separation $|\mathbf{P}|$ is approximately constant.

The regions of white in figure 6.7 illustrates tissue recesses (ridge valleys), whereas the region of gray represent the protrusions of the tissue (ridge crests).
The dermal ridge structures have significant implications for the properties of the speckle pattern that is generated in the configuration illustrated in figure 6.6. Particularly, it is expected that at the areas where there are ridge valleys the illuminating light will be totally internally reflected and thus unaltered by the interaction with the interface, whereas the regions of ridge crests generate a speckle pattern. These effects needs to be understood in details when designing sensors based on this type of configuration. To this end, an experiment was designed to verify the hypothesis of alternating scattering and specular reflecting structures formed by the dermal ridges at the interface between waveguide and fingertip.
The experimental setup used is illustrated in figure 6.8. A polarization stabilized Helium-Neon (HeNe) laser lasing at 633nm providing a Gaussian beam profile was used to illuminate the contact area where the fingertip interacts with the waveguide interface. A right angle prism made from BK7 glass was used to emulate the waveguide. The contact region between fingertip and interface was illuminated by the collimated HeNe laser at a 45° angle, and the scattered/reflected light was captured with a CMOS array in one of two ways: An imaging system with magnification 2x could be inserted to investigate the scattering geometry in the extreme near field ($z = 0$), or a free-space configuration could be employed to investigate intermediate regions between the extreme near-field and the far-field ($z = \infty$).

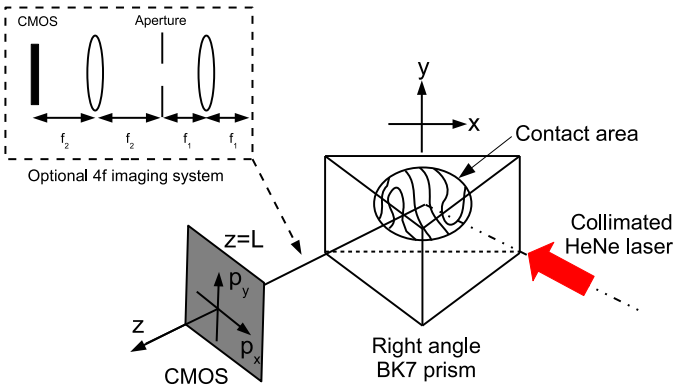

Figure 6.8 – Experimental setup for investigating the scattering properties of fingertips.

The angle of incidence of the illumination is 45°, while the critical angle of BK7 glass is 41°. The TIR condition ($\theta_i \geq \theta_c$) is thus fulfilled for this experimental configuration. The spot size of the illumination beam was in this case 1mm (e^{-2} intensity radius). The imaging system was used to investigate the interface region between the fingertip and the waveguide. The images were used to identify the different scattering and reflecting structures present in the contact area.

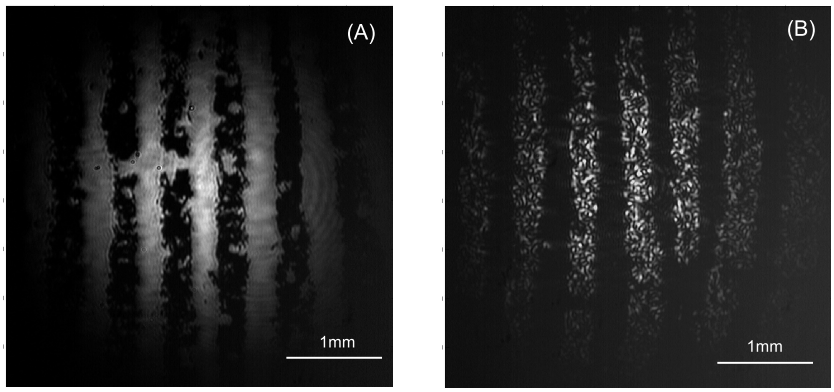

Figure 6.9 – Near-field observations obtained with the imaging system. (A) Specular contributions are transmitted through the imaging system. (B) Specular contributions are blocked by the aperture in the imaging system.

Images were recorded with two different conditions and shown in figure 6.9. In figure 6.9(A) the fingertip is contacting the interface with the imaging system aligned so that the specular reflection is directly transmitted to the CMOS. It is clear from this image that areas where the fingertip is in contact with the interface, the light is nearly completely coupled out and propagates into the tissue of the fingertip. On the other hand areas where the fingertip is not in contact with the interface (i.e. between the dermal ridge crests) the light is reflected with high

efficiency. This observation confirms the initial hypothesis and suggests that the strength of the specularly reflected light significantly exceeds the strength of the diffusely scattered light.
Conversely, if the specular part of the light is blocked, a diffusely scattering structure is revealed giving rise to fully developed speckles (i.e. an intensity modulation depth of ~1). This situation is shown in figure 6.9(B). Experimentally, the blocking of the specular light was achieved by repositioning the imaging system so that the contact region was imaged from a slightly different angle resulting in the specular reflection being blocked by the aperture in the imaging system.
To investigate free space propagation of the light after the interaction with the interface, the imaging system was removed and the CMOS placed at a distance of L = 55mm from the interface. In figure 6.10 an intensity distribution obtained in the free space propagation configuration is shown. It is observed that the periodic structures of specular reflection and diffusely scattering dermal ridges are still present but now a speckle pattern has also emerged at the position of the specular reflections.

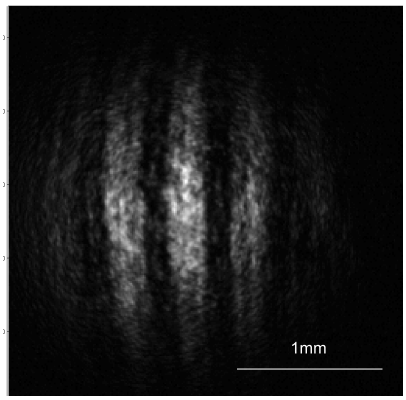

Figure 6.10 – Intensity distribution obtained in the free space propagation configuration at distance L = 55mm.

Based on the intensity distributions obtained with the imaging system it can be concluded that there are two distinct contributions to the measured intensity distribution: a specular, or directly reflected, contribution and a diffusely scattered contribution. Figure 6.10 shows the intensity distribution obtained after free space propagation of the scattered light where it is clear that mixing of the two contributions takes place. In other words, the specularly scattered light acts a local oscillator for the diffusely scattered light, thus increasing the impact of the diffusely scattered field.
A theoretical model can now be formulated, describing the intensity dynamics due to a movement of a fingertip over the illuminated region of the waveguide. The ensemble averaged intensity crosscorrelation function is the entity of interest. For ease of notation the abbreviations $U_s \equiv U_s(\mathbf{p}_1, t)$ and $U_s' \equiv U_s(\mathbf{p}_2, t+\tau)$ are adopted for the specular field contribution and similarly $U_d \equiv U_d(\mathbf{p}_1, t)$ and

$U_d' \equiv U_d(\mathbf{p}_2, t+\tau)$ for the diffuse field contributions. The ensemble-averaged intensity crosscorrelation function then becomes

$$\begin{aligned} C(\mathbf{p}_1, \mathbf{p}_2, \tau) &\equiv \langle I(\mathbf{p}_1, t) I(\mathbf{p}_2, t+\tau) \rangle \\ &= \left\langle (U_s + U_d)(U_s^* + U_d^*)(U_s' + U_d')(U_s'^* + U_d'^*) \right\rangle . \end{aligned} \tag{6.2}$$

Without specifying the optical system that transfers the field distributions from the object plane to the observation plane, eq. (6.2) can be rewritten as

$$\begin{aligned} C = {} & I_s I_s' + I_s I_d' + I_d I_s' + I_d I_d' \\ & + 2\,\mathrm{Re}\left\{ \left\langle U_s^* U_s' U_d U_d'^* \right\rangle \right\} + \left| \left\langle U_d U_d'^* \right\rangle \right|^2 , \end{aligned} \tag{6.3}$$

where $I_s \equiv |U_s|^2$, $I_s' \equiv |U_s'|^2$, $I_d \equiv |U_d|^2$ and $I_d' \equiv |U_d'|^2$. In deriving eq. (6.3), we have assumed circular symmetric Gaussian statistics for the diffusely scattered field. The term of most interest in eq. (6.3) is the fifth (cross) term that contains combination of the specular and diffuse contributions. Because the dermal ridge separation $\mathbf{P}$ generally must be considered to be spatially dependent and stochastic in nature, the cross-term becomes a fourth-order field correlation term that generally is difficult to evaluate. If however, an area of the finger tip is illuminated, over which the dermal ridge separation can be considered to be constant and deterministic, eq. (6.3) becomes

$$\begin{aligned} C = {} & I_s I_s' + I_s I_d' + I_d I_s' + I_d I_d' \\ & + 2\,\mathrm{Re}\left\{ U_s^* U_s' \left\langle U_d U_d'^* \right\rangle \right\} + \left| \left\langle U_d U_d'^* \right\rangle \right|^2 . \end{aligned} \tag{6.4}$$

The fourth order field correlation term is then reduced the evaluation of the product of two second order field correlation terms.
In [65] a model of the specular and diffuse field contribution obtained in the object plane is defined. The specular field contribution is assumed to on the form

$$U_s(\mathbf{r}) = \frac{U_i(\mathbf{r})}{2}\left[1 + \cos(\boldsymbol{\omega} \cdot \mathbf{r})\right], \tag{6.5}$$

where $U_i(\mathbf{r})$ is given by eq. (1.34) for $R_o \to \infty$ and $\boldsymbol{\omega} = 2\pi/\mathbf{P}$. The diffuse contribution is assumed to be of the form

$$U_d(\mathbf{r}) = \frac{U_i(\mathbf{r})}{2}\left[1 - \cos(\boldsymbol{\omega} \cdot \mathbf{r})\right]\Psi(\mathbf{r}), \tag{6.6}$$

where it is noted that the cosine term is 180° out of phase with respect to the corresponding term in eq. (6.5).
Based on these assumptions an analytical model is outlined that will form the basis for future work on the subject and hopefully provide insight that will aid the design process of ultra thin finger tracking devices.

Conclusion

The main result of this thesis is the development of a method for measuring all three velocity components of an optically rough rigid translating object using the spatial filtering technique. Based on an imaging system connecting the object and the observation plane both numerical and analytical models of the intensity distribution and dynamics, obtained when combining the imaging speckle pattern with an angular offset reference wave, were developed. These models predicted that the speckle pattern would move in response to the in-plane translation of the object and that the fringe pattern appearing due to the presence of the reference wave would move in response to the out-of-plane motion of the object. This was demonstrated experimentally in **Paper III**.

It was shown that components of in-plane rotation could be extracted by modification of the spatial filter configuration to include at least two spatially separated filter arrangements. Specifically, a radius-independent measurement of the angular velocity of a cylindrical object, rotating in-plane, was demonstrated in **Paper IV**.

The use of optical spatial filters to measure the motion of both the speckle and fringe patterns lends significant advantages as compared to camera-based methods such as those described in [49] and [60] in terms of temporal resolution. This is mainly due to the limited camera frame rates and signal processing time of these methods. Although the use of optical spatial filters is not well suited for measuring displacement fields of object subjected to load, which is the normal area of application for ESPI, the method presented in this thesis is well suited for measuring fast translating objects or flow fields. A comparison between signal levels in the conventional homodyne laser Doppler velocimetry detection scheme and the proposed method based on fringe translation was presented. It was shown that similar signal levels can be achieved in the two different configurations. However, in the latter case the directional ambiguity of the object motion is resolved by angular offsetting of the reference wave and introducing a suitable detector arrangement. The proposed method therefore needs no additional equipment such as e.g. frequency shifting devices. Furthermore, the proposed method eliminates the need for mechanically scanning the beam such as is necessary in the velocity azimuth display method, retaining a localized and point-like measurement.

The optical spatial filter used to measure the out-of-plane velocity component in **Paper III** was analyzed using ray tracing methods in the context of its original application as a two dimensional velocity sensor, used as an optical computer mouse. A sequential ray tracing model illustrated that the number of lenslets that can be accommodated in the optical spatial filter is limited by aberrations of the focusing lens. Because the number of lenslets is directly related to the attainable measurement precision of the optical spatial filter, this effect is important to address in order to obtain optimum performance. Furthermore, a non-sequential ray tracing model illustrated that an inhomogeneous illumination profile of the detector array, generally leads to the emergence of unwanted passbands in the spatial filter transfer function. These ray tracing models provided some quantitative results however

served best as ways to increase the insight into the fundamental workings of the optical spatial filter and as means to identify optimum design configurations.
Additionally, a diffractive optical element was designed and manufactured which was intended to provide an optimum illumination pattern of the surface in the optical mouse application. The manufacturing process of this diffractive optical element proved ultimately to be too unstable to provide a satisfactory result. However, given adequate control of the etching rate in the ion-beam etching technique used in the manufacturing process of the element, significant advantages may be achieved using this process to obtain the desired diffractive optical element of the beam shaping optics in the optical mouse application.
The performance characteristic of the optical spatial filter is critically linked to the geometrical parameters of the lenticular array. This includes the radius of curvature and grating period of the lenticular array. Because the optical spatial filter is manufactured by injection moulding, where high rates of production is possible, a quality assurance method was needed that could keep up with the rate of production, which in this particular case is on the order of seconds. This ruled out the use of scanning probe microscopy. A method to simultaneous measure both the radius of curvature end the grating period of the lenticular array was developed and verified using scanning probe techniques. Furthermore, a possible dedicated setup was proposed. Although not implemented and tested, the measurement cycle time was estimated to be on the order of 1 second. Lastly, few and relatively cheap components can be used to implement the method and the use of only one moving part makes it significantly more robust than scanning probe instruments.
During the work with optical touch devices and screens, most noticeably in the form of the WaveTouch technology, it became evident that significant commercial interest in very thin touch devices was present. To address this, a possible combination of the waveguide principles used in the WaveTouch technology and speckle patterns, was investigated. Special emphasis was placed on the case where coherent light is scattered off the interface between a fingertip in contact with a flat dielectric medium. This particular case was investigated experimentally, and based on the observations a theoretical model was formulated. The experiment revealed a possible beneficial effect that arises due to the dermal ridge patterns of the human fingertip. Alternating diffusely scattering and specular reflecting contributions mixes coherently when observed at certain free space distances, providing an enhanced speckle signal that may be utilized for tracking purposes. Applying spatial filters integrated in the waveguide structure could provide a means of finger tracking sensors that are significantly reduced in thickness and thus better suited for implementation into form factor critical application such as e.g. mobile phones.
The development of diode-laser based prototypes for wind speed measurement suitable for field trials was one of the original goals of the project. This was not achieved. Implementing the three-dimensional measurement principles for wind speed is associated with many challenges such as the presence of turbulence and generally weak signals. Many aspects still needs to be investigated theoretically and experimentally before implementation of the measurement principle can be attempted in field-trial prototypes for wind speed measurements. However, the work described in this thesis has put down much of the basic work needed, and the experiences learned in the process will undoubtedly be valuable in the next stages of development of such prototypes.

References

[1] J.W. Goodman, "Statistical properties of laser speckle patterns", in *Laser speckle and related phenomena*, J. C. Dainty, ed. (Springer-Verlag, Berlin, 1984).

[2] H. T. Yura, S. G. Hanson and M. L. Jakobsen, "Speckle dynamics resulting from multiple interfering beams", J. Opt. Soc. Am., **25** , 318-326, (2008).

[3] H. Fujii, K. Nohira, Y. Yamamoto, H. Ikawa and T. Ohura, "Evaluation of blood flow by laser speckle image sensing. Part 1", Applied Optics, **26**, 5321-5325, (1987).

[4] A. K. Dunn, H. Bolay, M. A. Moskowitz and D. A. Boas, "Dynamic imaging of cerebral blood flow using laser speckle", J. Cereb. Blood Flow and Metab., **21**, 195-201, (2001).

[5] M. Sjödahl,"Some recent advances in electronic speckle photography", Optics and Lasers Engineering, **29**, 125-144, (1998).

[6] S. S. Beauchemin and J. L. Barron, "The computation of optical flow", ACM computing surveys, **27**, 433-467, (1995).

[7] M. L. Jakobsen, H. T. Yura and S. G. Hanson,"Speckles and their dynamics for structured target illumination: optical spatial filtering velocimetry", J. Opt. A: Pure Appl. Opt. 11, 9pp, (2009).

[8] R. M. Huffaker," Laser Doppler detection systems for gas velocity measurement", Applied Optics, **9**, 1026-1039, (1970).

[9] C. J. Karlsson, F. Å. A. Olsson, D. Letalick and M. Harris,"All-fiber multifunction continuous-wave coherent laser radar at 1.55um for range, speed, vibration, and wind measurements", Applied Optics, **39**, 3716-3726, (2000).

[10] R. S. Hansen and C. Pedersen, "All semiconductor laser Doppler anemometer at 1.55um", Optics Express, **16**, 18288-18295, (2008).

[11] S. O'Brien, D. F. Welch, R. A. Parke, D. Mehuys, K. Dzurko, R. J. Lang, R. Waarts and D. Scifres, "Operating characteristics of a high-power monolithically integrated flared amplifier master oscillator power amplifier", IEEE J. Quant. Elec., **29**, 2052-2057, (1993).

[12] Borsen, Friday, December 4, (2009).

[13] E. A. Dakin, "Boosting power production – Project report on Nebraska public power district Vindicator® LWS field trial", Catch the Wind, Inc., 10781 James Payne Court, Manassas, VA 20110.

[14] D. Hausamann and B. W. Davis, ”Sign of wind vector: a simple method for its determination with a homodyne cw laser Doppler velocimeter”, Applied Optics, **29**, 2919-2928, (1990).

[15] M. Born and E. Wolf, *Principles of optics*, 7th ed., (Cambridge University Press, 1999).

[16] M. R. Spiegel and J. Liu, *Mathematical handbook of formulas and tables*, 2nd ed., (McGraw-Hill, 1999).

[17] J. W. Goodman, *Introduction to Fourier optics*, 3rd ed., (Roberts & Company Publishers, 2005).

[18] H. T. Yura and S. G. Hanson, ”Optical wave propagation through complex optical systems”, J. Opt. Soc. Am., **4**, 1931-1948, (1987).

[19] A. E. Siegman, *Lasers*, (University Science Books, 1986).

[20] A. Gerard and J. M. Burke, *Introduction to matrix methods in optics*, (Dover Publications, Inc., 1975).

[21] J. W. Goodman, *Statistical optics*, (John Wiley and Sons, Inc., 1985).

[22] H. T. Yura, B. Rose and S. G. Hanson, ”Dynamic laser speckle in complex ABCD optical systems”, J. Opt. Soc. Am., **15**, 1160-1166, (1998).

[23] M. L. Jakobsen H. T. Yura and S. G. Hanson, ”Speckle dynamics for dual beam optical illumination of a rotating structure”, Applied Optics, **48**, 1804-1811, (2009).

[24] L. E. Drain, *The laser Doppler technique*, (John Wiley and Sons, Inc., 1980).

[25] A. K. Prasad, “Particle image velocimetry”, Current Science, **79**, (2000).

[26] L. Lading, ”Estimating time and time-lag in time-of-flight velocimetry”, Applied Optics, **22**, 3637-3643, (1983).

[27] H. T. Yura and S. G. Hanson, ”Laser-time-of-flight velocimetry: analytical solution to the optical system based on ABCD matrices”, J. Opt. Soc. Am., **10**, 1918-1924, (1993).

[28] A. R. Gédance, ”Comparison of infra-red tracking systems”, Applied Optics, **51**, 1127-1130, (1961).

[29] J. T. Ator, ”Image velocity sensing by optical correlation”, Applied Optics, **5**, 1325-1331, (1966).

[30] M. Gaster, ”A new technique for the measurement of low fluid velocities”, J. Fluid Mech., **20**, 183-192, (1964).

[31] Y. Aizu and T. Asakura, *Spatial filtering velocimetry - Fundamentals and Applications*, (Springer-Verlag Berlin Heidelberg, 2006).

[32] U. Schnell, J. Piot and R. Dändliker, ”Detection of movement with laser speckle patterns: statistical properties”, J. Opt. Soc. Am., **15**, 207-216, (1998).

[33] M. L. Jakobsen and S. G. Hanson, ”Lenticular array for spatial filtering velocimetry of laser speckles from solid surfaces”, Applied Optics, **43**, 4643-4651, (2004).

[34] M. L. Jakobsen, F. Pedersen and S. G. Hanson, “Zero-crossing detection algorithm for arrays of optical spatial filtering velocimetry sensors”, Proc. SPIE, **7003**, (2008).

[35] F. Wyrowski, ”Diffractive optical elements: iterative calculation of quantized, blazed phase structures”, J. Opt. Soc. Am. A, 7, 961-969, (1990).

[36] W. W. Chow, K. D. Choquette, M. H. Crawford, K. L. Lear and G. R. Hadley, ”Design, fabrication, and performance of infrared and visible vertical-cavity surface-emitting lasers”, IEEE J. Quant. Elec., **33**, 1810-1824, (1997).

[37] B. M. Hawkins, R. A. Hawthorne III, J. K. Guenter, J. A. Tatum and J. R. Biard, ”Reliability of various size oxide aperture VCSELs”, Honeywell International, 830 E. Arapaho Road, Richardson, Texas 75081.

[38] V. R. Daria, P. J. Rodrigo and J. Glückstad, ”Programmable complex field coupling to high-order guided modes of micro-structures fibres”, Optics Communications, **232**, 229-237, (2004).

[39] M. L. Jakobsen and S. G. Hanson, ”Micro-lenticular array for spatial filtering velocimetry on solid surfaces”, Meas. Sci. Technol. **15**, 1949-1957, (2004).

[40] A. A. Tseng, ”Recent developments in micromiling using focused ion beam technology”, J. Micromech. Microeng., **14**, R15-R34, (2004).

[41] G. S. Kino and S. C. Chim, ”Mirau correlation microscope”, Applied Optics, **29**, 3775-3783, (1990).

[42] I. Kassamakov, K. Hanhijärvi, I. Abbadi, J. Aaltonen, H. Ludvigsen and E. Hæggström, ”Scanning white-light interferomettry with a supercontinuum source”, Optics Letters, **34**, 1582-1584, (2009).

[43] J. Garnaes, P.-E. Hansen, N. Agersnap, J. Holm, F. Borsetto and A. Kühle, ”Profiles of a high aspect ratio grating determined by spectroscopic scatterometry an atomic force micoscopy”, Applied Optics, **45**, 3201-3212, (2006).

[44] F. J. Giessibl, “Advances in atomic force microscopy”, Reviews of Modern Physics, **70**, (2003).

[45] A. Büttner and U. D. Zeitner, ”Calculation of the average lenslet shape and aberrations of microlens arrays from their far-field intensity distribution”, Applied Optics, **41**, 6841-6848, (2002).

[46] J. W. Bilbro, C. DiMarzio, D. Fitzjarrald, S. Johnson and W. Jones, “Airborne Doppler lidar measurements”, Applied Optics, **25**, (1986).

[47] S. M. Spuler, D. Richter, M. P. Spowart and K. Rieken, ”Optical fiber-based laser remote sensor for airborne measurement of wind velocity and turbulence”, Applied Optics, **50**, 842-851, (2011).

[48] C. Shakher and A. K. Nirala, ”Measurement of temperature using speckle shearing interferometry”, Applied Optics, **33**, 2125-2127, (1994).

[49] M. Sjödahl and H. O. Saldner, ”Three-dimensional deformation field measurements with simultaneous TV holography and electronic speckle photography”, Applied Optics, **36**, 3645-3648, (1997).

[50] Y. V. Chugui, V. S. Bazin, A. G. Verkhogliad, S. V. Kalichkin, V. E. Kalikin, S. N. Makarov and S. G. Savkov, ”Optical-electronic system for remote measurements of shifts and deformations in huge mechanical and engineering constructions”, Journal of Physics: Conference series **48**, 555-560, (2006).

[51] G. Giebel, U. S. Paulsen, J. Reuder, A. la Cour-Harbo, C. Thomsen and J. Bange, ”Autonomous aerial sensors for wind power meteorology”, EWEC 2010 Proceedings online, 12pp, (2010).

[52] A. E. Siegman, ”The antenna properties of optical heterodyne receivers”, Applied Optics, **5**, 1588-1594, (1966).

[53] J. F. Holmes and B. J. Rask, ”Optimum optical local-oscillator power levels for coherent detection with photodiodes”, Applied Optics, **34**, 927-933, (1995).

[54] H. T. Yura, S. G. Hanson and L. Lading, ”Laser Doppler velocimetry: analytical solution to the optical system including the effects of partial coherence of the target”, J. Opt. Soc. Am. A, **12**, 2040-2047, (1995).

[55] L. Z. Kennedy and J. W. Bilbro, “Remote intensity fluctuation measurements with a Doppler radar”, Applied Optics, **15**, (1976).

[56] L. Z. Kennedy and J. W. Bilbro, “Remote measurement of the transverse wind velocity component using a laser Doppler velocimeter”, Applied Optics, **18**, 3010-3013, (1979).

[57] J. H. Churnside and H. T. Yura, ”Laser vector velocimeter: a 3-D measurement technique”, Applied Optics, **21**, 845-850, (1982).

[58] A. E. Ennos, “Speckle interferometry”, part of *Laser speckle and related phenomina*, J. C. Dainty ed., (Springer-Verlag Berlin Heidelberg, 1984).

[59] O. Løkberg, ”Electronic speckle pattern interferometry”, Phys. Technol., **11**,16-22, (1980).

[60] T. Fricke-Begemann and J. Burke, ”Speckle interferometry: three-dimensional deformation field measurement with a single interferogram”, Applied Optics, **40**, 5011-5022, (2001).

[61] M. Takeda, H. Ina and S. Kobayashi, ”Fourier-transform method of fringe-pattern analysis for computer-based topography and interferometry”, J. Opt. Soc. Am., **72**, 156-160, (1982).

[62] M. L. Jakobsen and S. G. Hanson, ”Miniaturized optical sensors for industrial applications”, Proc. SPIE, 7726, (2010).

[63] C. Bauman, ”How to select a surface-capacitive touch-screen controller”, Information Display, **12**, 32-36, (2007).

[64] D. A. Stoney, “Distribution of epidermal ridge minutiae”, Am. J. of Phys. Anthrop., **77**, (1988).

[65] T. F. Q. Iversen and Steen Grüner Hanson, ”Analysis of laser speckle patterns from fingertips”, Proc. SPIE, **7726**, (2010).

Appendix

In this appendix the AC signal amplitude of the voltage signals $V_{13}(t)$ and $V_{24}(t)$ illustrated in figures 5.10(B) and 5.11(B) is derived.
Consider a signal

$$g(t) = b + a\cos(2\pi f_D t), \tag{A1}$$

where a, f_D and b are real-valued constants. The oscillatory part is characterized by the cosine term and the amplitude (AC part) of the oscillation is a. The Fourier transform of eq. (A1) is given by

$$S(f) = b\delta(f) + \frac{a}{2}\delta(f + f_D) + \frac{a}{2}\delta(f - f_D). \tag{A2}$$

From eq. (A2) it is clear that the amplitude a can, for this particular case, be obtained from the positive (non-zero) frequency part of the spectrum, i.e.

$$AC\{g(t)\} \equiv a = 2\int_{-\infty}^{\infty} \Pi(f)S(f)df \ , \tag{A3}$$

Where

$$\Pi(f) = \begin{cases} 1, f > 0 \\ 0, \text{else} \end{cases}, \tag{A4}$$

The voltage signal $V(t)$ is obtained from $V(t) = R_e i(t)$, where $i(t)$ is given by eq. (5.39). The corresponding spectrum $S(f)$ is given by

$$\begin{aligned} S(f) = {} & \alpha R_e \left(A^2 P_i + P_{LO}\right)\delta(f) + \\ & \frac{\alpha R_e A\sqrt{P_i P_{LO}}}{2}\left[\delta(f + f_D) + \delta(f - f_D)\right] \end{aligned}. \tag{A5}$$

Performing the integration outlined by eq. (A3) yields

$$AC(v(t)) = 2\alpha A R_e \sqrt{P_i P_{LO}}\ \mathrm{Erf}\left(\frac{DHW\sqrt{2}}{w}\right)^2. \tag{A6}$$

A similar calculation as above can be carried out for the detector configuration illustrated in figure 5.11(B). The photocurrents obtained from the individual detectors are

$$i_1(t) = \alpha \int_{-DHW}^{DHW} \int_{-DHW}^{-DHW/2} I(p_x, p_y, t) dp_x dp_y , \tag{A7}$$

$$i_2(t) = \alpha \int_{-DHW}^{DHW} \int_{-DHW/2}^{0} I(p_x, p_y, t) dp_x dp_y , \tag{A8}$$

$$i_3(t) = \alpha \int_{-DHW}^{DHW} \int_{0}^{DHW/2} I(p_x, p_y, t) dp_x dp_y , \tag{A9}$$

$$i_4(t) = \alpha \int_{-DHW}^{DHW} \int_{DHW/2}^{DHW} I(p_x, p_y, t) dp_x dp_y , \tag{A10}$$

The voltage signal for the in-phase signal is given by $V_{13}(t) = R_e[i_1(t) - i_3(t)]$. Similarly, the voltage signal for the phase quadrature signal is given by $V_{24}(t) = R_e[i_2(t) - i_4(t)]$. Performing the integrations eq. (A7)-(A10), following the same procedure as above and simplifying, yields

$$AC\{V_{13}(t)\} = \alpha A R_e \sqrt{P_i P_{LO}} \exp\left(-\frac{\pi^2 w^2}{8DHW^2}\right) \operatorname{erf}\left(\frac{DHW\sqrt{2}}{w}\right) \times \left[\begin{array}{l} \operatorname{erf}\left(\frac{DHW\sqrt{2}}{w} + \frac{i\pi w}{2DHW\sqrt{2}}\right) - \operatorname{erf}\left(\frac{DHW}{w\sqrt{2}} - \frac{i\pi w}{2DHW\sqrt{2}}\right) - \\ \operatorname{erf}\left(\frac{DHW}{w\sqrt{2}} + \frac{i\pi w}{2DHW\sqrt{2}}\right) - \operatorname{erf}\left(\frac{i\pi w}{2DHW\sqrt{2}}\right) \end{array}\right] . \tag{A11}$$

Part II

Paper I

J. Opt. A: Pure Appl. Opt. **11** (2009) 054014 (6pp) doi:10.1088/1464-4258/11/5/054014

Investigation of an optical method for determining the average radius of curvature of micro-optical lenticular lens arrays

Theis F Q Iversen[1], **Steen G Hanson**[2] **and Peter Kirkegaard**[3]

[1] OPDI Technologies A/S, Frederiksborgvej 399, PO 49, 4000 DK-Roskilde, Denmark
[2] DTU Photonics, Department of Photonics Engineering, Frederiksborgvej 399, PO 49, 4000 DK-Roskilde, Denmark
[3] Risoe DTU, Department of Information Technology, Frederiksborgvej 399, PO 49, 4000 DK-Roskilde, Denmark

E-mail: ti@opdi-technologies.com

Received 30 September 2008, accepted for publication 23 January 2009
Published 18 March 2009
Online at stacks.iop.org/JOptA/11/054014

Abstract
Micro-optical elements are of great importance in areas of optoelectronics and information processing. Establishing fast, reliable methods for characterization and quality control of these elements is important in order to maintain the optical performance in a high volume production process. We investigate an optical technique, applied to a polymer-based, injection moulded, lenticular array, but the method is also applicable for the tooling for these elements. The cylindrical lenses have feature sizes of 1–15 μm. The method is based on observation of the intensity distribution, which can be obtained in the far field of surface reflections resulting from a plane wave incident on the lenticular array. The intensity distribution of the diffraction orders is highly correlated with the shape of the illuminated lenslets. This is exploited to attain information about possible defects and shape variations that have arisen in the moulding process. The experimental results are compared with a model, based on the Fraunhofer approximation to the Huygens–Fresnel principle. Furthermore, the optical elements under investigation are probed using a scanning probe microscope. Hence, access to accurate topological data of the elements is attained and used to confirm the validity of the proposed optical technique.

Keywords: lens array, diffraction pattern, surface topology

(Some figures in this article are in colour only in the electronic version)

1. Introduction

Micro-optical lens arrays (MLAs) are widely used in a variety of applications [1–3] and are of great importance in optical signal processing. Modern production techniques [4, 5] enable the manufacturing of high precision MLA structures. But, especially, commercial micro-machining of MLAs in combination with injection moulding techniques allow high volume output, and this raises new requirements for the process of quality assurance. The performances of MLAs are intrinsically linked to the geometrical parameters, such as periodicity of the lens array (pitch), radius of curvature (R), and aspherical parameters, as is the case for any optical component. Therefore, quality assurance becomes a matter of extracting the geometrical parameters of the MLA under investigation [7].

Due to the high production rate possible, the speed of the quality assurance process is of great importance. As a result of the requirement for high speed inspection, well-known methods for geometrical and topographical characterization

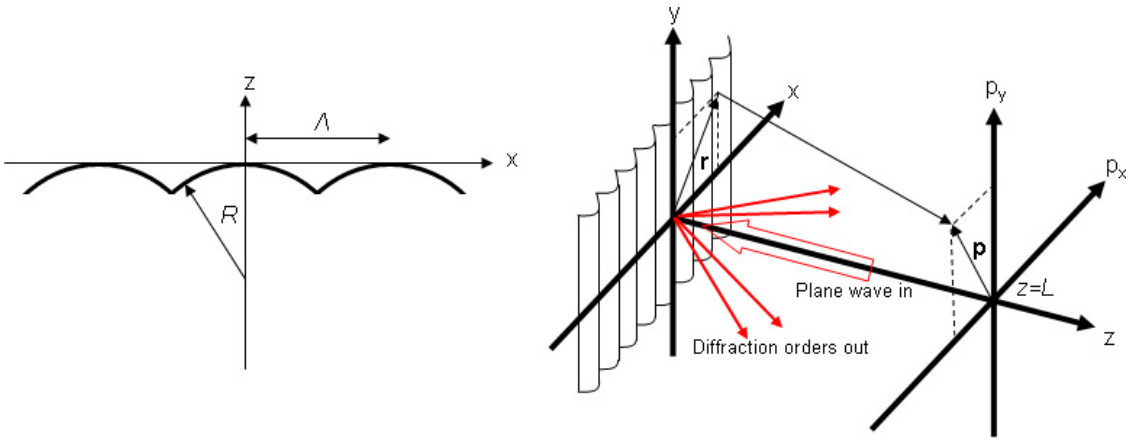

Figure 1. (Left) Cross-section of the cylindrical lens structure. (Right) Three-dimensional representation of the diffraction geometry connecting a point in the (x, y) plane to a point in the observation plane (p_x, p_y).

such as atomic force microscopy (AFM) or DEKTAK measurements become inapplicable.

We present a rugged, cheap, and potentially very fast optical technique for investigation of the average radius of curvature of a micro-optical cylindrical lens array. The simplicity and ruggedness of the method make it suitable for implementation in an industrial environment. The method is based on observation of the intensity distribution, which can be obtained in the far field of surface reflections from a plane wave incident on the MLA. The experimentally obtained data are compared with an analytical Fourier optical model, based on the Fraunhofer approximation to the Huygens–Fresnel principle.

To verify the validity of this optical method, the results obtained from experiments are compared with topographic data obtained using a DEKTAK scanning probe microscope.

2. Theory

We now calculate the reflected intensity distribution in the far field due to diffraction of a normally incident plane wave on a cylindrical lens array. We follow the methodology established for calculating Fraunhofer diffraction patterns in section 4.4 of [9].

First, the shape function $Z(x)$ of an individual cylindrical lenslet can be written as

$$Z(x) = -R + \sqrt{R^2 - x^2} = -\frac{x^2}{2R} - \frac{x^4}{8R^3} + \cdots. \quad (1)$$

Retaining only the first term of the expansion in (1), the phase function $P(x)$ due to the difference in path length across the aperture of an individual lenslet becomes

$$P(x) = \exp\left(\mathrm{i}\frac{4\pi}{\lambda}Z(x)\right) = \exp\left(-\mathrm{i}\frac{2\pi}{\lambda}\frac{x^2}{R}\right). \quad (2)$$

No phase perturbation is assumed along the y-direction. Note the factor of $4\pi/\lambda = 2k$ due to back-reflection of the plane wave. The higher-order terms of (1) are, for the time being, not considered.

To arrive at the field contribution from an individual lenslet, the phase function $P(x)$ is multiplied by the rectangular amplitude function $\mathrm{Rect}(x/\Lambda)$ which truncates the field at the lenslet extremities $x = \pm\Lambda/2$ in accordance with figure 1, where Λ is the period of the array. The field backscattered from a single lenslet within the array can then be written as

$$U_\Pi(\mathbf{r}) = U_{\mathrm{in}}(\mathbf{r})\mathrm{Rect}\left(\frac{x}{\Lambda}\right)P(x), \quad (3)$$

where $U_{\mathrm{in}}(\mathbf{r})$ is the field distribution of the incident probe beam, assumed here to be of the form

$$U_{\mathrm{in}}(\mathbf{r}) \propto \exp\left(-\frac{\mathbf{r}^2}{D^2}\right), \quad (4)$$

where D is the diameter of the beam illuminating the lens array. We will tacitly assume that $D \gg \Lambda$. Obviously, the expressions (3) and (4) are non-physical representations of the electrical fields in terms of spatial extent and energy content, but they are for the present of mathematical convenience and will have no influence on the final result. To obtain the Fraunhofer field distribution $U_{\mathrm{obs}}(\mathbf{p})$ in the observation plane $(\mathbf{p})$ at axial position $z = L$ we perform the following calculation based on the diffraction geometry defined in figure 1:

$$U_{\mathrm{obs}}(\mathbf{p}) = \frac{\exp(\mathrm{i}kL)\exp\left(\mathrm{i}k\frac{p^2}{2L}\right)}{\mathrm{i}\lambda L} \times \sum_{j=-\infty}^{\infty}\int_{-\infty}^{\infty} U_\Pi(\mathbf{r} - j\Lambda\hat{x})\exp\left(-\mathrm{i}\frac{2\pi}{\lambda L}\mathbf{r}\cdot\mathbf{p}\right)\mathrm{d}\mathbf{r}, \quad (5)$$

where j is the jth lenslet and $\hat{x}$ is the unit vector in the x-direction. The observed intensity distribution can now be obtained from

$$I_{\mathrm{obs}}(\mathbf{p}) = |U_{\mathrm{obs}}(\mathbf{p})|^2. \quad (6)$$

Figure 2(a) shows an example of the intensity distribution described by equation (6).

Figures 2(a) and (b) illustrate that the peak intensity of the diffraction orders can be evaluated using the envelope function

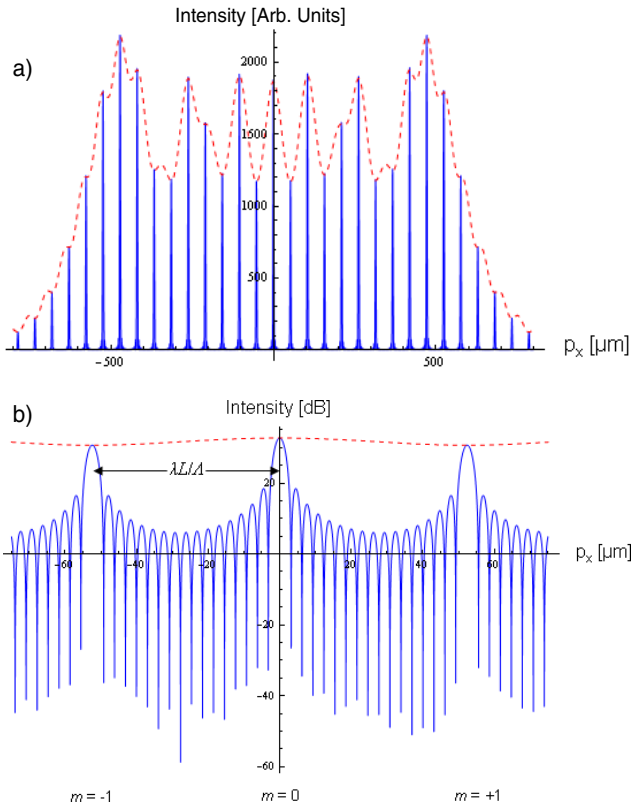

Figure 2. (a) The blue solid line (——) is the calculated intensity distribution for parameters $\lambda = 0.655\ \mu$m, $\Lambda = 12.5\ \mu$m, $R = 18\ \mu$m, $L = 1000\ \mu$m, $D = 250\ \mu$m and $p_y = 0$. The field is summed up over a total of 17 lenslets. The red dashed line (– – –) is the calculated intensity distribution, normalized to the peak intensity of (——) at $p_x = 0$, for the same set of parameters as the blue solid line but for only one lenslet, i.e. $j = 0$. This corresponds to an envelope function of the diffraction orders. (b) Enlargement of figure 2(a). The calculated intensity is displayed on a logarithmic scale. The separation of the individual orders is given by $\Delta p_x = m\lambda L/\Lambda$ and the width $(1/e^2)$ is given by $\sigma = \lambda L/D$.

$(j = 0) I_{\text{obs}}(m) = |U_{\text{obs}}(p_x)|^2$ letting $p_x \to m\lambda L/\Lambda$, m being the diffraction order. The peak intensity of a given diffraction order will be proportional to the power contained in that diffraction order under the assumption that the width of the diffraction orders is constant for all m. The peak field in the mth diffraction order can be calculated analytically, and we arrive at the following:

$$U_{\text{obs}}(m) \propto \exp\left(\frac{\mathrm{i}\pi m^2}{\xi}\right)\left\{\operatorname{erf}\left[\sqrt{\frac{\pi}{8\xi}}(1+\mathrm{i})(\xi - 2m)\right] + \operatorname{erf}\left[\sqrt{\frac{\pi}{8\xi}}(1+\mathrm{i})(\xi + 2m)\right]\right\}. \tag{7}$$

Here $\xi \equiv 2\Lambda^2/\lambda R$. Now the peak intensity in the mth diffraction order can be obtained by taking the absolute square of the field. To obtain the diffraction efficiency, we normalize with respect to the sum of the reflected peak intensities:

$$\eta_{\text{obs}}(m) = \frac{|U_{\text{obs}}(m)|^2}{\sum_m |U_{\text{obs}}(m)|^2}. \tag{8}$$

3. Experimental setup

The micro-optical lens array investigated here is part of a translation sensor system that in combination with a detector arrangement performs optical processing of speckle patterns [6]. The MLA structure is polymer based and is produced by injection moulding. The MLA consists of cylindrical lenses with $R \sim 18\ \mu$m arranged in an array with a periodicity of $\Lambda = 12.5\ \mu$m.

Figure 3 depicts the experimental setup. A diode laser with a wavelength of 655 nm produces a collimated output beam with ~2 mW of optical power. The polarization is directed along the y-axis. The MLA under investigation is placed in the focal plane of the focusing lens. The incoming

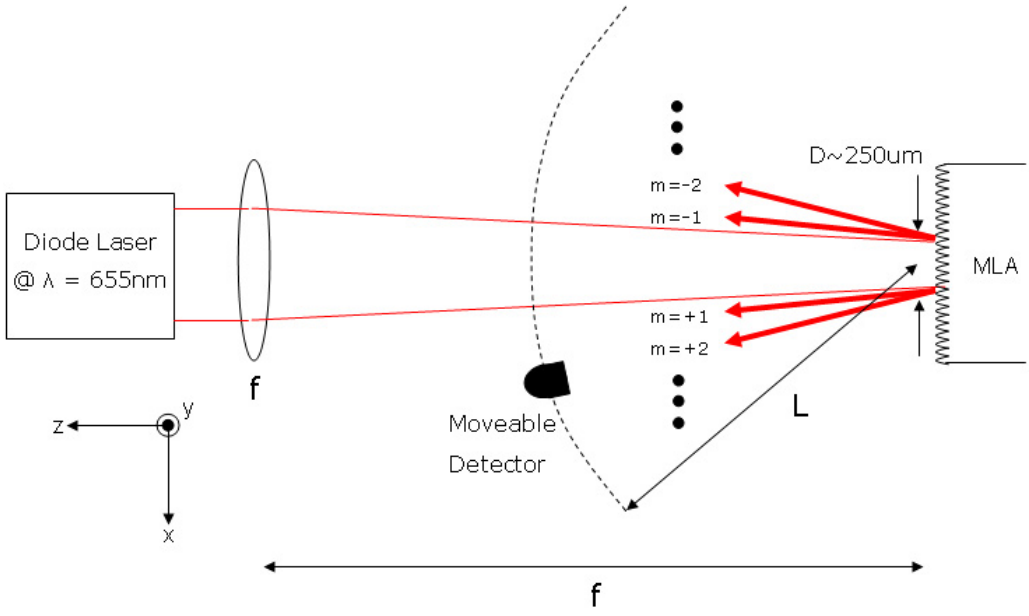

Figure 3. Schematic of the experimental setup.

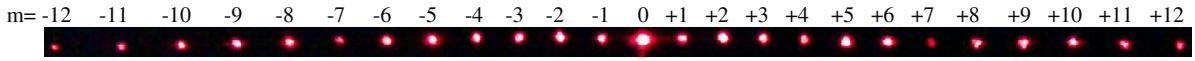

Figure 4. Image of the diffraction pattern, up to ±12th order, on a screen.

beam is focused by the lens to a beam of width $D \sim 250\ \mu$m. The beam is incident perpendicular to the MLA (in the plane of the figure) but slightly tilted out of plane, to allow measurement of the directly back-diffracted light (zero order). The diffracted intensity is collected with a swivel-mounted detector situated at a distance L from the optical unit. The distance L is selected to meet the requirements of the Fraunhofer diffraction regime, i.e. $L > kD^2/\pi$. In this case $kD^2/\pi \sim 20$ cm and L in this setup is ∼50 cm. In figure 4 an image of the diffraction pattern, projected onto a screen, is shown. The image in figure 4 was recorded with a camera.

4. Results

A single MLA structure was investigated. This particular MLA structure was manufactured with $\Lambda = 12.5\ \mu$m and an approximate (in principle unknown) radius of curvature of $R \sim 18\ \mu$m. The intensity distribution for this specific MLA structure was obtained and compared with the analytical second-order scalar diffraction theory developed in section 2. Furthermore, to investigate the validity of the optical method, a comparison with DEKTAK scanning probe data obtained from the specific MLA structure was performed.

In figure 5(a) the measured and the theoretically calculated diffraction efficiency are shown. An asymmetry about zero order can be observed in the measured data. This is due to an average asymmetric aberration of the lenslets in the measurement area that cannot be accounted for with the second-order analytical scalar theory. A measurement with the polarization of the illuminating beam aligned along the x-axis was performed. The observed diffraction efficiencies differed negligibly from the diffraction efficiencies obtained with the polarization along the y-axis. This suggests that vectorial effects are negligible, and that scalar wave theory is applicable at least for the polarization directed along the y-axis.

To relate the measured diffraction efficiencies to the average radius of curvature of the probed lenslets, the summed squared error (or SSE) is employed. The SSE value is calculated as

$$\mathrm{SSE} = \sum_m (\mathrm{Data}(m) - \mathrm{Theory}(m))^2. \qquad (9)$$

Here the summation includes the measured diffraction orders (m). The minimum value of the SSE is interpreted as the least-squares fit of the theory to the observed data. In figure 5(b) the calculated value of the SSE parameter is shown as a function of the radius of curvature for, first, the analytical second-order scalar diffraction theory based on (7) and (8), and second, a numerical calculation that incorporates the second (fourth-order) term in (1). It is observed that the minimum SSE value for the analytical scalar diffraction theory is 0.001 19, obtained at $R = 17.9 \pm 0.3\ \mu$m. Furthermore, it can be

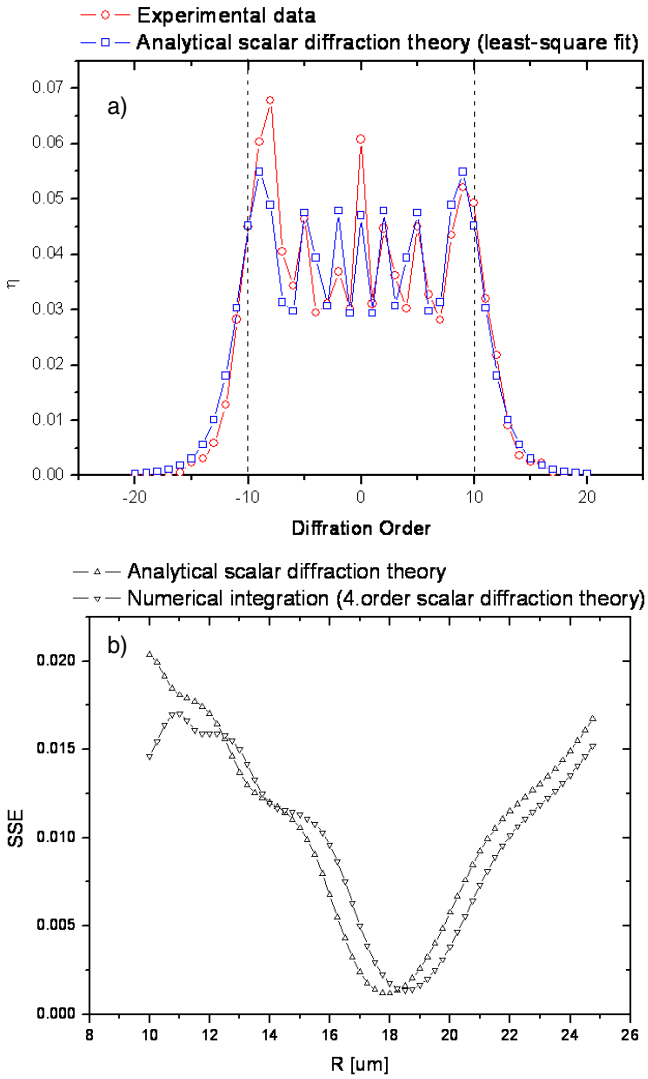

Figure 5. (a) The obtained experimental data (○) normalized according to (8) and the corresponding least-squares fit (□) of the analytical second-order scalar diffraction theory based on (7) and (8). The data are obtained with the polarization of the illuminating beam aligned along the y-axis (see figure 3). The vertical lines indicate the highest diffraction orders (∼±10), for which the paraxial approximation is valid [8]. (b) The summed squared error (SSE) between the experimental data and theory for a range of radii of curvatures. The plots show the SSE values for the second-order analytical scalar diffraction theory and the corresponding fourth-order scalar diffraction theory calculated by numerical integration.

observed that the minimum SSE value for the numerical fourth-order calculation is 0.001 39, obtained at $R = 18.5 \pm 0.3\ \mu$m. The uncertainties are estimated using interpolation.

The inclusion of higher-order terms in the expansion of the spherical profile of the lenslets leads to a higher calculated radius of curvature according to the numerical calculations of

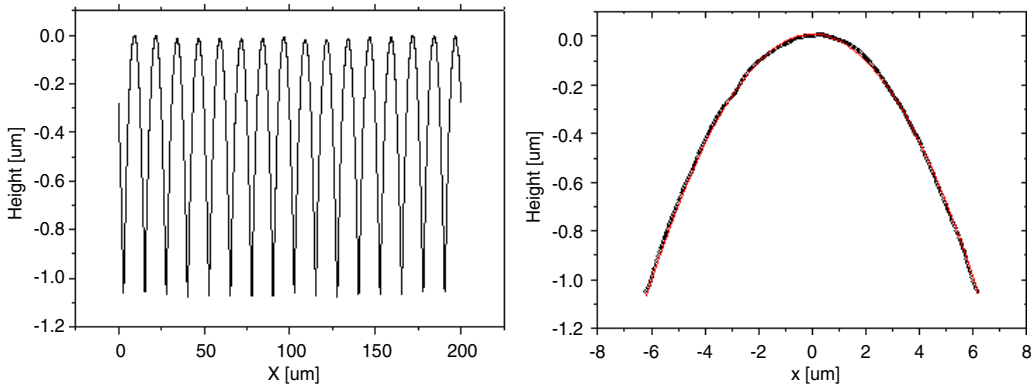

Figure 6. (Left) A 200 μm long scanning probe measurement along the x-axis of the MLA structure (note the difference between x and height). (Right) Selected data from the scan centralized about $x = 0$. This shows the shape profile of a single lenslet. The shape profile is fitted with a second-order polynomial (——).

Table 1. Comparison of the optical and the scanning probe method.

Analytical scalar theory (second order)	Scanning probe measurement (second-degree polynomial fit, average over 15 lenslets)
$R = 17.9 \pm 0.3$ μm $\mathrm{SSE}_{\mathrm{min}} = 0.001\,19$	$R = 18.0 \pm 0.1$ μm

figure 5. This is expected because the second-order scalar diffraction theory will in general underestimate the radius of curvature, in relation to a theoretical calculation that includes higher orders. The fourth-order scalar diffraction theory will give a more accurate estimate of the radius of curvature in terms of a spherical lenslet profile but will also be more time-consuming than a second-order calculation. The calculation time for the analytical second-order scalar diffraction theory is ∼6 times faster than the corresponding numerical integration in the current implementation.

4.1. Comparison with scanning probe measurements

To investigate the accuracy of the proposed optical method, the MLA structure investigated here was probed with a DEKTAK scanning probe microscope to attain accurate topographic data for comparison.

In figure 6 DEKTAK scanning probe data are shown. Table 1 shows a comparison of the calculated radius of curvature using, first, the optical method and, second, the scanning probe data. The radius of curvature calculated from the scanning probe data is derived using a second-degree polynomial fit to each individual lenslet probed in the scan and calculating R in accordance with the first term in (1). The average is the ensemble average (15 lenslets) of the calculated radius of curvature for each lenslet.

5. Conclusions

We have investigated an optical method for determining the average radius of curvature of an MLA structure given the pitch (Λ). Based on a parabolic approximation to the lenslet shape function, an analytical expression for the diffraction efficiency for each diffraction order, given the cylindrical geometry of the MLA structure, was derived. Thus, a direct parameterization of the diffraction efficiency as a function of the geometrical parameters of the MLA has been made available.

A comparison between the optical method and scanning probe measurements showed excellent quantitative agreement within the parabolic definition of the radius of curvature.

The method demonstrated here is not as such addressing high precision applications but is an alternative method to scanning probe methods for improvement in ruggedness, simplicity, and speed. These properties make the proposed method more suitable for automation than corresponding scanning probe measurements. Furthermore, the demonstrated method is only dependent on the MLA having a reflective surface. This means that it can be used on metallic MLA structures as well. This will benefit the control of a moulded specimen as compared to the mould, itself.

Acknowledgments

This work was partly supported by the Danish Council for Technology and Innovation under the Innovation Consortium Centre for Industrial Nano Optics (CINO).

References

[1] Jun A, Kawai H and Okano F 2006 Microlens arrays for integral imaging system *Appl. Opt.* **45** 9066–78
[2] Akatay A and Urey H 2007 Design and optimization of microlens array based high resolution beam steering system *Opt. Express* **15** 4523–9
[3] Matsuo S, Miyamoto T, Tomita T and Hashimoto S 2007 Application of a microlens array and a photomask to the laser microfabrication of a periodic photopolymer rod array *Appl. Opt.* **46** 8264–7
[4] Shi L, Du C, Dong X, Deng Q and Luo X 2007 Effective formation method for an aspherical microlens array based on an aperiodic moving mask during exposure *Appl. Opt.* **46** 8346–50
[5] Firestone G C and Yi A Y 2005 Precision compression molding of glass microlenses and microlens arrays—an experimental study *Appl. Opt.* **44** 6115–22
[6] Jakobsen M L and Hanson S G 2004 Micro-lenticular array for spatial-filtering velocimetry on solid surfaces *Meas. Sci. Technol.* **15** 1949–57

[7] Büttner A and Zeitner U D 2002 Calculation of the average lenslet shape and aberrations of microlens arrays from their far-field intensity distribution *Appl. Opt.* **41** 6841–8

[8] Siegman A E 1986 *Lasers* (Mill Valley, CA: University Science Books)

[9] Goodman J W 2005 *Introduction to Fourier Optics* (Englewood, CO: Roberts & Company)

Paper II

Meas. Sci. Technol. **21** (2010) 055301 (7pp) doi:10.1088/0957-0233/21/5/055301

Geometrical characterization of micro-optical cylindrical lens arrays using angular resolved diffraction

T F Q Iversen[1] **and S G Hanson**[2]

[1] OPDI Technologies A/S, Frederiksborgvej 399, PO 49, 4000 DK, Roskilde, Denmark
[2] DTU Fotonik, Department of Photonics Engineering, Frederiksborgvej 399, PO 49, 4000 DK, Roskilde, Denmark

E-mail: ti@opdi-technologies.com

Received 15 January 2010, in final form 4 March 2010
Published 13 April 2010
Online at stacks.iop.org/MST/21/055301

Abstract
The versatility of micro-optical lens arrays (MLA) is giving rise to many new applications often to be included in mass-produced parts and systems. The need for fast and robust methods of characterization and quality control, addressing an industrial manufacturing environment, is evident. It has been shown (Iversen *et al* 2009 *J. Opt. A: Pure Appl. Opt.* **11** 054014 (6pp), Büttner and Zeitner 2002 *Appl. Opt.* **41** 6841–8) that the average radius of curvature of an MLA structure can be extracted by observing the far-field diffraction pattern intensity distribution obtained from illumination of the MLA structure with a coherent light source. This method is based on *a priori* knowledge of the grating period. We here present a method that fully characterizes the geometrical properties, i.e. the grating period and the average radius of curvature of an MLA structure in a single measurement cycle. By scanning the angle of incidence of the coherent illumination and simultaneously observing the diffracted intensity, information about the grating period and the radius of curvature can be extracted. The method is implemented with emphasis on further development for compact, high-speed dedicated systems. We present experimental data extracted from two different MLA structures using the proposed method. The results are compared with atomic force microscopy measurements of the MLA geometry.

Keywords: lens array, diffraction pattern, surface topology

(Some figures in this article are in colour only in the electronic version)

1. Introduction

Micro-optical lens arrays are used in a wide selection of applications, ranging from imaging and illumination to optical signal processing [3–5]. Equally diverse are the manufacturing methods of many common and specialized MLA structures [6–8]. The functionality of most MLA structures is defined by three geometrical parameters: the fill factor, the radius of curvature and the grating period.

In this paper we investigate a one-dimensional (cylindrical) lens array with a fill factor of 1. The geometry is shown in figure 1. We denote the grating period as Λ and the radius of curvature as R, both defined as average values over the measured area.

Furthermore, the sag or height of the lenslet profile can be defined as $h(x)$, given by

$$h(x) = -R + \sqrt{R^2 - x^2} \qquad \text{for} \quad |x| \leqslant \frac{\Lambda}{2}. \tag{1}$$

The MLA structure under investigation here is an injection-moulded polymer with a refractive index of 1.65. The mould master is manufactured using a ruling technique that utilizes diamond tooling with a precision profile (in this case circular, i.e. with fixed radius of curvature) and high precision micro-machining equipment. The lateral (x, y) tool positioning using

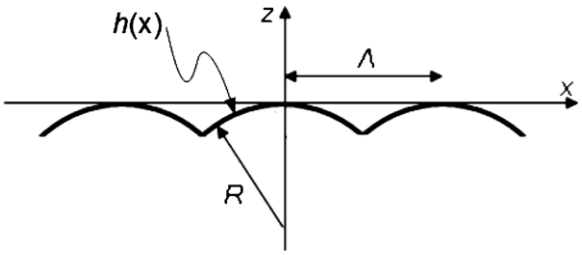

Figure 1. The one-dimensional geometry of the MLA structure.

this equipment is accurate to within 3 μm over a 200 mm range. Each lenslet is formed by a *single* ruling assuring that every lenslet has the exact same profile yielding a highly reproducible radius of curvature given that the same tool is used to fabricate all lenslets in the array of the master mould. This technique makes it possible to attain practically unity fill factor by controlling the tool depth in the ruling process. However, any deviations in the tool profile from the desired profile will also appear in the mould master. The industry term 'waviness' corresponds to the maximum peak–peak error in the cutting tool profile and is a measure of these deviations. The waviness profile of the cutting tool and subsequently the mould master will generally be transferred as aberrations to the lenslet profiles of the injection-moulded optical elements if the moulding process is complete, i.e. if the moulding material completely fills the mould master. The mould masters are fabricated in nickel-plated steel and were manufactured by Kaleido Technology A/S and the injection moulding of the MLA structures was performed by Kühn A/S using specialized micro-moulding equipment.

The manufacturing of high precision master moulds is a key issue but only for the first part of the process. Careful monitoring of the injection moulding process parameters (i.e. pressure, temperature, etc) ensures high quality of the finished optical elements, while wear of the master mould in a mass production context will ultimately degrade the quality. It is therefore important to have an *in situ* monitoring method to continuously ensure the quality of the optical elements. Very high production rates can be achieved with the injection moulding technique (tens of units per second) and therefore the method of characterization has to accommodate this. This condition rules out the use of scanning probe methods. Although a high measurement precision (∼1 nm) can be attained, alignment, scan time and robustness leave it too slow for this type of application. Furthermore, scanning probe instrumentation like DEKTAK can scratch and damage the surface due to the force of the stylus application. Optical methods on the other hand are non-contacting and will not damage the surface of the elements and are potentially very fast.

2. Theory

We derive the backscattered intensity distribution in the far field of a plane wave incident at an angle α on a cylindrical lenticular lens array. The diffraction geometry is shown in figure 2.

The field incident $U_i(\mathbf{r})$ on the array is assumed to be plane and represented in the following form:

$$U_i(\mathbf{r}) \propto \exp\left[-\frac{\mathbf{r}^2}{D^2} - \mathrm{i}k\sin(\alpha)x\right], \tag{2}$$

where D is the spatial extent of the field assumed to be $D \gg \Lambda$, and the complex factor represents the incident phase front due to the angle of incidence. In this particular case the plane of incidence is selected to be x–z in accordance with figure 2(b). The height profile of an individual lenslet is modelled as a parabolic profile irrespective of the incidence angle α. This is a valid approximation only in the case of a cylindrical lenslet profile as the phase perturbation does not change with angle, i.e.

$$h(x) = -\frac{x^2}{2R}. \tag{3}$$

The corresponding phase perturbation for the backscattered field can then be written as

$$P(x) = \exp\left[-2\mathrm{i}kh(x)\right] = \exp\left[\mathrm{i}k\frac{x^2}{R}\right]. \tag{4}$$

The full field distribution in the observation plane is given by

$$U_{\mathrm{obs}}(\mathbf{p}) = \frac{-\mathrm{i}k\exp(\mathrm{i}kL)\exp\left[\mathrm{i}k\frac{\mathbf{p}^2}{2L}\right]}{2\pi L}\sum_{j=-\infty}^{\infty} \times \int_{j\Lambda-\Lambda/2}^{j\Lambda+\Lambda/2} U_i(\mathbf{r})P(x - j\Lambda\hat{x})\exp\left[-\frac{\mathrm{i}k}{L}\mathbf{r}\cdot\mathbf{p}\right]\mathrm{d}\mathbf{r}. \tag{5}$$

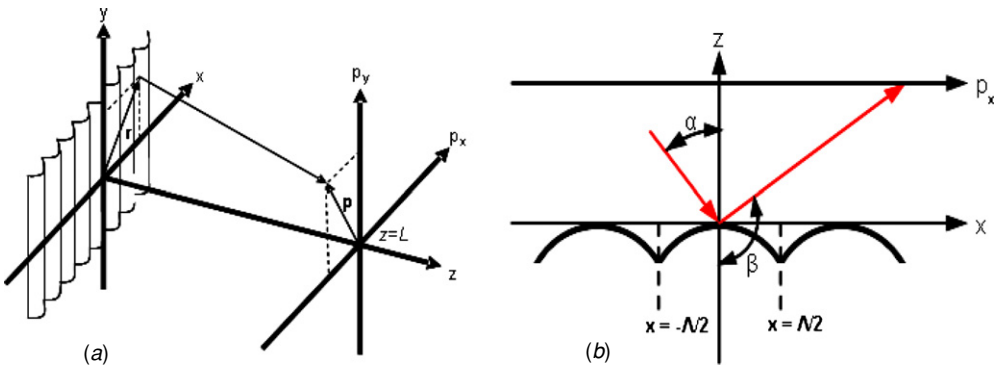

Figure 2. (a) Three-dimensional representation of the diffraction geometry connecting a point in the (x, y) plane to a point in the observation plane (p_x,p_y). (b) Cross-section of the cylindrical lens structure illustrating the diffraction geometry and the angle of incidence α.

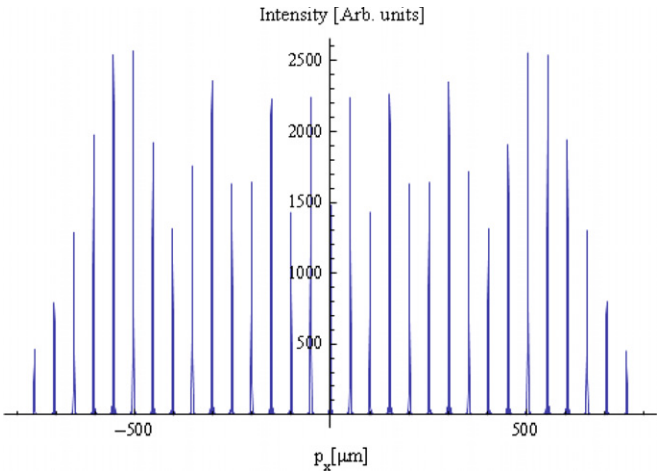

Figure 3. Theoretical intensity distribution for the parameters $\alpha = 0$, $D = 200$ μm, $L = 1$ mm, $\Lambda = 13$ μm, $R = 17$ μm, $\lambda = 0.655$ μm and $N = 21$, N being the number of lenslets contributing to the intensity distribution.

The limits of the integral account for the aperture function of the jth lenslet, and the convolution sum takes the array structure into account where $\hat{x}$ is the unit vector along the x-direction. The corresponding intensity distribution can be found from

$$I_{\text{obs}}(\mathbf{p}) = |U_{\text{obs}}(\mathbf{p})|^2 . \tag{6}$$

Figure 3 shows the intensity distribution $I_{\text{obs}}(p_x, 0)$ for a set of typical parameters.

As a matter of fact, the full intensity distribution of the diffraction orders and their fine structure are of little interest. However, the integrated intensity, i.e. the power contained in each diffraction order, is the information of interest and the quantity that will be measured in the experiment. It will be assumed that there exists a linear relationship between peak intensity and the power contained in each and all diffraction orders [1]. Based on this assumption, an expression that relates the peak intensity to the corresponding diffraction order can be derived. To do so, the condition for constructive interference in the far field is considered, cf [9]:

$$\Lambda\,(\sin(\alpha) - \sin(\beta)) = \frac{2\pi m}{k}. \tag{7}$$

When $\beta = \pi + \alpha$, expression (7) reduces to

$$\sin(\alpha) = \frac{\pi m}{\Lambda k}. \tag{8}$$

Evaluating the amplitude distribution at position $p_y = 0$, $p_x = L\sin(\alpha)$ and rearranging the following is obtained:

$$U_{\text{obs}}(m) \propto \exp\left(\frac{\mathrm{i}\pi m^2}{\xi^2}\right)\left\{\operatorname{erf}\left[\sqrt{\frac{\pi}{8\xi}}\,(1+\mathrm{i})\,(\xi - 2m)\right] + \operatorname{erf}\left[\sqrt{\frac{\pi}{8\xi}}\,(1+\mathrm{i})\,(\xi + 2m)\right]\right\}. \tag{9}$$

where $\xi \equiv k\Lambda^2/\pi R$. Upon closer inspection, it is observed that expression (9) is identical to the result obtained in [1]. The expression gives the peak amplitude of each diffraction order m when $\beta = \pi + \alpha$, i.e. in the directly backscattered direction.

Table 1. Design parameters of the MLA structures.

	Λ	R
MLA1	13 μm	17 μm
MLA2	15 μm	18 μm

To obtain the diffraction efficiency of each diffraction order, we normalize to the total reflected intensity:

$$\eta(m) = \frac{I_{\text{obs}}(m)}{\sum_m I_{\text{obs}}(m)}. \tag{10}$$

The relationship (8) can be rearranged to express the grating period Λ, given the angle of diffraction for order m

$$\Lambda = \frac{\pi m}{k\sin(\alpha_m)}, \tag{11}$$

where α_m is the angle of diffraction of the mth order. This relationship will later be utilized to experimentally extract the grating period.

3. Experiments

We investigate two different MLA structures, addressed here as MLA1 and MLA2. Each MLA structure is unique both in the geometrical parameters (Λ and R) and in the waviness profile given that the mould masters were fabricated using different cutting tools. The design parameters associated with the MLA structures are stated in table 1.

We stress that the design parameters in table 1 are the desired parameters from the manufacturing point of view and only serve as approximate parameters in the following. We present experimental data from both diffraction experiments based on the theory presented in section 2 and as a comparative study we also present experimental data obtained using the atomic force microscope at Danish Fundamental Metrology A/S that directly measures the lenslet profiles, although only over a limited spatial extent.

The experimental setup is illustrated in figure 4.

Measurement of the spot size formed by the focussing lens revealed that approximately 25–30 lenslets are probed by the beam in this configuration. Only s-polarized light is considered here, i.e. the polarization of the incoming beam is polarized perpendicular to the plane of incidence.

In order to make a full characterization of the MLA structure it is necessary to measure the grating period as well as the radius of curvature of the lenslet profiles. By rotating the MLA structure and simultaneously measuring the angle of rotation and the back-reflected power, it is possible to derive the grating period from the angle of rotation, and the radius of curvature from the diffracted power contained in the diffraction orders. This means that the measurement cycle is only a one-step process, but the calculation is a two-step process involving firstly the calculation of the grating period and secondly the calculation of the radius of curvature given the grating period and diffraction efficiency of each order.

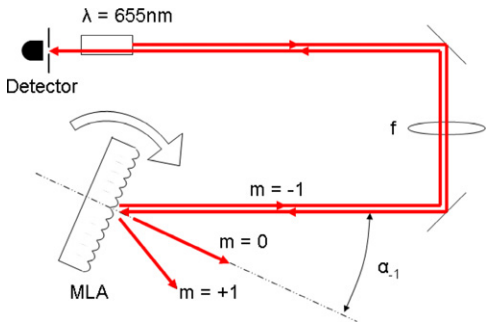

Figure 4. Experimental setup. A collimated diode laser lasing at a wavelength of $\lambda = 655$ nm is focused by a lens and the MLA structure is positioned in the focal plane of the lens. The MLA structure itself is mounted on the axis of rotation of a high precision rotational stage. The directly backscattered light is propagated back through the optical system and detected by an arrangement of a detector and slit aperture. The detector arrangement is in reality positioned just below the laser output aperture and the MLA structure is very slightly tilted to allow detection of the backscattered light. The overall distance between the detector and MLA is $L \sim 110$ cm and the detector is positioned $\sim$1 cm below the source.

3.1. Measurement of the grating constant

The grating period can be calculated using the condition for constructive interference in the far field given by (11). The accuracy of the measurement is highly dependent on the accurate measurement of the angle α_m. Bias and offset effects in the readout of the angle will impact accuracy, especially for small angles. Moreover, the slit aperture also limits the accuracy of the angle measurement due to the need to have an aperture dimension that will accommodate the integration of the entire intensity field of the spot pattern to yield an accurate estimate of the power. However, measurements based on simply maximizing the detected power through a fixed aperture have shown that angular alignment can be attained to within $1/60^\circ$, equal to the resolution of the rotational stage used here. This approach assumes that beam profiles of the diffracted light are symmetric in intensity around the true diffraction angle, which is a reasonable assumption based on experimental observations. More sophisticated methods of angular measurement and alignment can be implemented, but this approach is sufficient for the purposes of this paper.

Table 2. Average measured grating period.

MLA1	MLA2
$12.91 \pm 0.06\ \mu$m	$14.86 \pm 0.04\ \mu$m

In figure 5 the derived grating periods of MLA1 and MLA2 are shown for all orders of diffraction.

It is evident from figure 5 that the calculated grating period based on the measurement of the angle of diffraction is non-uniform over the range of diffraction orders considered. This non-uniformity is most dominant for small orders of diffraction where the angles are also small. The average of the measurements is summed up in table 2

3.2. Measurement of the radius of curvature

The measurement of the radius of curvature is based on *a priori* knowledge of the grating constant and the measured diffraction efficiency for each diffraction order.

In order to compare the theory presented in section 2 with the experimental data we define the summed squared error (SSE) value as

$$\mathrm{SSE} = \sum_m (\mathrm{Data}(m) - \mathrm{Theory}(m))^2, \qquad (12)$$

where m is the diffraction order. The minimum SSE value is interpreted as the best fit between the experimental data and the theory. In figures 6 and 7 experimental data obtained from both MLA 1 and 2 are shown alongside the best fit theoretical model. The calculation of the radius of curvature is based on the previously measured grating constant obtained from the angles of diffraction. Using equations (9) and (10) derived in section 2 as the theoretical model, a series of SSE values for different radii of curvature is calculated and the radius of curvature associated with the minimum SSE value obtained is interpreted as the measured value.

In table 3 the measured radius of curvature values are listed with the design parameters in parenthesis.

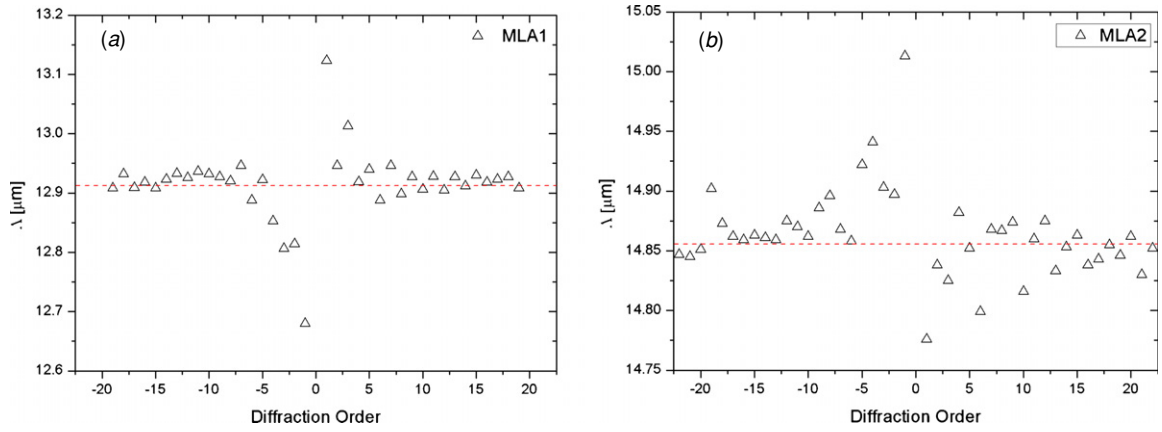

Figure 5. Measured grating periods of MLA1 (*a*) and MLA2 (*b*).

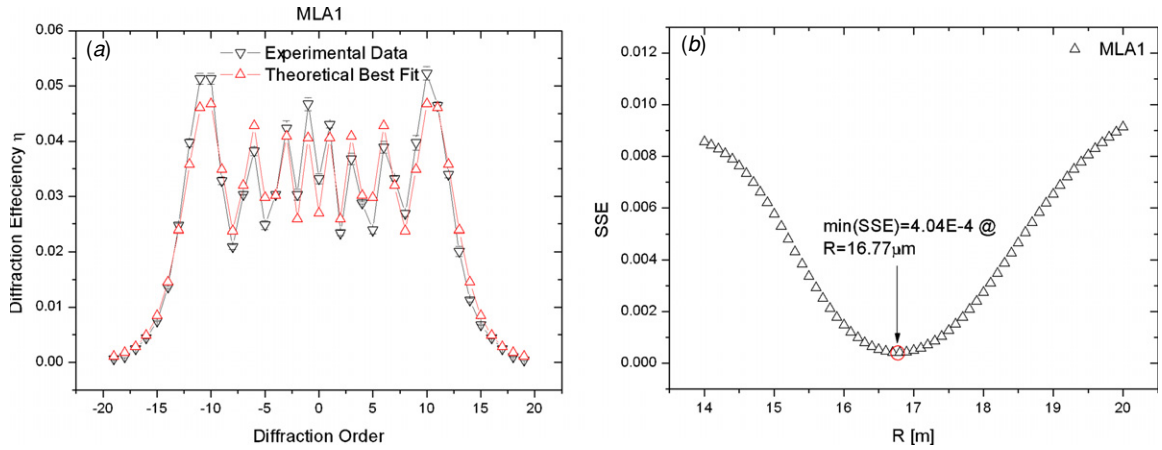

Figure 6. Experimental data obtained from MLA1 and comparison with theory. (*a*) Measured diffraction efficiency and the corresponding theoretical model associated with parameters $\Lambda = 12.91$ μm and $R = 16.8$ μm. The data points in the measurement plot are the average of three measurements. The error bars indicate the standard deviation associated with the measurement. (*b*) Summed squared error (SSE) values for a range of radii of curvature at fixed grating constant $\Lambda = 12.91$ μm that was measured by the diffraction method described above. In this case the minimum SSE value was attained at $R = 16.8$ μm.

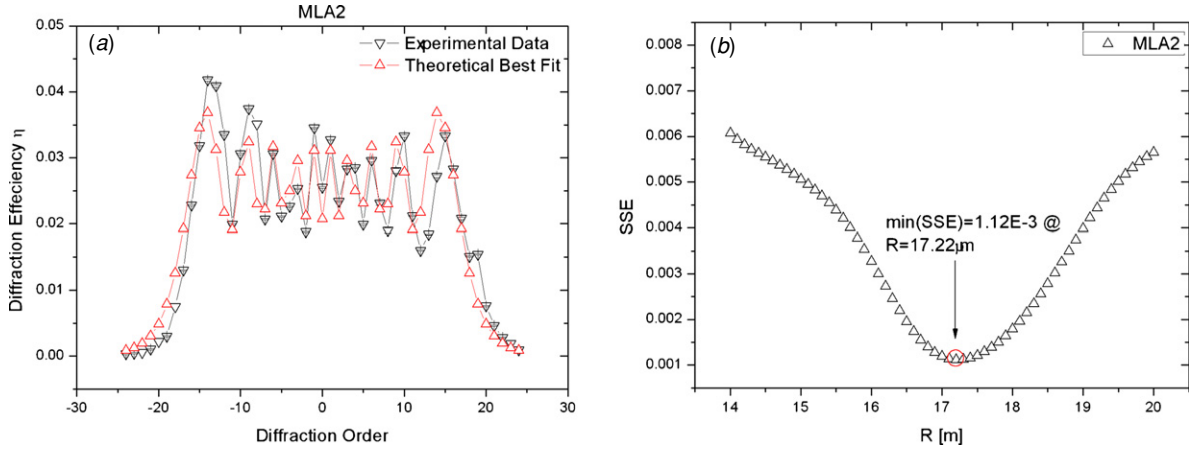

Figure 7. Experimental data obtained from MLA2 and comparison with theory. (*a*) Measured diffraction efficiency and the corresponding theoretical model associated with parameters $\Lambda = 14.86$ μm and $R = 17.2$ μm. The data points in the measurement plot are the average of three measurements. The error bars indicate the standard deviation associated with the measurement. (*b*) Summed squared error (SSE) values for a range of radii of curvature at a fixed grating constant $\Lambda = 14.86$ μm that was measured by the diffraction method described above. In this case the minimum SSE value was attained at $R = 17.2$ μm.

Table 3. Measured radius of curvature R.

MLA1	MLA2
16.8 μm (17 μm)	17.2 μm (18 μm)

3.3. Atomic force microscopy measurements

For the purpose of comparison measurements of the lenslet profiles have been conducted using an atomic force microscope. This specific atomic force microscope has a stationary tip mount and a moving sample stage that is positional monitored with an interferometric setup. This allows for very long scans (∼500 μm) with very high precision (∼1 nm).

In figures 8 and 9 sample scans are shown with an extract of a representative lenslet profile from each full scan.

Data from two different regions separated by 100 μm on each of the MLA structures were obtained. From each region, three line scans in the x direction were made (see figure 2 for reference). Each of the line scans was ensured to have the same starting position in the x direction but each displaced by 1 μm in the y direction with respect to the latter. Each of the individual lenslet profiles was extracted and fitted with a parabola. The compiled data are listed in tables 4 and 5. The number N is the number of lenslets that comprises the ensemble over which the average value and standard deviation are calculated.

The tip used in the measurements presented here has a guaranteed tip radius of 5 nm or better, and a tip angle of 10° up to a tip height over the apex of 200 μm. Simple calculations based on the geometrical characteristics of the tip and the approximate lenslet structure show that errors due to the finiteness of the tip geometry are on the order of or less

Table 4. Geometric parameters compiled using atomic force microscopic measurements of MLA1.

	Region 1			Region 2		
Λ (μm)	12.91 ± 0.04	12.91 ± 0.05	12.91 ± 0.05	12.91 ± 0.03	12.91 ± 0.03	12.91 ± 0.04
R (μm)	16.98 ± 0.06	16.99 ± 0.07	16.98 ± 0.05	16.94 ± 0.06	16.93 ± 0.06	16.92 ± 0.06
N	29	27	28	28	25	28

Table 5. Geometric parameters compiled using atomic force microscopic measurements of MLA2.

	Region 1			Region 2		
Λ (μm)	14.89 ± 0.04	14.88 ± 0.05	14.88 ± 0.04	14.88 ± 0.05	14.88 ± 0.04	14.88 ± 0.04
R (μm)	18.02 ± 0.12	18.05 ± 0.11	18.06 ± 0.11	18.10 ± 0.12	18.09 ± 0.14	18.10 ± 0.18
N	24	24	24	24	24	24

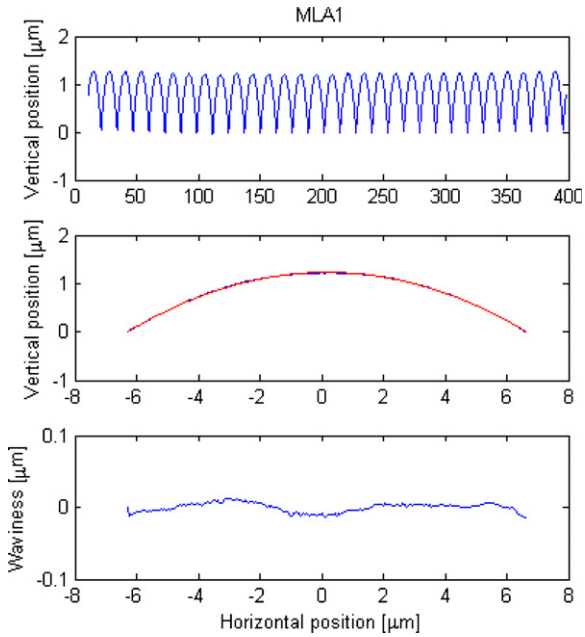

Figure 8. AFM data obtained from MLA1. The full scan (top) and a representative single lenslet profile extracted from the full scan and fitted with a parabolic profile (middle). The extracted waviness profile based on the parabolic fit (bottom). The waviness based on the parabolic profiled was determined to be 0.0267 μm.

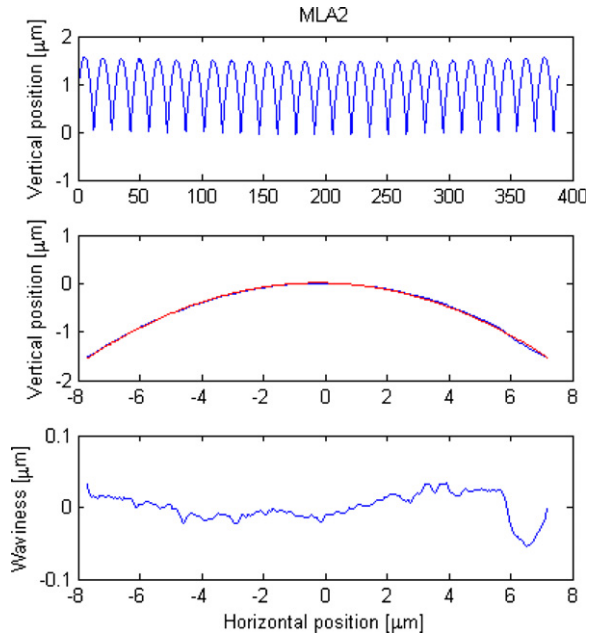

Figure 9. AFM data obtained from MLA2. The full scan (top) and a representative single lenslet profile extracted from the full scan and fitted with a parabolic profile (middle). The extracted waviness profile based on the parabolic fit (bottom). The waviness based on the parabolic profile was determined to be 0.0876 μm

than $\sim$1 nm in both vertical and horizontal scan directions. Thus, such effects can safely be disregarded in this context. Analysis of positional shifts of identifiable features from the three closely spaced line scans from each of the two regions revealed that the angle formed by the horizontal scan direction and the grating lines was perpendicular to within 3°. This was the case for both the MLA1 and MLA2 datasets. The resulting measurement error of the grating period from this effect is on the order of 0.1% and thus negligible in comparison with the statistical fluctuations observed in the data samples.

4. Discussion

The data obtained using the atomic force microscope reveal a highly accurate and coherent array structure in terms of grating constant and radius of curvature. This is especially true for MLA1. On comparison with the results obtained using the diffraction method it is evident that the measurement of the grating constant is comparable to the AFM measurements both in terms of accuracy and uncertainty. However, it is clear that a discrepancy exists when comparing the radius of curvature extracted using the two different methods. It seems that the diffraction method will underestimate the radius of curvature slightly. However, the error is within 5% in both cases. The slight tilt of the optical element introduced to allow the measurement of the diffracted intensity is indeed a source of this type of error, but calculations show that under the specific conditions investigated here the contribution is negligible in comparison with the observed error. It must also be taken into account that the profiles of the lenslet are not perfectly cylindrical but contain asymmetries that cannot be accounted for with the proposed theory. This is especially evident in the case of MLA2 given the waviness profile (figure 9 (bottom)) and the diffraction pattern obtained (figure 7(*a*)). Comparing this with the corresponding data from MLA1 it is evident that this waviness profile

(figure 8 (bottom)) and diffraction pattern (figure 6(*a*)) correspond much better with a cylindrical profile. This is also reflected in the extracted radius of curvature using the diffraction method that only deviates from the AFM measurements by ∼1% in this case.

The method proposed here is an attempt to address the need for fast, non-invasive and rugged characterization techniques for cylindrical lens arrays that fully map the geometry (i.e. both the radius of curvature and the grating constant) of the lenslets in the probe beam. However, the basic approach also suggests applicability to two-dimensional arrays, i.e. spherical lens arrays. More complex lens shapes such as acylindrical profiles require an extension of the theory, specifically accounting for the angular dependence of the height function across the lenslet aperture with regard to the angle of incidence of the probe beam, and this is beyond the scope of this work.

By incorporating a rotation to the optical element under investigation, the need for a moving detector, as proposed by the authors [1], is eliminated. This means that both the source and the detector can be fixed in relation to one another. Mechanically such a setup is more stable in terms of alignment and more easily implemented and maintained. Furthermore, this facilitates measurement of the grating period from the diffraction angles, while the power of the corresponding order is measured simultaneously thus decreasing the measurement cycle time and the need for a separate method for measuring the grating period. Although the measurement cycle time will be highly dependent on the specific implementation and cannot be accurately assessed in the setup described here, a rough estimation can be made considering the limiting aspects of the setup mechanics, data acquisition and data processing. Considering this and various available technologies it is estimated that the duration of a single measurement cycle of a future dedicated system can be below 1 s.

It could be argued that any asymmetry in the measured diffraction patterns would be an indicator of poor lens quality in any case. Furthermore, given that the method proposed works by reflection, a sample or 'master' diffraction pattern could be obtained from the mould master and used as a reference for comparison in a subsequent production of the optical lens arrays themselves. In this way, an extremely high reproducibility and homogeneity will be possible due the high sensitivity of the diffraction pattern to reveal defects in the lens profiles. Defects can both arise from fluctuations in the manufacturing process and be intrinsically introduced by the tool that manufactured the master mould itself. Furthermore, the reflection configuration of the proposed method also renders it largely independent of the refractive index of the sample, given the conditions investigated here, and thus widening the scope of application.

5. Conclusion

We have demonstrated a method that fully characterizes a cylindrical lens array in terms of grating constant and radius of curvature in a single measurement cycle. By introducing a rotation to the optical element under investigation, keeping the source and detector fixed, an in-line setup is achieved that is well suited for a compact and high-speed dedicated system. In terms of precision, the method presented here performed comparably to an atomic force microscopic measurement in determining the grating constant and determined the radius of curvature to within 1% and 5% of the AFM measurements based on two entirely different MLA structures.

Acknowledgment

This work was partly supported by the Danish Council for Technology and Innovation under the Innovation Consortium Centre for Industrial Nano Optics (CINO).

References

[1] Iversen T F Q, Hanson S G and Kirkegaard P 2009 Investigation of an optical method for determining the average radius of curvature of micro-optical lenticular lens arrays *J. Opt. A: Pure Appl. Opt.* **11** 054014

[2] Büttner A and Zeitner U D 2002 Calculation of the average lenslet shape and aberrations of microlens arrays from their far-field intensity distribution *Appl. Opt.* **41** 6841–8

[3] Jun A, Kawai H and Okano F 2006 Microlens arrays for integral imaging system *Appl. Opt.* **45** 9066–78

[4] Akatay A and Urey H 2007 Design and optimization of microlens array based high resolution beam steering system *Opt. Express* **15** 4523–9

[5] Jakobsen M L and Hanson S G 2004 Micro-lenticular array for spatial-filtering velocimetry on solid surfaces *Meas. Sci. Technol.* **15** 1949–57

[6] Matsuo S, Miyamoto T, Tomita T and Hashimoto S 2007 Application of a microlens array and a photomask to the laser microfabrication of a periodic photopolymer rod array *Appl. Opt.* **46** 8264–7

[7] Shi L, Du C, Dong X, Deng Q and Luo X 2007 Effective formation method for an aspherical microlens array based on an aperiodic moving mask during exposure *Appl. Opt.* **46** 8346–50

[8] Firestone G C and Yi A Y 2005 Precision compression molding of glass microlenses and microlens arrays—an experimental study *Appl. Opt.* **44** 6115–22

[9] Born M and Wolf E 2006 *Principles of Optics* 7th edn (Cambridge: Cambridge University Press)

Paper III

Speckle-based three-dimensional velocity measurement using spatial filtering velocimetry

Theis F. Q. Iversen,[1,*] Michael L. Jakobsen,[2] and Steen G. Hanson[2]

[1]OPDI Technologies A/S, Frederiksborgvej 399, 4000 Roskilde, Denmark

[2]DTU Fotonik, Department of Photonics Engineering, Technical University of Denmark, P.O. Box 49, DK-4000, Roskilde, Denmark

*Corresponding author: ti@opdi-technologies.com

Received 5 November 2010; accepted 10 January 2011;
posted 24 January 2011 (Doc. ID 137798); published 1 April 2011

We present an optical method for measuring the real-time three-dimensional (3D) translational velocity of a diffusely scattering rigid object observed through an imaging system. The method is based on a combination of the motion of random speckle patterns and regular fringe patterns. The speckle pattern is formed in the observation plane of the imaging system due to reflection from an area of the object illuminated by a coherent light source. The speckle pattern translates in response to in-plane translation of the object, and the presence of an angular offset reference wave coinciding with the speckle pattern in the observation plane gives rise to interference, resulting in a fringe pattern that translates in response to the out-of-plane translation of the object. Numerical calculations are performed to evaluate the dynamic properties of the intensity distribution and the response of realistic spatial filters designed to measure the three components of the object's translational velocity. Furthermore, experimental data are presented that demonstrate full 3D velocity measurement. © 2011 Optical Society of America

OCIS codes: 030.1640, 120.7250, 030.1670, 030.6140, 030.6600.

1. Introduction

The application of laser speckle patterns to measure in-plane motion of diffuse objects is well established in the literature and includes a multitude of methods. Methods such as speckle photography (SP) and electronic SP (ESP) [1] have been applied successfully to measure in-plane displacement fields of an imaged object under load. The related approach of speckle interferometry (SPI/ESPI) combines the speckle pattern with a reference wave incident on the image plane under an angle in order to measure the out-of-plane displacement by fringe analysis [2]. Furthermore, these two techniques have been combined partly to enhance the fringe analysis in applications where large in-plane displacements are considered and partly to measure a full three-dimensional (3D) displacement field [3]. However, these techniques are full-field measurements acquired by a digital camera or conventional photography. Therefore, they are limited by the fringe analysis to measure out-of-plane displacements on the order of a few wavelengths and are particularly not well suited for real-time studies and velocimetry.

Recently [4], it has been demonstrated that speckle patterns propagated in free space in combination with a conventional in-line Michelson interferometer realize single-point measurement of 3D displacement. However, this method will not be able to distinguish between translation and rotation of the object.

Another method that is dedicated to measure out-of-plane velocity is coherent Doppler lidar [5,6]. Here, the out-of-plane displacement is limited by the focal depth of the imaging system (typically on

0003-6935/11/111523-11$15.00/0

the order of a meter), and particle velocities on the order of several meters per second are measured in real time. Work has been carried out to measure small in-plane velocity components [7,8] in these types of systems. However, the implementations are inherently single mode in the spatial domain, and all spatial information in the image plane is discarded. The same type of system can be modified to include the dynamic speckle field in the image plane and, under certain circumstances, can be used to measure in-plane motion [9].

We investigate, by means of numerical calculations and experiments, the use of an imaging system to form an image of an area of a diffusely scattering rigid object illuminated by a coherent light source. The speckle pattern that arises in the image plane is combined with a coherent reference wave that coincides with the speckle image under an angle. The resulting intensity distribution will exhibit two distinct features: (i) a speckle pattern that translates according to the in-plane motion of the object and (ii) a regular fringe pattern that arises due to the interference between the reference wave and the speckle pattern. The fringe pattern will translate in response to an out-of-plane motion of the object. Methods from spatial filtering velocimetry [10] are implemented to measure all three velocity components. A numerical model, based on the complex ABCD matrix formalism [11], is developed to investigate the frequency characteristics of the output signals of realistic spatial filters and used to identify a suitable experimental configuration. The in-plane motion is addressed experimentally by a CMOS camera where the spatial filtering is implemented in the postprocessing. Previously, such methods have been demonstrated [10,12] and more recently described in a similar application [13]. The measurement of the out-of-plane motion is facilitated by an integrated optical spatial filter due to its high sensitivity [14]. The proposed method is intended for use in real-time studies where 3D translational velocity is of interest. Possible applications include remote sensing of structural dynamics, conditional monitoring, and fluid dynamics including aerosol flow. In the following section, the underlying theory of the numerical model is reviewed. In Section 3 the numerical model is presented and the results are discussed. The configuration of the experimental setup is based on the observations obtained from the numerical simulations and is described in Section 4. The experimental results are presented in Section 5. A general discussion and concluding remarks are included in Section 6.

2. Theoretical Review

In order to evaluate the performance of specific spatial filtering velocimetry methods that will be used to measure the velocity components of the object translation, a simple numerical model is developed based on the ABCD formalism. In Fig. 1 the geometry of the model is illustrated.

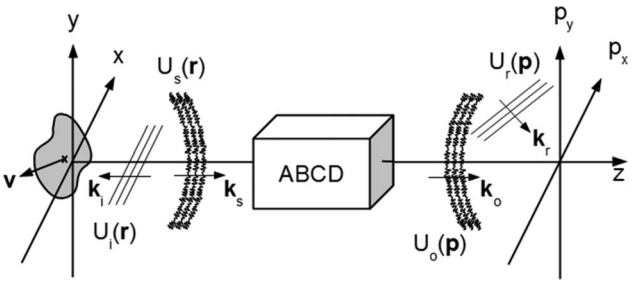

Fig. 1. ABCD model geometry.

A diffusing rigid object is located in the (x,y) plane, translating with constant velocity $\mathbf{v}$ and illuminated by a field $U_i(\mathbf{r})$ of the form

$$U_i(\mathbf{r}) = E_i \exp\left(-\frac{\mathbf{r}^2}{w_i^2}\right), \tag{1}$$

where w_i is the $1/e^2$ intensity radius. The scattered field $U_s(\mathbf{r},t)$ can then be written as

$$U_s(\mathbf{r},t) = U_i(\mathbf{r})\Psi(\mathbf{r},t), \tag{2}$$

where $\Psi(\mathbf{r},t)$ is the complex reflection coefficient of the object. It is assumed that $|\Psi(\mathbf{r},t)| = \text{const}$. Furthermore, it is assumed that the object surface structure does not evolve in time but moves as a "frozen" pattern. This attribute can be expressed by $\Psi(\mathbf{r},t+\tau) = \Psi(\mathbf{r}-\mathbf{v}\tau,t)$. The scattered field is propagated to the observation plane (p_x,p_y) by means of the paraxial Green's function defined by an ABCD matrix representing an imaging system. Thus, the field in the observation plane at time t can be obtained from

$$U_o(\mathbf{p},t) = \int_{-\infty}^{+\infty} \mathrm{d}^2\mathbf{r} U_s(\mathbf{r}) G(\mathbf{r},\mathbf{p}), \tag{3}$$

where

$$G(\mathbf{r},\mathbf{p}) = -\frac{ik}{2\pi B}\exp[-ikL']\exp\left[-\frac{ik}{2B}(A\mathbf{r}^2 - 2\mathbf{r}\cdot\mathbf{p} + D\mathbf{p}^2)\right]. \tag{4}$$

The entities A, B, and D represent the complex matrix elements of the optical system. The parameter k is the optical wavenumber, and L' is the optical path length from the object to the observation plane. Additionally, the refractive indices in the object and observation plane have been assumed to be identical. In the following, a specific ABCD system is considered with the following elements:

$$A = -\frac{f_2}{f_1}, \tag{5}$$

$$B = \frac{-2if_1f_2}{k\sigma^2}, \tag{6}$$

$$D = -\frac{f_1}{f_2}. \tag{7}$$

The ABCD system defined by Eqs. (5)–(7) constitutes a clean imaging system (i.e., a 4-f system) with magnification $M = -f_2/f_1$ and a Gaussian-apodized aperture of σ ($1/e$ field radius) in the exact Fourier plane. Combining Eq. (4) with Eqs. (5)–(7), the Green's function for the imaging system becomes

$$G(\mathbf{r},\mathbf{p}) = \frac{k^2\sigma^2}{4\pi f_1 f_2}\exp[-ikL']\exp\left[-\frac{k^2\sigma^2}{4f_2^2}\left(\frac{f_2}{f_1}\mathbf{r}+\mathbf{p}\right)^2\right]. \tag{8}$$

The field $U_o(\mathbf{p})$ is combined with a mutually coherent reference wave $U_r(\mathbf{p})$ at the observation plane. The reference wave is written as

$$U_r(\mathbf{p}) = E_r\exp\left(-\frac{\mathbf{p}^2}{w_r^2} - ik\boldsymbol{\theta}\cdot\mathbf{p}\right), \tag{9}$$

where w_r is the $1/e^2$ intensity radius and $\theta = (\theta_x,\theta_y)$ is the vector angle of incidence of the reference wave relative to the optical axis (the z axis) of the imaging system. Then the time-dependent intensity distribution in the observation plane can be obtained by

$$I(\mathbf{p},t) = |U_o(\mathbf{p},t) + U_r(\mathbf{p})|^2. \tag{10}$$

The power contained in each of the two contributions $U_o(\mathbf{p},t)$ and $U_r(\mathbf{p})$ is defined in the following way:

$$P_o = \int_{-\infty}^{\infty} \mathrm{d}^2\mathbf{p}|U_o(\mathbf{p},t)|^2. \tag{11}$$

$$P_r = \int_{-\infty}^{\infty} \mathrm{d}^2\mathbf{p}|U_r(\mathbf{p})|^2. \tag{12}$$

The intensity distribution at a later time $t+\tau$ can be obtained by letting

$$\Psi(x,y,t) \to \Psi(x-v_x\tau, y-v_y\tau, t+\tau)\exp(-ikv_z\tau), \tag{13}$$

where it is assumed that $\mathbf{v} = (v_x,v_y,v_z)$ is constant. It is noted that the optical distance L' in Eq. (8) must be modified by $L' \to L' + v_z\tau$. The range of axial displacements that is investigated in this context will be limited, so that the total axial displacement $|\Delta z| \ll d_o$ where $d_o = 4f_1^2/(k\sigma^2)$ is the depth of focus of the imaging system. Conversely, it can be argued that the depth of focus effectively localizes the measurement volume, facilitating a pointlike measurement, which is an advantage in many applications. If axial displacement significantly exceeds d_o, the ABCD system described by Eqs. (5)–(7) must undergo modification to accommodate this. Such considerations are beyond the scope of this work.

Having obtained the dynamic intensity distribution $I(\mathbf{p},t)$, determination of the temporal response of a spatial filter realized by a detector arrangement placed directly in the observation plane is called for. As the intensity distribution is sheared across the spatial filter, the time-dependent photocurrent signal can be obtained from [10], except for a proportionality factor

$$i(\mathbf{p_1}) = \int_{-\infty}^{+\infty} \mathrm{d}^2\mathbf{p} I(\mathbf{p_1}-\mathbf{p})h(\mathbf{p}), \tag{14}$$

where $\mathbf{p_1} = Mvt + \mathbf{p_0}$ and $\mathbf{p_0}$ is a constant vector.

The quantity $h(\mathbf{p})$ is the spatial filter response function. According to the convolution theorem, the power spectrum of the output signal described by Eq. (14) can be written as

$$P(\boldsymbol{\xi}) = |S_I(\boldsymbol{\xi})|^2|H(\boldsymbol{\xi})|^2, \tag{15}$$

where $\boldsymbol{\xi} = (\xi_x,\xi_y)$ denotes the spatial frequency vector in the $\mathbf{p}$ plane and $|S_I(\boldsymbol{\xi},t)|^2$ and $|H(\boldsymbol{\xi})|^2$ are the power spectral density of the intensity distribution and the spatial filter response function (the transfer function), respectively. The properties and configuration of the response function $h(\mathbf{p})$ can vary depending on the application, but in general it will consist of detector elements arranged in a periodic structure combining alternating elements with sum or differential amplifiers. The purpose of such an arrangement is to realize a narrow spatial bandpass filter that monitors the temporal phase evolution of the selected range of spatial frequencies. Accordingly, the detected photocurrent, i.e., the output signal of the spatial filter, will oscillate at a frequency proportional to the velocity component in the direction of the spatial filter periodicity. The frequency of this oscillation is given by the relation

$$F = \frac{Mv}{\Lambda}, \tag{16}$$

where Λ is the spatial period of the spatial filter, M is the magnification of the imaging system, and v is the velocity component of the object in the direction of the periodicity of the spatial filter.

The detector arrangement that will be used here has been demonstrated by Schnell *et al.* [12]. The detector aperture function can be written as

$$h(\mathbf{p}) = \left[h_{\mathrm{win}}(\mathbf{p})\sum_{m=-\infty}^{\infty}\delta(p_x - m\Lambda_x)\right] \otimes [h_{\mathrm{unit}}(p_x)\otimes h_{\mathrm{det}}(p_x)], \tag{17}$$

where

$$h_{\mathrm{win}}(\mathbf{p}) = \mathrm{Rect}\left(\frac{p_x}{L_x}\right)\mathrm{Rect}\left(\frac{p_y}{L_y}\right), \tag{18}$$

$$h_{\mathrm{unit}}(p_x) = \delta(p_x + p_\varphi) - \delta(p_x - p_\varphi), \tag{19}$$

$$h_{\mathrm{det}}(p_x) = \mathrm{Rect}\left(\frac{p_x}{W_d}\right), \tag{20}$$

and $\delta(x)$ denotes the Dirac-delta function. Selecting $W_d = \Lambda_x/4, p_\varphi = \Lambda_x/4$ and $L_x \to N\Lambda_x$, the power spectral density of the response function will be given by

$$|H(\boldsymbol{\xi})|^2 = \mathrm{sinc}^2(L_y\xi_y)\sum_{m=-\infty}^{\infty}\mathrm{sinc}^2[N(\Lambda_x\xi_x - m)][1 - \cos(\pi\Lambda_x\xi_x)]\mathrm{sinc}^2\left(\frac{\Lambda_x\xi_x}{4}\right), \quad (21)$$

where an unimportant proportionality factor has been omitted. The parameters W_d and p_φ are selected based on the experimental configuration used (see Section 4). A second detector arrangement is now interlaced with the first one, providing a second signal that will be in phase quadrature with the signal obtained from the first detector arrangement, facilitating an unambiguous directional discrimination of the translation. The two response functions of the detector arrangements are defined as $h_0(\mathbf{p}) \equiv h(\mathbf{p})$ and $h_{90}(\mathbf{p}) \equiv h(p_x - \Lambda_x/4, p_y)$. The power spectral density will be identical for both filters, as only a complex phase factor distinguishes the spectrum of one from the other. The orientation of the detector arrangements defines the direction of the velocity components to be measured. Generally, the in-plane motion is measured with two orthogonally orientated spatial filters, placed directly in the observation plane and tuned to the speckle size. However, a spatial filter can attain any angle in the observation plane. This feature will be necessary for determining all three velocity components and can be accommodated by introducing a new coordinate system that incorporates an arbitrary rotation of the filter orientation, here implemented in the spatial frequency domain

$$\xi_x' = \xi_x\cos(\Omega) + \xi_y\sin(\Omega), \quad (22)$$

$$\xi_y' = \xi_y\cos(\Omega) - \xi_x\sin(\Omega). \quad (23)$$

Figure 2 shows the detector arrangement and orientation. In Fig. 3, the power spectral density of an eight unit cell spatial filter is shown. The filter not only contains a spatial bandpass region around the first harmonic (fundamental) but also several higher harmonics of odd numbers are seen to contribute significantly. This is a well-known property of rectangular detector arrangements. It has been shown [14] that the Kth harmonics can, under certain conditions, be suppressed by selecting $W_d = \Lambda/K$. Given the detector configuration described above, the fourth harmonic will be suppressed but the third and fifth harmonics may constitute significant passbands in the spatial power spectrum of the spatial filter.

3. Numerical Results

To investigate the dynamic behavior of the intensity distribution in response to a 3D object translation and determine the temporal response of various spatial filtering implementations, a numerical model was developed. The object plane and the observation plane are both represented as matrices of 128 × 128 points. The spatial sampling periods are defined as Δx and Δy and correspond to the physical separation between sampling points (pixels) along the horizontal and vertical directions, respectively. In this model, we select $\Delta x = \Delta y = 5\,\mu$m.

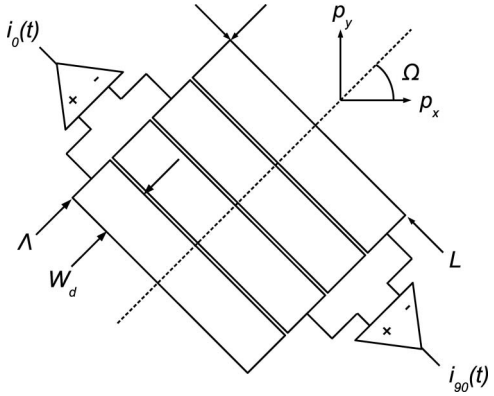

Fig. 2. Spatial filter unit cell combining both the $h_0(\mathbf{p})$ and $h_{90}(\mathbf{p})$ filters. The rotation angle of the detector arrangement in relation to the observation plane coordinate system is Ω.

The scattering properties of the object are defined by a random spatial distribution of scattering points in the object plane, having an identical scattering cross section. An individual scattering point (or particle) is represented by a single pixel in the numerical model. Each scattering point is attributed with a spatially delta-correlated complex random phase factor $\exp(-i\phi)$ where the phase ϕ is a stochastic variable described by a uniform probability distribution function (PDF) of the form

$$\mathrm{PDF}(\phi) = \begin{cases} \frac{1}{2\pi}, & -\pi \le \phi \le \pi \\ 0, & |\phi| > \pi \end{cases}. \quad (24)$$

When the imaging system is not able to resolve the individual scattering particle and the number of scattering particles is large, the resulting field distribution obtained in the observation plane will exhibit

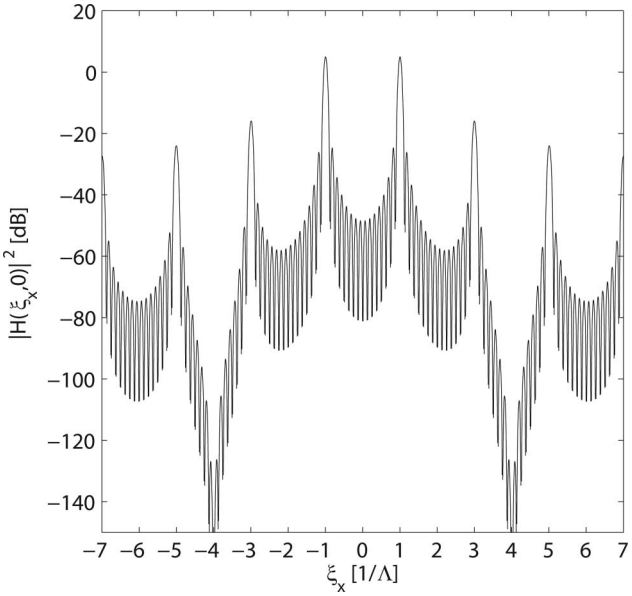

Fig. 3. Spatial power spectral function of the spatial filter described by Eq. (21) for $\Lambda \to \Lambda_x$, $L \to L_y$, $\Omega \to 0°$, and $N = 8$.

circular complex Gaussian statistics, giving rise to a fully developed speckle pattern [15]. It is straightforward to calculate the intensity distributions at different times in the object plane as the field of scattering points is translated according to Eq. (13) combining Eq. (1)–(10). The model implemented here assumes that effects of shot noise and thermal noise are negligible. Furthermore, it must be noted that due to the now discrete nature of the object and observation planes, the integrals are replaced with a corresponding summation operation. For simplicity, $w = w_r = (f_2/f_1)w_o$, $f_1 = f_2 = f$, and the aperture is apodized as a Gaussian function in the following. In Fig. 4 a representative simulated intensity distribution is shown. In the following, the parameters listed in Fig. 4 will be maintained.

It can be observed that the intensity distributions generally contain a random speckle pattern and a regular fringe pattern that is enclosed by the individual speckles. Furthermore, the entire speckle field is weighted by the image of the illumination spot on the object. The reference wave responsible for the regular fringe pattern formation exhibits a completely deterministic optical phase front across the observation plane, whereas the optical field distribution producing the speckle pattern exhibits an uncorrelated phase relationship between individual speckles. In the spatial frequency domain, the spectral content representing the fringe pattern is effectively bandlimited by the speckle pattern given the conditions of Fig. 4. Figure 5 shows the power spectra corresponding to the intensity distribution.

Investigating the features of Figs. 5–7 reveals the characteristic low-frequency speckle band that isotropically occupies the spatial frequency spectrum around the origin along with the sharp peak that originates from the image of the illumination spot. Additionally, the presence of two high-frequency sidebands located on the ξ_x axis is observed in Figs. 5 and 6. These sidebands originate from the regular fringe pattern. The above-mentioned band-limiting effect of the fringe pattern can be observed in Fig. 6. The effect is evident when the aperture in the Fourier plane of the imaging system is changed, and thus the average speckle size is changed as well. As a result, the width of the spatial fringe pattern band changes according to the width of the spatial speckle band.

Based on observations from Fig. 5, the spatial periods and spatial filter directionality can be determined to optimize the subsequent signals that form the basis of the velocity measurements. Table 1 summarizes these selections, and Fig. 8 shows the power spectrum of the intensity distribution along with the spectral peak locations of the passbands for the spatial filters.

In order to calculate the velocity components v_x, v_y, and v_z of the simulated particle distribution in the object plane, the time-dependent instantaneous output signal $i(t)$ of the spatial filters is considered. This quantity can be obtained from

$$i(t) = \int_{-\infty}^{\infty} \mathrm{d}^2\mathbf{p} I(\mathbf{p}, t) h(\mathbf{p}). \tag{25}$$

In the case of a discrete intensity distribution, the integral of Eq. (25) is replaced by the corresponding summation operation. The measurement of a given velocity component is obtained by observing the temporal power spectrum of Eq. (25) given the response function $h(\mathbf{p})$ of the spatial filter addressing its respective velocity component. The particles in the object plane translate in the plane with the following velocities $v_x = \Delta x/\tau$, $v_y = \Delta y/\tau$, where τ is the time between samples. This means that each time the output signal is sampled, the particle field is translated one spatial period (or pixel) in both the x and y directions. The corresponding normalized frequencies, which are expected to be observed in the temporal power spectra of the output signals, can be

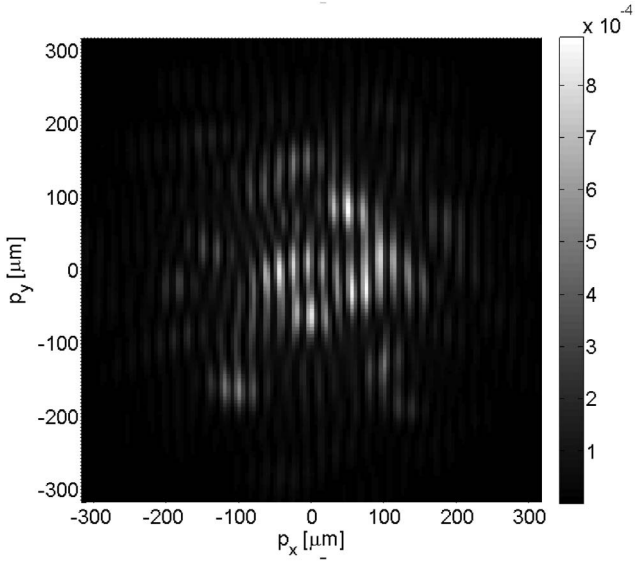

Fig. 4. Intensity distribution for $w = 250\,\mu$m, $f = 250$ mm, $P_o = P_r$, $\theta_x = 0.0316$ rad, $\theta_y = 0$ rad, and $\sigma = 1.5$ mm.

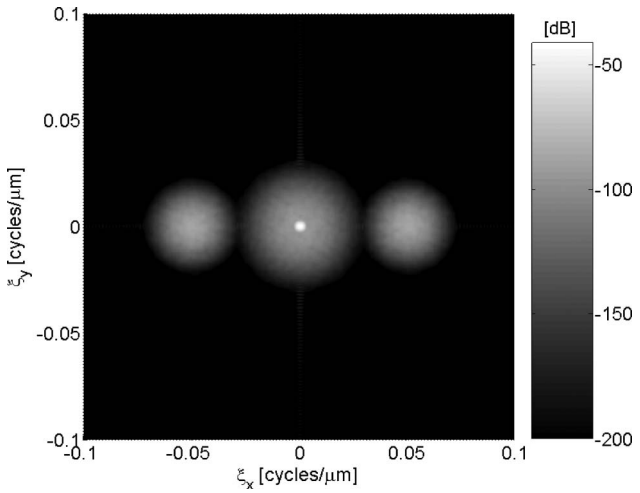

Fig. 5. Ensemble averaged spatial power spectrum $|S_I(\xi_x, \xi_y)|^2$ for $\theta_x = 0.0316$ rad, and $\theta_y = 0$ rad. The data set is the result of averaging 50 power spectra.

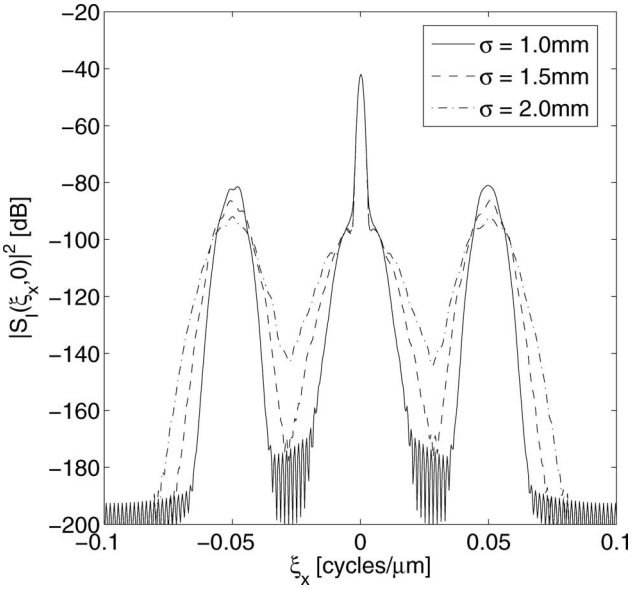

Fig. 6. Cross section along ξ_x axis of the spatial power spectrum in Fig. 5 for different values of the aperture size σ.

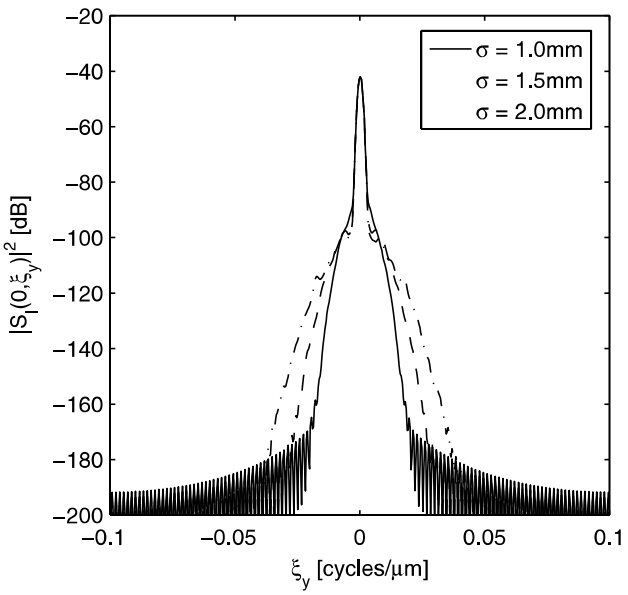

Fig. 7. Cross section along ξ_y axis of the spatial power spectrum in Fig. 5 for different values of the aperture size σ.

obtained from Eq. (16), are given by

$$f_x^{\mathrm{FUN}} = F_x \tau = \frac{\Delta x}{\Lambda_x} = \frac{5\,\mu\mathrm{m}}{80\,\mu\mathrm{m}} = \frac{1}{16}, \tag{26}$$

where F_x is given by Eq. (16) for $v = v_x$. The equivalent expression is valid for f_y^{FUN}. The out-of-plane velocity is selected so that $v_z = \lambda/(8\tau)$. The fringe pattern will undergo a full oscillation in response to an out-of-plane displacement of $\lambda/2$. Because the spatial frequency of the fringe pattern is arranged so that a spatial period exactly matches the spatial period of the spatial filter, a conversion factor of the actual axial displacement to the in-plane translation of the fringe pattern, must be taken into account. This factor can be written as $\alpha = 2\Lambda_z/\lambda$. Therefore, the normalized frequency is expected to be

$$f_z^{\mathrm{FUN}} = F_z \tau = \frac{\alpha v_z}{\Lambda_z}\tau = \frac{1}{4}. \tag{27}$$

In Fig. 9 the temporal power spectra of the output signals are shown along with the expected frequencies as given by Eq. (26) and (27) displayed as vertical lines.

Figure 9 shows that the spectral position of all three velocity components support the theoretical predictions of Eqs. (26) and (27). However, two additional features denoted $f_{xz}^{(-)}$ and $f_{xz}^{(+)}$ appear in the temporal spectrum of the signal from the spatial filter, measuring the v_x component. The spectral peaks at the frequency positions denoted $f_{xz}^{(-)}$ and $f_{xz}^{(+)}$ originate because the third and fifth harmonic passbands of the spatial filter, measuring the v_x component, overlap with the spatial frequency band occupied by the fringe pattern—as can be observed from Fig. 8. A more detailed study of the spectral positions of these two peaks confirms the following dependencies:

$$f_{xz}^{(-)} = f_z^{\mathrm{FUN}} - f_x^{\mathrm{FUN}}, \tag{28}$$

$$f_{xz}^{(+)} = f_z^{\mathrm{FUN}} + f_x^{\mathrm{FUN}}. \tag{29}$$

These "crosstalk" frequencies can disrupt the velocity determination, especially due to their dynamic behavior. However, a solution to this problem can be identified: if the angle of incidence of the reference wave is changed so that

$$\boldsymbol{\theta} = (\lambda/(\Lambda_z\sqrt{2}), \lambda/(\Lambda_z\sqrt{2})), \tag{30}$$

then the spatial period of the fringe pattern is numerically preserved, but the orientation is changed

Table 1. Spatial Passband Center Frequencies for the Spatial Filters Used in the Numerical Model

	Velocity Component		
	Center Frequency (Cycles/μm)		
	v_x	v_y	v_z
First Order and Its Harmonics	$\Lambda_x = 80\,\mu$m, $\Omega = 0°$	$\Lambda_y = 80\,\mu$m, $\Omega = 90°$	$\Lambda_z = 20\,\mu$m, $\Omega = 0°$
First	$\pm 1/80$	$\pm 1/80$	$\pm 1/20$
Third	$\pm 3/80$	$\pm 3/80$	$\pm 3/20$
Fifth	$\pm 5/80$	$\pm 5/80$	$\pm 1/4$

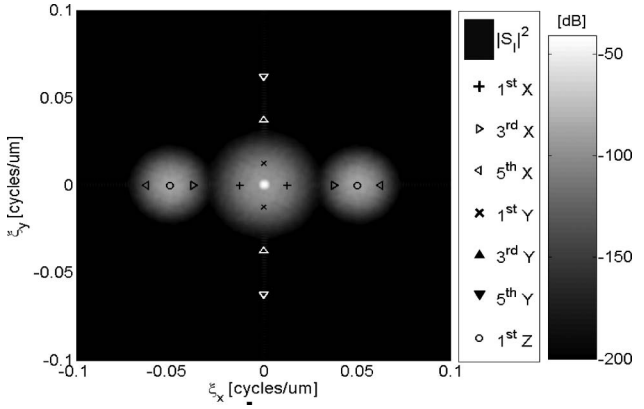

Fig. 8. Ensemble averaged spatial power spectrum $|S_I(\xi_x,\xi_y)|^2$ for $\theta_x = 0.0316\,\text{rad}$, $\theta_y = 0\,\text{rad}$ shown along with the center frequency locations of spatial frequency bands corresponding to spatial filters observing the v_x, v_y, and v_z components of translation. The data set is the result of averaging 50 power spectra.

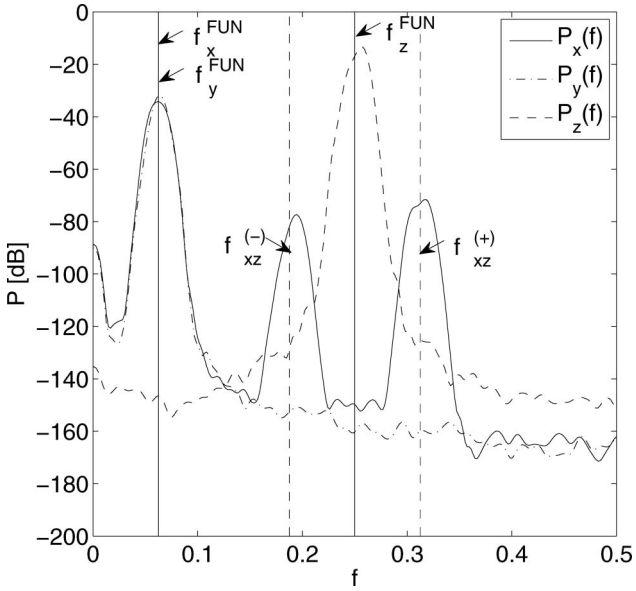

Fig. 9. Temporal power spectra as a function of normalized frequency obtained by FFT. The quantity $P_i(f)$ for $i = \{x,y,z\}$ denotes the power spectrum of the output signal of the spatial filter observing the v_x, v_y, and v_z components, respectively. The data set is the result of averaging 10 power spectra.

by 45°. If the spatial filter observing v_z component is implemented with $\Omega = 45°$, then the measurement of v_z is maintained while the spatial frequency band of the fringe pattern is isolated from the passbands of the spatial filter measuring the v_x component. This configuration was implemented in the experimental setup and a discussion of the effects is included in Section 6.

4. Experiment

The experimental data are obtained using the setup illustrated in Fig. 10.

The coherent light source used in this experiment is a polarization-controlled He–Ne laser operating at a wavelength of $\lambda = 633\,\text{nm}$. The radiation from the laser is collimated to a spot size of $\sim 1\,\text{mm}$ ($1/e^2$ intensity radius) with a beam expander. The expanded beam is split by a nonpolarizing beam splitter (BS). One of the beams is directed toward the object and forms the illumination beam. The other beam is directed toward the observation plane coinciding with the image of the object under an angle of incidence of $\boldsymbol{\theta} = (0.030\,\text{rad}, 0.030\,\text{rad})$ relative to the optical axis of the imaging system, thereby establishing the reference wave. The object is mounted on a translation stage, and it consists of an aluminum surface that has been treated to ensure a suitable rough surface for generation of a fully developed speckle pattern. The direction of translation can be adjusted to ensure both in-plane and out-of-plane translation with respect to the measurement directions of the spatial filters. Finally, the speed of translation can be varied.

The object plane is imaged onto the observation plane with a clean imaging system [11] consisting of two lenses and an adjustable diameter aperture placed in the Fourier plane of the system. The focal lengths of the two lenses are $f_1 = f_2 = 250\,\text{mm}$. This configuration is identical to the optical system emulated with the ABCD matrices described in Section 3, apart from the aperture. In the experimental setup, the amplitude transmittance function is circular with a radius of $\sigma = 1\,\text{mm}$ rather than apodized with a Gaussian function. For this specific imaging system, the depth of focus (d_o) is approximately $\sim 25\,\text{mm}$.

By implementing a 50:50 nonpolarizing BS immediately behind the second lens (f_2) of the imaging system, the observation plane is effectively split into two. This enables implementation of two separated

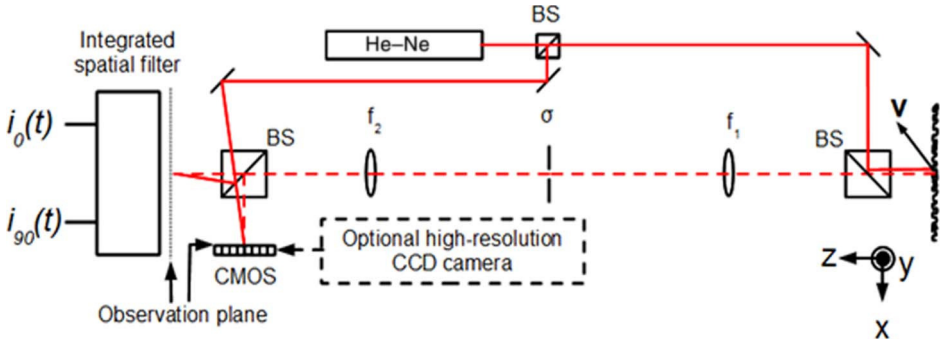

Fig. 10. (Color online) Experimental setup.

systems for velocity measurement. In order to measure the in-plane velocity components, a CMOS detector array is utilized. The CMOS array used here consists of a 256 × 256 matrix of detectors with pixel dimensions of 10.6 μm × 10.6 μm. A frame-grabber records a sequence of images as the object translates. The spatial filtering operation is implemented by means of the method described in Section 3.

The out-of-plane velocity measurement is performed by an integrated optical spatial filter that is rotated corresponding to $\Omega = 45°$ in relation to the observation plane coordinate system, whereas the CMOS detector array is orientated in a configuration that is equivalent to $\Omega = 0°$. Figure 11 illustrates the integrated optical spatial filter.

The optical spatial filter in this device is injection molded and combined with a detector array containing four elements. The optical spatial filter consists of an array of cylindrical lenses (lenslets) separated by a distance of Λ_z. The radius of curvature of the lenslets is denoted R_3. Each of the lenslets in the array forms a one-dimensional imaging system with a large, single lens on the back side of the optical element. This lens has a radius of curvature of R_4. The photocurrents generated by the four individual detectors in the array are converted into voltage signals and directed to a set of differential amplifiers in the manner illustrated in Fig. 11. The detectors are arranged so that

$$d_{180} = \frac{\Lambda_z R_4}{2R_3}. \tag{31}$$

Given the relationship of Eq. (31), a backpropagation of the detector array through the optical system [16] will result in a reduced and repeated image of the detector array being projected to the input plane of the spatial filter device. If the lenslet array contains N lenslets, and assuming perfect imaging, the spatial transfer function of this system will be given by Eq. (21) where the width of the filter in its direction of periodicity is $L_z = N\Lambda_z$ and the width of a single backpropagated detector is $W_d = \Lambda_z/4$. The output signals from the two differential amplifiers are digitized by an analog-to-digital converter, resulting in an in-phase signal and a signal in phase quadrature for directional discrimination. A more detailed description of this type of system can also be found in [14].

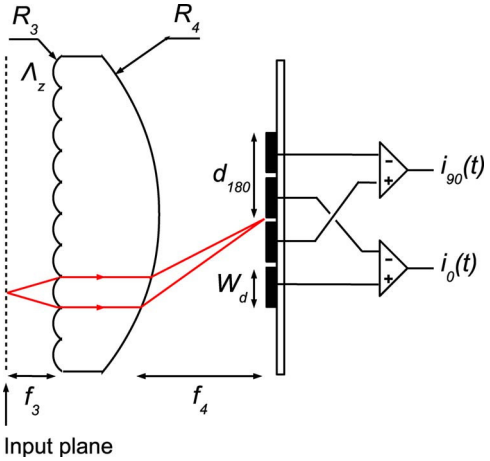

Fig. 11. (Color online) Integrated optical spatial filter. The physical parameters of the filter are $\Lambda_z = 15\,\mu$m, $R_3 = 18\,\mu$m, $R_4 = 1$ mm, and $W_d = 187.5\,\mu$m.

Table 2 lists the parameters and orientation of the spatial filters used in the measurements.

5. Results

Using a high-resolution camera, an intensity distribution in the observation plane was recorded. This distribution is shown in Fig. 12. This shows that the fringe pattern is enveloped by the speckle patterns as expected. The fringe pattern is oriented so that the fringes are parallel with the cylindrical lenslets of the integrated optical spatial filter, and the spatial frequency of the fringes matches the fundamental passband of the filter.

In Fig. 13, the spatial power spectrum of the intensity distribution is shown along with the center frequencies of the passbands of the spatial filters. It can be observed that the frequency distributions of both the fringe and speckle signal segments exhibit a different functionality than the frequency distributions obtained in the numerical simulations. This is due to the transmission function of the aperture in the Fourier plane of the imaging system being circular [15] in the experimental configuration rather than Gaussian as was the case in the numerical simulations.

Comparing the signals in the spatial frequency domain with the center frequencies of the passbands listed in Table 2, it can be observed that the fundamental frequencies of all three filters for in-plane and out-of-plane velocity measurements overlap their respective signal segments.

Table 2. Spatial Passband Center Frequencies for the Spatial Filters Used in the Experiment

	Velocity Component		
	Center Frequency (Cycles/μm)		
	v_x	v_y	v_z
First Order and Its Harmonics	$\Lambda_x = 84.8\,\mu$m, $\Omega = 90°$	$\Lambda_y = 84.8\,\mu$m, $\Omega = 0°$	$\Lambda_z = 15\,\mu$m, $\Omega = 45°$
First	±0.0118	±0.0118	±0.0667
Third	±0.0354	±0.0354	±0.2000
Fifth	±0.0590	±0.0590	±0.3333

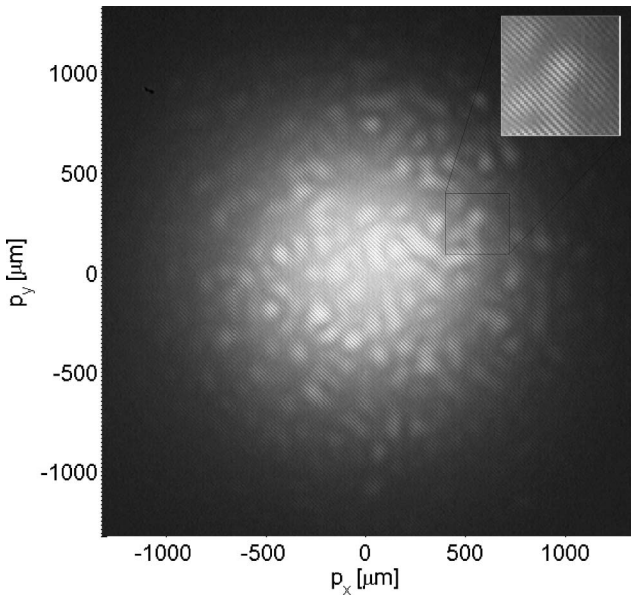

Fig. 12. Intensity distribution obtained using a high-resolution CCD camera.

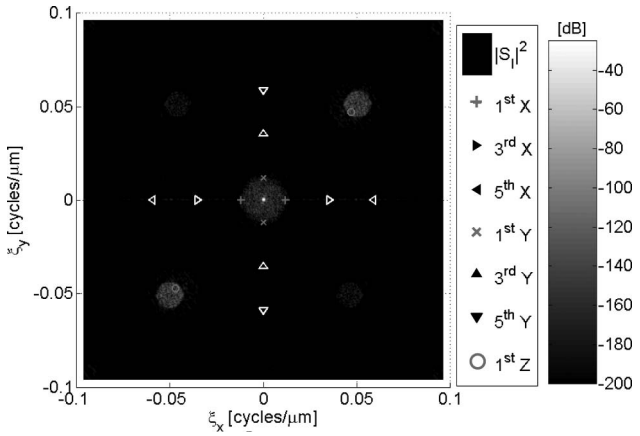

Fig. 13. Spatial power spectrum of the intensity distribution obtained with the high-resolution CCD camera.

The object is now arranged in such a way that the velocity components in relation to the measurement axis can be written as

$$(v_x, v_y, v_z) = (v_{\mathrm{obj}} \cos(45°) \sin(93.3°), v_{\mathrm{obj}} \sin(45°) \times \sin(93.3°), v_{\mathrm{obj}} \cos(93.3°)), \quad (32)$$

where v_{obj} is the (constant) speed of the object.

The time series of intensity distributions was recorded with the CMOS camera and processed with the numerically defined spatial filters, while the output signal of the optical spatial filter measuring the v_z component was recorded using an oscilloscope. An object speed of $v_{\mathrm{obj}} = \pm 0.1\,\mathrm{mm/s}$ was selected for the top and bottom lines of the plots in Fig. 14. In the top of the individual plots, the entire signals are displayed. In the main plots, an excerpt corresponding to the interval outlined with the two vertical lines is shown. It can be observed that as the translation direction is reversed, the phase relationship between the in-phase and phase-quadrature signal changes sign, indicating a reversal of direction. This can be observed for all three measurements corresponding to the v_x, v_y, and v_z components, demonstrating that the directionality of all three velocity components can be discriminated.

To measure the magnitude of the three velocity components, the temporal power spectrum of the spatial filter signals is considered for different values of v_{obj}.

Figures 15–17 show the power spectra of the spatial filter signals for observing the v_x, v_y, and v_z components for four different values of v_{obj}. The vertical

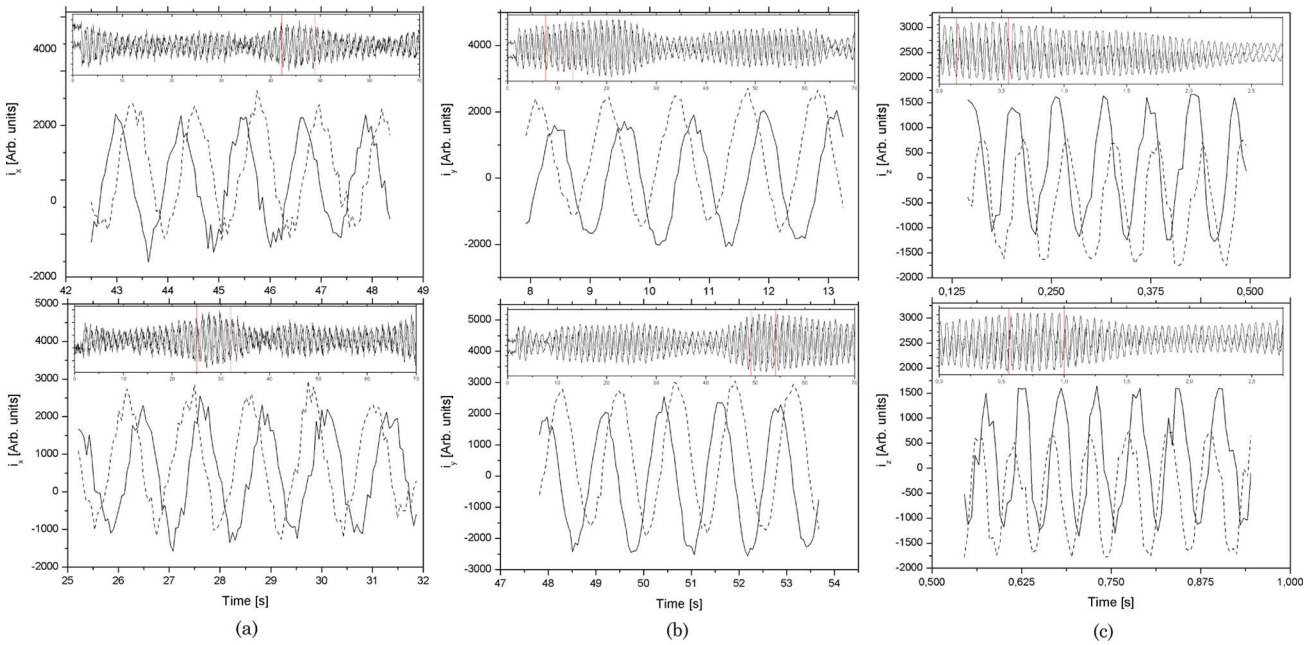

Fig. 14. (Color online) Spatial filter output signals. Vertical lines delimit the excerpts shown in the main plot. Top, $v_{\mathrm{obj}} = 0.1\,\mathrm{mm/s}$. Bottom, $v_{\mathrm{obj}} = -0.1\,\mathrm{mm/s}$. Plots (A)–(C) correspond to v_x, v_y and v_z, respectively.

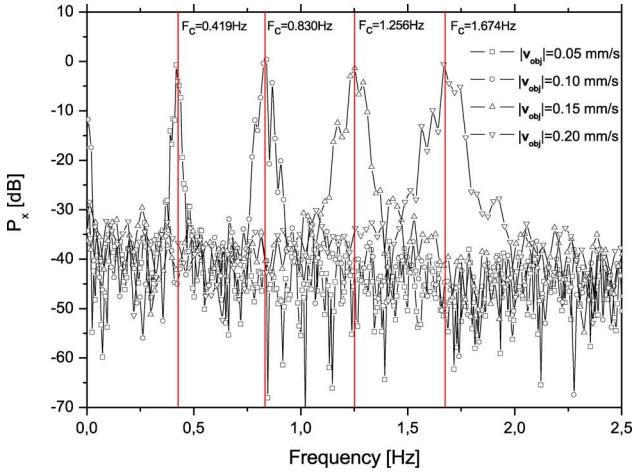

Fig. 15. (Color online) Power spectra of output signal from the spatial filter observing the v_x velocity component for different values of v_{obj}.

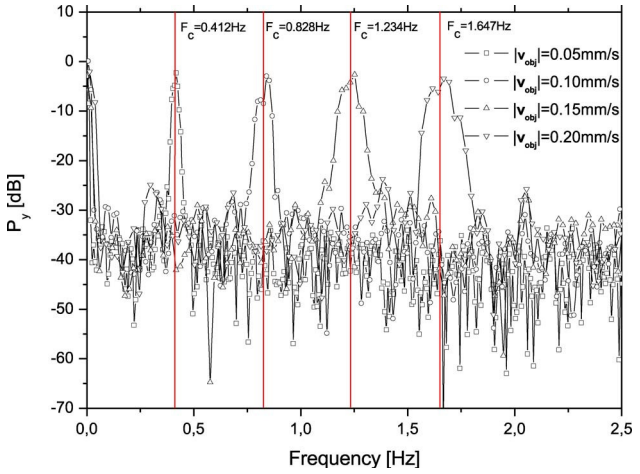

Fig. 16. (Color online) Power spectra of output signal from the spatial filter observing the v_y velocity component for different values of v_{obj}.

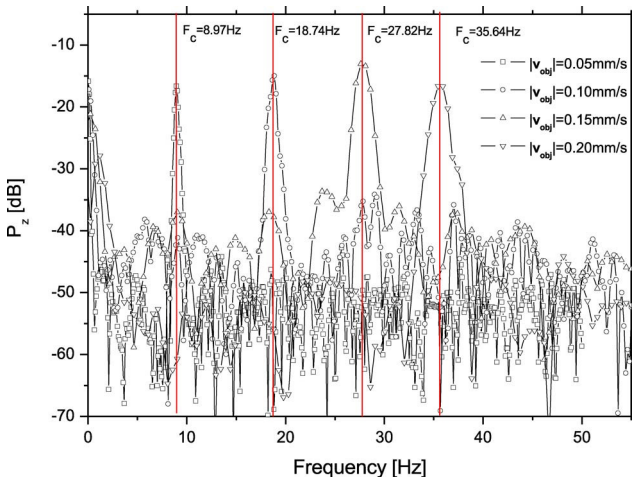

Fig. 17. (Color online) Power spectra of output signal from the spatial filter observing the v_z velocity component for different values of v_{obj}.

Table 3. Best Fitting Parameters of the Linear Relationship Relating the Measured Velocity to the Actual Velocity

Velocity Component	c_0 (mm/s)	c_1	R^{2a}
v_x	−0.0003	1.007	0.99996
v_y	0.0001	0.987	0.99997
v_z	0.0001	0.987	0.99658

[a]Indicates the accuracy of the fit. When the value $R^2 \to 1$, the model, in this case described by Eq. (33), approaches perfect correlation with the sample data, i.e., a perfect fit.

lines mark the measured center frequencies based on the centroid determined within a frequency window that is centered about the frequency peak and truncated at the noise floor. It is expected that there exists a linear relationship between the measured velocity components and the theoretically predicted values. This relationship is assumed to be of the form

$$v_i^{\mathrm{measured}} = c_0 + c_1 v_i^{\mathrm{actual}}, \tag{33}$$

where $i = \{x, y, z\}$. The center frequencies obtained from the measurements are expected to be related to the velocity component through Eq. (16). In Table 3, the best fitting values of c_0 and c_1 are listed for all three velocity components along with the associated correlation coefficient (R^2).

6. Discussion and Conclusion

It has been demonstrated that all three velocity components of a diffusely scattering rigid object can be extracted using imaging speckles combined with an angular offset reference wave and methods based on spatial filtering velocimetry. This was achieved by tuning the fundamental spatial passbands of spatial filters to the speckle pattern and the regular fringe pattern, respectively. A numerical model was developed to determine the output of realistic spatial filter implementations such as a rectangular apodized detector arrangement. The numerical model showed that all three velocity components could, in principle, be extracted using a two-dimensional detector array. However, the model also predicted a crosstalk phenomenon that could impact the measurement negatively. A solution that solved this problem optically was identified. The fringe pattern orientation was changed by altering the angle of the incidence vector of the reference wave, effectively removing the spatial frequency component of the fringe pattern from the passbands of the higher harmonics of the spatial filters tuned to the speckle pattern.

Using a CMOS camera and an integrated optical spatial filter, the numerical model predictions were experimentally verified. It was successfully demonstrated that the direction of translation could be extracted for all three velocity components using a combination of an in-phase and phase-quadrature detector arrangement. The magnitude of each velocity component was varied by adjusting the speed of the translation stage. The measured velocities were in good agreement with the actual velocities.

Generally, the accuracy with which the velocity can be determined using the proposed method depends on the specific experiment and implementation used. The limitation on measurement accuracy imposed by the spatial filters is related to the relative spectral width of the fundamental passband and is inversely proportional to the number of unit cells in the array constituting the filter. This number effectively determines how many signal oscillations can be observed. A treatment of the accuracy of spatial filtering velocimetry techniques can be found in [10]. The method described here relies on speckle translation to measure the transverse velocity components. The fringe pattern, used to measure the out-of-plane component, is limited by the correlation properties of the speckle pattern. Thus, speckle decorrelation (boiling) will be the limiting factor of the measurement accuracy of the transverse components if the speckle decorrelation length is significantly shorter than the spatial filter window ($L = N\Lambda$). Similarly, when imaging the object, the depth of focus determines the axial correlation length of the speckles in the observation plane [17]. Thus, the average number of oscillations in the output signal of the spatial filter observing the out-of-plane component will be $\sim 2d_0/\lambda$. Generally then, the system should be designed to accommodate the maximum number of unit cells in the spatial filter that will contribute constructively to the signal in order to maximize the number of signal oscillations. Fundamentally, the detection noise and finite measurement time will ultimately dictate the attainable accuracy.

The methodology described here is well suited for measuring translational velocity of rigid objects or surfaces. The velocities that were investigated were fairly small. This was due to a limited frame rate of the camera system. For high-speed applications, the use of integrated optical spatial filters to measure the in-plane velocity components, similar to that used for the measurement of the out-of-plane object translation, is required. Because of the fact that the detector array only contains four detectors and the spatial filtering is performed optically, these devices run routinely with sample rates in the megahertz regime.

Another interesting application is in flow velocity measurements—particles suspended in fluid or aerosols in the atmosphere. However, the effects of turbulence will increase the rate of decorrelation of the speckle pattern and thus reduce signal quality and availability. Also, the effects of noise will become critical as the backscattered signal becomes small, as is the case for probing atmospheric flows. These effects must be understood in detail to determine the viability of the methodology for such applications.

This work has been partly funded by OPDI Technologies A/S.

References

1. M. Sjödahl, "Some recent advances in electronic speckle photography," Opt. Lasers Eng. **29**, 125–144 (1998).
2. P. Meinlschmidt, K. D. Hinsch, and R. S. Sirohi, eds., "*Electronic Speckle Pattern Interferometry*," Vol. MS 132 of SPIE Milestone Series (SPIE, 1996).
3. M. Sjödahl and H. O. Saldner, "Three-dimensional deformation field measurements with simultaneous TV holography and electronic speckle photography," Appl. Opt. **36**, 3645–3648 (1997).
4. S. L. Yeh, S. T. Lin, and Y. H. Chang, "Precise displacement measurement for a local surface," Opt. Lett. **34**, 3406–3408 (2009).
5. J. W. Bilbro, C. DiMarzio, D. Fitzjarrald, S. Johnson, and W. Jones, "Airborne Doppler lidar measurements," Appl. Opt. **25**, 3952–3960 (1986).
6. R. S. Hansen and C. Pedersen, "All semiconductor laser Doppler anemometer at 1.55 μm," Opt. Express **16**, 18288–18295 (2008).
7. L. Z. Kennedy and J. W. Bilbro, "Remote intensity fluctuation measurements with a laser Doppler radar," Appl. Opt. **15**, 2008–2008 (1976).
8. J. O'Shaughnessy and W. R. M. Pomeroy, "Single beam atmospheric transverse velocity measurement," Opt. Quantum Electron. **10**, 270–272 (1978).
9. J. H. Churnside and H. T. Yura, "Laser vector velocimetry: a 3-D measurement technique," Appl. Opt. **21**, 845–850 (1982).
10. Y. Aizu and T. Asakura, *Spatial Filtering Velocimetry: Fundamentals and Applications* (Springer-Verlag, 2006).
11. H. T. Yura and S. G. Hanson, "Optical beam wave propagation through complex optical systems," J. Opt. Soc. Am. A **4**, 1931–1948 (1987).
12. U. Schnell, J. Piot, and R. Dandliker, "Detection of movement with laser speckle patterns: statistical properties," J. Opt. Soc. Am. A **15**, 207–216 (1998).
13. S. Bergeler and H. Krambeer, "Novel optical spatial filtering methods based on two-dimensional photodetector arrays," Meas. Sci. Technol. **15**, 1309–1315 (2004).
14. M. L. Jakobsen and S. G. Hanson, "Lenticular array for spatial filtering velocimetry of laser speckles from solid surfaces," Appl. Opt. **43**, 4643–4651 (2004).
15. J. W. Goodman, "Statistical properties of laser speckle patterns," in *Laser Speckle and Related Phenomena*, J. C. Dainty, ed. (Springer-Verlag, 1984), Chap. 2.
16. A. E. Siegman, "The antenna properties of optical heterodyne receivers," Appl. Opt. **5**, 1588–1594 (1966).
17. H. T. Yura, S. G. Hanson, R. S. Hanson, and B. Rose, "Three-dimensional speckle dynamics in paraxial optical systems," J. Opt. Soc. Am. A **16**, 1402–1412 (1999).

Paper IV

Speckle and fringe dynamics in image shearing interferometry for spatial filtering velocimetry

M. L. Jakobsen[1,*], T. F. Q. Iversen[2], H.T. Yura[3] and S. G. Hanson[1]

[1]*DTU Fotonik, Department of Photonics Engineering, Technical University of Denmark, P.O. Box 49, DK-4000, Roskilde, Denmark*

[2]*OPDI Technologies A/S, Frederiksborgvej 399, 4000 Roskilde, Denmark*

[3]*Electronics and Photonics Laboratory, The Aerospace Corporation, P.O. Box 92957, Los Angeles, California, 90009, USA*

[*]*Corresponding author: mlja@fotonik.dtu.dk*

This paper analyzes the dynamics of laser speckles and fringes, formed in an image-shearing speckle-pattern interferometer with the purpose of sensing linear 3D motion and out-of-plane components of rotation in real-time, using optical spatial-filtering-velocimetry techniques. The ensemble-average definition of the cross-correlation function is applied to the intensity distributions, obtained in the observation plane at two positions of the object. The theoretical analysis provides a description for the dynamics of both the speckles and the fringes. The analysis reveals that both the magnitude and direction of all three linear displacement components of the object movement can be determined. Simultaneously, out-of-plane rotation of the object including the corresponding directions can be determined from the spatial gradient of the in-plane fringe motion throughout the observation plane. The theory is confirmed by experimental measurements.

OCIS codes: 030.1640, 120.6150, 120.6160, 070.6110, 100.2650.

1. Introduction

Speckle interferometry, combining an image of an object with an angularly off-set reference wave, are basic configurations for e.g. electronic speckle pattern interferometry (ESPI) [1]. ESPI is a well established nondestructive optical measurement technique used extensively to measure out-of-plane displacement fields of object deformations under load. Speckle photography [2] and digital speckle photography (ESP) [3] are a well established and theoretically well described [4] optical measurement techniques for measuring in-plane displacement fields of an imaged object during deformation or movement. Furthermore, these two techniques have been combined simultaneously to provide three-dimensional deformation field measurements of an object with a camera [5].

Considering rigid objects only, a design [6] for single-point measurements of three-dimensional motion of a rigid object has been proposed. This system is based on shearing of free-space-propagation speckle patterns for lateral movement and in-line Michelson interferometer for axial movement. However, this system will not differentiate between translation and rotation of the object. Therefore, a design [7], based on shearing a reference wave with a speckle field propagated through an imaging system, has been proposed. Combined with spatial-filtering velocimetry [8], three-dimensional motion of a rigid object has

been extracted and measured from the image plane, without contamination of rotational motion of the object and potentially in real time.

The in-line Michelson interferometer can be modified by angling the reference wave relative to the optical axis of the imaging system in order to implement the image-shearing speckle-pattern interferometer [9]. The sheared phases will produce a regular fringe pattern in the image plane. This fringe pattern will translate through the image plane with a displacement/velocity that can be related directly to the out-of-plane displacement/velocity of the object. In contrast to previous studies, this configuration is designed for measuring out-of plane motion of a rigid object [7] with optical spatial filtering velocimetry [10] having the center frequency of the spatial band-pass filter tuned to the fringe spacing. Spatial filtering velocimetry can provide both the displacement/velocity and the direction of the fringe pattern in real-time. With an adequately chosen point-spread function of the imaging system, and in case the object has an optically rough surface, speckles large enough to enclose the regular fringes will occur in the image of the illuminated part of the object. These speckles will translate in the image plane when the object performs an in-plane displacement or has an in-plane velocity component [4,7]. Again, optical spatial filtering sensors, tuned to the mean speckle size, can monitor the speckle motion in two-dimensions and together with the optical spatial filter monitoring the regular fringes pattern full three-dimensional information of a rigid objects motion can be obtained simultaneously, and in real-time.

In case the object rotates in the object plane of an imaging system (Speckle photography) the dynamics of the speckles will reveal no direct information about the angular velocity of the object. However, because there is a reference wave present in the observation plane the phase or phase change of the individual speckles can be measured as e.g. a local fringe movement or fringe velocity in the observation plane.

In order to theoretically describe the combined effects of both the fringe pattern and speckles in such a system, we consider the ensemble-average cross-correlation function of the intensity distributions that is obtained in the image plane for two positions of the object. The analytical expression will allow us to study the dynamics of the speckles and the fringes and their decorrelation lengths in response to object translation and rotation. Thus, the work presented here will address applications within the field of real-time, compact optical sensors, and therefore, pursue the possibilities of merging speckle interferometry and optical spatial filtering velocimetry. The theoretical work is supported with experimental work.

2. Theory

The basic setup for describing the development and interaction of fields in the image-shearing speckle-pattern interferometer is illustrated in Figure 1. A rigid object with a rough surface at time t_1 is illuminated with a fundamental Gaussian (TEM_{00}) laser beam. The in-plane coordinates of the object are denoted by the vector $\mathbf{r}_1 = (x,y)$, while the axial position is designated by the z-coordinate, z_1. We define a rough surface as a surface having an rms. surface roughness greater than the optical wavelength, and we illuminate a region on the object having a radius w_i that is large compared to any in-plane scale of the surface roughness. Light, scattered from the object surface is collected and propagated through an imaging system. The optical axis of the imaging system is aligned with the z-axis. The imaging system is described with a complex *ABCD* matrix [11], and has a limiting aperture in order to ensure that any scale of the surface roughness is unresolved in the image. Thus, fully developed speckles will modulate the image of the illuminated object in the image plane. The image plane is positioned at a distance of L from the object plane, and the intensity distribution in the image plane is designated by the two-dimensional vector, $\mathbf{p} = (p_x,p_y)$. A second fundamental Gaussian laser beam, incident in the image plane at an angle $\boldsymbol{\varphi}$ relative to the z axis is added as a reference field. This angle can be decomposed into two orthogonal components $\boldsymbol{\varphi} = (\varphi_x,\varphi_y)$. At time t_2 the object is located at $\mathbf{r}_2$, where $\mathbf{r}_2 = \mathbf{r}_1+\Delta\mathbf{r}$, and $z_2 = z_1+\Delta z$.

For definiteness, we assume that the object is at rest at both t_1 and t_2, and that we have mixing between waves of equal optical wavelengths. Secondly, the description of the model will initially focus on linear displacement. Allowing the object to move with a constant velocity (v_x,v_y,v_z) within the time interval

$\tau = t_2 - t_1$ creating a Doppler shift of the backscattered light, will provide the same result. In this case, in the results presented below we can directly replace $\Delta\mathbf{r}$ by $\mathbf{v}\tau$, and Δz by $v_z\tau$, where $\mathbf{v} = (v_x, v_y)$ and v_z are in-plane and out-of-plane components of the object velocity, respectively. Allowing the object to carry out an out-of-plane angular displacement with one of two components $\boldsymbol{\theta} = (\theta_x, \theta_y)$ we can use the same model as specified for linear displacement by inserting a virtual negative lens with a focal length of $f_o = -R/2$, where R is the radius of rotation of the corresponding surface motion, and directly replace $\Delta\mathbf{r}$ with $R\Delta\boldsymbol{\theta}$ [15]. In the special case where the object is a cylinder, which rotates with respect to its axis of symmetry, R is the radius of the cylinder, $R\Delta\boldsymbol{\theta}$ is the peripheral displacement of the cylinder, and the virtual lens is a cylinder lens, orientated parallel to the axis of symmetry of the object.

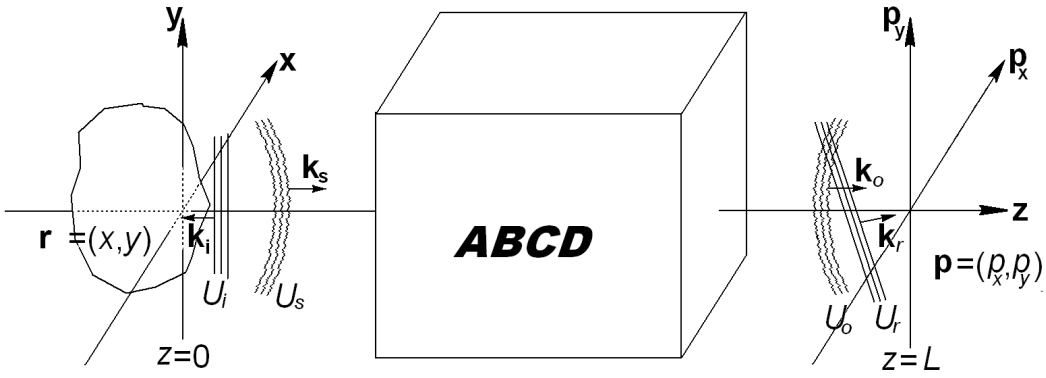

Figure 1. Setup for describing the image-shearing speckle-pattern interferometer.

We assume that both axial motion (Δz) and surface elevations ($\Delta z_e = w_i^2/R$) throughout the illuminated area of the object are small compared to both the depth of focus (d_o) of the imaging system and the confocal parameter ($2b$) of the illuminating beam: Δz, $\Delta z_e << d_o$, $2b$. Hence, the illumination and the image configuration are not affected by the motion or the shape of the illuminated part of the object.

2.1 The ensemble average cross-correlation function

For a stochastic process the ensemble-average cross-correlation function of two intensity measurements, obtained at two positions in the observation plane due to light scattered from the object at time t_1 and t_2, can be expressed as [14]:

$$C(\mathbf{p}_1, \mathbf{p}_2; \Delta\mathbf{r}, \Delta z) = C(\mathbf{p}, \mathbf{p}+\mathbf{q}; \Delta\mathbf{r}, \Delta z) = \left\langle I(\mathbf{p}, t_1)\, I^*(\mathbf{p}-\mathbf{q}, t_2) \right\rangle, \tag{1}$$

where the asterisk denotes the complex conjugate, and angular brackets denote the ensemble average over the stochastic realization of the surface-height fluctuations of the rough surface. The two intensities $I(\mathbf{p},t_1)$ and $I(\mathbf{p}\text{-}\mathbf{q},t_2)$ denote the optical intensity (real) at the two positions $\mathbf{p}$ and $\mathbf{p}\text{-}\mathbf{q}$ in the image plane at the two time events considered above, respectively.

In order to use the complex field amplitudes, we assume that the polarization of the incident field is maintained during reflection, and that the object and reference fields have identical polarizations in the image plane. The incident object field in the image plane is denoted as $U_o(\cdot)$, and the corresponding complex field amplitude of the reference field is denoted as $U_r(\cdot)$. Inserting these fields into Eq.1 yields:

$$C(\mathbf{p},\mathbf{p}+\mathbf{q};\Delta\mathbf{r},\Delta z)=\left\langle \begin{array}{l}\left(U_o(\mathbf{p},t_1)+U_r(\mathbf{p})\right)\left(U_o(\mathbf{p},t_1)+U_r(\mathbf{p})\right)^* \\ \times\left(U_o(\mathbf{p}-\mathbf{q},t_2)+U_r(\mathbf{p}-\mathbf{q})\right)\left(U_o(\mathbf{p}-\mathbf{q},t_2)+U_r(\mathbf{p}-\mathbf{q})\right)^*\end{array}\right\rangle \tag{2}$$

The complex field amplitude of the reference field $U_r(\mathbf{p})$ is described locally at the image plane, while the complex field amplitude of the object field scattered off the object, $U_s(\mathbf{r},t_i)$, is propagated to the observation plane via the Green's function, $G(\mathbf{r},\mathbf{p};z(t_i))$, to yield the corresponding image plane complex amplitude $U_o(\mathbf{p},t_i)$: We have

$$U_o(\mathbf{p},t_i)=\int_S \mathrm{d}^2\,\mathbf{r}\,U_s(\mathbf{r},t_i)\,G\left(\mathbf{r},\mathbf{p},z(t_i)\right), \tag{3}$$

where the index (i = 1,2) link t_i and z_i to the two object positions under consideration, and where

$$G(\mathbf{r},\mathbf{p};z_i)=-\frac{\mathrm{i}k}{2\pi B}\exp\left(-\mathrm{i}k(L'+z_i)\right)\exp\left(-\frac{\mathrm{i}k}{2B}\left(A\mathbf{r}^2-2\mathbf{r}\cdot\mathbf{p}+D\mathbf{p}^2\right)\right) \tag{4}$$

is the paraxial Green's function for propagation of a scalar field through an arbitrary paraxial optical system, described by the *ABCD*-formalism [12]. The optical wavenumber is denoted by k, and L' describes the optical path length from object to observation. While L is the physical distance, L' is the optical propagation length through air and glass components. We assume an ideal clean imaging system with two lenses (of focal lengths f_1 and f_2) with a limiting Gaussian aperture located in the Fourier plane and having an e^{-1} transmission radius σ [11]. The assumption that the imaging system is unaffected by the object movement from time t_1 to t_2, ensures that the same *ABCD* elements can be used for both Green's functions. However, the initial ($L'+z_1$) and final ($L'+z_2$) optical path lengths must be inserted.

The complex field amplitude of the reflected field at the object plane is modeled as:

$$U_s(\mathbf{r},t)=U_i(\mathbf{r})\Psi(\mathbf{r},t), \tag{5}$$

where $U_i(\mathbf{r})$ is the complex field amplitude, of light incident on the object, and $\Psi(\mathbf{r},t)$ is a complex reflection coefficient of zero mean, $\langle\Psi(\mathbf{r},t)\rangle = 0$. However, the modulus of $\Psi(\mathbf{r},t)$ is assumed to be constant, and equal to unity (no absorption). The complex reflection coefficient models the spatial phase distortion of the scattered light as a stationary stochastic process. From time t to time $t+\tau$, the object moves as a rigid body by an amount of $\Delta\mathbf{r}(\tau)$, and accordingly $\Psi(\mathbf{r},t)$ will change in time so that $\Psi(\mathbf{r}+\Delta\mathbf{r}(\tau),t+\tau) = \Psi(\mathbf{r},t)$.

Following the analysis described in [15], the correlation function for the complex reflection coefficient is modeled by a Gaussian function and can be expressed as

$$B_\psi(\mathbf{r}_1,\mathbf{r}_2)=\left\langle\Psi(\mathbf{r}_1,t_1)\Psi^*(\mathbf{r}_2,t_2)\right\rangle=\frac{4\pi}{k^2}\left(\frac{2}{\pi r_c^2}\exp\left[-\frac{2\left|\mathbf{r}_2-\mathbf{r}_1\right|^2}{r_c^2}\right]\right), \tag{6}$$

where r_c is a measure of the phase correlation length of the target surface. However, in the following we assume complete spatial incoherence (i.e. $r_c \to 0$), and find accordingly that Eq.6 becomes

$$B_\Psi(\mathbf{r}_1,\mathbf{r}_2)=\left(\frac{4\pi}{k^2}\right)\delta(\mathbf{r}_2-\mathbf{r}_1), \tag{7}$$

where $\delta(\cdot)$ is the Dirac delta function.

The spatial cross-correlation function given in Eq.2 can be expanded and categorized into the following sum of product terms:

$$\begin{aligned} C(\mathbf{p},\mathbf{p}+\mathbf{q};\Delta\mathbf{r},\Delta z) = {} & C_{oooo}(\mathbf{p},\mathbf{p}+\mathbf{q};\Delta\mathbf{r},\Delta z) + C_{rrrr}(\mathbf{p},\mathbf{p}+\mathbf{q};\Delta\mathbf{r},\Delta z) + C_{oorr}(\mathbf{p},\mathbf{p}+\mathbf{q};\Delta\mathbf{r},\Delta z) \\ & + C_{oror}(\mathbf{p},\mathbf{p}+\mathbf{q};\Delta\mathbf{r},\Delta z) + C_{ooor}(\mathbf{p},\mathbf{p}+\mathbf{q};\Delta\mathbf{r},\Delta z) + C_{orrr}(\mathbf{p},\mathbf{p}+\mathbf{q};\Delta\mathbf{r},\Delta z) \end{aligned}, \quad (8)$$

where the indices "*o*" and "*r*" reflects the various combinations of object and reference fields in the product terms. [13] has shown that a scattering surface, which in a free-space propagation system can produce fields with circular symmetric complex Gaussian and ergodic random variables, will produce fields of the same statistics in an imaging-configuration system. Therefore, the first term, containing the product of four scattered fields, can be expressed in terms of mutual second-order field correlations [14]:

$$C_{oooo}(\mathbf{p},\mathbf{p}+\mathbf{q};\Delta\mathbf{r},\Delta z) = \left|\left\langle U_o(\mathbf{p},t_1)U_o^*(\mathbf{p}-\mathbf{q},t_2)\right\rangle\right|^2 + \left\langle I_o(\mathbf{p},t_1)\right\rangle\left\langle I_o(\mathbf{p}-\mathbf{q},t_2)\right\rangle, \quad (9)$$

where the intensity of the object field is denoted as, $I_o(\cdot) = U_o(\cdot)U_o^*(\cdot)$. Inserting Eq.3 and Eq.5 into Eq.9 and changing the order of integration yields:

$$\begin{aligned} C_{oooo}(\mathbf{p},\mathbf{p}+\mathbf{q};\Delta\mathbf{r},\Delta z) = {} & \left| \iint_{S_r} d^2\mathbf{r}_1 d^2\mathbf{r}_2 \left[\begin{array}{l} \left\langle \Psi(\mathbf{r}_1,t_1)\Psi^*(\mathbf{r}_2,t_2)\right\rangle \\ \times U_i(\mathbf{r}_1)G(\mathbf{r}_1,\mathbf{p},z_1)U_i^*(\mathbf{r}_2)G^*(\mathbf{r}_2,\mathbf{p}-\mathbf{q},z_2) \end{array} \right] \right|^2 \\ & + \iint_{S_r} d^2\mathbf{r}_1 d^2\mathbf{r}_1' \left[\begin{array}{l} \left\langle \Psi(\mathbf{r}_1,t_1)\Psi^*(\mathbf{r}_1',t_1)\right\rangle \\ \times U_i(\mathbf{r}_1)G(\mathbf{r}_1,\mathbf{p},z_1)U_i^*(\mathbf{r}_1')G^*(\mathbf{r}_1',\mathbf{p},z_1) \end{array} \right] \\ & \times \iint_{S_r} d^2\mathbf{r}_2 d^2\mathbf{r}_2' \left[\begin{array}{l} \left\langle \Psi(\mathbf{r}_2,t_2)\Psi^*(\mathbf{r}_2',t_2)\right\rangle \\ \times U_i(\mathbf{r}_2)G(\mathbf{r}_2,\mathbf{p}-\mathbf{q},z_2)U_i^*(\mathbf{r}_2')G^*(\mathbf{r}_2',\mathbf{p}-\mathbf{q},z_2) \end{array} \right] \end{aligned} \quad (10)$$

As we assume complete spatial incoherence (i.e. $r_c \to 0$), Eq.7 dictates that the only non-zero contribution to the integration is obtained for $\mathbf{r_2} = \mathbf{r_1} + \Delta\mathbf{r}$, where $\Delta\mathbf{r}$ is the in-plane displacement of the object from t_1 to t_2. Thus, we obtain:

$$\begin{aligned} C_{oooo}(\mathbf{p},\mathbf{p}+\mathbf{q};\Delta\mathbf{r},\Delta z) = {} & \left(\frac{4\pi}{k^2}\right)^2 \left| \int_{-\infty}^{\infty} d^2\mathbf{r} U_i(\mathbf{r})G(\mathbf{r},\mathbf{p},z_1)U_i^*(\mathbf{r}+\Delta\mathbf{r})G^*(\mathbf{r}+\Delta\mathbf{r},\mathbf{p}-\mathbf{q},z_1+\Delta z) \right|^2 \\ & + \int_{-\infty}^{\infty} d\mathbf{r} I_i(\mathbf{r})G(\mathbf{r},\mathbf{p},z_1)G^*(\mathbf{r},\mathbf{p},z_1) \\ & \times \int_{-\infty}^{\infty} d\mathbf{r} I_i(\mathbf{r}+\Delta\mathbf{r})G(\mathbf{r}+\Delta\mathbf{r},\mathbf{p}-\mathbf{q},z_2)G^*(\mathbf{r}+\Delta\mathbf{r},\mathbf{p}-\mathbf{q},z_2) \end{aligned} \quad (11)$$

The reference wave field is independent of the ensemble of surfaces and the position of the object, thus the term containing the product of four reference fields is deterministic, i.e.:

$$C_{rrrr}(\mathbf{p},\mathbf{p}+\mathbf{q};\Delta\mathbf{r},\Delta z)=I_r(\mathbf{p})I_r(\mathbf{p}-\mathbf{q}), \tag{12}$$

where the intensity of the reference wave is denoted as, $I_r(\cdot)=U_r(\cdot)U_r^*(\cdot)$. The four terms of the spatial cross-correlation function, containing products of two object fields and two reference fields, have been divided into the following two groups:

$$\begin{aligned} C_{oror}(\mathbf{p},\mathbf{p}+\mathbf{q};\Delta\mathbf{r},\Delta z)&=U_r^*(\mathbf{p})U_r^*(\mathbf{p}-\mathbf{q})\left\langle U_o(\mathbf{p},t_1)U_o(\mathbf{p}-\mathbf{q},t_2)\right\rangle+cc \\ &+U_r^*(\mathbf{p})U_r(\mathbf{p}-\mathbf{q})\left\langle U_o(\mathbf{p},t_1)U_o^*(\mathbf{p}-\mathbf{q},t_2)\right\rangle+cc \end{aligned} \tag{13}$$

and

$$C_{oorr}(\mathbf{p},\mathbf{p}+\mathbf{q};\Delta\mathbf{r},\Delta z)=I_r(\mathbf{p}-\mathbf{q})\left\langle I_o(\mathbf{p},t_1)\right\rangle+I_r(\mathbf{p})\left\langle I_o(\mathbf{p}-\mathbf{q},t_2)\right\rangle, \tag{14}$$

The first term of $C_{oror}(\mathbf{p},\mathbf{p}+\mathbf{q};\Delta\mathbf{r},\Delta z)$ on the right hand side of Eq.13 is a product of fields, where the individual fields do not appear together with their corresponding complex conjugated fields and thus the product becomes equal to zero upon integration. For the second term of $C_{oror}(\mathbf{p},\mathbf{p}+\mathbf{q};\Delta\mathbf{r},\Delta z)$ and its complex conjugated we substitute Eq.3 and Eq.5, into the expression, change the order of integration, use Eq.7 and obtain:

$$\begin{aligned} C_{oror}(\mathbf{p},\mathbf{p}+\mathbf{q};\Delta\mathbf{r},\Delta z)&=\left(\frac{4\pi}{k^2}\right)U_r^*(\mathbf{p})U_r(\mathbf{p}-\mathbf{q}) \\ &\times\int_{-\infty}^{\infty}d^2\mathbf{r}U_i(\mathbf{r})G(\mathbf{r},\mathbf{p},z_1)U_i^*(\mathbf{r}+\Delta\mathbf{r})G^*(\mathbf{r}+\Delta\mathbf{r},\mathbf{p}-\mathbf{q},z_1+\Delta z) \\ &+cc \end{aligned} \tag{15}$$

Again, substituting Eq.3 and Eq.5, into Eq.14, change the order of integration and using Eq.7 we obtain:

$$\begin{aligned} C_{oorr}(\mathbf{p},\mathbf{p}+\mathbf{q};\Delta\mathbf{r},\Delta z)&=\left(\frac{4\pi}{k^2}\right)I_r(\mathbf{p}-\mathbf{q})\int_{-\infty}^{\infty}d^2\mathbf{r}I_i(\mathbf{r})G(\mathbf{r},\mathbf{p},z_1)G^*(\mathbf{r},\mathbf{p},z_1) \\ &+\left(\frac{4\pi}{k^2}\right)I_r(\mathbf{p})\int_{-\infty}^{\infty}d^2\mathbf{r}I_i(\mathbf{r}+\Delta\mathbf{r})\times G(\mathbf{r}+\Delta\mathbf{r},\mathbf{p}-\mathbf{q},z_2)G^*(\mathbf{r}+\Delta\mathbf{r},\mathbf{p}-\mathbf{q},z_2) \end{aligned}, \tag{16}$$

Further, all product combinations containing only a single object or reference field become zero upon integration.

The optical field incident on the object surface is assumed to be a plane wave with a Gaussian distributed field propagating along the optical axis of the system:

$$U_i(\mathbf{r})=E_i\exp\left(-\frac{|\mathbf{r}|^2}{w_i^2}\right), \tag{17}$$

where the phase in the object plane is assumed equal to zero. At the object surface (at $z = 0$), the amplitude of the field is E_i and the profile radius is w_i. The optical reference field incident at the observation plane is also a plane wave with a Gaussian distributed field:

$$U_r(\mathbf{p}) = E_r \exp\left(-\frac{|\mathbf{p}|^2}{w_r^2} + \mathrm{i}\, k\boldsymbol{\varphi}\cdot\mathbf{p} \right) \tag{18}$$

The phase of the field is set equal to zero at the origin of the observation plane. At the observation plan the amplitude of the reference field is E_r and the profile radius is w_r.

2.1.1. Speckle and fringe dynamics for a linearly displaced object

In order to measure linear translation of the object we insert into Eq.4 the *ABCD* elements, specifying a clean imaging system: $A = -f_2/f_1$, $B = -2\mathrm{i}\, f_1 f_2/(k\sigma^2)$, $D = -f_1/f_2$. Then, inserting z_1, z_2, Eq.4, Eq.17 and Eq.18 into Eq.11, Eq.12, Eq.15 and Eq.16, and carrying out the resulting Gaussian integrations, we find the following non-zero correlation terms. Specifically, for the object fields solely we find:

$$C_{oooo}(\mathbf{p},\mathbf{p}+\mathbf{q};\Delta\mathbf{r},\Delta z) = \frac{16E_i^4}{k^4\rho^4\left(1+\frac{f_1^2}{f_2^2}\frac{\rho^2}{2w_i^2}\right)^2} \times \exp\left(-\frac{2\left(|\mathbf{p}|^2+|\mathbf{p}+\mathbf{q}|^2\right)}{\frac{\rho^2}{2}+\frac{f_2^2}{f_1^2}w_i^2} \right) \times \left(1+\exp\left(-\frac{2\left|\mathbf{q}+\left(\frac{f_2}{f_1}+\frac{4f_1f_2}{k^2\sigma^2w_i^2}\right)\Delta\mathbf{r}\right|^2}{\rho^2\left(1+\frac{4f_1^2}{k^2\sigma^2w_i^2}\right)} \right) \right) \tag{19.a}$$

where $\rho = 2\sqrt{2}f_2/(k\sigma)$ is the mean e^{-2} speckle radius. As in [15], the exponential function in the second line of Eq.19.a describes the speckle translation due to in-plane displacement of the object, while the exponential function in the first line depicts the relation between the image intensity and the correlation function. The peak value of the correlation function depends on the image intensity via the positions of the two points to be correlated (**p** and **p**+**q**). The corresponding contribution, for the reference fields only, is given as:

$$C_{rrrr}(\mathbf{p},\mathbf{p}+\mathbf{q};\Delta\mathbf{r},\Delta z) = E_r^4 \exp\left(-\frac{2\left(|\mathbf{p}|^2+|\mathbf{p}+\mathbf{q}|^2\right)}{w_r^2} \right) \tag{19.b}$$

Further, the cross terms $C_{oorr}(\mathbf{p},\mathbf{p}+\mathbf{q};\Delta\mathbf{r},\Delta z)$ and $C_{oror}(\mathbf{p},\mathbf{p}+\mathbf{q};\Delta\mathbf{r},\Delta z)$ are given as

$$C_{oorr}\left(\mathbf{p},\mathbf{p}+\mathbf{q};\Delta\mathbf{r},\Delta z\right)=\frac{4E_i^2E_r^2}{k^2\rho^2\left(1+\frac{f_1^2}{f_2^2}\frac{\rho^2}{2w_i^2}\right)^2}\times\exp\left(-\left(\frac{2}{w_r^2}+\frac{2}{\frac{\rho^2}{2}+\frac{f_2^2}{f_1^2}w_i^2}\right)|\mathbf{p}|^2\right)$$
$$\times\left(\exp\left(-\frac{2}{w_r^2}\left(2\mathbf{p}\cdot\mathbf{q}+|\mathbf{q}|^2\right)\right)+\exp\left(-\frac{2\left(2\mathbf{pq}+|\mathbf{q}|^2\right)}{\frac{\rho^2}{2}+\frac{f_2^2}{f_1^2}w_i^2}\right)\right), \quad (19.c)$$

and

$$C_{oror}\left(\mathbf{p},\mathbf{p}+\mathbf{q};\Delta\mathbf{r},\Delta z\right)=\frac{4E_i^2E_r^2}{k^2\rho^2\left(1+\frac{f_1^2}{f_2^2}\frac{\rho^2}{2w_i^2}\right)}\times\cos\left(k(2\Delta z+\boldsymbol{\varphi}\cdot\mathbf{q})\right)$$
$$\times\exp\left(-\frac{\left|\mathbf{q}+\left(\frac{f_2^2}{f_1^2}+\frac{4f_1f_2}{k^2\sigma^2w_i^2}\right)\Delta\mathbf{r}\right|^2}{\rho^2\left(1+\frac{4f_1^2}{k^2\sigma^2w_i^2}\right)}\right), \quad (19.d)$$
$$\times\exp\left(-\left(\frac{1}{w_r^2}+\frac{1}{\frac{\rho^2}{2}+\frac{f_2^2}{f_1^2}w_i^2}\right)\left(|\mathbf{p}|^2+|\mathbf{p}+\mathbf{q}|^2\right)\right)$$

Eq.19.b and Eq.19.c are independent of the displacement $\Delta\mathbf{r}$, and therefore of no interest for the present discussion**.** The speckle dynamics in Eq.19.d is similar to Eq.19.a, except for the influence of the width of the reference beam w_r in the image-intensity-related correlation term. However, the cosine function describes a uniform fringe structure modulating the speckles with a fringe spacing ($\Lambda_{fr} = \lambda/|\boldsymbol{\varphi}|$) and fringe orientation defined by the angle ($\boldsymbol{\varphi}$) between the object and reference waves. Moreover, the fringes will shift uniformly in the observation plane as the object is displaced out-of-plane, and the fringes will move in a direction that depends on the direction of the out-of-plane motion of the object.

The individual speckles define areas of coherence and constructive interference in the observation plane. Therefore, the phases of the fringe patterns in different speckles are completely uncorrelated. Further, as the speckles decorrelate, the fringes will decorrelate as well.

2.1.2. Speckle and fringe dynamics for an angular displaced object

In order to measure angular velocity, we insert into Eq.4 the *ABCD* elements, specifying a clean imaging system with the virtual lens emulating the angle of rotation located in the object plane: $A = -f_2/f_1 - 4i\, f_1 f_2/(Rk\sigma^2)$, $B = -2i\, f_1 f_2/(k\sigma^2)$, $D = -f_1/f_2$. We replace $\Delta\mathbf{r}$ with $R\Delta\boldsymbol{\theta}$ and insert z_1, z_2, Eq.4, Eq.17 and Eq.18 into Eq.11, Eq.12, Eq.15 and Eq.16 and carry out the resulting Gaussian integrations. Finally, we find the following two correlation terms, which have changed due to introducing the virtual lens:

$$C_{oooo}\left(\mathbf{p},\mathbf{p}+\mathbf{q};\Delta\boldsymbol{\theta},\Delta z\right)=\frac{16E_i^4}{k^4\rho^4\left(1+\frac{f_1^2}{f_2^2}\frac{\rho^2}{2w_i^2}\right)^2}\times\exp\left(-\frac{2\left|\left|\mathbf{p}\right|^2+\left|\mathbf{p}+\mathbf{q}\right|^2\right|}{\frac{\rho^2}{2}+\frac{f_2^2}{f_1^2}w_i^2}\right)$$
$$\times\left(1+\exp\left(-\frac{2\left|\Delta\boldsymbol{\theta}\right|^2}{\frac{4}{k^2w_i^2}+\frac{\sigma^2}{f_1^2}}\right)\times\exp\left(-\frac{2\left|\mathbf{q}+\left(\frac{f_2}{f_1}+\frac{4f_1f_2}{k^2\sigma^2w_i^2}\right)R\Delta\boldsymbol{\theta}\right|^2}{\rho^2\left(1+\frac{4f_1^2}{k^2\sigma^2w_i^2}\right)}\right)\right) \quad (20.a)$$

The second exponential function in the second line in Eq.20.a describes the speckle translation due to out-of-plane rotation of the object. However, in accordance with literature [15], the speckle dynamics does not measure the angular velocity; it merely measures the peripheral velocity of the object, which is proportional to R. The first exponential function in the second line describes the decorrelation of the speckle pattern.

The decorrelation arises as the object rotates and the corresponding speckle pattern rotates as a 3D structure. As a 3D speckle structure rotates $|\Delta\boldsymbol{\theta}|$ through the entire light-collecting angle (σ/f_1) of the imaging system including a diffractive contribution ($2/(kw_i)$), the speckle pattern decorrelates completely in the observation plane.

Specifically, when comparing the decorrelation term with the minimum measurable angular displacement ($\Delta\theta_{min}$), defined as the angular shift which shifts the speckle pattern by a single speckle radius $\Delta\theta_{min} = \rho/R$, we find $R^2 = d_o^2$, where the focal depth is defined as $4f_1^2/(k\sigma^2)$. In case of $R^2 << d_o^2$, the speckle boiling due to object rotation will be so strong that the speckle correlation cannot resolve any speckle shift due to the peripheral velocity. Therefore, any measured shift in the speckle pattern is caused by linear in-plane translation of the object.

The cross term $C_{oror}\left(\mathbf{p},\mathbf{p}+\mathbf{q};\Delta\boldsymbol{\theta},\Delta z\right)$ is given as:

$$C_{oror}\left(\mathbf{p},\mathbf{p}+\mathbf{q};\Delta\boldsymbol{\theta},\Delta z\right)=\frac{4E_i^2E_r^2}{k^2\rho^2\left(1+\frac{f_1^2}{f_2^2}\frac{\rho^2}{2w_i^2}\right)}\cos\left(k(2\Delta z+\boldsymbol{\varphi}\cdot\mathbf{q})+\frac{k\left(2\mathbf{p}+\mathbf{q}\right)\cdot\Delta\boldsymbol{\theta}}{\frac{f_2}{f_1}+\frac{\rho^2}{2w_i^2}}\right)$$
$$\times\exp\left(-\frac{\left|\mathbf{q}+\left(\frac{f_2^2}{f_1^2}+\frac{4f_1f_2}{k^2\sigma^2w_i^2}\right)R\Delta\boldsymbol{\theta}\right|^2}{\rho^2\left(1+\frac{4f_1^2}{k^2\sigma^2w_i^2}\right)}\right) \quad , \quad (20.b)$$
$$\times\exp\left(-\left(\frac{1}{w_r^2}-\frac{1}{\frac{\rho^2}{2}+\frac{f_2^2}{f_1^2}w_i^2}\right)\left(\left|\mathbf{p}\right|^2+\left|\mathbf{p}+\mathbf{q}\right|^2\right)-\frac{2\left|\Delta\boldsymbol{\theta}\right|^2}{\frac{4}{k^2w_i^2}+\frac{\sigma^2}{f_1^2}}\right)$$

The speckle dynamics in Eq.20.b is equivalent to Eq.20.a except for the influence of the width of the reference beam w_r in the image-intensity-related correlation term. However, the cosine function, describing the fringe structure, now contains a second term which dictates a phase shift with a spatial gradient with regard to **p,** and as a function of the angular velocity $\Delta\boldsymbol{\theta}$ – not the peripheral velocity.

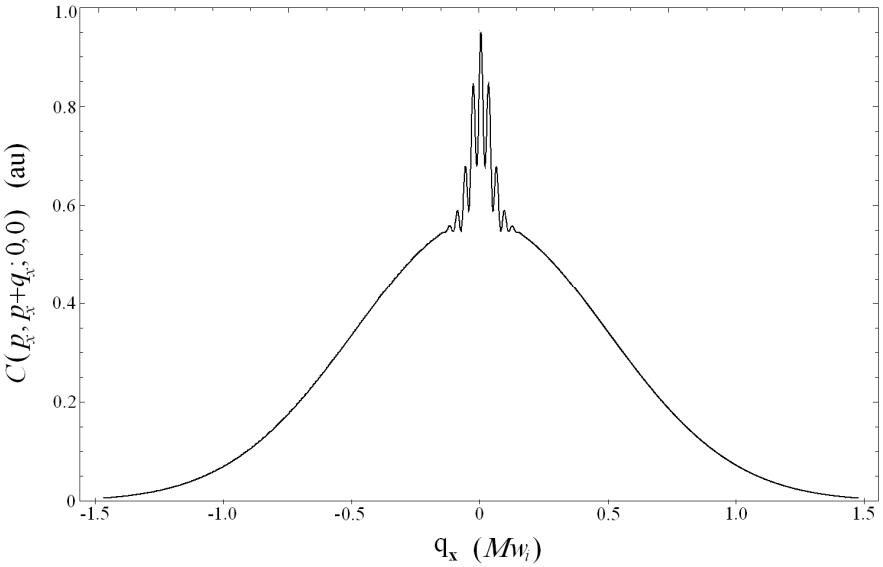

Figure 2. The ensemble averaged correlation function plotted versus q_x in units of Mw_i.

For a more detailed discussion, we assume that the plane of incidence is parallel with the *xz*-plane, $\boldsymbol{\varphi} = (\varphi_x,0)$, $|M| = |f_2/f_1| >> \sigma/(2w_i)$, $Mw_i = w_r$ and that $|\varphi_x| >> |\Delta\theta_x/M|$. This means that the fringe intensity vary along the x-axis. In Figure 2, the corresponding correlation function illustrates the main contributions: The Gaussian background with an e^{-2} radius of Mw_i is the sum of the individual correlation functions of the image of the illuminated region on the object (Eq.20.a), the reference beam (Eq.19.b) and the corresponding cross terms (Eq.19.c). The oscillations are due to the correlation function of the fringe patterns (Eq.20.b). The Gaussian pedestal located just underneath the oscillations, having a radius of $0.1\times Mw_i$, is the correlation function of the speckles (Eq.20.a).

In case the object undergoes an out-of-plane rotation with respect to the *y*-axis, $\Delta\boldsymbol{\theta} = (\Delta\theta_x,0)$, a constant argument of the cosine function dictates that the fringe patterns move along the p_x-direction, according to:

$$q_x = -\frac{2}{\varphi_x}\left(\Delta z + \frac{\Delta\theta_x p_x}{M}\right), \tag{21}$$

while the fringe patterns carry out no displacement along the p_y-direction. The response of the fringe motion q_x to object rotation $\Delta\theta_x$ is independent of *R*, and increases linearly with the distance p_x. Measuring the displacement of the fringes at two arbitrary positions in the observation plane, though with a mutual distance of d_p, the angular displacement $\Delta\theta_x$ can be found independent of Δz and the centre of rotation:

$$\Delta\theta_x = \frac{\varphi_x M}{2d_p}\left(q_{x2} - q_{x1}\right), \tag{22}$$

In case the object moves simultaneously along the z-axis and the centre of rotation is unknown, the actual p_x-position of the centre of rotation must be determined in order to measure the correct value of Δz. The fringe spacing is uniform throughout the observation plane, and defined by $\Lambda_{fr} = \lambda/\varphi_x$. However, in case the criterion of $|\varphi_x| >> |\Delta\theta_x/M|$ is not fulfilled there will be a minor correction to the fringe spacing, which depends on the angular displacement. Accordingly, the fringe spacing will be $\Lambda_{fr} = \lambda/(\varphi_x+\Delta\theta/M)$.

In case the object carries out an out-of-plane rotation with respect to the x-axis, $\Delta\boldsymbol{\theta} = (0,\Delta\theta_y)$, the fringe intensity will still vary uniformly along the p_x-axis. Again, the fringe patterns move in the p_x-direction, while now there is a gradient in fringe movement with respect to the p_y-position:

$$q_x = -\frac{2\Delta\theta_y}{\varphi_x M} p_y, \tag{23}$$

The response of the fringe motion q_x to object rotation $\Delta\theta_y$ is independent of R, and increases linearly with the distance p_y. Again, the displacement of the fringes can be measured at two arbitrary positions in the observation plane, though with a mutual distance of d_p, and the angular displacement $\Delta\theta_y$ can be found as:

$$\Delta\theta_y = \frac{\varphi_x M}{2d_p}\left(q_{y2} - q_{y1}\right), \tag{24}$$

In case the object moves simultaneously along the z-axis and the centre of rotation is unknown, the actual y-position of the centre of rotation must be determined in order to measure the correct value of Δz.

2.2 Optical spatial filtering velocimetry

The technology of optical spatial filter velocimetry [10] is applied to the intensity distribution in the observation plane in order to extract and track any movement of the speckles and the fringes individually and instantaneously. However, it is necessary to distinguish between speckle correlation and optical spatial filtering. Doing speckle correlation as described in section 2.1, a spatial displacement of $\mathbf{q}$ of an intensity structure during two image acquisitions is measured. Applying optical spatial filtering velocimetry, an intensity variation is obtained as a selected spatial frequency component in the intensity distribution travels across the filter located at a fixed position in the observation plane ($\mathbf{q} = \mathbf{0}$). In the same limit as Eq.21, the phase shift $\Delta\phi$ of the cosine function can be written as:

$$\Delta\phi\left(\Delta\theta_x\right) = 2k\left(\Delta z + \frac{\Delta\theta_x p_x}{M}\right). \tag{25}$$

Therefore, in the limit of $|\varphi_x| >> |\Delta\theta_x/M|$, the two measurement techniques differ only by a proportionality factor given as $q_x/\Delta\phi = \Lambda_{fr}/(2\pi)$. In the limit of $|\varphi_x| \sim |\Delta\theta_x/M|$, the proportionality factor deviates with the angular displacement dependent term, however, with regard to the signal-phase shift, Eq.25 still holds because $q_x = 0$. In case we measure motion ($\Delta q_x/\Delta t$) of the fringes rather than displacement, and signal frequency ($2\pi f_s = \Delta\phi/\Delta t$) rather than signal phase shift; we have:

$$\begin{aligned} f_s &= \frac{2}{\lambda}\left(v_z + \frac{\Delta\theta_x}{\Delta t}\frac{p_x}{M}\right) \\ &= \frac{1}{\Lambda_{fr}}\frac{\Delta q_x}{\Delta t} \end{aligned}. \tag{26}$$

Therefore, in the following we assume that the fringe spacing $\Lambda_{fr} = \lambda/\varphi_x$ is a well calibrated constant.

In principle, a filter dedicated for optical spatial filtering velocimetry responds to the presence of a narrow spatial frequency component, and produces one or several photocurrents $i_\theta(\mathbf{s})$ at mutually different phase steps, indicated by the index, θ. Say that the addressed optical structure shifts along the p_x-axis of the observation plane by a distance of s_x according to object movement, then the photocurrents oscillate through a phase change proportional to s_x. The response of such a photocurrent $i_\theta(\mathbf{s})$ can be described as a function of the displacement $\mathbf{s}$ of the addressed optical structure relative to the spatial filter:

$$i_\theta(\mathbf{s}) = \int_{-\infty}^{\infty} d^2\mathbf{p}\, I(\mathbf{p}-\mathbf{s})\, h_\theta(\mathbf{p}). \tag{27}$$

The response function of the spatial filter is $h_\theta(\mathbf{s})$, where $\mathbf{s}$ might be a function of time. The spatial power spectrum of the photocurrent is given by $P_i(\boldsymbol{\xi}) = P_I(\boldsymbol{\xi})H(\boldsymbol{\xi})$, where $P_I(\boldsymbol{\xi})$ is the spatial power spectrum of the optical intensity distribution, $I(\mathbf{p})$, and $H(\boldsymbol{\xi})$ is the spatial power spectrum of the transmission function.

An optical spatial filter with a rectangular-weighted, linear rectangular-array transmission function [16] can be implemented as a comb array of N equally weighted unit cells. The spacing between the unit cells in the array is labeled as Λ_i, where the index indicates the component of displacement to be measured. The number (N) of unit cells and the spacing (Λ_i) between unit cells determines the selectivity and the spatial centre frequency of the filter, respectively. The unit cell contains four rectangular photodetectors with the dimensions of $w \times L = (\Lambda_i/4) \times L$, having rectangular transmission functions. The corresponding unit cell is illustrated in Figure 3 and produces two differential photocurrents, having a mutual phase step of $\pi/2$. The differential photocurrents are $i_1(\mathbf{s}) = i_0(\mathbf{s}) - i_\pi(\mathbf{s})$ and $i_2(\mathbf{s}) = i_{\pi/2}(\mathbf{s}) - i_{3\pi/2}(\mathbf{s})$.

The corresponding spatial power spectrum $H(\boldsymbol{\xi})$ for the transmission function [16] of the spatial filter producing each of the differential photocurrents becomes:

$$H(\xi) = (2\xi_0 D\Lambda_i w)^2 \left\{ \sum_{n=-\infty}^{\infty} \delta(\xi - (2n+1)\xi_0) \times \mathrm{sinc}^2(w\xi) \right\} \otimes \mathrm{sinc}^2(D\Lambda_i \xi) \tag{28}$$

where N is the number of unit cells within the truncated transmission function (i.e. the length of the spatial filter is $N\Lambda_i$), $\xi_0 = 1/\Lambda_i$ is the fundamental spatial frequency of the filter, and $\otimes$ indicates convolution. The power spectrum is plotted for $N = 9$, 65 and 3 in Figure 4, Figure 5 and Figure 6, respectively. The power spectrum contains no information about the individual phases of the spatial filter, thus Eq.28 is identical for both parts of the spatial filter producing the two differential signals, $i_1(\mathbf{s})$ and $i_2(\mathbf{s})$. Optical spatial filters with higher suppression of the harmonics can be found in e.g. [10].

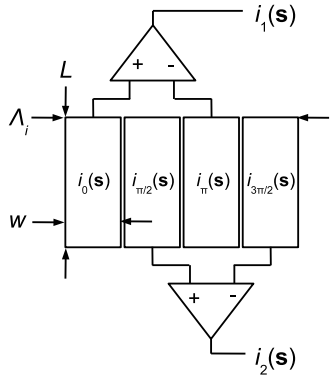

Figure 3. The four detectors define a single unit cell from a spatial band-pass filter with N unit cells. The four detectors provide two differential signals in mutual phase quadrature.

In case of linear translation of the object in 3D, Eq.19.a and Eq.19.d predict that the fringe spacing is uniform throughout the observation plane, and that the displacement of the fringes or the speckles in response to object motion is uniform as well. Therefore, an optical spatial filter with a relative high selectivity (N = 8-100) applied to this type of fringe and speckle dynamics can provide measurements with high precision. The selectivity increases with the number of unit cells in the array [10,25]. Nevertheless, the maximum selectivity of the photocurrent is limited by the decorrelation length of the speckles. The ensemble average power spectrum of the intensity distribution ($P_I(\boldsymbol{\xi})$ can be determined as the Fourier transform of the cross-correlation function in Figure 2, and is illustrated in Figure 4. The narrow Gaussian contribution at the top and centered at $\xi = 0$ consists of the spectra of the image of the illuminate spot and the reference beam. The broad Gaussian contribution below and centered at $\xi = 0$ is the speckle spectrum, and the two satellite peaks centered at $\xi = \pm 6$ are the spectrum of the fringes patterns. Further, Figure 4 illustrates the power spectrum, $H(\boldsymbol{\xi})$, for a spatial filter, designed to track the uniform displacement of the speckle pattern. The power spectrum is determined from Eq.28, and due to the speckles being relative large structures, the spatial filter is designed with a moderate selectivity with N = 9 unit cells. As mentioned for Eq.27, the power spectrum of the photocurrent ($P_i(\boldsymbol{\xi})$) is defined as the product of the two spectra ($P_I(\boldsymbol{\xi})H(\boldsymbol{\xi})$). Therefore, Figure 4 illustrates how the fundamental frequencies ($\pm 1/\Lambda_{x/y}$) of the spatial filter have to coincide with a significant spatial frequency contribution within the speckle spectrum to ensure sufficient signal level. At the same time, the higher harmonics of the spatial filter should preferably be located beyond the spectral contents of the speckles to provide a sufficient suppression of their influence. As illustrated in Figure 4, the second harmonic of the spatial filter is designed to coincide with the e^{-2}-radius of the Gaussian speckle spectrum in order to suppress the higher harmonics. The corresponding criterion for the spatial filter can be written as:

$$\Lambda_{x/y} = 3\sqrt{2}\,\frac{\lambda f_2}{\sigma} \tag{29}$$

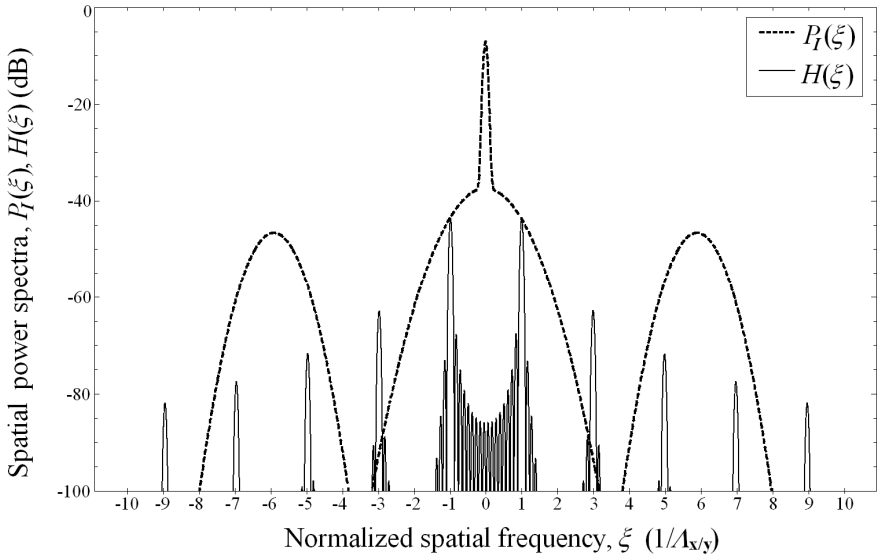

Figure 4. The spatial power spectrum (Eq.28) of a spatial filter, designed to respond to the presence of speckles, is illustrated. The spatial filter is designed with a moderate selectivity, defined by N = 9 unit cells in the array. The unit of the spatial frequency is $1/\Lambda_{x/y}$. The fundamental frequency of the spatial filter is designed to coincide with the

spectral content of the speckles. The logarithmic scales for the two power spectra are equivalent. However, the absolute magnitudes are arbitrary.

Figure 5 illustrates the power spectrum for a spatial filter designed for tracking the uniform displacement of the fringe patterns. The fringe spacing is the smallest structure, thus the spatial filter is designed with a high selectivity (N = 64). In this case, the higher harmonics of this spatial filter are irrelevant for the filter response to fringes because the relative width of spectral contents of the fringe patterns is relatively narrow. The criterion for this spatial filter can be written as:

$$\Lambda_z = \Lambda_{fr} = \frac{\lambda}{|\boldsymbol{\varphi}|} \tag{30}$$

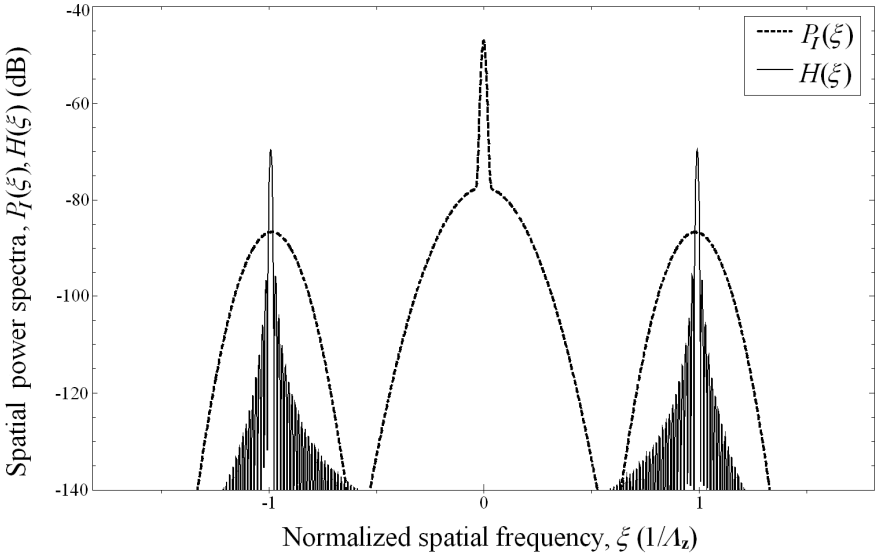

Figure 5. The spatial power spectrum (Eq.28) of a spatial filter, designed to respond to the presence of fringes, is illustrated. The spatial filter is designed with a high selectivity, defined by N = 64 unit cells in the array. The unit of the spatial frequency is $1/\Lambda_z$. The fundamental frequency of the spatial filter is designed to coincide with the spectral content of the fringe patterns. The logarithmic scales for the two power spectra are equivalent. However, their absolute magnitudes are arbitrary.

This behavior of speckles and fringes is numerically and experimentally documented in [7] in full agreement with Eq.19.d. Linear translation of an object in three dimensions, including directions, are measured by using two orthogonal spatial filters responding to the speckles, and one spatial filter responding on the fringe patterns. The three velocity components are measured with an uncertainty of less than ±1%. Figure 4 illustrates that the 5´th and 7´th harmonics of the spatial filter, responding on the speckle patterns, do overlap with the spatial frequency band of the fringe patterns, and therefore cross-talk from fringe motions could possibly contaminate the measurements of speckle motion. This is demonstrated numerically in [7], with a similar setup. However, as it is demonstrated, by choosing a $\boldsymbol{\varphi} = (\varphi_x, \varphi_y)$ where $|\varphi_x| = |\varphi_y|$, a complete suppression of any crosstalk between measurements on fringes and speckles is obtained.

In the case of measuring angular velocity (Eq.22 or Eq.24), the fringe spacing is uniform throughout the observation plane and independent of angular velocity. However, the signal phase shift ($\Delta\phi$) given a certain angular shift $\Delta\theta_x$ varies proportional to the position p_x of the filter in the observation plane. Even, when addressing the two halves of the observation plane with two separate spatial filters, a

spatial filter with a relative large number (N) of unit cells will broaden the relative spectral width significantly, and accordingly reduce the accuracy of this measurement. Instead, a small number of unit cells (N = 1-8) will optimize this specific measurement. In Figure 6, the corresponding spatial power spectrum of a spatial filter is illustrated for N = 3. The criterion for this spatial filter is given in Eq.30. Nevertheless, because the fringe intensity is a sinusoidal intensity distribution, even a single unit cell provides a quasi-sinusoidal photocurrent in response to a constant fringe velocity. Further, the differential measurement used in Eq.22 to determine the angular shift $\Delta\theta_x$ independent of the centre of rotation of the object will be carried out by two spatial filters which are separated by a distance d_p in the observation plane.

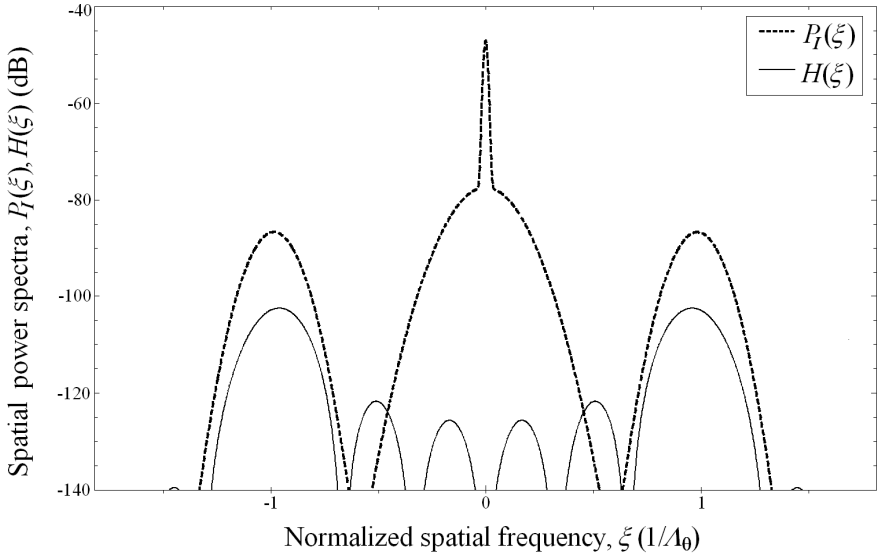

Figure 6. The spatial power spectrum (Eq.28) of a spatial filter, designed to respond to the presence of fringes, is illustrated. The spatial filter is designed with a very low selectivity, defined by N = 3 unit cells in the array. The unit of the spatial frequency is $1/\Lambda_{x/y}$. The fundamental frequency of the spatial filter is designed to coincide with the spectral content of the fringe patterns, see Eq. 30. The logarithmic scales for the two power spectra are equivalent. However, their absolute magnitudes are arbitrary.

3. Experiments and results

The setup is illustrated in Figure 7. A linearly polarized He-Ne laser emits light at a wavelength of 633 nm. With a beam expander the laser light is collimated to a beam with a radius (e^{-2}) of approximately 1 mm, and a confocal parameter of $2b$ = 10 m. The expanded beam is split in two by a non-polarizing beam splitter (BS). The first beam is directed towards the object to illuminate a region on its surface. The illuminated surface region is imaged onto the observation plane by a clean imaging system, consisting of two lenses $f_1 = f_2$ = 250 mm (M = 1.0) and an adjustable aperture located in the focal plane shared by the two lenses. In the experiment, the amplitude transmission function of the aperture is circular with a radius of σ = 0.75 mm. The depth of focus of the given imaging system is approximately d_o = 45 mm. The second beam establishes the reference wave and is directed towards the observation plane, where it coincides with the image of the object under an angle of $\boldsymbol{\varphi}$ = (0.0171 rad, 0.0 rad) relative to the optical axis of the imaging system. The experiment obtains data from three cylindrical objects with radii of R = 3.0, 4.0 and 5.0 mm. The objects are made of aluminum and their surfaces have a grounded finish, which produces fully developed speckles.

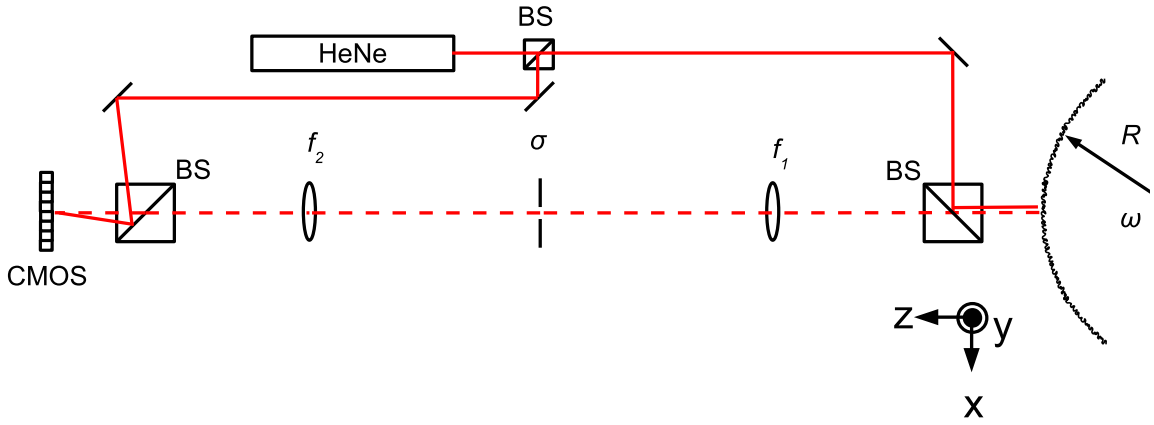

Figure 7. The schematic of the setup for obtaining the experimental data is illustrated. He-Ne: laser, BS: non-polarizing beam splitters, f_1 and f_2: lenses of the imaging system, σ: circular aperture, CMOS; a CMOS camera, and R is the radius of the object. The object rotates with an angular velocity of $\omega = \Delta\theta_x/\Delta t$.

The objects are mounted on a rotational stage. The axes of symmetry of the cylindrical objects are adjusted to coincide with the axis of rotation of the rotational stage. Three different angular velocities have been calibrated for this experiment; $\Delta\theta_{x1}/\Delta t = 1.28\times10^{-3}$ rad/s, $\Delta\theta_{x2}/\Delta t = 1.89\times10^{-3}$ rad/s and $\Delta\theta_{x3}/\Delta t = 2.49\times10^{-3}$ rad/s within a standard deviation of ±0.5%. Note that the angular displacement of the object is parallel with the plane of incidence defined by the optical axis and reference beam. Therefore, the angular displacement of the object and the corresponding fringe displacement will vary in the p_x direction (Eq.22). A CMOS camera is located in the observation plane and has an array of $N_r \times N_c = 256\times256$ pixels with centre spacings of 10.6×10.6 μm^2. The CMOS camera acquires 2-300 sequential images with a well defined frame rate of 17.6 ± 0.1 frames/s. The uncertainty for the frame rate is less than 1%. Therefore, the images are acquired with three angular steps of $\Delta\theta_{x1} = 7.26\times10^{-5}$ rad/frame, $\Delta\theta_{x2} = 1.07\times10^{-4}$ rad/frame and $\Delta\theta_{x3} = 1.41\times10^{-4}$ rad/frame, dependent on the respective angular speed. The sequences of images are stored for later processing. Note that all the images are obtained during a total angular displacement of less than 1% of a revolution of the objects.

During the post processing, the images are multiplied one-by-one, pixel-by-pixel with a set of masks which implements the required phase stepped photocurrents of the spatial filter under consideration [10]. In the image obtained at a displacement of **s**, the photocurrent $i_{s,r,c}$ is obtained due to light incident upon the pixel indexed by row r and column c. The mask contains a transmittance value $\alpha_{\phi,r,c}$ for each individual pixel in the image. During processing of an image sequence, the corresponding photocurrent $i_\phi(\mathbf{s})$ is determined as:

$$i_\phi(\mathbf{s}) = \sum_{c=1}^{N_c}\sum_{r=1}^{N_r} \alpha_{\phi,r,c} i_{\mathbf{s},r,c} \,, \tag{31}$$

Figure 8 illustrates a small fraction of a mask implementing a spatial filter with a rectangular-weighted, linear rectangular-array transmission function with its phase labeled by ϕ. A single unit cell is encapsulated by the thick black frame, and in this case the unit cell is implemented by a structure of a total of $N_u \times N_L$ pixels, and in this case $N_u = 4$. The unit cell is taken out of a linear array of N equivalent unit cells. The physical spacing between the unit cells is $\Lambda_m = N_u \times 10.6$ μm, $w_m = 10.6$ μm is the width of the individual rectangular elements in the unit cells and $L_m = N_L \times 10.6$ μm is the height of the unit cell. In the

experiment, the number of unit cells and height of the unit cell will vary depending on the application. The individual transmittances are illustrated in Figure 8. A second mask, which can produce the phase-shifted photocurrent $i_{\phi+\pi/2}(\mathbf{s})$ is implemented by shifting the transmittances of the first mask one column left or right.

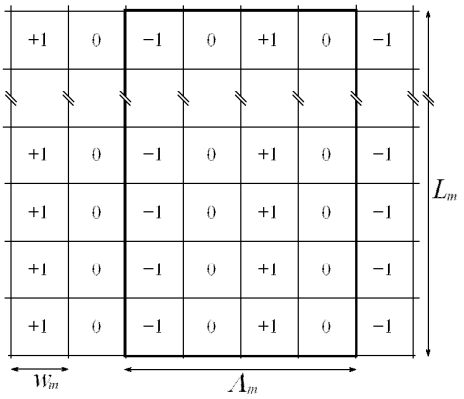

Figure 8. A small fraction of the transmittance mask illustrates a unit cell, being a part of a spatial filter, producing the photocurrent $i_{\phi}(\mathbf{s})$ when processing a sequence of images. A second mask, which produces the photocurrent $i_{\phi+\pi/2}(\mathbf{s})$ in phase quadrature with $i_{\phi}(\mathbf{s})$, is equivalent to the first mask but shifted one column.

The two differential photocurrents, $i_1 = i_{\phi}(\mathbf{s})$ and $i_2 = i_{\phi+\pi/2}(\mathbf{s})$, introduced in section 2.2, are produced directly with these masks. Because the frame rate of the camera is well defined, the two differential photocurrents are listed in the same chronological order as the corresponding images in order to produce sets of time records. Figure 9 illustrates a set of time records of the two photocurrents obtained with a sampling rate of 17.6 S/s. Clearly, the two photocurrents are two similar quasi-sinusoidal signals in mutual phase quadrature. The signal-frequency (f_s) is determined by calculating the power spectra of the time records, and finally, applying a peak-finding algorithm to the power spectra. The signal-frequency is expected to be proportional to the horizontal position in the observation plane. Thus, the spatial average signal-frequency measured by the spatial filter is assumed to represent the displacement at the centre of the spatial filter. As the images progress with the maximum angular displacement rate of $\Delta\theta_{x3}$, the relative deviation in the fringe spacing due to the term, $\Delta\theta_{x3}/(M\varphi_x)$, is predicted to be of the order of 1.0% of the fringe spacing at $\Delta\theta_x = 0$. Thus we assume that the proportionality factor ($q_x/\Delta\phi = 1/(\mathrm{k}\varphi_x)$) between fringe displacement and signal phase shift is independent of the angular displacement throughout these experiments.

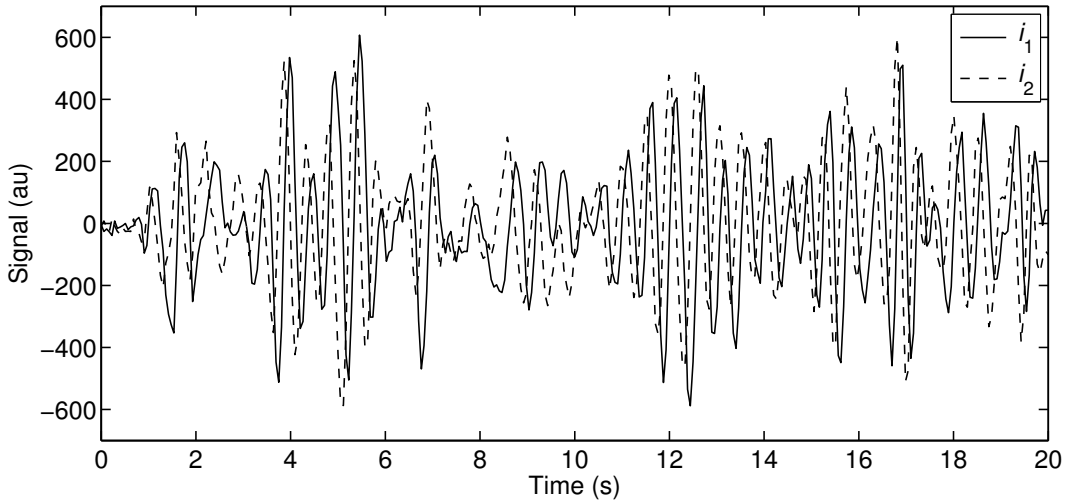

Figure 9. The two time records illustrate the two constructed differential photocurrents, i_1 and i_2, as quasi-sinusoidal functions of time. The two photocurrents are in mutual phase quadrature.

The image in Figure 10 illustrates the regular fringes and the random speckles obtained from the object with a radius of 5.0 mm. The speckle radius is $\rho = 95$ μm and the fringe spacing is estimated from a power spectrum of the image to be $\Lambda_{fr} = 37.0$ μm, thus the mean speckle contains $2\rho/\Lambda_{fr} = 5.1$ fringes. The angular displacement of the object per frame is of $\Delta\theta_{x1} = 7.26\times10^{-5}$ rad/frame. As discussed under Eq.20.a and Eq.20.b, an important limit was defined by the criterion of $R^2 << d_o^2$, where speckle boiling dominates any speckle translation in response of the peripheral velocity of the object. As $d_o = 45$ mm compared to $R = 5.0$ mm, the criterion indicates that Eq.20.a and Eq.20.b are well within the limit, and accordingly we observe no measurable speckle translation in any of the image sequences. Therefore, in case we observe a translation of the speckles with an optical spatial filter, the measurement will contain no information about the angular displacement of the object.

The displacement rate of the fringes throughout the observation plane is measured by probing the intensity in the observation plane with a spatial filter, using the following parameters $N = 8$ unit cells and $L_m = 32\times10.6$ μm. Thus, the total area of the spatial filter is 32×32 pixels, and the filter is scanned by 8×8 steps in order to measure throughout the entire frame. As the centre frequency of the spatial filter is specified by a pitch of the unit cells of $\Lambda_m = 4\times10.6$ μm = 42.4 μm ($\neq\Lambda_{fr}$), the spatial filter does not match the fringe spacing exactly. Still, the signal levels are sufficient for the experiments. The signal-frequencies have been plotted as the corresponding fringe-displacements rates in a vector map, and the vector map has been printed superimposed on the image in Figure 10. As we expect from Eq.21, the local horizontal signal-frequency ($f_{s,x}(p_x) = f_{s,x}(p_x,p_y)$) for the spatial filter is proportional to the horizontal centre position p_x of the spatial filter in the observation plane. Vertically, the signal-frequency ($f_{s,y}(p_x,p_y)$) is less than the measurement uncertainty at any position. Note that the centre of rotation does not coincide exactly with the origin of the image. Further, the measurements in the corner of the vector map fails due to the lack of image intensity, as expected from the image-intensity-related correlation term in Eqs.20.a and 20.b.

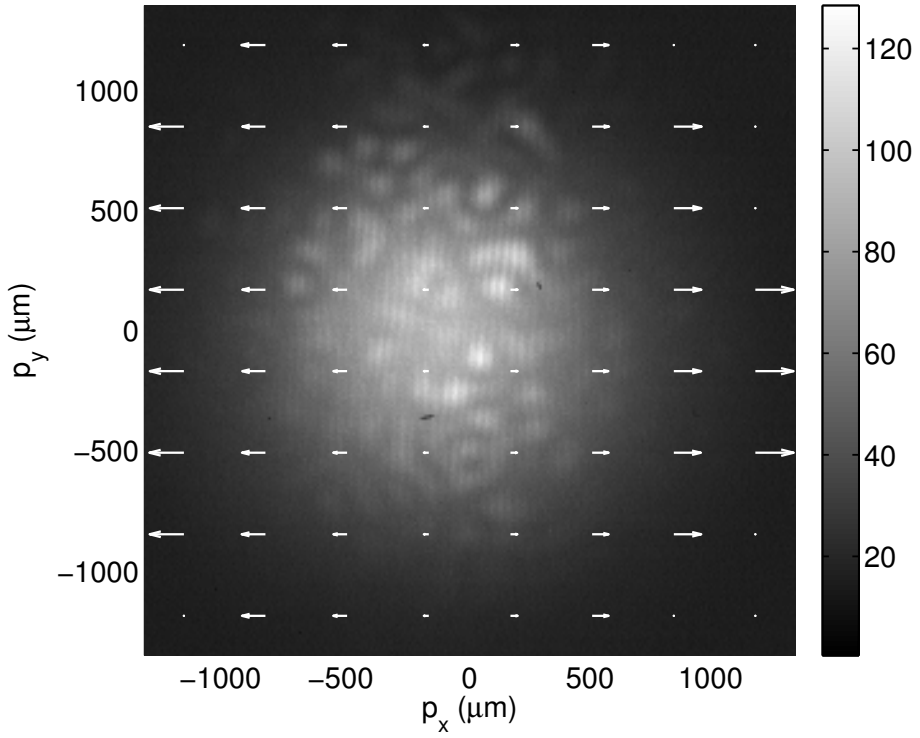

Figure 10. The image illustrates the fringes and the speckles and is overlaid with a vector map that illustrates the horizontal displacement rate of the fringes as the object rotates in the horizontal plane.

The influence of the number of unit cells in the spatial filter when probing local fringe displacement rate have been investigated for four different values: $N = 1$, 2, 4 and 8 unit cells. The height of the spatial filters is $L_m = 256 \times 10.6$ μm and its angular velocity is 1.28×10^{-3} rad/s. Clearly, by increasing the number of unit cells from $N = 1$ to $N = 2$, the selectivity of the filter increases and the relative spectral width in the power spectra of the signal decreases. However, for $N > 2$ the relative spectral width increases due to the increasing range in the phase rates of the fringes, as the physical extent of the spatial filter increases with the number of unit cells. Therefore, we select the spatial filter with $N = 2$ unit cells in the rest of this paper. As the gradient of the signal-frequency with respect to the horizontal axis in the observation plane is constant, the spectral widths of the signals are independent of the horizontal position of the spatial filter (constant N). Therefore, the relative spectral width of the signals decreases with increasing horizontal position in the observation plane (assuming that $\Delta z = 0$). As mentioned above, the signal power drops with the image intensity as the distance to the centre of the image increases. Therefore, a compromise between signal power and filter selectivity is of relevance when selecting the two optimum positions for a differential measurement of angular velocity, according to Eq.24.

The expected behaviour of Eq.21 can be quantized in more details. Three image sequences are obtained for an object with a radius of $R = 4.0$ mm, and rotating at the three calibrated angular velocities. With the spatial-filter parameters as selected above ($N = 2$, $L_m = 256 \times 10.6$ μm), the spatial filter is scanned horizontally throughout the images. In Figure 11 the signal-frequency measurements are plotted as the corresponding displacement rate of the fringes ($\Delta q_x/\Delta t = \Lambda_{fi} f_s$, Eq.26) versus the horizontal position of the spatial filter in the observation plane. In this way, the phase quadrature between i_1 and i_2 gives the direction of the fringe displacement rate. The theoretically obtained curves calculated from Eq.21 are plotted as lines in Figure 11.

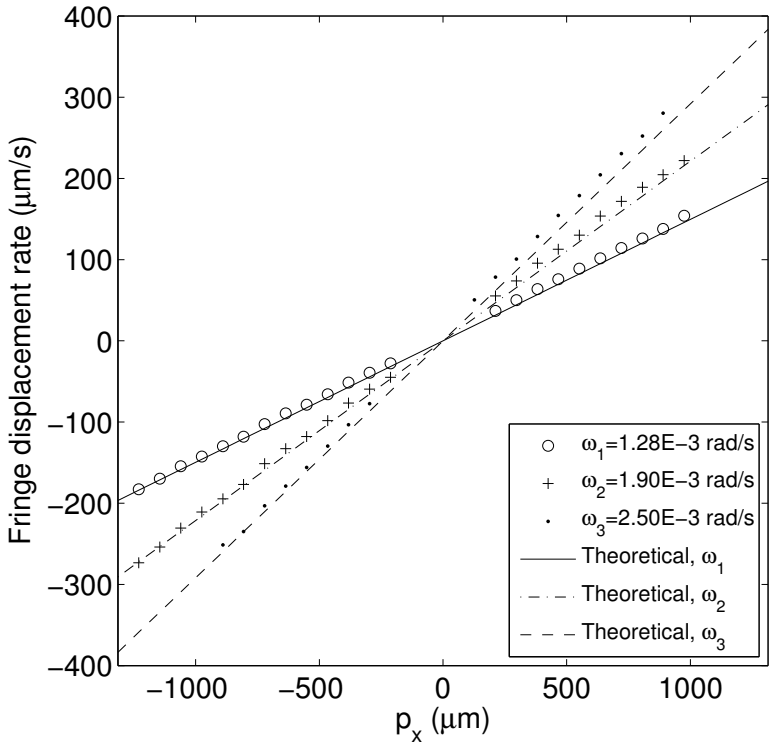

Figure 11. The signal-frequencies are plotted as the local fringe displacement rates versus the horizontal position of the spatial filter in the observation plane. The three calibrated angular velocities are addressed.

Linear regression is applied to the signal-frequency measurements in Figure 11 and provides the statistics listed in Table 1. The parameter c_1 is the first derivative of Eq.26 with respect to p_x, and when adjusted by a factor of $M\varphi/2$ it provides a differential measurement of the angular velocity of the object – equivalent to Eq.22. The corresponding deviations reflect systematic errors, which are apparent in Figure 11. The column of $-c_0/c_1$ reflects the measured position of the image of the centre of the rotation in the observation plane, assuming that the object is stationary along the axial direction, $\Delta z = 0$. The root-mean-square-error (RMSE) indicates the spread of the data points around the trends provided by linear regression. The RMSE value is relative to the angular velocity at $p_x = 1.0$ mm.

To verify that the fringe patterns move with respect to the angular velocity and not due to the peripheral surface velocity, three image sequences are recorded with the three objects, having different radii. All the objects rotate with an angular velocity of $\Delta\theta_{x1}/\Delta t = 1.28\times10^{-3}$ rad/s, and the spatial filter parameters are the same as used above, where $N = 2$ and $L_m = 256\times10.6$ μm. In Figure 12 we have plotted the difference between the measured angular velocities and the theoretical angular velocities (Eq.21) in order to see the deviations between the plots for the three different radii. The best fitted linear regression lines have been plotted as well, and their parameters and the statistics have been listed in Table 2.

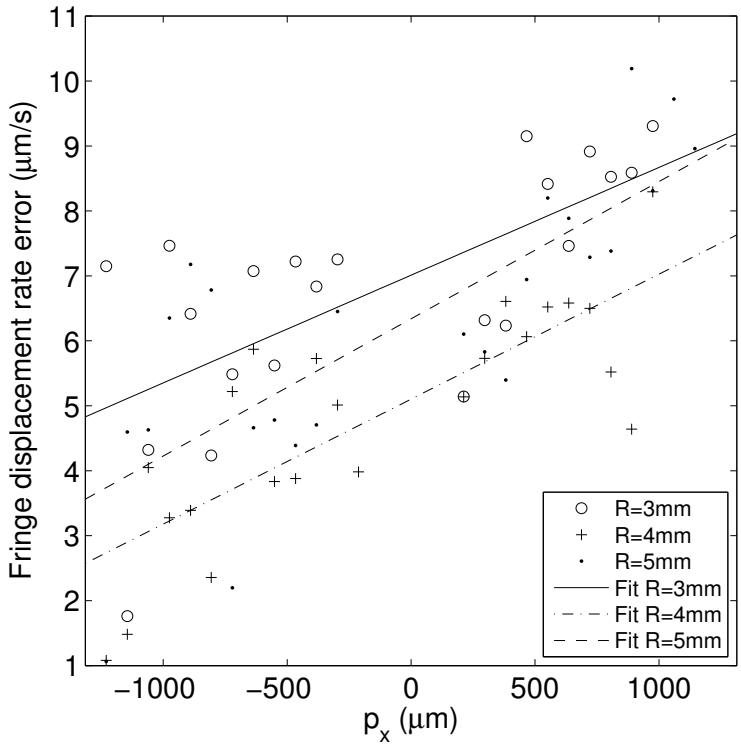

Figure 12. The signal-frequencies are plotted versus the horizontal position of the spatial filter in the observation plane. Three different object radii are addressed; R = 3.0mm, R = 4.0mm and R = 5.0mm.

The finite slopes of the linear regression lines for the angular velocity plots versus p_x are listed in the column $M\varphi c_1/2$ in Table 2 as angular velocities. Again, the slopes reflect the deviation between the measured and the expected values for the angular velocity, being approximately 1%. A correction to this value by 1% brings all the lines of linear regression close to being horizontal lines, separate vertically due to the individual offsets of the centre of rotation of the three objects. Note that throughout the column of c_0/c_1^*, the value for c_1^* is replaced with the value of c_1 determined for $\Delta\theta_x/\Delta t$ = 1.28 mrad/s in Table 1. The column lists the image position of the centre of rotation for the three different objects.

4. Discussion and conclusion

It has been demonstrated theoretically that, by combining speckle photography techniques with speckle interferometry in order to reveal the absolute phase of speckles by interference with a local oscillator (the reference wave), measurements of linear object movement in 3D can be obtained, and conditioned for spatial filtering velocimetry. The expectations are experimentally illustrated in [7], where the linear object motion in 3D is obtained with full directionality, and more importantly, any crosstalk between measurements of fringes and speckle dynamics can be removed completely.

Secondly, the theoretical work indicates that by investigating the dynamics of the optical structures in the observation plane locally, measurements of both out-of-plane rotation components can be obtained. In this work, measurements of angular velocity in the plane of object and reference beam incidence, have been demonstrated to provide systematic errors within few percents, and random errors within 1%.

It was observed experimentally that any effects of the peripheral motion of the surface on the speckle motions could be suppressed satisfactorily by letting the focal depth of the imaging system be substantially larger than the radius of the object ($R^2 << d_o^2$). This means that the speckle decorrelation

length is significantly shorter than any speckle translation obtained in the work here. In case of using a different design where the criterion is different (e.g. $R^2 >> d_o^2$), the peripheral velocity will be directly measurable [18].

With knowledge of the position (p_{cr}) where the image of the centre of rotation of the object is located in the observation plane, Eq.25 reveals both the angular velocity $\Delta\theta_x$ and Δz (to be measured at $p_x = p_{cr}$) for the corresponding type of rotation. However, in case the centre of object rotation is unknown, Δz must be determined by other means. The presence of a second reference beam with a different angle of incidence could be either multiplexed with the original reference beam in time or space. In case the angles of incidence of the primary and secondary reference beams are $-\varphi$ and φ respectively, the centre of rotation will coincide in the measurements from both mixing options for $\Delta z = 0$. If $\Delta z \neq 0$ then Δz will introduce an equivalent magnitude of offset in the measurements, but with a positive or negative sign when mixing with one or the other reference beam. Therefore, the position of the centre of rotation of the object can be found using the symmetric influence of $\Delta z \neq 0$, and finally can the correct Δz be estimated.

Measurement of the orthogonal out-of-plane rotation will require a unit cell of similar Λ_m and orientation as the one use in the experimental work above. However, the height L_m of the unit cell should only be a fraction of the image height in order to avoid a severe spectral broadening of the signal. Instead, the number of unit cells can be increased to e.g. extend the spatial filter across the entire image. To perform differential measurements of the angular displacement $\Delta\theta_y$ or velocity $\Delta\theta_y/\Delta t$, the two spatial filters should be separated by the distance of d_p along the p_y-axis, instead.

The possibility of measuring in-plane rotation is present as well, and has been described thoroughly in [17]. As the object carries out an in-plane rotation with regard to a point in the object plane, similarly will the speckles rotate in the observation plane around a related point in the observation plane. The challenge will be to design the optimum geometry for the optical spatial filter.

The benefit of applying optical spatial filtering velocimetry to the field of speckle interferometry is to obtain real-time measurements without time consuming correlation methods. In this work, a camera based device has been used, but here merely in order to simulate the function of an optical spatial filter and demonstrate the viability of the technique. A complete implementation of speckle and fringe interpretation by optical spatial filtering velocimetry is not within the scope of this work. [7] demonstrates measurements of the axial component Δz with an optical spatial filter, though the processing of the data is carried out still with frequency analysis. In order to implement real-time processing algorithms such as zero-crossing-detection [19], zero-crossing rate detection [20,21] or phase unwrapping of two signals in phase quadrature [22] are required.

Conclusively, the proposed technique can measure motion in all six degrees of freedom. However, as discussed in [7], the decorrelation effects of the speckles will determine the limits and accuracy of the various combinations of measurements obtained from both speckles and fringes simultaneously.

5. Acknowledgement

This work has been partly funded by OPDI Technologies A/S.

6. References and Notes

1. A.E. Ennos, “Speckle Interferometry,” in *Laser Speckle and Related Phenomenon*, J. C. Dainty, ed. (Springer-Verlag, Berlin 1984), pp x-x.
2. J. M. Burke and J. M. J. Tokarski, “Production of multiple beam fringes from photographic scatters,” Opt. Acta **15,** 101 (1968).
3. M. Sjödahl, “Some recent advances in electronic speckle photography,” Opt. Lasers Eng. **29,** 125-144 (1998).
4. I. Yamaguchi, “Fringe formation in deformation and vibration and measurements using laser light,” Progress in Optics **22,** ed. E. Wolf, Elsevier, Amsterdam 1985, 272-340.

5. M. Sjödahl and H. O. Saldner, “Three-dimensional deformation field measurements with simultaneous TV holography and electronic speckle photography,” Applied Optics **36,** 3645-3648 (1997).
6. S.L. Yeh, S.T. Lin and Y.H.Chang, “Precise displacement measurement for a local surface,” Optics Letters **34,** 3406-3408 (2009).
7. T.F.Q. Iversen, M.L. Jakobsen and S.G. Hanson, ”Speckle-based three-dimensional velocity measurement using spatial filtering velocimetry,” Applied Optics **50,** x-x (2011).
8. J.T. Ator, “Image velocity sensing by optical correlation,” Applied Optics **5,** 1325-1331 (1966).
9. J. A. Leendertz and J. N. Butters, "An imaging –shearing speckle-pattern interferometer for measuring bending moments," J. Phys. E: Sci. Instrum. **6,** 1107-1110 (1973).
10. Y. Aizu and T. Asakura, *Spatial filtering velocitmetry: Fundamentals and applications*, (Springer-Verlag, Berlin Heidelberg 2006).
11. H. T. Yura and S.G. Hanson, “Optical beam wave propagation through complex optical systems,” J. Opt. Soc. Am. A **4,** 1931-1948 (1987).
12. A.E. Siegman, *Lasers*, (University Science, Mill Valley, Calif. 1986).
13. S. Lowenthal and H. Arsenault, "Image formation for coherent diffuse objects: statistical properties," J. Opt. Soc. Am. **60,** 1478-1483 (1970).
14. J.W. Goodman, *Speckle phenomena in optics: Theory and applications*, (Roberts and Company Publishers, Greenwood Village, 2006).
15. H.T. Yura, B. Rose and S.G. Hanson, "Dynamic laser speckle in complex ABCD optical systems," J. opt. Soc. Am. A **15,** 1160-1166, (1998).
16. U. Schnell, J. Piot and R. Dändliker, “Detection of movement with laser speckle patterns: statistical properties,” J. Opt. Soc. Am. A **15,** 207-216 (1998).
17. H.T. Yura, B. Rose and S.G. Hanson, “Speckle dynamics from in-plane rotating diffuse objects in complex ABCD optical systems,” J. opt. Soc. Am. A **15,** 1167-1173, (1998).
18. M.L. Jakobsen and S.G. Hanson, “Miniaturised optical sensors for industrial applications,” Proc. SPIE **7726,** 77260P-1 (2010).
19. N. Takai, T. Iwai, and T. Asakura , “Real time velocity measurements for a diffuse object using zero-crossing of laser speckle,” J. Opt. Soc.Am. **70,** 450-455 (1980).
20. R. Barakat, “The level-crossing rate and above-level duration time of the intensity of a Gaussian random process,” Inf. Sci. (NY) **20,** 83-87 (1980).
21. M.L.Jakobsen, F. Pedersen and S.G. Hanson, “Zero-crossing detection algorithm for arrays of optical spatial filtering velocimetry sensors,” Proc. SPIE **7003,** 70030T-1 (2008).
22. M.L. Jakobsen., H.E. Larsen and S.G. Hanson, “Optical spatial filtering velocimetry sensor for submicron, in-plane vibration measurements,” J. Opt. A: Pure Appl. Opt. **7,** S303-S307 (2005).

7. Tables

Table 1. The fitted parameters of a linear regression applied to angular velocities estimated from the measured signal frequencies plotted in Figure 11 can be specified as: $f_{s,x}^{measured} = c_0 + c_1 p_x$, and are listed below. The RMSE value is relative to the angular velocity at p_x = 1.0 mm.

Angular velocity $\Delta\theta_x/\Delta t$ (mrad/s)	$-c_0/c_1$ (μm)	$M\varphi c_1/2$ (mrad/s)	R-square	RMSE (% @ p_x = 1 mm)
1.28	-33.7	1.29	0.9999	0.71
1.89	-31.1	1.93	0.9998	1.15
2.49	-41.0	2.58	0.9999	0.67

Table 2. The fitted parameters of a linear regression applied to the measured velocity data plotted can be specified as: $f_{s,x}^{measured} - f_{s,x}^{theoretical} = c_0 + c_1 p_x$, and are listed below. The RMSE value is relative to the angular velocity at p_x = 1.0 mm.

Radius of curvature R (mm)	$-c_0/c_1^*$ (μm)	$M\varphi c_1/2$ (mrad/s)	R-square	RMSE (% @ p_x = 1 mm)
3	-46.2	1.42×10^{-2}	0.451	0.92
4	-33.7	1.64×10^{-2}	0.635	0.72
5	-41.8	1.81×10^{-2}	0.591	0.94

8. Figure list

Figure 1. Setup for describing the image-shearing speckle-pattern interferometer.

Figure 2. The ensemble averaged correlation function plotted versus q_x in units of Mw_i.

Figure 3. The four detectors define a single unit cell from a spatial band-pass filter with N unit cells. The four detectors provide two differential signals in mutual phase quadrature.

Figure 4. The spatial power spectrum (Eq.28) of a spatial filter, designed to respond to the presence of speckles, is illustrated. The spatial filter is designed with a moderate selectivity, defined by $N = 9$ unit cells in the array. The unit of the spatial frequency is $1/\Lambda_{x/y}$. The fundamental frequency of the spatial filter is designed to coincide with the spectral content of the speckles. The logarithmic scales for the two power spectra are equivalent. However, the absolute magnitudes are arbitrary.

Figure 5. The spatial power spectrum (Eq.28) of a spatial filter, designed to respond to the presence of fringes, is illustrated. The spatial filter is designed with a high selectivity, defined by $N = 64$ unit cells in the array. The unit of the spatial frequency is $1/\Lambda_z$. The fundamental frequency of the spatial filter is designed to coincide with the spectral content of the fringe patterns. The logarithmic scales for the two power spectra are equivalent. However, their absolute magnitudes are arbitrary.

Figure 6. The spatial power spectrum (Eq.28) of a spatial filter, designed to respond to the presence of fringes, is illustrated. The spatial filter is designed with a very low selectivity, defined by $N = 3$ unit cells in the array. The unit of the spatial frequency is $1/\Lambda_{x/y}$. The fundamental frequency of the spatial filter is designed to coincide with the spectral content of the fringe patterns, see Eq. 30. The logarithmic scales for the two power spectra are equivalent. However, their absolute magnitudes are arbitrary.

Figure 6. The schematic of the setup for obtaining the experimental data is illustrated. He-Ne: laser, BS: non-polarizing beam splitters, f_1 and f_2: lenses of the imaging system, σ: circular aperture, CMOS; a CMOS camera, and R is the radius of the object. The object rotates with an angular velocity of $\omega = \Delta\theta_x/\Delta t$.

Figure 7. A small fraction of the transmittance mask illustrates a unit cell, being a part of a spatial filter, producing the photocurrent $i_\phi(\mathbf{s})$ when processing a sequence of images. A second mask, which produces the photocurrent $i_{\phi+\pi}(\mathbf{s})$ in phase quadrature with $i_\phi(\mathbf{s})$, is equivalent to the first mask but shifted one column.

Figure 8. The two time records illustrate the two constructed differential photocurrents, i_1 and i_2, as quasi-sinusoidal functions of time. The two photocurrents are in mutual phase quadrature.

Figure 9. The image illustrates the fringes and the speckles and is overlaid with a vector map that illustrates the horizontal displacement of the fringes as the object rotates in the horizontal plane.

Figure 10. The signal-frequencies are plotted as the local fringe displacement rates versus the horizontal position of the spatial filter in the observation plane. The three calibrated angular velocities are addressed.

Figure 11. The signal-frequencies are plotted versus the horizontal position of the spatial filter in the observation plane. Three different object radii are addressed; $R = 3.0$mm, $R = 4.0$mm and $R = 5.0$mm.

Paper V

Optical touch screen technology based on waveguide sensing

Henrik C. Pedersen[1], Michael L. Jakobsen[1], Steen Hanson[1],
Morten Mosgaard[2], Theis Iversen[2], and Jorgen Korsgaard[2],
[1]*DTU Fotonik, Technical University of Denmark, 4000 Roskilde, Denmark*
[2]*OPDI Technologies A/S, Frederiksborgvej 399, 4000 Roskilde, Denmark*

(Received xxxx; accepted xxxxx; published xxxxx)

We disclose a simple optical touch screen device comprising a planar injection molded polymer waveguide, a single laser (VCSEL) and a small linear detector array. The solution significantly reduces the complexity and cost as compared to existing optical touch technologies. Force detection of a touching finger is also demonstrated.

The introduction of Apple's iPhone in 2007 was indeed responsible for a breathtaking development of touch screens. Not only did the worldwide production of touch screens explode (>400 M units in 2009[1]) but the technical evolution experienced a great boost as well. Features like dual touch (allowing magnifying/rotating pictures), internet and e-mail access and advanced gaming were all contributing to raise the bar for the touch screens to come. On top of that there has been an on-going development towards larger screens, such as tablet computers and laptops.

Today, at least twelve different touch screen technologies have made it to the market; however, two technologies are dominating: resistive and projected capacitive[1]. Resistive is still the preferred technology due to low price, but projected capacitive is catching up especially for portable devices like smart phones.

Optical touch screens have been available on the market for more than 40 years[2]. The classical types known from industrial control panels rely on traditional "over-the-surface" techniques, in which two arrays of light emitters arranged along two adjacent sides of the display pass light above the display towards corresponding arrays of light detectors at the opposite sides. When a finger touches the display, two perpendicular light beams are blocked, respectively, in the x and y directions, leading to an immediate determination of the finger location. Such systems do have certain advantages over capacitive touch screens used in many handheld devices today (e.g. Apple's iPhone), in that no force needs to be exerted on the screen and no electrically conducting coatings need to be applied to the screen; the latter reducing the visibility of the display. Moreover, the optical solution is easily scalable to large size, unlike the electronic solutions. There are, however, also several draw-backs of the over-the-surface solutions, such as sensitivity to ambient light, high cost and complexity (because of the large amount of light sources and detectors) and the fact that a bezel is needed around the edge of the display, which especially for handheld devices is undesirable.

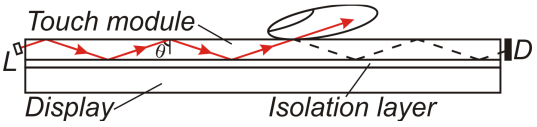

FIG. 1. Principle of a waveguide-based touch screen. *L* = light source, *D* = detector, θ = angle of interrogation.

In a second type of optical touch screen the grid of light beams are guided in a dielectric sheet placed right on top of the display. The light blocking then relies upon disturbing the total-internal-reflection[3-5], as illustrated in Fig. 1. The angle of interrogation θ is chosen between

$$\theta_{c,il} < \theta < \theta_{c,f} \ ,$$
$$\theta_{c,il} = \arcsin(\frac{n_{il}}{n_{wg}}), \ \ \theta_{c,f} = \arcsin(\frac{n_f}{n_{wg}}) \ , \qquad (1)$$

- where $\theta_{c,il}$ and $\theta_{c,f}$ are the critical angles at the isolation layer and the finger, respectively, and $n_{il,wg,f}$ are the refractive indices of isolation layer, waveguide, and finger, respectively. In this case the light is picked up a touching finger, leaving the corresponding detector dark. Hence, by arranging arrays of light emitters along two sides of the touch module and arrays of detectors along the two opposite edges, the touch location is easily derived from the two dark detectors. However, due to the large amount of light sources and detectors needed to cover the entire display area, this type of touch screen was never commercialized.

The objective of the present paper is to present a waveguide based optical touch screen in which the amount of light sources and light detectors is significantly reduced.

The touch screen is based on the same total-internal-reflection principle, as shown in Fig. 1. However, the light rays are distributed quite differently, as shown in a top view in Fig. 2. The touch module comprises a transparent plastic plate (PMMA), acting as the waveguide, a single laser *V* placed at one corner of the waveguide and a small linear detector array *D.A.* placed at the opposite corner. The lower right corner is shaped as a concave, cylindrical lens that couples light from the laser into the waveguide. The cylindrical lens expands the laser beam into a ±45-deg fan, so that the entire plane of the waveguide is illuminated. The light propagates in the waveguide towards the two opposite

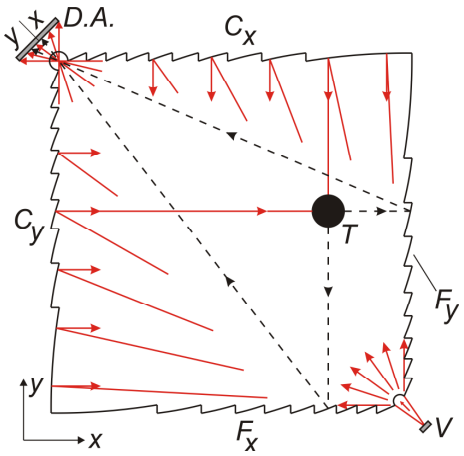

FIG. 2. Top view illustration of the touch module comprising a polymer plate with specially shaped edges, a light source V = Vertical Cavity Surface Emitting Laser (VCSEL) and a linear detector array $D.A.$ $C_{x,y}$ = collimating edges, $F_{x,y}$ = focusing edges, T = touch point. The two x- and y-parts of the detector array are dedicated to the x- and y-scanning rays, respectively.

collimating edges $C_{x,y}$ that are shaped as Fresnel-parabolas and are coated with gold. Here the beams are redirected and collimated along the $-y$ and x axes, respectively, see Fig. 2. At the opposite edges $F_{x,y}$ the beams are redirected and focused at the out-coupling corner (upper left), at which a convex, cylindrical shape carries out the out-coupling towards the x- and y-parts of the detector array.

When touching the surface at position T, the total internal reflection is disturbed in the same manner as illustrated in Fig. 1. As a result, two dark spots are generated at the detector array, which readily gives the x and y coordinates of the touch. This waveguide design solves the problems encountered by the current optical touch screens, since the amount of light sources and detector elements are reduced significantly and there is no bezel along the edges.

However, there is a fundamental issue to be taken care

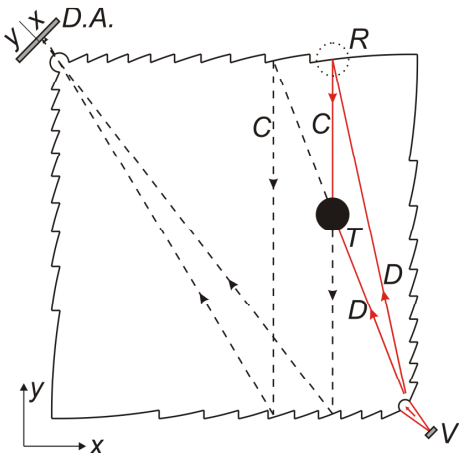

FIG. 3. The fact that both the collimated rays C and the diverging rays D are touch sensitive, leads to unintended, multiple dark spots at the detector array, here illustrated by the two dark spots appearing on the x-part of the detector array. Similarly, two dark spots will appear on the y-part.

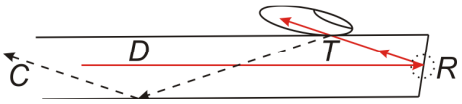

FIG. 4. Cross-sectional view at the reflection point R in Fig. 3. The tilted edge at R alters the angle of interrogation of the reflected rays, making them touch sensitive.

of, since not only the collimated rays are sensitive to touch. This is illustrated further in Fig. 3 showing that also the diverging rays D are disturbed by the touch. This leads to two dark "x-spots" at the detector array. In addition, the focusing rays are also touch sensitive, giving rise to two dark "y-spots". Hence, a single touch leads to a total of four dark spots at the detector array, making the detector signal ambiguous.

Our way of solving this problem is to introduce a tilt to the Fresnel-shaped edges, which is shown in Fig. 4. Here the diverging ray D is incident virtually along the plane of the waveguide, meaning that the angle of interrogation is close to 90 deg. The critical angle for the PMMA/finger interface is arcsin(1.47/1.49) = 80.6 deg,[6] meaning that - according to Eq. (1) - the diverging rays are not touch sensitive. After being reflected, the interrogation angle is decreased by $2\cdot\gamma$, where γ is the tilt angle of the edge. In our case the edge is tilted by 9 deg, meaning that the interrogation angles of the collimated rays are well below the required 80.6 deg, meaning that they become touch sensitive, as illustrated in Fig. 4.

The focusing edges are tilted oppositely, so that the interrogation angles of the focusing rays are also close to 90 deg, making them non-sensitive to touch. In this manner the unintended dark spots are eliminated, leading to the desired two-spot, unambiguous detector signal.

The realized PMMA waveguide is photographed in Fig. 5. The dimensions are 40 x 40 x 1 mm; the Fresnel structures are 0,5 mm deep. As an illustration, the transition from a non-sensitive, in-the-plane ray to a sensitive zig-zag ray is shown. The single zig-zag ray shown may leave the impression that there are only distinct points of interrogation at the surface. However, in reality an angular fan of rays is launched into the waveguide, which smears out the interrogation points to form a continuum. The waveguide is therefore touch sensitive all over the surface.

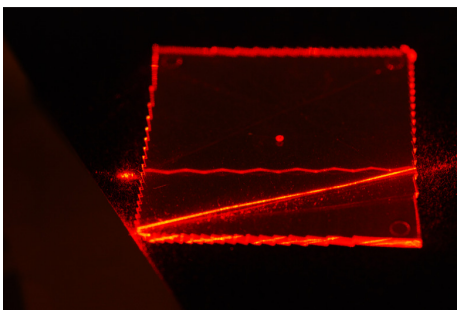

FIG. 5. Photograph of the PMMA waveguide illustrating the effect of the tilted Fresnel-shaped edge: an in-the-plane ray originating from the lower left corner is transformed into a zig-zag ray with interrogation angle = 72 deg.

To test the touch performance, the waveguide was mounted on a block of polytetrafluorethylen (PTFE), which has a refractive index of 1.35 and therefore is well suited as an isolating substrate. A VCSEL (Optowell SS67-4U001, single mode, λ = 670 nm) was used as a light source and a CMOS camera (EHD, SMX-160, 6.6 Mpixel) was used as a detector array. The in-coupling lens had a radius of 0.2 mm, the out-coupling lens had a radius of 3 mm.

The touch module was tested by touching with a finger in different locations, as shown in Fig. 6(a). By subtracting the resulting detector signal from the reference frame (= signal without touch) two peaks appear, as shown in Fig. 6(b). A peak finding algorithm was developed to locate the peaks and from this calculate the finger location, which is shown in Fig. 6(c). Based on this a 5 x 5 keypad was realized and tested successfully. Furthermore, sliding movements across the device were successfully tracked by the algorithm.

The influence of the touch force was also investigated. The device was placed on a scale and the signals resulting from different touch forces were recorded. The results are shown in Fig. 7, revealing that a threshold force of 10 grams was needed to obtain a 10% local change of the signal. The signal increases almost linearly up to 250 grams. The force sensitivity is a very interesting feature for future touch screens, in which a third dimension is necessary. One example is navigating a mouse in three dimensions.[7]

(a)

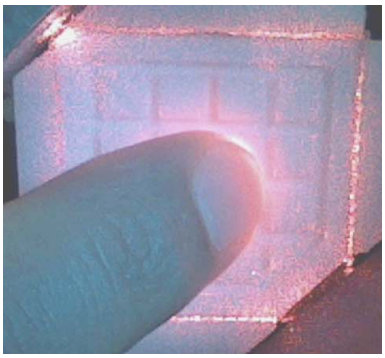

(b)

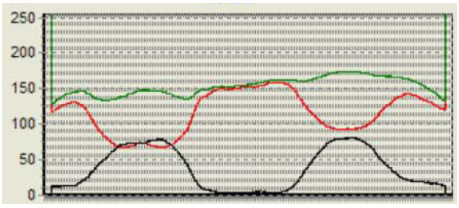

(c)

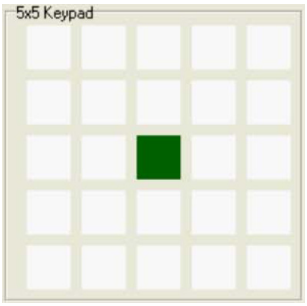

FIG. 6. (a) Realized touch module being tested. Laser light is being launched at the upper left corner, the camera is placed at the opposite corner. (b) Green curve is the un-touched camera signal, red curve is the touched camera signal, the black curve is a result of a subtraction of the green and red curves. (c) Result of the peak finding algorithm that tells the touch location.

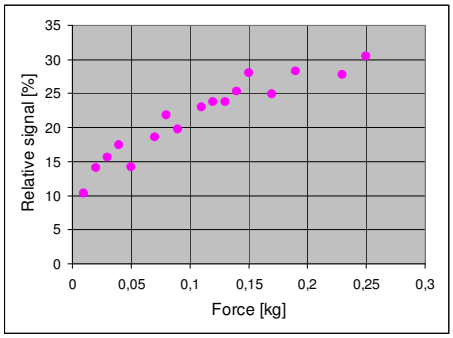

FIG. 7. Average, relative peak heights (in relation to reference signal) of the *x* and *y* peaks versus force applied by the finger.

In conclusion, we have reported an optical touch technology that considerably reduces the cost compared to existing optical technologies. Force detection is also demonstrated, a feature that may add a third dimension to the existing smart phone interactions. We believe that the presented technology is attractive for the high volume touch screen market.

This work was supported by the Danish Council for Technology and Innovation under the Innovation Consortium CINO (Centre for Industrial Nano Optics), grant #75823.

1. M.J. Miller, PCMAG.com, March 3 (2010) http://www.pcmag.com/article2/0,2817,2360930,00.asp
2. I. Maxwell, Information Display, **12,** p. 26 (2007).
3. R.G.Johnson and D. Fryberger, US Patent 3,673,327 (1972).
4. H. Ma and J. A. Paradiso, US patent 2004/0252091.
5. J. Moeller and A. Kerne, *Proceedings of the fourth international conference on Tangible, embedded, and embodied interaction*, Jan. 25-27, p. 73 (2010).
6. The refractive index of a finger was found in A. Knüttel and M. Boehlau-Godau, J. Biomed. Optics, **5**, p. 83 (2000).
7. D. A. Soss, Information Display, **12,** p. 20 (2007).

References with titles

1. M.J. Miller, “Fragmented Touch-Screen Tech Drives Forward”, PCMAG.com, March 3 (2010) http://www.pcmag.com/article2/0,2817,2360930,00.asp
2. I. Maxwell, “An overview of optical-touch technologies”, Information Display, **12,** p. 26 (2007).
3. R.G.Johnson and D. Fryberger, “Touch actuble data input panel assembly”, US Patent 3,673,327 (1972)
4. H. Ma and J. A. Paradiso, “Input device based on frustrated total internal reflection”, US patent 2004/0252091.
5. J. Moeller and A. Kerne, “Scanning FTIR: Unobtrusive optoelectronic multi-touch sensing through waveguide transmissivity imaging”, in *Proceedings of the fourth international conference on Tangible, embedded, and embodied interaction*, Jan. 25-27, 2010, p. 73.
6. The refractive index of a finger was found in A. Knüttel and M. Boehlau-Godau, “Spatial confined and temporally resolved refractive index and scattering evaluation in the human skin performed with optical coherence tomography”, J. Biomed. Optics, **5**, 83 (2000).
7. D. A. Soss, “Advances in force-based touch panels”, Information Display, **12,** p. 20 (2007).